SYNTHESIS AND CHARACTERISATION OF TiO_2/ZnO NANOCOMPOSITES IMMOBILIZED ON KAOLIN FOR THE TREATMENT OF TANNERY WASTEWATER

BY

MUSTAPHA, Saheed
PhD/SPS/2015/703

A THESIS SUBMITTED TO THE POSTGRADUATE SCHOOL FEDERAL UNIVERSITY OF TECHNOLOGY, MINNA NIGERIA IN PARTIAL FULFILMENT OF THE REQUIREMENTS FOR THE AWARD OF DEGREE OF PHILOSOPHY (PhD) IN ANALYTICAL CHEMISTRY

JUNE, 2021

ABSTRACT

In this study, the adsorption effect on selected physicochemical parameters from tannery wastewater onto the beneficiated kaolin, kaolin/TiO_2, kaolin/ZnO and kaolin/TiO_2/ZnO nanocomposites was investigated by employing the batch adsorption technique. The effects of pH value on crystal size of TiO_2 and ZnO nanoparticles prepared by sol-gel method were also examined. The kaolin/TiO_2 (KT), kaolin/ZnO (KZ) and kaolin/TiO_2/ZnO (KTZ11, KT21 and KTZ12) nanocomposites were prepared bywet impregnation methods. The prepared adsorbents were characterized using X-ray diffraction (XRD), nitrogen gas adsorption-desorption Brunauer-Emmett-Teller (BET), Fourier transform infrared (FTIR), High Resolution Scanning Electron Microscopy (HRSEM), Energy Dispersive X-ray spectroscopy (EDX), High Resolution Transmission Electron Microscopy (HRTEM) and X-ray Photoelectron Spectroscopy (XPS). The results of the characterization showed the morphology, phase identification, surface area, functional groups as well as the adsorption process involved of the nanoadsorbents. From XRD patterns, it was found that the crystallite size of the synthesized TiO_2 at pH 4-12 and ZnO at pH 6-12 calcined at 450 ^oC were from 5.67 to 15.02 nm and 11.84 to 24.82 nm respectively. The kaolinite (plate-like), anatase (tetragonal) and zincite (hexagonal) shapes of kaolin, TiO_2 and ZnO were further confirmed by the HRSEM and HRTEM. The BET results showed that the surface areas of kaolin/TiO_2 and kaolin/ZnO nanocomposites increased compared to the surface area of the beneficiated kaolin. The XRD and HRTEM results demonstrated that the TiO_2 and ZnO nanoparticles were distributed within the kaolin framework. The EDX analysis also established that the loading correlated to the anchored different ratios of the nanoparticles on the beneficiated kaolin by wet impregnation method. The adsorption method was established to investigate the influence of some experimental parameters such as contact time, adsorbent dosage and temperature. The adsorption isotherm studies were investigated at different temperatures (30-70 ^oC). The adsorption data were fitted to Jovanovic, Halsey, Flory-Huggins and Redlich-Peterson isotherm models. The results indicated that Jovanovic isotherm model best fitted the data in the temperature range studied with correlation coefficient, $R^2 > 0.999$. However, the Flory-Huggins adsorption isotherm explained the spontaneous adsorption system. The experimental results at different contact times were subjected to kinetic adsorption models (fractional power, Bangham and Avrami) and adsorption mechanism determinations (Boyd and intra-particle diffusion). The results showed that the kinetic adsorption process followed Banghham kinetic model. The mechanism for the adsorption of tannery wastewater onto the adsorbents indicates that external mass transfer is the rate-determining step since the plots of Boyd and intra-particle diffusion did not pass through the origin. Thermodynamic studies showed that the adsorption system is temperature dependent since increase in temperature showed increase in the adsorption of the pollutants, indicating that the adsorptivity was endothermic and spontaneous. The values of the thermodynamic parameters; change in enthalpy (ΔH) and change in entropy (ΔS), calculated from Vant's Hoff plots confirmed the spontaneity of the adsorption process. A mechanistic pathway for the synthesized nanocomposites was presented and the nanocomposite filter produced was resistant to temperature above 900 ^oC. The flow rate optimized by changing the proportion of kaolin and saw dust for the filter pot formulation was observed and this served as the controller of the flow rate and percentage porosity of the filter pot. The bactericidal effects of TiO_2 and ZnO nanoparticles in the composites explained the nanoscale and physicochemical properties of the nanoparticles along with surface area of the kaolin. The filtrates using the nanocomposites filter pots gave

concentrations of some investigated physicochemical parameters less than the WHO and NESREA standards. This illustrates that the filter pots nanocomposites could be a potentially safe and viable adsorbent in water filters for water purification systems.

TABLE OF CONTENTS

Content

Page

LIST OF TABLES

Table

Page

LIST OF FIGURES

Figure **Page**

LIST OF PLATES

Plate

Page

ABBREVIATIONS

A and B Redlich-Peterson isotherm constant (L/mg) and exponent, respectively

K_F	Freundlich isotherm constant (mg/g)
Q_m	Maximum monolayer adsorption capacity (mg/g)
n	Adsorption intensity
B_T	Tempkin isotherm constant
ε	Dubinin-Radushkevich isotherm constant
K_s	Sips isotherm model constant (L/mg)
β_s	Sips isotherm model exponent
B and A	Harkin-Jura constants
K_J	Jovanovic isotherm constant (L/mg)
B_K, p and A_K	Koble-Carrigan's isotherm constants
K_e	Elovich equilibrium constant (L/mg)
H, p and F	Jossens isotherm constants
K_{FH}	Flory-Huggins isotherm equilibrium constant (L/g)
θ	Degree of surface coverage
K_1	Hill-de Boer constant (L/mg)
K_2	Energetic constant of the interaction between adsorbed molecules (KJmol^{-1})
K_i	Kiselev equilibrium constant (L/mg)
C_e	Equilibrium concentration (mg/L)
C_{BET}	Adsorption isotherm relating to the energy of surface interaction (L/mg)
C_s	Adsorbate monolayer saturation concentration (mg/L)
q_e	Amount of adsorbate in the adsorbent at equilibrium (mg/g)
q_t	Quantity of adsorbate adsorbed at time t (mg/g)
k_1	Rate constant for the pseudo-first-order sorption (min^{-1})
k_2	Rate constant of the pseudo-second-order kinetic equation (g/mgmin^{-1})

$\propto$	Constant related to chemisorption rate
n_{AV}	Avrami model exponent of time related to the mechanism of adsorption
K_{AV}	Avrami constant
t	Time (min)
C_i	Initial concentration of adsorbate (mg/L),
M	Mass of adsorbent (g)
V	Volume of solution (L)
K_{id}	Rate constant for intraparticle diffusion
F	Fraction of adsorbed metal ion at time, t
R	Universal gas constant (8.314 J/molK)
K_d	Distribution coefficient
T	Temperature (K)
ΔG	Change in Gibbs free energy (kJ/mol)
ΔH	Change in enthalpy (kJ/mol)
ΔS	Change in entropy (J/molK)

CHAPTER ONE

1.0 INTRODUCTION

1.1 Background to the Study

In the last couple of years, population growth, migration, increasing urbanization, industrialization and climate change have influenced the supply and demand chain for

freshwater resources. According to United Nations Department of Economic and Social Affairs (UNDESA, 2013), the world population is projected to reach 9.1 billion by 2050, with more than 2.4 billion living in Sub-Saharan Africa (SSA) without access to sustainable water resources. World Health Organization (WHO, 2015) also reported that more than 1.1 billion people in Africa do not have access to clean drinking water and sanitary facilities due to growing populations and increasing economic activities with deprivation of environmental services.

Industrial production, intensive agriculture, mining and untreated urban run-off have led to increase in water use, having potential impacts on the quality of water. The availability of potable drinking water to households in underdeveloped and developing countries still remains a challenge due to several natural and human factors (Samans *et al.*, 2017). For instance, the continuous discharge of domestic wastewater either black or grey and industrial effluents containing a variety of organic and inorganic pollutants into the ecosystem has become a daily occurrence. Until now, about 20 % of the world wastewater is effectively treated and UN (2016) revealed that almost 70 % of untreated industrial effluents were discharged into the environment. The absence of wastewater management process coupled with anthropogenic activities poses momentous threats to economic activities and well-being of the human race. In Nigeria, many people do not have access to safe water, leading to a looming water crisis (Naik, 2017). This is principally because of water pollution placing the country on the danger of greater outbreak of diseases such as typhoid, polio, cholera and dysentery (Atuyambe *et al.*, 2017). Among various organic and inorganic contaminants discharged into the environment, potential toxic metals (PTMs) also known as heavy metals have been identified as possible causes of human diseases (Vasistha and Ganguly, 2020). These toxic metal ion pollutants in the water bodies have become topic issues to the human race and other living organism due to their detrimental effects. These

metals are mobile, non-biodegradable, recalcitrant and toxic to aquatic species even at low concentrations. The sources of heavy metals in water bodies include electroplating, mining, smelting, pharmaceuticals, battery manufacturing, textile and tannery industries. Specifically, tanning activities generate almost forty million litres of wastewater yearly, containing constituents such as chromium, chloride, lime with high dissolved and suspended salts and other contaminants (Ahmed *et al.,* 2016). In most developing countries like Nigeria, tanning industries discharged wastewater without proper treatment into the sewage system causing a serious detrimental effect on the environment. Therefore, the removal of toxic pollutants such as chromium and other related toxic metals in tannery wastewater is considered imperative.

Several conventional techniques such as reverse osmosis, membrane filtration, electro-coagulation, electro-dialysis, chemical precipitation, adsorption, membrane bioreactor, sludge reactor, amongst others have been employed for the treatment of wastewater. Of all these methods, adsorption is widely used due to its unique nature such as distinct energy saving, cost-effectiveness, simplicity, wide operational range of factors such as pH, concentration, dosage and temperature, environmental friendliness, fast reclamation of organic and inorganic pollutants and easy recycling of the sorbents (Sani *et al.,* 2017; Vahidhabanu *et al.,* 2017). On the other hand, adsorption technology with respect to material used, sometimes does not readily degrade and typically remove pollutants from the wastewater treatment system. In the viewpoint of the shortcomings of adsorption process via the material used, nanotechnology involving the use of nanomaterials as nanoadsorbents has been incorporated to achieve greater efficiency.

Several natural adsorbents such as chitosan (Preethi *et al.,* 2017), carboxymethyl cellulose (Zahedi *et al.,* 2017), clay minerals (Motshekga *et al.,* 2016), zeolite and carbon nanotubes (Bhattachajee *et al.,* 2016) have been used for the sequestration of contaminants from

wastewater. A wide documentations on clay minerals such as kaolinite, bentonite, montmorillonites (smectite), illites, vermiculites and chlorites composed mainly of silica, alumina, water and weathered rock which could serve as alternative cheap materials for remediation of wastewater, free of toxic chemicals have been studied (Uddin, 2016). They possess some unique characteristics compared to other natural adsorbents, used for adsorption of heavy metals and also serve as remedies for ailments and can be used as excellent adsorbents for environmental bioremediation of wastewater (Unuabonah *et al.,* 2017).

In addition, nanoparticles such as metal oxides with dimensions less than 100 nm exhibit exceptional physical and chemical properties and have been utilized for wastewater treatment (Zhang *et al.,* 2016). Crystal morphology and particle size play vital roles in the application, which have led scientific researchers to focus on the synthesis of different nanoparticles like zirconium oxide (ZrO_2) (Zinatloo-Ajabshir and Salavati-Niasari, 2016), zinc oxide (ZnO) (Chang *et al.,* 2020), titanium oxide (TiO_2) (Boudjemaa and Gómez-Ruiz, 2020), magnesium oxide (MgO) (Sagadevan *et al.,* 2020), palladium oxide (PdO) (Muniz-Miranda *et al.,* 2020) and lots more. Both physical and chemical methods have been employed for the synthesis of ZnO nanoparticles which include sol-gel, thermal plasma synthesis, hydrothermal synthesis, spray pyrolysis, chemical precipitation, combustion synthesis and electrochemical routes. Extensive literature evaluation concludes that sol-gel is the commonly selected method for the synthesis of nanoparticles. This is because this method produces excellent crystalline structure and narrow size distribution. It also requires low-temperature, easy composition control and low cost-effectiveness (Mourdikoudis *et al.,* 2018).

The nanosized metal oxides such as zinc oxide and titanium oxide exhibit favourable sorption towards organic and inorganic pollutants and have higher adsorption capacity than

conventional adsorbent (Chouchene *et al.*, 2017; Syngouna *et al.*, 2017). TiO_2 nanoparticles (T-NPs) have received much attention due to their extensive characteristics such as low cost, non-toxicity, high stability (Nasirian and Mehrvar, 2016; Dariani *et al.*, 2016; Lin *et al.*, 2018). In the same vein, zinc oxide is mostly considered as nanoadsorbent due to its non-toxic profile, high adsorptive properties, effective antibacterial activity, chemical, mechanical and thermal stability (Ibrahim and Asal, 2017). ZnO nanoparticles have a higher adsorption capacity than titania nanoparticles for heavy metals removal (Rafiq *et al.*, 2014). However, these nanoparticles are difficult to separate from wastewater after treatment and steps have been adopted to overcome these shortcomings. These include doping and co-doping of metal oxide nanomaterials and immobilization of nanomaterials on suitable matrices (Soltani *et al.*, 2016; Belver *et al.*, 2017). These substrates could function as supports in order to overcome the difficulties involved in post-separation and recovery of the nanoparticles.

More so, the support of nanosized semiconductor materials on matrices help in enhancing their binding activities towards contaminants compared to ordinary bulk nanomaterials (Zhao *et al.*, 2020). Different clay matrices such as kaolinite, montmorillonite and bentonite have been employed as supports. Kaolinite, for instance, has exceptional crystallochemical features and thus could act as a suitable matrix for anchoring TiO_2 and ZnO nanoparticles (Dědková *et al.*, 2015; Hadjltaief *et al.*, 2017). Immobilization and anchoring of nanosized TiO_2 and ZnO nanoparticles on the surface of clay minerals provide more active surface sites, reduce the agglomeration of the nanoparticles and prevents the leaching of nanoparticles to the environment (Ruiz-Hitzky *et al.*, 2019).

Taking into account the fact that rural dwellers are mostly affected by these contaminants from wastewater; a cheaper and more environmentally friendly method for wastewater treatment needs to be adopted before the discharge of industrial wastewaters. Therefore, in

addressing these difficulties, this study focused on the preparation, characterization and application of clay/TiO_2/ZnO filters for the treatment of tannery wastewater.

1.2 Statement of the Research Problem

The contamination of water bodies caused by the discharge of industrial effluents has become alarming. This has led to serious environmental problems because of the high toxicity of the discharged contaminants. Parameter indicators such as temperature, total suspended solids, odour, colour, taste, pH, biological oxygen demand, chemical oxygen demand dissolved oxygen, heavy metals, nitrates and coliform bacteria affects level of contaminants in wastewater. Waterborne diseases such as typhoid fever and dysentery are caused by bacteria, viruses and parasitic worms via water pollution. These diseases have seriously affected man. Sequel to their threat to human and aquatic organism, various attempts have been employed towards removing them from wastewater using techniques such as chemical precipitation, coagulation, electro-dialysis, ion exchange, adsorption, photocatalysis and membrane filtration (Adebayo *et al.*, 2021). Most of these have however been found to be costly and ineffective to completely remove the contaminants from wastewater (Asses and Ayed, 2021). For instance, photocatalysis produces hazardous by-products and are thus difficult to separate from solution after the treatment of effluents (Wang *et al.*, 2020). Several investigations have been submitted on the application of TiO_2 and ZnO nanoparticles for the removal of contaminants from wastewater. However, studies have revealed that these nanoparticles do not possess high specific areas and have strong colloidal stability or low settling velocities in water, making recycling expensive and time-consuming. Thus, immobilization of these nanoparticles on suitable porous carriers is necessary. This will help to enhance filtration and reusability of the nanoparticles during wastewater treatment.

Leather tanning industries have been identified as a major cause of environmental pollution releasing a large quantity of untreated effluent into the atmosphere and water bodies (Jahan *et al.*, 2014). The public concern over tanneries has been pollutants such as chlorides, chromium, sulphide, lead and cadmium. These substances are toxic and persistent causing serious health problem. The common health issues are asthma, diarrhoea, jaundice/typhoid, blood pressure, urticaria, militia, folliculitis, sores, pruritus, eczema, gastrointestinal and eye problems (Mahamudul *et al.*, 2016). Thus, the removal of these substances from tannery wastewater is a key requirement for the safety of public health and the environment.

Various methods have been used to treat tannery wastewater such as flotation, electrochemical treatment, sedimentation, coagulation, filtration, ultra-filtration and reverse osmosis process. However, these methods faced limitations of being highly expensive and energy consuming (Hashem *et al.*, 2020). It is also characterized by high operation and maintenance cost for tannery wastewater and sludge production. On the contrary, nanotechnology offers vast potentials for wastewater treatment and could substitute conventional wastewater treatment technologies. The removal of harmful pollutants in wastewater by TiO_2 and ZnO nanoparticles could be popular materials due to low toxicity of the materials. However, some limitations present in the use of pure TiO_2 and ZnO nanoparticles are low adsorption capacity of pollutants related to its low surface area affecting the removal efficiency of pollutants. Other practical problems are catalyst agglomeration and formation of uniform suspension in water which makes it difficult to recover. This implies that the removal of these nanoparticles could require costly phase separation methods.

1.3 Justification of the Study

Pollutants have globally gained increasing attention due to their detection in the environment and their detrimental effects on human and other life. Over the years, standard

purification techniques have been adopted to remove these pollutants. Amongst these, adsorption has proved to be a simple and environmentally friendly alternative method. This method relies on the use of low-cost adsorbents, which can significantly reduce process costs. Because of its simplicity and cost-effectiveness, the adsorption process has been studied for decades for the treatment of pollutants in tannery wastewater. Thus, adsorption treatment of tannery wastewater will aid in reducing the release of organic and inorganic substances that are hazardous to the environment, human and animal health (Rafiq *et al.,* 2014).

TiO_2 and ZnO nanoparticles are effective nanoadsorbents with low cost and toxicity, a long life span, high activity, and exceptional stability. Because of their decreased mobility in aqueous media, these nanoparticles may be less toxic if properly anchored via a chemical bond to suitable matrices such as kaolin. Kaolin, a cheap, locally available and effective adsorbent as reported by Adeyemo *et al.* (2015), if used for this purpose will certainly solve a lot of water purification problems due to the interaction involved between adsorption and the catalytic activity of the exchangeable cations in wastewater. As a result of the aforementioned features, clay/TiO_2/ZnO nanocomposites will be of interest in this research work considering its enormous surface area and enhanced porosity which is expected to ensure availability of enhanced surface active sites. This in effects will be helpful in improving adsorption and is expected to have enhanced adsorption capacity compared to the mono-metallic nanocomposites.

1.4 Aim and Objectives of the Study

The aim of this research work was to synthesize and characterize titanium oxide/ zinc oxide nanocomposites immobilized on kaolin for the treatment of tannery wastewater. The aim of the study was achieved through the following objectives:

i) Beneficiation and characterization of kaolin

ii) Synthesis of TiO_2 and ZnO nanoparticles by sol-gel method and kaolin/TiO_2, kaolin/ZnO and kaolin/TiO_2/ZnO nanocomposites via wet impregnation.

iii) Characterization of TiO_2 and ZnO nanoparticles, kaolin/TiO_2, kaolin/ZnO and kaolin/TiO_2/ZnO nanocomposites for their surface areas, elemental composition, morphologies, phase structures as well as functional groups.

iv) Determination of physicochemical parameters and bacterial analysis of the tannery wastewater before and after batch adsorption processes.

v) Fabrication of filter pots developed from the beneficiated kaolin, kaolin/TiO_2. kaolin/ZnO and kaolin/TiO_2/ZnO for tannery wastewater.

vi) Performance evaluation of the fabricated filters on the removal of some physicochemical parameters in tannery wastewater.

CHAPTER TWO

2.0 LITERATURE REVIEW

2.1 Water and its Environment

Water is known as one of the abundant natural resources on earth consumed by humans and also as an essential part of life as a universal solvent (Anjum *et al.*, 2016). Among people

in rural communities, the dependence on the use of water from rivers, stream and dams is tremendous. The demand for water for human consumption is affected by growth in urbanization and industrialization. Clean sources of water are becoming scarce, leading to many urban and rural dwellers to pay high price to water vendors. The availability of untreated water has caused debilitating water borne diseases such as diarrhoea, cholera and dysentery (Kumar, 2020). With the continuous trend of this, the global water demand had been projected to increase.

Variation in the distribution and availability of water resources as shown in Figure 2.1 indicates that access to safe water is actually deteriorating. Most problems militating against water availability in developing countries like Nigeria are due to natural and anthropogenic activities which often result to release of pollutants from industrial production, intensive agriculture, mining and runoff of untreated wastewater. In these regions, dwellers who enjoy pipe-borne water are limited. In Nigeria, industrial wastewaters are discharged without proper treatment (UN, 2016). This clearly shows that access to safe drinking water will continue to be a major problem if innovative solutions or advanced technologies are not implemented.

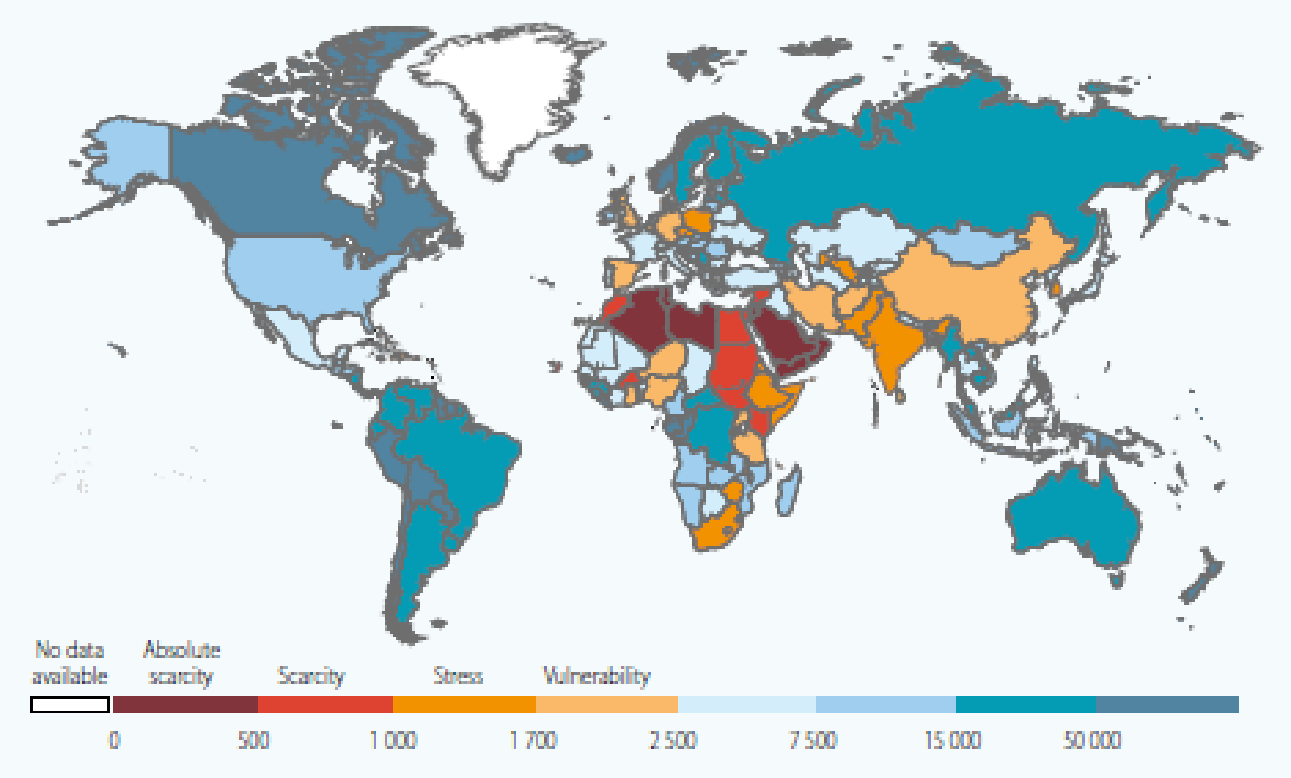

Figure 2.1: Variation in the Distribution and Availability of Water Resources (UNICEF, 2014)

2.2 Water Pollution

Environmental pollutants and their toxicity are a global concern due to adverse changes and severe health challenges. Water pollution has become a global phenomenon, undermining the economic growth, environmental as well as health of many people. Water pollution is a result of introduction of contaminants from natural and anthropogenic activities into water bodies. The release of these contaminants involves using different types of chemicals in industrial sectors (textiles, mining, electroplating, dyeing and tanning), agricultural sectors (such as pesticides, fertilizers, herbicides, fungicides) and medical sectors (such as pharmaceuticals, hormones and personal care products) which are extremely toxic chemicals (Awaleh and Soubaneh, 2014). Most developing countries do not have the required technology to remove contaminants prior to discharge into the environment.

2.3 Industrial Wastewater

For years, rapid industrialization involving the use of synthetic chemicals in various industries during operation in order to meet consumers demand has aggravated the release of toxic substances into the environment. Globally, about 80 % of industrial wastewaters which contain heavy metals, toxic sludge and organic compounds characterized by high chemical oxygen demand (COD), biological oxygen demand (BOD), high pH value, odour, total dissolved solids (TDS), sulphate, phosphate, nitrate and turbidity are released to the water bodies (Khalid, 2018). Specifically, tannery industries (TI) releases wastewater containing phenolic compounds, sulphonated oils, chromium salts, polychlorinated biphenyl used for the conversion of raw hides into leather products (Saxena *et al.*, 2016). The tanning operation involves: (1) wet blue, (2) crust, (3) finished leather. Other sub-processes of tanning include involved bathing, pickling, tanning dyeing and oil.

According to the Nigerian Tanners Council (NTC), tannery industries in Nigeria are among the oldest industries (The News, 2014). Owing to the high production of livestock, Nigeria is rated as one of Africa's leather producing countries. In the past, the leather industry has generated employment the young people in the North-West region of Nigeria. However, the current situation has moribund due to Federal government's intervention on banning of wet blue and crust exports. This has led to the closure of many tannery industries across the nation, making the foreign-owned tanneries to invest on new equipment and other types of machinery. Also, the number of skins produced by traditional tanners has fallen due to the use of low grade skins and wet blue. In view of this, the local tannery industries have relocated to villages and improper disposal of wastewater into water bodies is the order of the day. Since the pattern of activities of these industries have changed, it has led to increase in the release of chemicals into the environment. The release of these toxic substances has

a negative influence on man, plant and other abiotic and biotic forms. A description of tannery wastewater generated from a tannery is displayed in Plate I.

Plate I: Local Tannery Industry (Economist's Correspondent Eleanor Whitehead) (The News, 2014)

2.3.1 Tannery effluents

The tanning process is associated with pre-tanning chemicals such as lime, sodium sulphide, ammonium sulphate, sodium chloride, hydrogen tetraoxosulphate (VI) acid, chromium sulphate and sodium bicarbonate. This technique involves a series of steps as identified in Figure 2.2. The soaking, liming and deliming operations lead to release of toxic pollutants in the effluent. The flow chart shows the input of waste that is either liquid or solid which affect water parameters like COD, BOD, total organic compound, total dissolved solids and heavy metal contents.

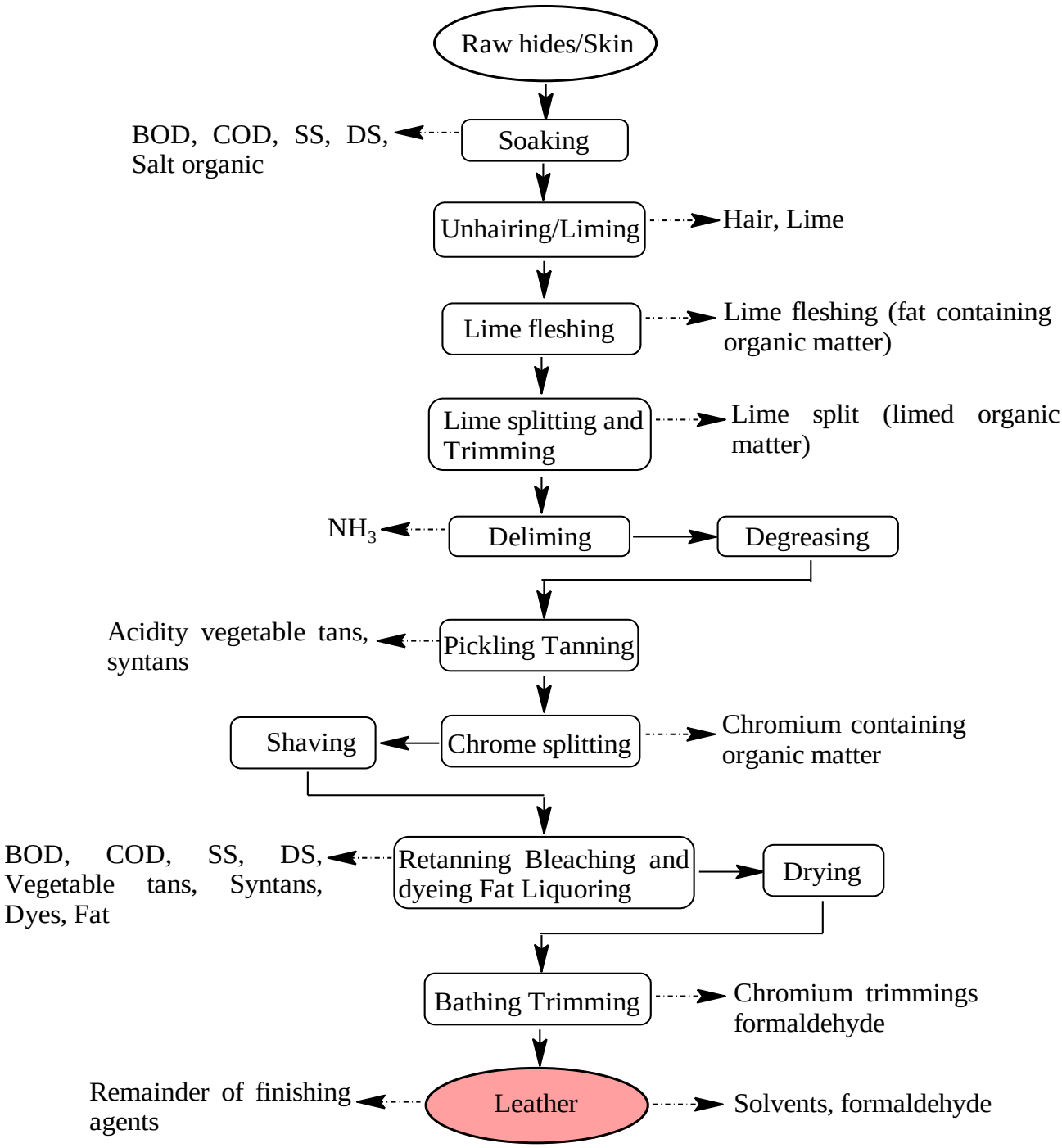

Figure 2.2: A Schematic Diagram of Types of Pollutants Generated in Tanning Process (Hansen *et al.*, 2021)

2.3.2 Effect of tannery effluents

It is asserted that the stages of tanning are capable of releasing effluents that affect environmental parameters. These parameters have a great influence on the quality of water for drinking and farming. The local area of tanning affects people along the swamp and sadly, some of the dwellers appear not to know the health implications of the released wastes in the area. More so, the operators are less or not concerned with the effects of the released chemicals to the water bodies. This poses risks to human health and safety because in most cases, the residents of these areas virtually operate without properly constructed effluent treatment plants. Figure 2.3 illustrates different pollutant pathways affecting the ecosystem

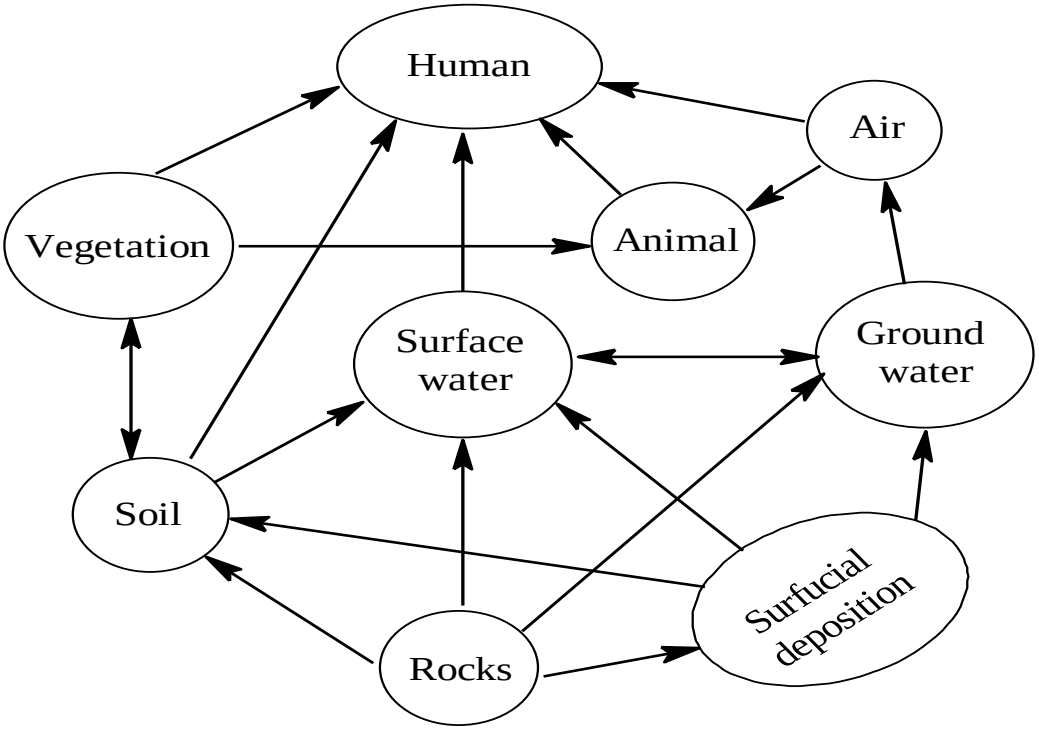

Figure 2.3: The Flow Diagram of Toxic Pollutants Discharged from Tannery Industry in the Environment

The following highlighted points show tannery wastewater as the major source of water and soil pollution

a) Contamination of soil has become a serious problem in most industrialized areas in underdeveloped and developing countries. Soil is referred to as a sink for organic and

inorganic forms of pollutants discharged into the environment via industrial wastewater (Chowdhary *et al.,* 2020). The inappropriate discharge of tannery wastewater leads to soil pollution as well as acidification due to the high concentration of salts present in wastewater (Saxena *et al.,* 2016). The high degree of sulphide content in tannery wastewater has led to the inadequacy of some micronutrients like zinc, copper and iron in the soil subsequently, changing the structure of soil microbial communities and increase in the reactive oxygen species in plants (Langat, 2018). This reduces the growth of plants and a commonest heavy metal, chromium, from tannery wastewater also reduces the bioremediation and thus enter into the food chain. The phytotoxic concentrations of this metal cause skin irritation, ulceration, eardrum perforation, and lung carcinoma in man (Chaudhary *et al.,* 2017).

b) Vegetables planted in most farms are exposed to pollutants in industrial wastewater. The uptake and accumulation of metals at high concentrations from tannery wastewater as a primary polluter is due to the direct/indirect discharge of wastewater into canals/rivers. This water is used by farmers for the irrigation of crops, leading to the movement of toxic metals from water to plants. The bioaccumulation of these potentially toxic pollutants disrupts the physiological and cytological processes in plant cells causing genotoxic problems (Gatta *et al.,* 2018). Furthermore, the effect of tannery wastewater on seedling growth induced the chlorosis, photosynthetic impairment and death of the plant. According to Dixit *et al.* (2015), there has been an increasing concern regarding the release of many endocrine-disrupting compounds (EDCs) along with tannery wastewater (TWW) in the environment. EDCs disturb the delicate hormonal balance and compromise the reproductive fitness of living beings and ultimately may lead to carcinogenesis.

The effluent released to the environment without treatment produces a vast amount of chromium within years causing the contamination of soils and water. Thus, polluting

terrestrial and aquatic ecosystems. To eradicate this, effective effluent treatment processes are needed.

2.4 Wastewater Treatments

Different methods have been developed and used for the treatment of wastewater. Some of the adopted techniques include centrifugation (Peeters, 2015), filtration (Cardenas *et al.*, 2016), flotation (de Oliveira da Mota *et al.*, 2015), oxidation, evaporation (Li *et al.*, 2016), distillation (Ji, 2018), ion exchange (Tan *et al.*, 2017), precipitation (Sun *et al.*, 2017), electrolysis (Huang *et al.*, 2016), electrodialysis (Akhter *et al.*, 2018), adsorption (Guillaume *et al.*, 2018), crystallization (Lu *et al.*, 2107), micro and ultra-filtration (Pinto *et al.*, 2017), sedimentation and gravity separation, reverse osmosis (Venzke *et al.*, 2017) and coagulation (Mousa and Hadi, 2016). Moreover, these technologies have some advantages and disadvantages as shown in Table 2.1.

Table 2.1: Advantages and Disadvantages of Different Techniques in Wastewater Treatment

Methods	Merits	Demerits
Filtration	• Removal of toxic elements • Kill microorganism	• Require regular maintenance
Centrifugation	• Removal of odour • Sedimentation of a heterogeneous mixture	• High energy consumption • Require specialized maintenance
Crystallization	• High efficiency • Energy saving • Low cost	• High heating vapour • Complex operation • High electricity consumption
Flotation	• Good water quality • High sedimentation and removes low-density particles	• High energy consumption • High operating cost • High capital cost
Evaporation/ Vacuum distillation	• Low labour cost • Usable treated water	• Very high capital cost • High cost of chemical consumption • High energy cost • High maintenance costs
Distillation	• High efficiency • Relatively cheap	• High amount of energy • Applicable only a large scale
Reverse osmosis/membrane process	• Relatively low labour cost	• High cost of chemical consumption • High energy cost • High maintenance cost • Low efficiency
Precipitation	• Rapid and efficient process • High quality treated effluent • No loss of sorbent on regeneration	• Expensive • Accumulation of concentrated sludge • High energy cost • High chemical consumption required
Oxidation	• Remove taste and odour • Kill bacteria	• Increased risk of diseases

Electrodialysis	• High quality treated effluent • No sludge production • Little or no consumption of chemicals	• Economically unfeasible • Formation of byproduct • Technical constraints
Solvent extraction	• Decolourization	• Non-removal of nonbiodegradable residues
Ion exchange	• High efficiency • No sludge production	• High cost • Formation of by-product
Bioremediation	• Degradation of organic compounds	• Long treatment time • Large area requirement
Coagulation	• Improve primary treatment • High sedimentation	• Effective at a certain pH range

Sources: Donkadokula *et al.* (2020); Sadegh and Ali, (2021)

2.4.1 Treatment techniques of tannery wastewater

Effluent treatment processes are categorized into: physical, chemical and biological methods. The choice of effluent treatment technique solemnly depends on factors such as efficiency, cost and environmental capability.

2.4.1.1 Physical tannery effluent treatment

The physical tannery effluent treatment process does not require chemicals or biological materials. During this process, tannery effluent is screened to filter out a large object and then treated by means of sedimentation (Bezirgiannidis *et al.*, 2019). Other physical means include oxygenation of the wastewater and the channel of the water through the filter to remove solid materials. The three (3) methods of physical effluent treatment are mechanical treatment, post-purification, sedimentation and sludge handling (Dargo and Ayalew, 2014).

Mechanical treatment

This method includes the screening of the raw effluent to remove coarse materials. Nearly 30-40 % of suspended solids in the raw effluent are removed. This treatment method includes skimming of fat, grease, oil and gravity settling.

Post-purification, sedimentation and sludge handling

These stages are the last steps of effluent treatment from the water phase by gravity settlement. The sludge is dewatered via filter presses and up to 40 % sludge cake is produced.

2.4.1.2 Chemical effluent treatment

Chemical tannery effluent treatment is employed ton remove substances that are detrimental in the tannery effluent. Chemicals such as ferric chloride, alum, ozone, chlorine and lime are used in this treatment method in order to kill harmful microorganisms and remove hazardous toxins. The significance of this method includes the neutralization of the acid content of the water. Lime acts as a base and is added to the acidic tank in order to neutralize the contents (Saranya and Shanthakumar, 2019a).

Chemical oxidation method

Chemical oxidation technology allows the use of chemical oxidants in order to eliminate organic pollutants but the removal of total organic carbon is always difficult (Saranya and Shanthakumar, 2019b).

Ozonation

Ozone is a strong oxidizing agent, soluble in water at certain pressure and temperature. It is unstable and then reacts to form:

$$O_3 + H_2 + e^- \rightarrow O_2 + H_2O \qquad (2.1)$$

It is effective as a decolourization agent and also as an oxidant of organic material (Sivagami *et al.,* 2018).

2.4.1.3 Electrochemical method

Electrochemical treatment is employed to improve the performance of effluent treatment by coagulation and flocculation method. It has also demonstrated that a high amount of total organic carbon removal is faster than biological treatment (Chandrasekaran *et al.*, 2019). This is attributed to the oxidation of adsorbed organic compounds to carbon dioxide. Some heavy metals that are successfully removed by this method are arsenic, lead, chromium and cadmium. However, the electrochemical method can also be used in post-treatment stage.

2.4.1.4 Coagulation and flocculation

The coagulation-flocculation method is used to separate solid materials in tannery effluent, stabilize the charged particles, allowing inter-particles collision to occur and thus generate floc. The principal goal of this method is to destabilize the charged particles of suspended solids in the effluent (Fersi *et al.*, 2018). The addition of coagulants to tannery effluent neutralizes the negative charge of the suspended particles thereby coagulating the suspended particles to form larger particles. This step is followed by flocculation where the particle size will be transformed to visible suspended solid (Verma *et al.*, 2019).

2.4.1.5 Advanced oxidation technique

The advanced oxidation technologies (AOTs) such as wet oxidation, ozonation, Fenton, photo-Fenton, photocatalysis and wet oxidation and generate radicals in driving oxidation for the treatment of tannery effluents. Among the AOTs, Fenton process is the most promising technique for the treatment of tannery effluents. Although, the cost implication of this method is quite challenging, as AOTs are much more expensive than other methods (Korpe *et al.*, 2019).

2.4.1.6 Electro-oxidation (EO)

The electrochemical oxidation of tannery wastewater is employed on application of electricity both in the direct and indirect systems. The effectiveness of this method depends

on the nature of the electrode used and the mode of operation. Over the decades, it has been reported that the electro-catalytic and electrochemical stability of electrode affects the process performance, mechanisms and kinetics of pollutant degradation in effluents (Arokianathana *et al.,* 2019).

2.4.1.7 Biological treatment

Biological treatment of tannery wastewater is favourable and economical compared to some physicochemical methods. This method is usually employed as a secondary treatment option after primary treatment for the removal of dissolved organic and nutrient from tannery effluent. Different microorganisms are used to reduce pollutants either in the presence or absence of oxygen. Biological treatment method includes aerobic and anaerobic biological processes (Le Luu *et al.,* 2020).

Aerobic biological treatment

The aerobic biodegradation is the process where oxygen is needed by degradable organisms in their metabolic sites. The microorganism uses growth substrate as organic carbon in the effluent and converts it to carbon dioxide. During this process, a large amount of sludge is produced at high energy consumption rate. The aerobic biodegradation is sub-classified into activated sludge reactor and membrane bioreactor (Sodhi *et al.,* 2020).

Anaerobic biological treatment

The method of anaerobic degradation is the breaking down of biodegradable materials using microorganisms in the absence of oxygen. This method converts organic pollutants and organic acids in tannery effluents into small amounts of sludge and biogas (methane and carbon dioxide). This anaerobic degradation does not only reduce the COD and BOD the tannery effluents, but also generates renewable energy**.** This treatment technique is sub-divided into anaerobic activated sludge process and anaerobic biological membrane process (Alemu *et al.,* 2016). Among the methods enumerated above, adsorption is found to be the

most promising method owing to its simplicity, environmental friendliness, adsorption efficiency and cost-effectiveness.

2.5 Adsorption Technology

Adsorption is a process which is widely used to remove pollutants from fluid phases. In water treatment systems, adsorption is a multiple sequestration of solutes. As presented in Figure 2.4, the solid surface (adsorbent) provides the surface for the adsorption of adsorbates. The change in properties of sorbates like concentration, temperature, dosage and pH affect its release from the surface and transfer back into the liquid phase (a process called desorption).

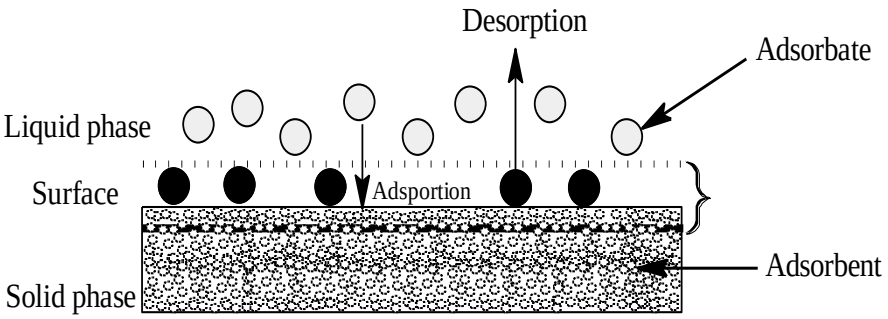

Figure 2.4: Basic Terms in Adsorption

Adsorption technology depends on utilization of either modified or unmodified adsorbents controlled by parameters such as contact or residence time, pH, concentration, temperature and adsorbent dosage based on batch adsorption mode (Al-Essa and Khalili, 2018). The phenomena governing the uptake of pollutants from wastewater onto different adsorbents are strong forces and weak bonds. Another adsorption process can be by column studies, although the batch adsorption is widely utilized for wastewater treatment based on its simplicity and general application on small scales in order to assess the adsorptive capacities of adsorbents in static conditions (De Gisi *et al.*, 2016).

2.5.1 Physical and chemical parameters affecting adsorption

The commonly discussed parameters relevant to adsorption processes include contact time, temperature, adsorbent dosage and concentrations. This section focuses on the characteristics of adsorption capability based on surface chemistry, density and porosity.

2.5.1.1 Surface chemistry

The surface chemistry of adsorbent depends on its interaction with sorbate. Parameters such as electrostatic interaction, bonding and presence of acidic/basic sites influence adsorption. Another important adsorption parameter is the pH of adsorption. The surface charge of adsorbent depends on the variation of solution pH in accordance with isoelectric point (Marco-Brown *et al.,* 2018).

2.5.1.2 Density and porosity

Adsorbents are porous solids and their behaviour in aqueous solutions differ with porosity and density. In general, distinctions among adsorbents are based on the material, particle size and bulk density which solely depend on volume. The porosity of an adsorbent describes the void space on the total volume. The porosities of adsorbents are derived from their densities and the total volume is distinguished between the particle and the bulk porosity (Ladshaw *et al.,* 2019).

2.5.2 Adsorption isotherms and kinetics

Some theoretical approaches have been employed to explain the interaction between adsorbents and adsorbates. These include equilibrium isotherm, kinetic and thermodynamic studies. Adsorption equilibrium provides the physicochemical results applicable to sorption processes while kinetic measures the transport mechanism of the adsorbates in the adsorbent and this comprises external mass transfer of the sorbate from the bulk solution to the surface of the sorbent, the internal diffusion of the sorbate to the adsorption site and adsorption process (González and Pliego-Cuervo, 2014). On the other hand, thermodynamic describes

the attractive and repulsive interactions such as electrostatic or dipole and van der Waals, expressed in terms of free energy (Prusty *et al.*, 2018).

Over the decades, various types of equilibrium isotherms and kinetic models have been used to discuss the dynamic adsorption behaviour of pollutants onto adsorbents. Table 2.2 shows some equilibrium isotherm and kinetic models used in wastewater adsorption process that are formulated in terms of modelling analysis, operational design and applicability.

Table 2.2: List of Adsorption Isotherms and Kinetics Models

Model	Equation	Linear form	Reference
Isotherm	Freundlich	$\ln q_e = \ln K_F + \frac{1}{n}\ln C_e$	Freundlich (1906).
	Langmuir	$\frac{C_e}{q_e} = \frac{1}{bQ_o} + \frac{C_e}{Q_o}$	Langmuir (1916)
	Tempkin	$q_e = a + B_T \ln C_e$	Temkin and Pyzhev (1940)
	Dubinin-Radushkevich	$\ln q_e = \ln Q_m - k\varepsilon^2$	Dubinin and Radushkevich (1947).
	Redlich-Peterson	$\ln \frac{C_e}{q_e} = \beta \ln C_e - \ln A$	Redlich and Peterson (1959)
	Sips	$\beta_s \ln(C_e) = -\ln\left(\frac{K_s}{q_e}\right) + \ln(a_s)$	Sips (1948)
	Harkin-Jura	$\frac{1}{q_e^2} = \frac{B}{A} - \left(\frac{1}{A}\right)\ln C_e$	Jura and Harkins (1944)
	Jovanovic	$\ln q_e = \ln q_{max} - K_J C_e$	Jovanovic (1969)
	Koble-Carrigan	$\frac{1}{q_e} = \left(\frac{1}{A_K C_e^p}\right) + \frac{B_K}{A_K}$	Koble and Corrigan (1952)
	Jossens	$\ln\left(\frac{C_e}{q_e}\right) = -\ln(H) + F q_e^p$	Jossens *et al.* (1978)
	Elovich	$\ln\left(\frac{q_e}{C_e}\right) = \ln K_e q_m - \frac{q_e}{q_m}$	Elovich and Larinov (1962)

	Flory-Huggins	$\ln\left(\frac{\theta}{C_o}\right) = \ln K_{FH} + n\ln(1-\theta)$	Flory (1941)
	Hill-Deboer	$\ln\left[\frac{C_e(1-\theta)}{\theta}\right] - \frac{\theta}{1-\theta} = -\ln K_1 - \frac{K_2\theta}{RT}$	De Boer (1953)
	Kiselev	$\frac{1}{C_e(1-\theta} = \frac{K_i}{\theta} + K_i K_n$	Kiseler (1958)
	Brunauer-Emmett-Teller	$\frac{C_e}{q_e(C_s - C_e)} = \frac{1}{q_m C_{BET}} + \frac{(C_{BET}-1)C_e}{q_m C_{BET} C_s}$	Bruanuer *et al.* (1938)
Kinetic	Pseudo-first-order	$\ln(q_e - q_t) = \ln q_e - k_1 t$	Lagergren (1898)
	Pseudo-second-order	$\frac{t}{q_t} = \frac{1}{q_e^2 k_2} + \frac{t}{q_e}$	
	Elovich	$q_t = \propto \ln(a\alpha) + \alpha \ln t$	Elovich and Larinov (1962)
	Avrami	$\ln[-\ln(1-\propto)] = n_{AV}K_{AV} + n_{AV}\ln t$	Avrami (1940)
	Boyd	$F = \frac{q_t}{q_e} = 1 - \frac{6}{\pi^2}\exp(-B_t)$	Boyd *et al.* (1947)
	Bangham	$\log\left[\log\left(\frac{C_i}{C_i - q_t M}\right)\right] = \log\left(\frac{K_j M}{2.303V}\right) + \alpha \ln t$	
	Weber and Morris	$q_t = K_{id}\sqrt{t} + A$	Weber and Morris (1963)
	Fractional power	$\log q_t = \log K + V \log t$	

2.6 Nanotechnology for Wastewater Treatment

The application of physical, chemical and biological processes for wastewater treatment has some drawbacks due to the presence of some non-biodegradable pollutants which are sometimes toxic to microorganisms. Currently, nanotechnology in lieu of traditional

treatment methods has shown some potentials in the areas of adsorption for wastewater remediation (Zekic *et al.*, 2018).

Over the past decades, researchers have shown vast interests in the area of nanotechnology for wastewater treatment and possible improvement of the existing methods. Nanotechnology is a field of science where materials with dimensions less than 100 nm are developed in various forms (Jeevanandam *et al.*, 2018). These include nanotubes, nanowires, particles, films, fibres, colloids, nanorods and quantum dots or nanocrystals as shown in Figure 2.5.

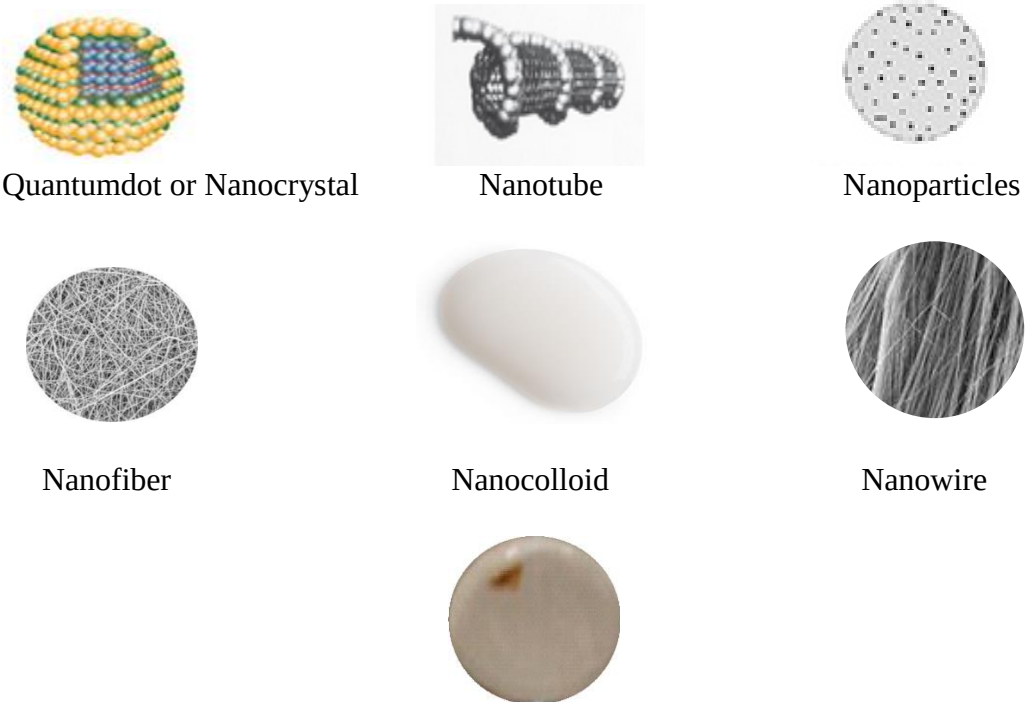

Figure 2.5: Images of some Nanomaterials (Jeevanandam *et al.*, 2018)

The environmental applications of nanotechnology include removal or degradation of hazardous materials, production of sensors for environmental protection and pollution preventers (Khan *et al.*, 2017). The unique properties of nanomaterials are high reactivity, large surface area, easy separation, small size, act as catalysts and presence of active sites for binding of pollutants (Khan *et al.*, 2019).

Nanomaterials are categorized into (1) nano-adsorbents (2) nano-membranes and (3) nano-catalysts (Singh *et al.,* 2017). Numerous works have been done using nanoadsorbent materials in water adsorption technology. The properties of these nanomaterials are responsible for high removal capacities of pollutants in wastewater. The commonly used materials for wastewater remediation are clay, activated carbon and silica, metal oxides such as titanium oxide, zinc oxide, nickel oxide, iron oxide, tungsten oxide, copper oxide, alumina, gold and zirconia. Along with other metal oxide nanomaterials, titanium oxide (TiO_2) and zinc oxide (ZnO) have attracted the interest of scientists in wastewater treatment processes. Apparently, nanomaterials have effectively contributed to the establishment of robust and cost-effective water adsorption techniques (Gehrke *et al.,* 2015).

2.7 Nanoparticles

2.7.1 TiO_2 nanoparticles

Titanium dioxide (TiO_2) is popularly known as a promising semiconductor material which has drawn a lot of attention due to its non-toxicity, chemical and biological stability and photocatalyst-adsorption activities (Khalid *et al.,* 2017). TiO_2 has proved some successful applications in various areas such as environmental purification (degradation of pollutants and anti-microbial properties), solar cells, generation of hydrogen gas, catalyst support, filler, gas sensors, pigment, anti-fog and anti-freeze mirrors (MiarAlipour *et al.,* 2017; Askari *et al.,* 2017).

The aforementioned characteristics and applications strongly depend on the morphology structure, particle size, surface area and phase of the nanoparticles. During the application of this material as an adsorbent in aqueous solution, recovery of the catalyst remains the major setback. This problem is projected to be overcome by the application of porous adsorbents as suitable supports in order to reduce or eliminate the expensive TiO_2 recovery techniques (de Oliveira-Pereira *et al.,* 2019).

2.7.2 ZnO nanoparticles

ZnO is classified as II-VI type semiconducting metal oxide with physical and chemical properties such as non-toxicity, chemical stability, radiation absorption, electrical activity and high photostability (Modwi *et al.,* 2016). ZnO nanoparticles were found to be cheap to produce, safe and easily handled. This catalyst is also known as a multifunctional material due to its wide range of applications. The unique properties of ZnO like sunscreen lotion make it extensively applicable in biomedicine like drug delivery, anti-cancer, anti-diabetic, anti-fungal and anti-bacterial properties. Owing to the anti-bacterial properties of ZnO nanoparticles, it is used as a dermatological substance for curing inflammation and itching (Basnet *et al.,* 2018).

2.7.3 Synthesis and characterization of nanoparticles

Basically, the methods of synthesizing ZnO and TiO_2 nanoparticles are mainly classified into the top-down and the bottom-up techniques. The top-down is further sub-divided into physical and chemical processes. This involves metallurgical, laser ablation, solid-state and mechanochemical processes. The bottom-up method involves co-precipitation, hydrothermal, solvothermal, sol-gel and spray pyrolysis techniques (Mokhena *et al.,* 2020). Lastly, there is the biological method of nanoparticles synthesis using plant extracts.

Furthermore, the synthesis of titanium oxide and zinc oxide nanoparticles as shown in Figure 2.6 can be categorized into three major classes: (1) liquid phase (2) gas phase and (3) vapour phase.

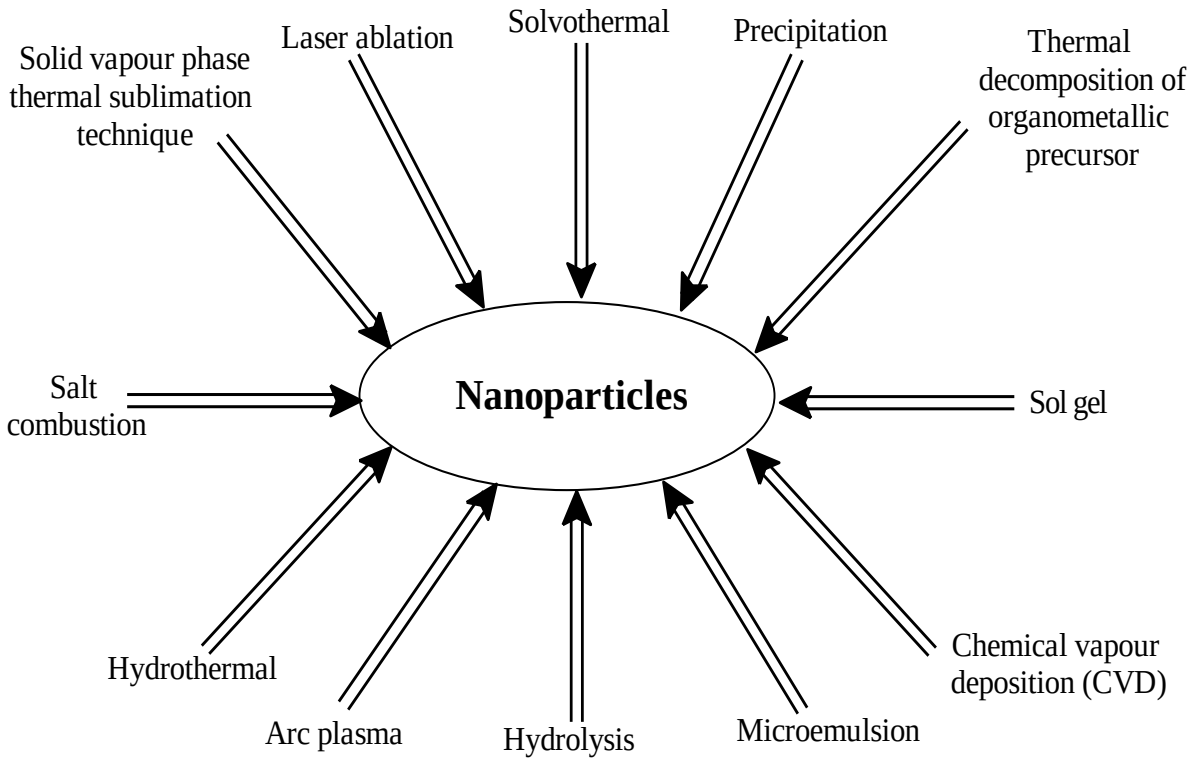

Figure 2.6: Techniques for the Formation of Titanium (IV) oxide and Zinc oxide Nanoparticles

Different methods have been utilized to prepare TiO_2 and ZnO nanoparticles and the ensuing explanations on the synthesis of the nanoparticles emphasized on some chemical and physical techniques.

2.7.3.1 Hydrothermal method

Hydrothermal synthesis is conducted in an autoclave with Teflon liners under controlled temperature. This method is employed without the use of organic solvents and further processing of the products which makes it environmentally friendly and an easy method. This technique occurs in an autoclave, where the mixture of substrates is heated at 100-300 ^{o}C and then left for days. Due to heating followed by cooling, crystal nuclei develop, which then grow into particles. The advantages of this method include synthesizing at low temperature, the different shapes of the resulting crystals depend on the composition of the precursors, degree of crystallinity of the product, purity of the precursors, the process temperature and pressure (Qin *et al.*, 2019).

2.7.3.2 Controlled precipitation

The controlled precipitation method is commonly used to produce a material with repeatable properties. The technique involves a spontaneous and fast reduction of a solution of zinc or titanium salt via reducing agents, to obtain the growth of crystalline particles with common dimensions, followed by precipitation of the starting material from the solution. Afterwards, the starting material undergoes thermal treatment, followed by milling to get rid of impurities. The method of precipitation is controlled by pH, temperature and stirring time in order to prevent agglomerated particles (Hosseini *et al.*, 2019).

2.7.3.3 Microemulsion or emulsion method

An emulsion is classified into two groups based on the nature of the external phase. These groups are oil-in-water (O/W) and water-in-oil (W/O) emulsions. This method involves the use of a stable, transparent, isotropic liquid consisting of an aqueous and oil layer and a surfactant. For example, precipitation of TiO_2 and ZnO from metallic oleate (dissolved in decane) with sodium hydroxide dissolved in ethanol/water. In this method, the material is either formed spontaneously or non-spontaneously in appropriate conditions (Wang, 2019).

2.7.3.4 Mechanochemical method

ZnO and TiO_2 can be produced in large scale using mechanochemical approach. This method is energy consuming which initiates a reaction through dry milling. A thinner, in the form of NaCl, is added to the system that acts as a reaction medium and separates the nanoparticles. The advantages of this method include small grain sizes, a low tendency for particles to cluster and high homogeneity of the grain structure and morphology. One of the disadvantages is the milling time which leads to a large amount of impurities. This is as a result of uniform grinding of the powder and reduction of crystals to the required size (Al-Shaeri *et al.*, 2019).

Other methods of preparing TiO_2 and ZnO include liquid-phase, vapour transport and microwave-sonochemical methods. An example of liquid-phase method is the laser ablative deposition (PLD) which involves the production of nanoparticles with a narrow size distribution and low level of impurities. The vapour transport process is used to synthesize ZnO and TiO_2 in the catalyst-free vapour solid (VS) process and catalyst-assisted vapour liquid-solid (VLS) process. The VS process is used to produce nanowire, nanorods and nanobelt (Liu *et al.,* 2018).

2.7.3.5 Solvothermal process

The solvothermal method is similar to the hydrothermal method except that the solvent used is non-aqueous and high temperature is needed for the production of the nanoparticles. The solvothermal method has better control of the crystallinity, size and shape distribution of ZnO and TiO_2 nanoparticles. Furthermore, this method has been found to be a versatile technique for the synthesis of TiO_2 and ZnO having narrow size distribution and dispersivity (Prabakaran *et al.,* 2019).

2.7.3.6 Chemical vapour deposition

The vapour deposition is a technique in which the precursor in the vapour state is condensed to form a solid-phase material. This process is used to form coatings to change the mechanical, optical, thermal, optical, electrical, corrosion and wear resistance characteristics of different substrates. Chemical vapour deposition requires thermal energy to heat the gases in the coating chamber and drive the deposition reaction. The deposition is controlled to nanoform under the influence of flow rate, gas composition, deposition temperature, pressure, and deposition chamber geometry (Dediu *et al.,* 2019). The wet chemical methods have been known to be the best and these include microemulsion, hydrothermal, solvothermal and precipitation. Among these methods, the sol-gel method

has been reported to be simple, economical and most often used to synthesize TiO_2 (Dodoo-Arhin *et al.,* 2018) and ZnO (Kaneva *et al.,* 2016) nanoparticles.

2.7.3.7 Sol-gel method

Sol-gel is a sophisticated method used in the field of material science also known as chemical solution deposition for the production of nanoparticles. The sol-gel method mainly encompasses the use of a chemical solution which acts as the precursor for the gel of either separate or network particles. The method helps to control the stability of the precursor and phase formation of nanoparticles. During this process, the gel which contains alcohol, precursor and water comprises interconnected porous matrix. An integrated network gel-like diphasic solution containing both liquid and solid phases is produced while the typical precursors of the metal oxide nanoparticles on addition of water form a colloids (Kumar *et al.,* 2015). At this stage, the particle density may be low in such a way that the amount of fluid may need to be evacuated for a complete gel-like property to be known. This can be achieved firstly, by allowing sedimentation to occur and then pour off the liquid and secondly, by centrifugation for phase separation (Matter *et al.,* 2019).

The removal of the remaining solvent phase needs a drying process to enable densification and reduction in size. Afterwards, the metal oxide as aerogel would be obtained either by evaporating the solvent used during the time of washing from the wet gel or by supercritical drying. Importantly, the produced gel can be classified into two forms depending on the kind of solvent utilized namely; aqueous (use of water) and non-aqueous (use of organic solvent) sol-gel (Rao *et al.,* 2017). Further treatment of the wet gel could also convert the gel into dense glass or ceramic, which offers high purity, uniform nanoparticles at low processing temperature, molecular homogeneity and fine particle size as shown in Figure 2.7. However, parameters such as the addition of reactants, temperature of calcination, pH

and solubility of chemicals in the solvents affect the molecular homogeneity of the gel (Bahar *et al.*, 2017).

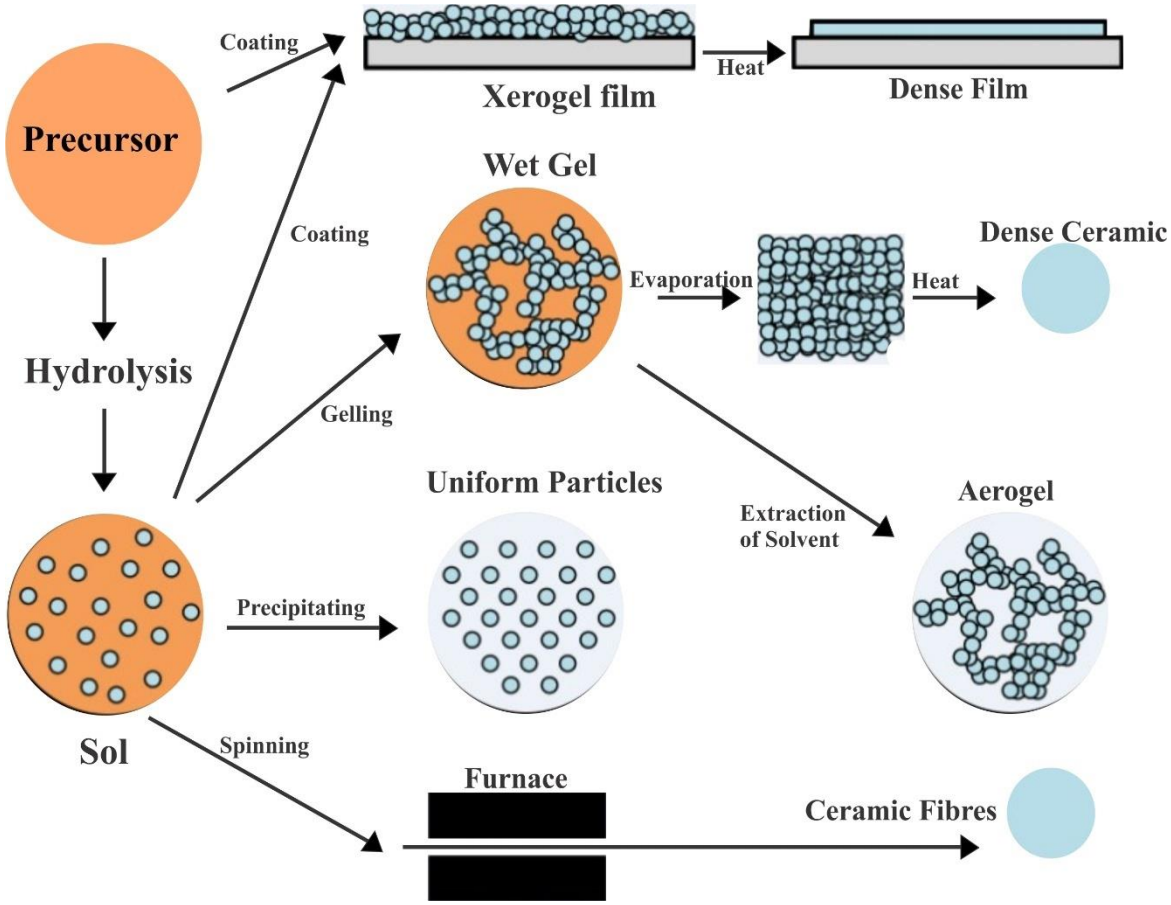

Figure 2.7: Different Stages and Routes of the Sol-gel Method (Rao *et al.*, 2017).

2.8 Synthesis and Mechanism of TiO_2 Nanoparticles Formation

TiO_2 is a white solid crystalline powder insoluble in water. TiO_2 has been considered a non-toxic nanomaterial that possesses high stability and catalytic efficiency (Bagheri *et al.*, 2014). TiO_2 is also known as titania and naturally exists in three forms namely anatase, rutile, and brookite. Both the anatase and rutile forms have tetragonal shapes while brookite has an orthorhombic shape as described in Figure 2.8. Other phases that can be produced are TiO_2B, TiO_2H (hollandite-like form), TiO_2R (ramsdellite-like form), TiO_2II (α-PbO_2-like form), akaogiite (baddeleyite-like form, 7 coordinated Ti), TiO_2O, cubic form, and TiO_2

OII (cotunnite $PbCl_2$ like) (Ullatti *et al.*, 2017). Hydrolysis, condensation and calcination are usually involved in the synthesis of anatase, rutile and brookite phase TiO_2 nanoparticles.

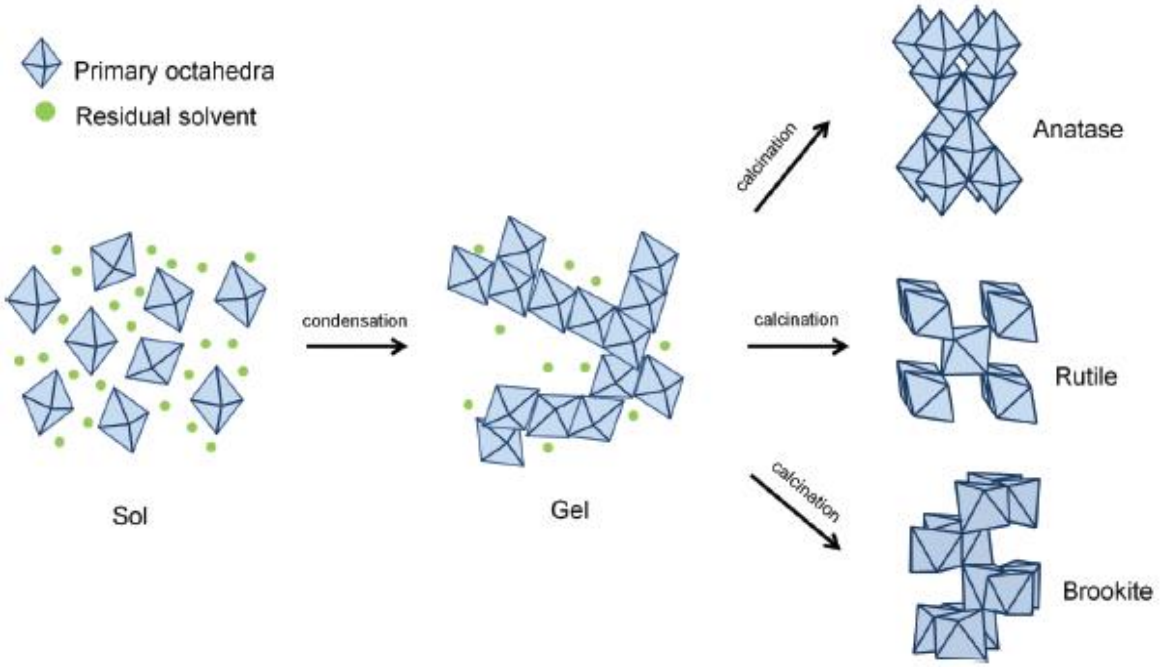

Figure 2.8: Steps for the Synthesis of Crystalline Anatase, Rutile and Brookite TiO_2 Nanoparticles (Yahaya *et al.*, 2017).

The sol-gel method is commonly used to synthesize TiO_2 nanoparticles and the frequent metal and non-metal alkoxides precursors are titanium(IV) tetraisopropoxide (TTIP), titanium chloride, titanium(IV) tert-butoxide, bis (cyslooctatraene) titanium, tetraisopropylorthotitanate (TIPT), potassium titanium oxalate (KTO), butyl titanate (TBT) and titanium(IV) butoxide (Morales *et al.*, 2013; Singh *et al.*, 2017). During this process, the colloid is formed after the hydrolysis and polycondensation reactions. An acid and a base help in the hydrolysis of the precursor followed by the growth and agglomeration of particles. This process proceeds by hydrolytic polycondensation of titanium precursors being alkoxides or chlorides in the presence of solvents, modifiers, and organic templates. The reaction starts with hydrolysis, which is the formation of Ti-OH moieties by the substitution reaction of water with Ti-OR groups. The precursors undergo condensation

reactions to produce Ti-O-Ti by oxolation or Ti-OH-Ti bonds by olation (Islam *et al.*, 2017). The mechanisms for the formation of TiO_2 nanoparticles are presented in Figure 2.9.

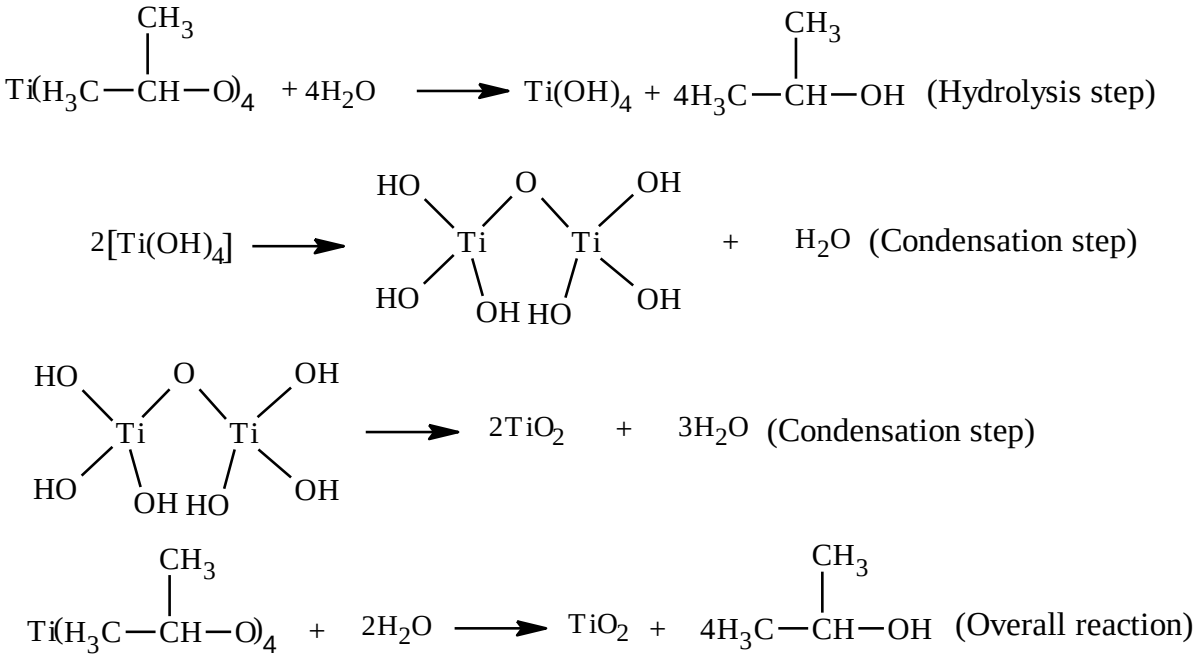

Figure 2.9: Hydrolysis and Condensation Reactions of Titanium isopropoxide for TiO_2 Production.

Various researchers have outlined some steps for the synthesis of TiO_2 which are as follows: According to Devi *et al.* (2014), TiO_2 powder was synthesized using TTIP as a precursor via sol-gel method. The synthesis was carried out by mixing TTIP with HCl, ethanol and deionized water for 1 h 30 min at pH 1.5. The solution was stirred for 2 h at room temperature. The resultant solution was first allowed to dry at room temperature and finally calcined at 120 ^oC for 1 h.

The preparation of TiO_2 via sol-gel method as described by Phonkhokkong *et al.* (2016) was between the mixture of titanium(IV) butoxide ($Ti(OBu)_4$) and ethanol as a complexing agent. The solution was stirred for 2 h and hydrolyzed on the addition of water and ethanol in drops. The mixture was stirred for another 2 hr and a white precipitate was formed on copious washing with ethanol and distilled water. Furthermore, the obtained precipitate was oven-dried at 100 ^oC and calcined at 400 ^oC for 2 h.

Titanium isopropoxide ($Ti(OCH(CH_3)_2)_4$) and citric acid ($((C_3H_5O(COO)_3)H_3 \cdot H_2O$) were used as precursors at the mole ratio of 1:3 respectively according to the method adopted by Pookmaneea and Phanichphant (2014) to synthesize TiO_2 powder. The solution pH was adjusted with NH_4OH to obtain the pH value of 2, 4 and 6. The white precipitate formed was washed, filtered and oven-dried at 80 ^oC for 24 h. The white powder was further calcined at 400 ^oC and 800 ^oC for the three classes of TiO_2 powder.

Liu *et al.* (2014) prepared TiO_2 powder using dibutyl phthalate and ethyl alcohol. The solution was stirred for 30 min, mixed with de-ionized water and drops of concentrated HCl were added to the mixture. The authors failed to ascertain the exact pH of the solution. The resultant gel was oven-dried at 80 ^oC for 7 h. the TiO_2 powder nanoparticles were obtained by calcining the dried sample at 550 ^oC for 2 h.

A sol-gel technique of synthesizing mesoporous TiO_2 using polyacrylamide (PAM) and polyethylene glycol (PEG) was applied by Yin *et al.* (2016). The starting material, tetrabutyl titanate was mixed with nitric acid and ethanol. The mixture was stirred at room temperature for 1 hr. To the solution, PAM and PEG were added and vigorously stirred. A white gel was formed and then dried at 80 ^oC for 10 h.

TiO_2 nanostructures were prepared by sol-gel method as reported by Kavitha *et al.* (2014). The single-step method of TiO_2 powder nanoparticles synthesis was obtained by mixing TTIP, acetic acid and distilled water. The resultant solution, $Ti(OH)_4$ was stirred vigorously for 1 hr and allowed to age for 24 h. The solution was oven-dried at 70 ^oC for 12 h and TiO_2 nanoparticles were obtained by further oven drying the powder.

Bahar *et al.* (2017) synthesized TiO_2 nanoparticles by sol-gel method using $TiCl_4$ as the precursor. The synthesis of TiO_2 powder occurred as a result of the mixture of $TiCl_4$ with ethanol, stirred at 2500 rpm but the authors did not stipulate the time required for the stirring of the nanoparticles. The solution was left at ambient temperature for 24 h, oven-dried for

80 °C and then calcined at 450 °C. The authors failed to specify the time required for stirring the mixture and the calcination temperature.

Divya *et al.* (2017) synthesized TiO_2 nanoparticles using sol-gel process. In their preparation, TTIP was added in drops to water ad propanol. The pH of the solution was adjusted using HNO_3 and a white precipitate was formed before and after stirring. The precipitate was oven-dried at 60 °C for 1 h 30 min in order to allow the precipitate to settle. The precipitate was washed for the removal of impurities and further oven-dried to obtain a white powder of TiO_2.

In another study by Hayle and Gonfa (2014), TiO_2 powder was synthesized by sol-gel technique. The $TiCl_4$ was added to de-ionized water and ethanol and vigorously stirred for 30 min at ambient temperature. The precipitate was formed on dropwise addition of NH_4OH and neutralized with de-ionized water by washing. The precipitate was washed with de-ionized water for the removal of impurities and chloride ions. The precipitate was oven-dried at 200 °C for 4 h and amorphous TiO_2 nanoparticles were obtained at the calcinated temperatures of 250 °C, 400 °C and 600 °C for 4 h.

Moussaoui *et al.* (2017) prepared nanocrystals of TiO_2 xerogel and aerogel using an acid-catalyzed sol-gel method. The synthesis of these nanoparticles began by reacting the solution of TTIP in isopropyl alcohol with water. The solution was stirred at room temperature and the formation of white precipitate known as $Ti(OH)_4$ was left overnight in order to ensure complete hydrolysis. The alcohol was then separated from the mixture using rotary evaporator and drops of acetic acid were added. The precipitate was transferred to a Teflon-lined stainless-steel autoclave and heated at 300 °C and 100 bars for 1 h to produce TiO_2 aerogel. However, the second class of the nanoparticles known as TiO_2 xerogel was prepared by drying at 200 °C under an atmospheric condition for ten days.

In general, the sol-gel method consists of the transformation of a system from a liquid phase (sol) to a solid phase (gel) (Danks *et al.*, 2016). Various precursors such as organic alkoxides and acetates, in addition to inorganic salts like chlorides, are utilized for the synthesis of nanoparticles. Alcohols are greatly used among various kinds of solvents, although some other solvents could be used for some alkoxides. Some parameters such as the amounts of reactants, the temperature, stirring time, the ratio of water to titanium, the solubility of reagents in the solvents and the pH affect the homogeneity of the gel. Calcination temperature and pH are paramount factors which help in giving the nanoparticles better surface areas. All researchers that have worked on the production of TiO_2-NPs using sol-gel method, examined and confirmed the formation of these methods using instruments such XRD (X-ray diffraction), SEM (scanning emission microscope), PL (photo-luminescence), HRTEM (high-resolution transmission microscopy), BET (Brunauer Emmett Teller), TGA (thermogravimetry analysis) and SAED (selected area electron diffraction). These researches include Sharma *et al.* (2014), Phonkhokkong *et al.* (2016) and Kavitha *et al.* (2014).

2.8.1 Factors affecting TiO_2 nanoparticles synthesis

The forms of TiO_2 vis-a-vis arrangement of titanium and oxygen atoms in the crystal lattice depend on the nature of the solvent, precursor type, calcination temperature, pH, additives, and stirring time which ultimately determines the phase types of TiO_2 synthesized (Agartan *et al.*, 2013; Islam and Basu, 2015).

2.8.1.1 Effect of calcination

Calcination is a thermal treatment process in the presence of a limited supply of air required for thermal decomposition. The effect of calcination temperature on the phase of TiO_2 from 100 to 1000 °C was evaluated by Pavel and Radovan (2015). The authors reported the formation of anatase TiO_2 at 500 °C, which however transformed to rutile phases at 800 °C.

The authors concluded that 600 °C was the convenient temperature to achieve the highest efficiency of the nanoparticles of the anatase phase of TiO_2 synthesized.

Abdullah *et al.* (2017) demonstrated the effects of calcination temperature on nanocomposite used in the photocatalytic degradation of phenol by ZnO/TiO_2 nanocomposites under visible light. The nanocomposites (ZnO/TiO_2) produced at 600 ^oC was found to be more effective in the destruction of the pollutant due to the formation of hydroxyl radicals on the surface of the nanocomposite. Not only that, the formation of the anatase phase enhanced the degradation of the targeted pollutant. Thus, it was reported that calcination temperature controlled the properties of crystalline phase of TiO_2 nanoparticles (their homogeneity and surface areas). Also, the particle size of TiO_2 was found to increase with calcination temperature, suggesting that different calcination temperatures affect the degradation of pollutant in wastewater.

Furthermore, calcination temperature affects the application or activity of a particular nanoparticle produced. In this vein, He *et al.* (2014) found that uncalcined TiO_2 showed a low photocatalytic effect owing to low crystallization. With an increase in calcination temperature, the photocatalytic effect of the TiO_2 increased due to the high crystallization of the particles and evacuation of CO_2 from the system. In another research conducted by Wang *et al.* (2017) on TiO_2 nanoparticles at temperature range of 300 to 600 ^oC for photodegradation of an organic pollutant, it was observed that at lower temperatures, the crystals of TiO_2 were not formed but as the calcination temperature increased, crystallization and change of phase were observed. During the degradation of the organic pollutant, the removal efficiency became low signifying the importance of TiO_2 phase in its application. Very recently, Haq *et al.* (2018) submitted that a decrease in the surface area and pore volume was observed when the calcination temperature increased due to rearrangement and growth of TiO_2 crystallites.

2.8.1.2 Effect of pH

The pH of a medium significantly affects crystal structure and surface morphology such as the size and entanglement of TiO_2 nanostructures (Selman *et al.*, 2014; Xue *et al.*, 2014; Mohite *et al.*, 2015). Due to the small particle size, the Van der Waals interaction increases exponentially as the particle size decreases leading to the growth of clusters. Tsega and Dejene (2017) reported that the morphology and crystallinity of TiO_2 depend on the pH of the precursor solution. Lower acidity promotes anatase structure and greater crystallite size. This shows that the degree of crystallinity of anatase is pH-dependent and lower acidity enhances the crystallinity, which also promotes the formation of big crystallite size. On the contrary, Mutuma *et al.* (2015) reported the formation of a mixed-phase (anatase and brookite) of TiO_2 calcined at 600 °C in a strongly acidic medium.

However, the possibility of anatase structure in acidic medium is apparent. Therefore, the investigation of TiO_2 nanoparticles synthesized by a facile sol-gel method under acidic and basic media is necessary for the clarification of the crystals formed (micro/nanostructure and optical properties of TiO_2 nanoparticles).

2.9 Synthesis and Mechanism of ZnO Nanoparticles

Zinc oxide is a white-yellowish crystal soluble in both acidic and basic media. It has attracted interest among researchers due to its strong activity. ZnO agglomeration in water may be due to its polarity which often leads to deposition. It exists in three highly crystalline forms namely, zinc blende, wurtzite and rock-salt (Sirelkhatim *et al.*, 2015). The wurtzite structure is the most common and stable form of zinc oxide at room conditions. At high pressure, ZnO transforms to rock-salt phase. ZnO has a small covalent property and also a very strong ionic character in Zn-O. These crystals are depicted in Figure 2.10 and the grey and yellow-shaded spheres signify Zn and O atoms, respectively.

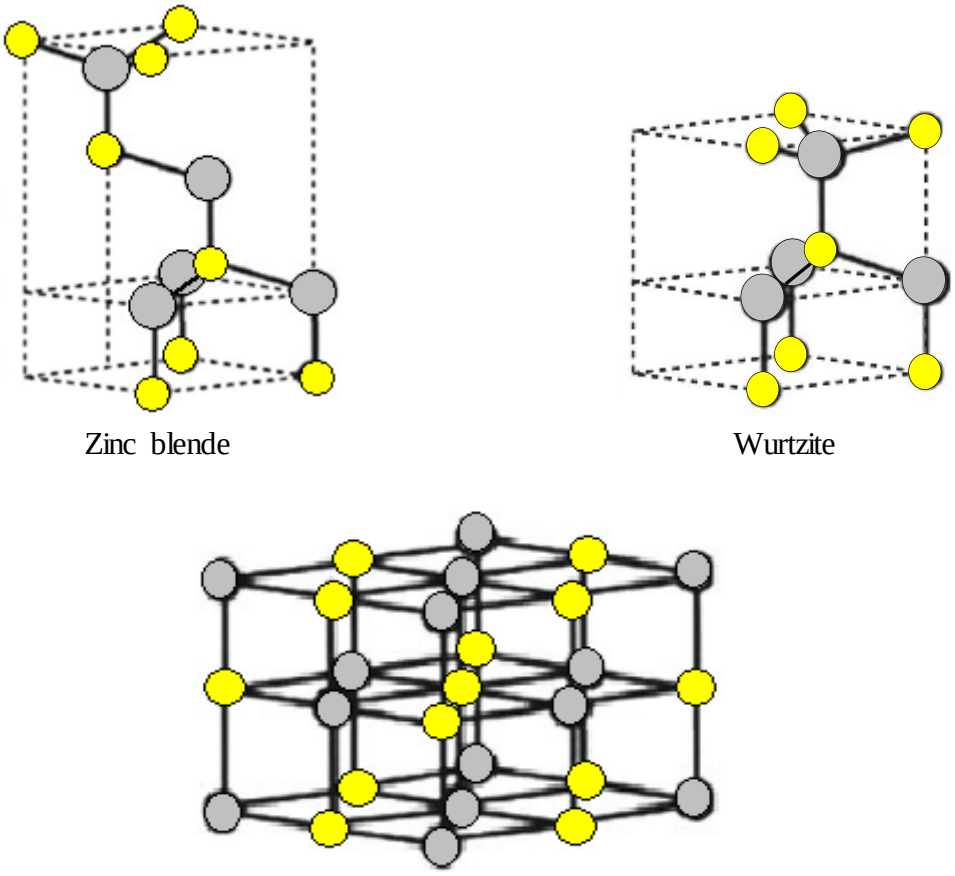

Figure 2.10: Different forms of ZnO (Sirelkhatim *et al*., 2015).

Various approaches for the synthesis of ZnO nanomaterials are categorized into solution and vapour-based techniques. Among these methods, the sol-gel method which is part of the solution-based techniques is found to offer better control of the size and distributions of the nanostructures (Ong *et al.*, 2018). The properties of the obtained ZnO nanomaterials either by the pilot or laboratory plant scale methods depend on the zinc precursors, precipitating agent, unit and process conditions used. The formation of these particles undergo four stages namely; solvation, hydrolysis, polymerization and transformation (Briffa, 2017). The physical and chemical parameters such as solvent types, pH, precursors and the temperature affect the morphological structures and sizes of ZnO nanoparticles.

Examples of precursors used are zinc acetate dihydrate, zinc nitrate hexahydrate, zinc chloride, zinc sulphate and zinc acetylacetonate. The commonly used precursors are zinc acetate dihydrate and zinc nitrate hexahydrate. The reaction mechanisms of ZnO nanomaterials controlled in a basic medium using these precursors as initial materials are represented in Figure 2.11.

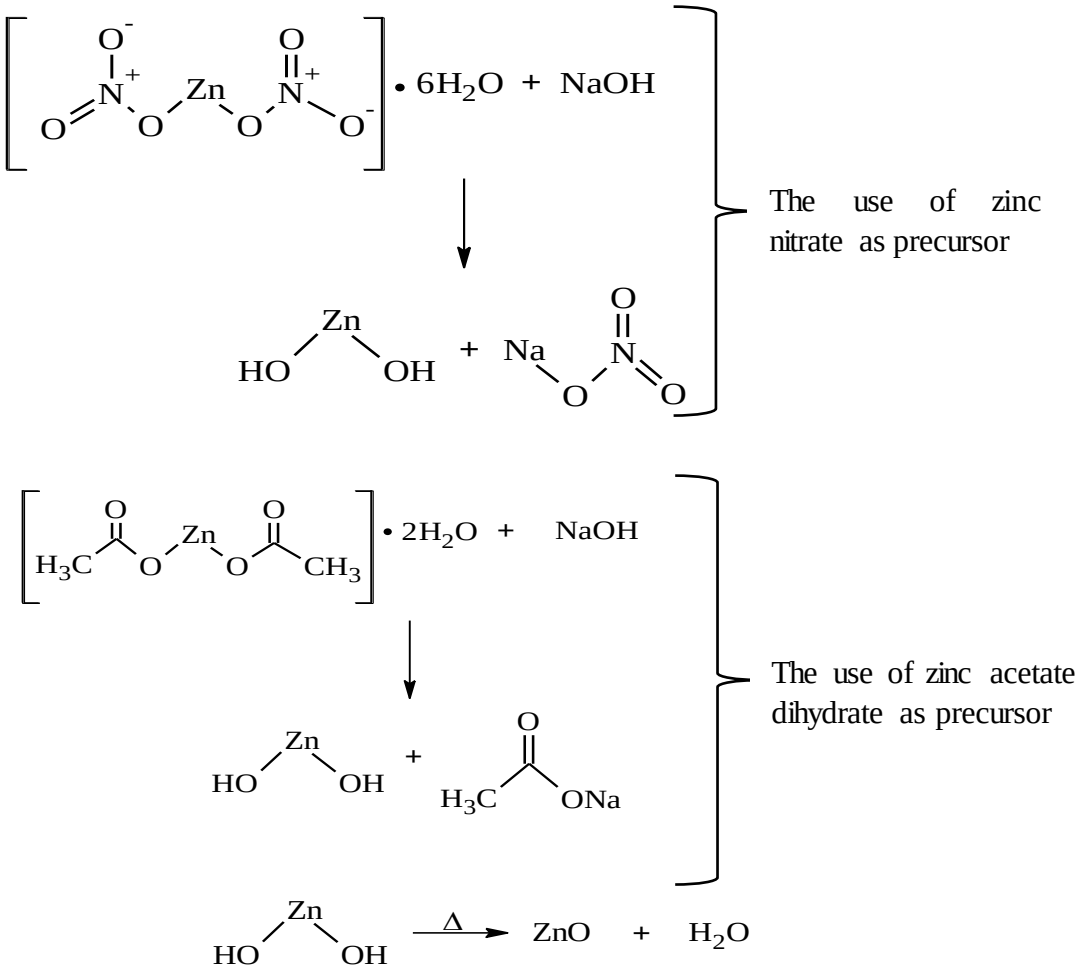

Figure 2.11: Reaction Mechanisms of ZnO

Zinc hydroxide is produced in both steps and upon heating, ZnO nanoparticles are formed. This zinc hydroxide separates into Zn^{2+} and OH^{-}, followed by polymerization of hydroxyl complex to yield Zn-O-Zn and finally converted into ZnO. Thermochromism which is the ability to change colour once there is a temperature change is a unique property of ZnO during synthesis. The colour of ZnO changes from white to yellow at temperatures above

400 °C and becomes white on cooling. This could be as a result of the formation of crystalline lattice due to loss of oxygen. The use of different precursors, variation in temperature and calcination temperature, pH and organic solvent have been employed for the preparation of ZnO nanomaterials by sol-gel method (Salavati-Niasari *et al.*, 2016).

Parra and Haque (2014) synthesized ZnO powder by sol-gel route without using capping agents such as PEG and PAM. $Zn(CH_3COO).2H_2O$ was dissolved in distilled water and NaOH which served as precipitating agent and pH controller was subsequently added to the solution to maintain pH 8. During the process, a white precipitate was formed and washed with de-ionized water and ethanol. A milky white colour ZnO nanoparticles powder were obtained at temperatures of 200 °C, 400 °C and 500 °C for 3 h. A similar investigation was conducted by Ashraf *et al.* (2015) on the structural and optical properties of ZnO nanoparticles.

Bhardwaj *et al.* (2018) synthesized ZnO nanoparticles using $Zn(CH_3COO)_2.2H_2O$ and KOH by sol-gel route. The solution was stirred to form a milky precipitate, centrifuged at 3000 rpm and then dried at 80 °C for 6 hr. In their findings, the formation of ZnO spherical nanoparticles were formed. The synthetic approach for ZnO nanoparticles in this study was relatively different from the study conducted by Shaban *et al.* (2018). Precursor, organic solvent and stabilizer used were zinc acetate [$Zn(CH_3COO)_2.2H_2O$], 2-methoxy ethanol ($C_3H_8O_2$) and monoethanolamine (C_2H_7NO) respectively. The effect of concentration of precursor and variation in pH were investigated on the resultant material, oven-dried at 60 °C for 2 h and allowed to age for a day at room temperature. Similar precursor and stabilizer but different organic solvent were reported in the study of Aryanto *et al.* (2017). In their study, $Zn(CH_3COO)_2.2H_2O$, C_2H_5OH and C_2H_7NO mixture was stirred at ambient temperature with a magnetic stirrer for 1 h to produce ZnO nanoparticles.

The report of Manikandan *et al.* (2018) on the synthesized ZnO nanoparticles by sol-gel technique showed that the nanoparticles were prepared at pH 8 using NaOH as pH adjuster. Zinc acetate was added to ethanol and then stirred for 1 h. NaOH was added to the solution and further stirred for 3 h to obtain the homogeneous gel. Firstly, the gel was oven-dried at 60 ^{o}C and allowed to age overnight and washed with distilled water and ethanol. The dried gel was finally calcined at 500 ^{o}C for 4 h to obtain ZnO nanoparticles.

Acosta-Humanez *et al.* (2015) prepared ZnO by sol-gel method using $Zn(NO_3)_2.6H_2O$ as the pioneering material and citric acid ($C_6H_8O_7.H_2O$) as a complexing agent at 70 ^{o}C with vigorous stirring until gel formation and calcined at 130 ^{o}C for 12 h. It was confirmed that the ZnO nanoparticles (wurtzite structure) were dominant. The authors came up with the reaction equation for the formation of zinc oxide as shown in equ. 2.2.

$$Zn(NO_3)_2.6H_2O + C_6H_8O_7.H_2O + 4O_2 \rightarrow ZnO + 2NO_2 + 6CO_2 + 11H_2O \qquad (2.2)$$

Mohan and Renjanadevi (2016) synthesized ZnO using $ZnSO_4.7H_2O$ as precursor and NaOH as a precipitating agent and stirred for several hours. The white precipitate was filtered and washed with distilled water, calcined at 100 ^{o}C and then ground to form fine powders. It was observed that a noticeable colour change from white to a dark ash colour of ZnO nanoparticles was formed. The prepared ZnO powder was calcined at a temperature ranging from 500 ^{o}C to 900 ^{o}C at 200 ^{o}C interval. Akkari *et al.* (2017) prepared ZnO nanoparticles by dissolving zinc acetate in methanol with KOH in methanol under vigorous stirring. The resulting precipitate was washed with ethanol. Prior to the authors' experimental design, the generated colloidal ZnO nanoparticles were sealed in a container and kept for further use.

In general, the properties of the prepared ZnO nanomaterials strongly depend on synthesis conditions such as precursor types, temperature, and pH. For instance, looking at the effect of pH, it was reported that synthesis of ZnO in acidic medium resulted in non-uniformity

and agglomeration of ZnO but as the pH was increased to alkaline region, there was significant growth of ZnO nanocrystallites (Shaban *et al.*, 2018). It has also been reported that increase in the precursor concentration affects the Zn-O bond length in the range of 1.9651-1.9745 Å (Aryanto *et al.*, 2017). They confirmed that there was an increase in the lattice volume of the ZnO nanomaterial.

Also, it has been reported that the particle sizes of ZnO nanostructures increased with increase in calcination temperature (Kayani *et al.*, 2015). Likewise, Thirumavalavan *et al.* (2013) revealed that the nano-ZnO increased in size as the calcination temperature increased. In addition, the authors also found that the surface areas of the nano-ZnO at high temperatures were reduced and their crystal sizes became agglomerated. They further gave explicit explanations on this effect viz; (i) particle-size broadening as a result of a morphological diffracting domain within the grains and (ii) the microstrain broadening due to disparity in the d-spacing by odd crystalline stresses.

2.10 Characterization of TiO_2 and ZnO Nanoparticles

Nanoparticles are mainly investigated using different characterization techniques for morphological, structural, particle size and surface area studies of TiO_2 and ZnO nanoparticles. These includes high resolution scanning electron microscopy (HRSEM), high resolution transmission electron microscopy (HRTEM), X-ray diffraction (XRD), Fourier transform infrared spectroscopy (FTIR), Brunauer-Emmett-Teller (BET), X-ray photoelectron spectroscopy (XPS), dynamic light scattering (DLS), photoluminescence (PL) and ultraviolet-visible (UV-Vis). In this study, the nanoparticles of interest are the TiO_2 and ZnO nanoparticles.

2.10.1 HRSEM

HRSEM is a technique that provides information on the particle size, shape and surface morphology of powder samples but offers limited information on size distribution. The

SEM has the disadvantages of time-consumption and high cost. However, its major advantage is that the information obtained from HRSEM preparation is less tedious (Mast *et al.*, 2015). The morphological shapes of particles are investigated by scanning electron microscope (SEM). This instrument uses a focused beam of high energy electron to produce different signals at the surface of solid material. The signals from the electron shows information about the sample material like chemical composition, external morphology, crystalline structure and orientation. The beam of electron produced and accelerated from the electron source passes through condenser and objective lenses which focus the electron beam. Accelerated electrons in SM pull a high amount of kinetic energy and this energy is dissipated as signals produced by an interaction between electron and sample when the incident electrons are decelerated in the solid material. These signals comprise of the secondary, electron, backscattered electrons, photon and visible light. The secondary and backscattered electrons include electrons for showing morphology topography and illustrating composition in the multiphase sample. In general, SEM is used to generate a high-resolution image of the sample, identify phases based on qualitative chemical or crystalline structure and spatial variation in chemical composition (Inkson, 2016).

According to Jurablu *et al.* (2015), it was observed that at low calcined temperature, the ZnO particles formed were clusters, but high homogeneity occurred in the sample surface as the temperature increased. Likewise, at high temperature, less agglomeration was observed and the particle sizes changed to the spherical nanocrystal in the range of 20-80 nm in diameter. The authors failed to give a reliable fact on this disparity of their findings. Here, the differences in their morphologies could be as a result of weak physical force in the synthesized ZnO.

The TiO_2 nanoparticles at different calcination temperatures were investigated by Yudoyono *et al.* (2017). The scholars observed that the higher the calcination temperature,

the larger the particles size. At the highest calcination temperature, grain boundaries were clearly observed. At 300 ^{o}C to 700 ^{o}C, crystalline sizes of anatase and brookite were 10-18 nm and 4-13 nm respectively. This appears that the higher the calcination temperature the greater the grain size.

2.10.2 HRTEM

The transmission electron microscopy provides morphological, surface behaviour, observation and measurement on the lattice fringes of nanomaterials. High-resolution transmission electron microscopy (HRTEM) gives information on porosity and structural defects within crystals and crystallinity via electron diffraction. The operating system is quite different from SEM, hitherto it produces similar type of information. Images generated by HRTEM are different from those of the HRSEM, but the electron dispersive X-ray (EDX) combined with the equipment provides the elemental data of the nanomaterials due to the involvement of a single phase. Importantly, EDX explains the effects of some parameters such as calcination temperature, pH and ageing time on the equivalent elemental composition of the nanoparticles. Golsheikh *et al.* (2018) revealed that ZnO nanoparticles prepared at calcination temperature of 500-600 ^{o}C gave high magnification HRTEM images of the ZnO nanoparticles. The produced nanoparticles were spherical, lattice fringes space of 0.24 nm and the average particle size increased with increase in the calcination temperature.

The TEM analysis of as-prepared TiO_2 nanoparticles at the experimental condition: pH, drying and calcination temperature were studied by EL-Mekkawi *et al.* (2017). It was established that as the temperature gradually increased from 450 to 650 ^{o}C, the predominant TiO_2 phase was anatase in the present of mix anatase and rutile phases. Phase transformation of the nanoparticles was not only affected, the degree of crystallinity and size distribution slightly changed. The measured particle sizes of the synthesized TiO_2 at 450 ^{o}C, 550 ^{o}C and

650 ^{o}C ranged from 5 to 25 nm, 35 to 70 nm and 40 to 120 nm respectively. The authors clearly pointed out that as the temperature increased crystallite size and phase ratios were influenced.

2.10.3 XRD

XRD is a characterization tool used for identification of the phase of crystalline material. It helps to provide information on unit cell dimensions of nanomaterials, interatomic distance and angle of an atom. XRD also gives a rough estimate on crystallite size through Debye Scherer formula, concluding on the importance of this tool for the successful structural characterization of nanomaterials in both single and multiphase. X-ray diffraction (XRD) determines the structural arrangement of atoms packed together in the crystalline state from which a beam of X-ray is scattered from the electron. The study of matter at the atomic level was a difficult task but the aid of electromagnetic radiation wavelength between the gamma rays and ultraviolet make it possible. As the atomic distance in the matter is comparable with the wavelength of X-ray, the diffraction penetrates it and produces a result that corroborates the crystalline structure. X-ray diffraction is an important tool used for qualitative and quantitative characterization of crystalline materials. This powerful tool is best known for the determination of lattice constants, identifying the type of phases of unknown solid samples, film thickness, stress-strain and crystallographic planes of materials (Motazedian *et al.*, 2019).

The patterns of prepared ZnO nanoparticles at different calcination temperatures as described by Golsheikh *et al.* (2018) indicated that wurtzite phase of ZnO nanoparticles was indexed, average crystallite sizes of the nanoparticles at 500, 600 and 700 ^{o}C were 15, 18 and 22 nm respectively. It was established that as the calcination temperature increased there was an increase in the peak intensities and crystallite sizes.

X-ray diffractograms of TiO_2 nanoparticles calcined at 400 °C and 500 °C were studied by Romeiro *et al.* (2017). They demonstrated that the most peaks at Bragg's angle of 25° signify the anatase phase where small amounts of rutile were also observed at other diffraction angles. Using the Scherrer equation, the scholars came up with the crystalline sizes of 10.5 nm and 19.6 nm for the synthesized nanoparticles at 400 °C and 500 °C respectively. A similar finding was reported by Haider *et al.* (2017) on the prepared TiO_2 nanoparticles by sol-gel method calcined at different temperatures. They went further to explain the transformation of the TiO_2 phase. The particle size of the anatase phase became smaller than other TiO_2 phases as the calcination temperature due to the aggregation of nanoparticles. In addition to their view, the formation of anatase at low temperature could be as a result of high cell lattice that involved nucleation and growth process, breaking and reformation of bonds.

2.10.4 Some other analytical techniques

The large surface area of nanomaterials plays a vital role during applications. BET analysis is known to be the best method to determine the surface area of nanomaterials (Ealias and Saravanakumar, 2017). This technique is based on adsorption and desorption theory and possible types of adsorption isotherms are Type-I, Type-II, Type-III, Type-IV and Type-V. Most often, the Type-V is very similar to Type-IV and is not applicable to BET. According to Golsheikh *et al.* (2017), the BET surface areas of synthesized ZnO nanoparticles under different temperatures of 300, 600 and 700 °C were 26.7, 19.7 and 14.8 m^2/g, respectively. A previous study on ZnO doped with CuO nanoparticles annealed at the temperature range of 250-550 °C showed that a remarkable decrease in surface areas was observed with decrease in pore volumes and increase in pore diameters (Modwi *et al.*, 2016). During their investigation the obtained isotherm for pure ZnO and doped ZnO calcined at 550 °C were similar. A plausible reason could be that clogging pores result by aggregation at high

temperature. Following the opinions of different scholars, multi-element doped TiO_2 nanoparticles via sol-gel method were calcined at 200, 300 and 400 ^oC by de-Luna *et al.* (2018) and they found that the decrease in the specific area (204.23 to 127.31 m^2/g), increase in average pore size (7.79 to 10.99 nm) and decrease in volume were (0.40 to 0.35 m^3/g) were due to pore blocking during the N_2 gas adsorption-desorption isotherm. Synthesized TiO_2 nanoparticles at pH 8 and calcination temperatures of 300-800 ^oC (Khan, 2017) and TiO_2 samples calcined at 350-600 ^oC (Fu *et al.*, 2017) gave similar trends studied. Therefore, findings of different scholars signify that these nanoparticles, when subjected to intense calcination temperature, tend to have lower surface areas due to the crumpling pores. FT-IR and Raman spectroscopies are used for vibrational information of nanoparticles. They provide fingerprint regions for the chemical bonds in molecules. In this case, molecule absorb frequencies that are properties of their constituents. The frequencies of the absorbed radiation correspond to the frequencies of the group that vibrate in the molecules. The detection of energy lies on the shape of the molecular potential energy surface, the masses of the atoms and the vibronic coupling (Singh, 2014). Infrared spectroscopy provides qualitative information on a given material based on the size and region of the peaks in the spectrum of the material. It is used to analyse materials in different forms such as bulk, thin, films, liquids, solids, pastes, powders and fibres (Dazzi *et al.*, 2017). It analyses samples up to 11 mm in diameter and the produced spectra of the pure compounds are like molecular "fingerprints".

In this respect, the FT-IR spectra of synthesized ZnO and TiO_2 nanoparticles calcined at different temperatures by sol-gel technique using zinc acetate dihydrate and titanium isopropoxide as their precursors were presented by Kayani *et al.* (2015) and Fernández-Catalá *et al.* (2017). The strong peaks of C=O and O-H stretching mode of vibration gradually diminished at high temperatures were reported. It was reported that the ZnO peak

appeared between 435.06 and 413.36 cm^{-1} and this became sharpened indicating an increase in crystallinity of the nanoparticles by increasing temperature.

The FTIR spectra of the TiO_2 samples prepared at 250-900 ^oC were described by Fernández-Catalá *et al.* (2017). The broadband at 3000 to 3500 cm^{-1} and 1600 cm^{-1} were attributed to the OH stretching of physisorbed water on the surface of TiO_2. As the calcination temperature increased, the OH band diminished in intensity, signifying the loss of physisorbed water on the TiO_2 surface. As such, it was reported that the weakness in the Ti-OH vibration bands during calcination might be detrimental to its applications industrially.

2.11 Adsorption Behaviour of ZnO and TiO_2 Nanoparticles

Numerous adsorbents have been developed for the removal of pollutants from wastewater, however, some of these materials have certain drawbacks. Owing to the properties such as surface area, porosity, site density and crystallinity of TiO_2 and ZnO, these nanoparticles have been recognized to be effective for the removal of heavy metal cations and organic pollutants from aqueous solutions (Gusain *et al.*, 2019). In any case, pore size and surface chemistry have been reported to govern the adsorption capability of nanomaterials. Porous nanomaterials are generally categorized into microporous (< 2 nm), mesoporous (2-50 nm) and macroporous (> 50 nm) (Thommes *et al.*, 2015, IUPAC Technical Report). The microporous sizes of TiO_2 and ZnO help to perfect the adsorption and separation techniques using these oxide nanoparticles while the use of meso and macroporous nanomaterials would ease mass transfer.

Basically, adsorption processes in wastewater using TiO_2 and ZnO are divided into physisorption (physical) and chemisorption (chemical). The degrees of the two types of adsorption are influenced by weak intermolecular interactions like London van der Waals forces, hydrogen or covalent bonding, electrostatic interaction, dipole-dipole interaction,

polarity and hydrophobicity (Tong *et al.*, 2019). Although, ion exchange between sorbents and sorbates occurs in chemisorption.

TiO_2 and ZnO as nanoadsorbents for water treatment have been pointed out to be more advantageous due to the high adsorption capacity and great affinity for pollutants. They have been asserted to be among the most promising nanomaterials for water treatment (Chaturvedi and Dave, 2019). Since in certain circumstances, applications of these nanomaterials occasionally render them ineffective. One nanoparticles into other and in this case, since ZnO and TiO_2 have been reported as being among the best for sorption studies, efforts are made to incorporate them into natural materials like clay for the development of nanocomposites and subsequently apply them to the removal of toxic organic, inorganic and microbial constituents from wastewater are strongly encouraged.

2.12 Clay as Natural Adsorbents

Clays are indispensable natural materials and their wide ranges of applications include polymer, water, cosmetics, ceramics, paints, pharmaceutical, pulp and paper industries (Asamoah *et al.*, 2018). Clays are referred to as naturally occurring fine particles which comprise fine-grained and crystal minerals such as silicon oxide, carbonates and metal oxides, which become hardened when fired (Valášková, 2015). The clay components are in different structural layers and compositions as a result of their polytypic and structural arrangements called polytypism. Clay minerals are hydrous aluminosilicates that can retain large amounts of water with other properties such as colloidal behaviour, swelling and adsorption capacities. The clay minerals are classified into kaolinite, illite, montmorillonite (smectite) and chlorite (Adeyemo *et al.*, 2015).

The kaolinite, montmorillonite, illite, and bentonite are commonly used due to their high specific areas, availability, stability and structural characteristics. These minerals are abundant in nature, non-toxic and have significant roles in scavenging pollutants in

wastewater either via ion-exchange or adsorption processes or both (El-Naggar *et al.,* 2019). Hence, they are basically used as depolluting agents. The adsorption processes which occur on the solid surface in contact with ionic solution involves the adsorption of potential determining ions which gives the surface either positive or negative charge with respect to the charge originated from the crystal lattice (Preocanin *et al.,* 2016). The layer which comprises double (negatively charged) and the edge double layer that is amphoteric (either negatively or positively) charged depends on the composition of the aqueous solution. Notably, the adsorption processes are cation exchange in nature on the surface layers while the chemisorption of anions occurs at the edge surfaces (Alexander *et al.,* 2019).

2.12.1 Forms of clay minerals

Kaolinite

Kaolinite group is classified as 1:1 type layer silicates with a tetrahedral sheet of silica (SiO_4) joined together with an oxygen atom and octahedral sheet of alumina (AlO_6) as seen in Figure 2.13. Kaolinite possesses high chemical stability, low expansion and cation exchange capacity. The kaolinite group is structurally divided into dioctahedral and trioctahedral minerals (Uddin, 2016). The dioctahedral minerals include kaolinite, dickite, nacrite and halloysite while the trioctahedral minerals comprise the antigorite, chrysotile, chamosite and cronstedite. The general formula of dioctahedral groups is $Al_2Si_2O_5(OH)_4$ with a theoretical structural composition of 46.54 % SiO_2, 39.50 % Al_2O_3 and 13.96 % H_2O (Kloprogge, 2019). The clay mineral consists of silicate sheet (Si_2O_5) bonded to aluminium hydroxide [$Al_2(OH)_4$] known as the gibbite layer with the non-existence of interlayer swelling and charges. The kaolinite, dickite and nacrite are polytypes and occur as plates while the halloysite (hydrated polymorph) exist as tubular shape.

The clay mineral that is rich in kaolinite is called kaolin which is a soft and whitish powder; with a melting point of 1750 ^oC and found together naturally with other minerals such as

muscovite, feldspar, quartz, and anatase (Fadzil *et al.*, 2017; Uddin, 2018). Structural transformations occur upon thermal treatment of kaolinite group in the air at atmospheric temperature. At 100 ^{o}C, the water in the kaolin is dried off and the end state is called leather dryness. Bone dryness is observed at temperatures between the range of 100 ^{o}C and 550 ^{o}C. Endogenic dehydration of kaolin starts from 550 ^{o}C-600 ^{o}C to produce metakaolin, ($Al_2Si_2O_7$), but the continuous loss of hydroxyl (dehydroxylation) is achievable at 900 ^{o}C. Further application of heat transforms the metakaolin to aluminium-silicon spinel, $Al_4Si_3O_{12}$ (at the temperatures of 925-950 ^{o}C) and then finally to platelet and needle mullite, upon calcination at temperatures of 1050 to 1400 ^{o}C.

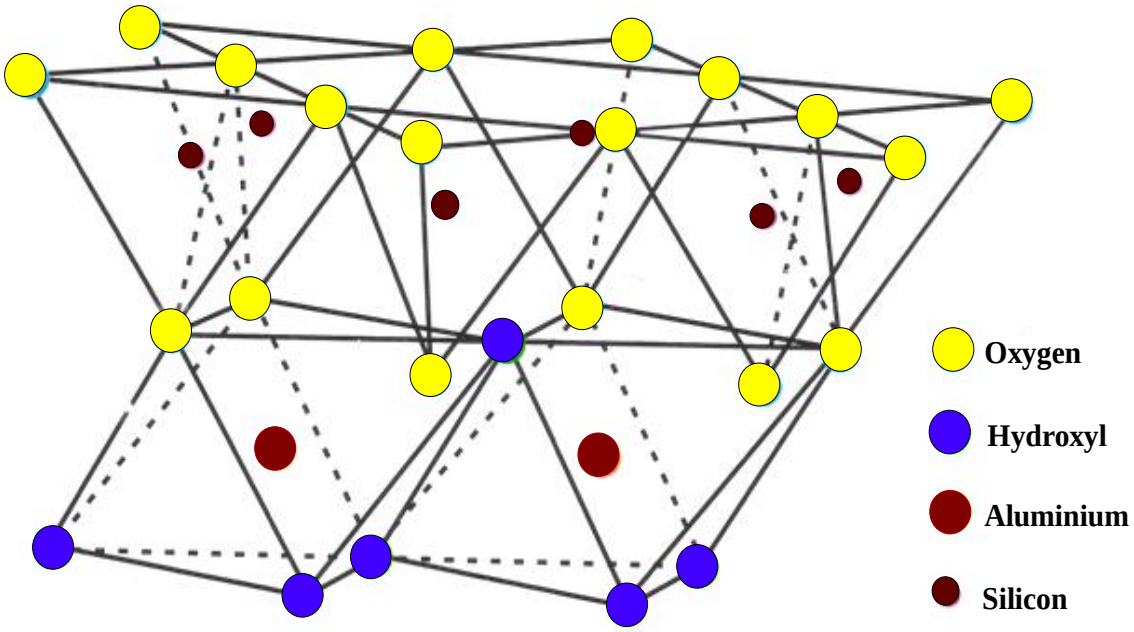

Figure 2.13: Structure of Kaolinite

2.12.2 Characteristics of clays

The features of clay minerals strongly depend on their chemical compositions, sizes and surface layers which allow more understanding of the nature of clay minerals. The commonest properties associated with clay are plasticity, surface area and ion exchange capacity. Clays become plastic when combined with water and variations in plasticity may

be linked to conserving interstitial materials during weathering. Shrinkage determines the plasticity of clay; the greater the shrinkage the more plastic a clay material. When fired, the new form of clay is achieved without any attempt to return to the original physical and chemical properties (Clay Minerals Society, 2018).

In general, the surface area enhances the adsorption capacities that result from the negative charge on the structure of clay mineral. Importantly, the sizes and charges of the cations of clay determine its swelling property. A swelling clay is that with the ability to retain water and expand upon hydration (Carrier *et al.*, 2013; Carrier *et al.*, 2014).

2.13 Adsorption Characteristics of Clay Minerals

The chemistry of phyllosilicate in clays determines their adsorptive behaviour and exchangeable cations. While the hydroxyl and oxygen are responsible for their physical adsorption due to van der Waals interaction, chemisorption and catalytic capacity (Novikova and Belchinskaya, 2016). The adsorption ability of a given clay is explicitly explained under the influence of parameters such as contact time, pH, initial concentration, dosage and temperature. The literature of the last five years (2013-2018) by various researchers on the application of clays, clay/ZnO and clay/TiO_2 nanocomposites for the removal or degradation of contaminants from wastewater has been studied in order to know their adsorptive abilities for various pollutants

2.13.1 Clays for wastewater treatment

The interests of scholars preferably using clay for removing pollutants from contaminated waters as shown in Table 2.3 have been in the used as adsorbents around the globe.

Table 2.3: Summary of the Clay used for the Removal of Pollutants from Wastewater

Adsorbent	Characterization	Experimental condition	Finding	Pollutant	Author
Saudi Arabian clay	SEM, EDX	Initial pH	The significance of pH during the adsorption and desorption study	Heavy metals	Lukman *et al.* (2013)
Natural clay	SEM, EDX	Initial concentration, contact time, pH, temperature dosage	The rate of adsorption increased with increase in pH	Methylene blue	Fatiha and Belkacem (2015)
Algerian kaolin	XRD, BET, SEM	Contact time, initial concentration, pH, dosage, temperature	Experimental data favoured Langmuir isotherm and pseudo-second-order kinetic	Tannery (acidic dye)	Zen *et al.* (2018)
Brazilian kaolin	XRF. XRD, BET, FTIR, SEM, TGA, DLS	Concentration	The adsorption system obeyed Elovich kinetic model and Langmuir model	Malachite green dye	Caponi *et al.* (2018)
Bentonite (Jeddah, Saudi Arabia)	XRD, BET, XRF	Temperature	Metal ion adsorption increased with an increase in temperature The adsorption process was found to be endothermic	Copper and nickel ions	Alijlil *et al.* (2014)
Sepiolite, kaolin and talc		Concentration, pH	The zeta potential analysis showed that the adsorption capacity of the clay samples in acidic medium was higher than in basic conditions	Anionic reactive dye	Rahman *et al.* (2015)
Algerian kaolin	BET	Contact time, initial concentration, stirring speed, salt concentration, dosage	Dubinin-Radusshkevich and Temkin models were found to be the best that fitted the adsorption process. The thermodynamic study showed that the adsorption process was endothermic	Methylene blue	Rida *et al.* (2013)

Calcareous, smectitic clay	XRF	Initial concentration, contact time, pH, temperature	The pH and the presence of carbonate impurities affected abilities of the clay samples to remove the metal ions.	Copper and zinc ions.	Sdiri *et al.* (2014)
Kaolin	XRD, SEM	Reaction time, initial concentration	The experimental data fitted well for the Langmuir isotherm model	Dye	Hajjaji *et al.* (2016)
Organobentonite	XRD, SEM, BET, FTIR, Zeta potential	pH, initial concentration	The Langmuir and pseudo-second-order models were favoured. The adsorption system was endothermic and spontaneous	Dye	Huang *et al.* (2017)
Bentonite and kaolin		pH, dosage, ionic strength	The increase in pH and facilitate the removal of cationic xylan copolymer	Cationic polymer	Konduri and Fatehi (2017)
Algerian clay	XRD, SEM, FTIR	Initial concentration, pH, contact time, dosage	The pH value increased as the adsorption rate decrease The increase in surface area with an increase in adsorbent dosage enhanced the elimination of pharmaceutical pollution The Langmuir model was a better fit than the Freundlich model.	Pharmaceutical (diclofenac and potassium)	Mabronki and Akretche (2015)
Organobentonite	BET, FTIR, SEM, XRD, potentiometer	pH, surface modification, initial concentration, contact time	The adsorption data follow the pseudo-second-order equation and Freundlich isotherm model	Basic dye	Anirudhan and Ramachandran (2015)
$Mg(OH)_2$/Algerian bentonite	XRF, XRD, TGA, BET, SEM, FTIR	Contact time, temperature, adsorbent	The adsorption process was found to be physisorption,	Reactive dye	Chinoune *et al.* (2016)

		dosage, ionic strength, initial concentration	endothermic and spontaneous in nature		
Modified kaolin	SEM, XRD, XRF, FTIR		Functional groups such as hydroxyl, ammonium and nitrate ions on the surface of kaolin were responsible for the adsorption of chromium The process of adsorption obeyed pseudo-second-order kinetic and Langmuir model The process was spontaneous and exothermic in nature	Chromium ion	Lin *et al.* (2014)
Kaolin		Initial concentration, contact time	The correlation coefficient depicted that Freundlich adsorption isotherm model was more favoured than the Langmuir model	Nitrate	Mohsenipour *et al.* (2015)
Bentonite	XRD, BET, FTIR, TGA, XPS	Contact time, pH, initial concentration	The isotherm fitted well by Langmuir and Redlich-Peterson models. The adsorption occurred due to the interaction of silanol groups with anion and hydroxyl/sulphonic groups	Reactive dye	Aguiar *et al.* (2017)
Natural clay (China)	XRD, SEM, XRF, FTIR, CEC, BET, Zeta potential analyzer	Agitation time, initial concentration, solution pH, adsorbent dosage	Adsorption process followed the pseudo-second-order kinetics and Langmuir model. The adsorption capacity was attributed to its structure and surface properties.	Ammonium ion	Alshmeri *et al.* (2018)
Bentonite	FTIR, XRD	Shaking speed, pH, temperature, initial	Harkin Jura was the most favoured and the adsorption	Reactive black 5 dye	Amin *et al.* (2015)

		concentration, particle size	process follows pseudo-second-order kinetic. Bentonite clay depicted the dual nature of exothermic and endothermic, spontaneous and non-spontaneous properties reflecting the effects of temperature on its adsorption capacity		
Algerian clay	XRD, BET, Zetaphoremeter	Contact time, initial concentration, pH, dosage and temperature	The adsorption process obeyed the Langmuir model and adsorption kinetic follows the pseudo-second-order model	Acid dye (derma blue R67)	Zen and Berrichi (2014)

Nanocomposites like clay/TiO_2, clay/ZnO and clay/TiO_2/ZnO are multiphase solid materials in nano-size explored as good adsorbents for water treatment. The formation of new materials with unique flexibility and improved properties such as affinity to contaminants, mitigate the release of nanoparticles and enhanced strong antibacterial activity is a welcome idea. The development of nanomaterials that have been shown to possess most of these properties is attracting the attention of researchers. Thus, researchers have considered their applications to be important in the field of water sanitation.

2.13.2 Clay/TiO_2 for wastewater treatment

The use of TiO_2 nanocomposites for the treatment of water has served as an alternative to that of commercial TiO_2 due to their high adsorptive properties, low cost and regeneration possibilities. Table 2.4 described the synthesis and characterization of clay/TiO_2 nanocomposites used for the removal/degradation of contaminants in wastewater.

Table 2.4: Summary of the Clay/TiO_2 Nanocomposites used for the Removal of Pollutants from Wastewater

Adsorbent	Characterization	Experimental condition	Finding	Pollutant	Author
TiO_2/Tunisian clay	BET, XRD, FTIR, TGA	Oxidizing agent, initial concentration	High photodegradation was as a result of stability of the TiO_2 anatase phase. Hydrogen peroxide serves as a promising oxidant for degradation of dye under UV	Anionic reactive dye	Hadjltaief *et al.* (2019)
TiO_2/Polish halloysite	XRF, XRD, TEM, FTIR, BET	Time	The presence of TiO_2 in the nanocomposites photo-degraded aniline and chloro derivatives greater the commercial TiO_2.	Chloroaniline	Szczepanik *et al.* (2017)
TiO_2/Montmorillonite	XRD, SEM, FTIR, BET, TG-DTA	Time	The TiO_2 nanoparticles had large photocatalytic activity and the adsorbent for environmental remediation such as regeneration possibilities	Methylene dye	Chen *et al.* (2014)
TiO_2/Bentonite	XRD, BET	Time	The pollutants are removed via adsorption and photocatalyst	Anionic and cationic dye	Sahel *et al.* (2014)
TiO_2/WO_3/Bentonite	XRD, EDS, FTIR, BET, AFM, SEM	Time, initial pH, temperature, initial concentration	There was an increase in the specific surface of the nanocomposites compared to bare clay	Methylene dye	Yang *et al.* (2015)
TiO_2/Clay	XRD, FTIR, AFM, SEM	Time	The nanocomposites showed high crystallinity degree and surface for adsorption of methylene blue and simultaneous removal of	Methylene blue and Cadmium	Guillaume *et al.* (2018)

			pollutant matrix (MB and cadmium)		
TiO_2/Montmorillonite	FTIR, TG-DTA, BET, XRD, SEM, EDX	Time	The synthesized nanocomposites exhibit good adsorption and photodegradation properties and recovery process	Dye	Djellabi *et al.* (2014)
TiO_2/Bentonite	FTIR, SEM, XRD, BET	Temperature	The formation of hydroxyl radical from TiO_2 acts as an active site for a photocatalytic agent in the degradation process. The adsorption of dye molecule in an aqueous phase fitted best for Langmuir isotherm model	Methylene blue and Rhodamine B.	Laysandra *et al.* (2017)
TiO_2/Clay	XRD, TEM, FESEM, FTIR, BET	Time	The photodegradation of methylene blue and chlorobenzene depend on the clay texture as well as the surface area.	Methylene blue and chlorobenzene	Mishra *et al.* (2017)
TiO_2/Clay	SEM, XRD, TEM, EDX, BET	Time	The clay exhibited good support for TiO_2 nanoparticles which serve as excellent photocatalytic performance and regeneration study	Methylene blue	Wu *et al.* (2019)
TiO_2/Sepiolite	HRTEM, XRD, FESEM, EDX, XPD	Time, pH	The nanocomposites have photocatalytic properties for the photodegradation of organic pollutants	Dyes	Lui *et al.* (2018)

TiO_2/Kaolin	XRD, FTIR, SEM, EDX, BET	Time, calcination temperature, concentration	The nanocomposites calcined at lowest temperature have the best performance photocatalytic activity due to its high surface area and porosity The nanocomposites are recovered and reused for three consecutive cycles.	Coomasie brilliant blue dye	da Silva Lopes *et al.* (2019)

2.13.3 Clay/ZnO for wastewater treatment

The advantages of embedded ZnO nanoparticles in or on the surface layers of clay for the formation of matrices are due to swelling, photocatalytic and ion exchange properties. Table 2.5 presents the synthesis and characterization of ZnO nanocomposites for adsorption and photocatalytic degradation of pollutants in wastewater.

Table 2.5: Summary of the Clay/ZnO Nanocomposites used for the Removal of Pollutants from Wastewater

Adsorbent	Characterization	Experimental condition	Finding	Pollutant	Author
ZnO/Montmorillonite	XRD, FTIR, SEM	Time, initial pH, initial concentration	The degradation ability of the nanocomposites was almost two-third higher than ZnO	Phenol	Ye *et al.* (2015)
ZnO/Montmorillonite	XRD, FESEM	Contact time, dosage, initial concentration, pH	The presence of ZnO nanoparticles increased the surface area resulting in a higher adsorption rate. The regeneration of the nanocomposites after three times of use showed that the adsorbent still had adsorption capacity for divalent ions	Lead and copper ions	Sani *et al.* (2017)
ZnO/Bentonite	XRD, SEM	pH, initial concentration, dosage	The nanocomposites effectively removed safranine dye and decrease TOC under sunlight irradiation. Regeneration study indicated the advantage of the practical application of the nanocomposites due to its stability and reusability.	Safranine dye	Sonawane *et al.* (2016)
ZnO/Fe_2O_3/Rectorite	SEM, XRD, FTIR, TGA, BET	Dosage, time, initial concentration	The ZnO assisted in the removal of methylene blue with a proposed mechanism	Methylene dye	Wang *et al.* (2018)
ZnO/Sepiolite	FTIR, XRD, SEM	Time, initial concentration	The nanocomposites had the surface area and functional groups capable of adsorbing the dye	Congo red dye	Vahidhabanu *et al.* (2017)
ZnO/Bentonite	XRD, XRF, FTIR	Dosage, pH, initial concentration	The photodegradation increases with decreasing the dye concentration	Textile azo dye	Boutra and Trari (2016)

ZnO/Bentonite	XRD, SEM	Time, pH	The radical oxidation reagents are responsible for photodegradation process	Ciproxin	Sponza and Oztekin (2015)
ZnO/Clay	XRD, FE-SEM, TEM, FTIR, UV-vis, TG-DTA, BET	Time	The ZnO/clay nanocomposites have better adsorption efficiency than ordinary ZnO nanoparticles	Methylene blue	Akkari *et al.* (2015)
ZnO/Fe2O3/Sepiolite	FTIR, XRD, FE-SEM, EDX, TEM, TG, BET	Temperature, time	The nanocomposites decolourized methylene blue dye and maintained its photocatalytic activity after reuse in consecutive cycles	Methylene blue	Akkari *et al.* (2017)
ZnO/Sepiolite	XRD, TEM, EDX, BET, SEM, FTIR	Time	The nanocomposites were used for the photodegradation of some emerging contaminants under solar light irradiation	Pharmaceuticals	Akkari *et al.* (2018)
ZnO/Clay	XRD, BET, FTIR, SEM, HRTEM, EDX	Time, pH, dosage, initial concentration, inorganic anions	The removal of dye via heterogeneous photocatalytic process under solar irradiation The nanocomposites have high recyclability	Dye	Bel-Hadjltaief *et al.* (2018)
ZnO/Kaolin	PL, XRD, SEM	Concentration, dosage, pH	The nanocomposites act as photocatalyst in water purification under sunlight The nanocomposite catalysts were easily recovered through filtration and no significant loss in the adsorbent after successive cycles	2-Chlorophenol	Zyoud *et al.* (2019)

2.13.4 Clay/TiO_2/ZnO for wastewater treatment

Only a few research studies have been done on the synthesis and characterization of TiO_2/ZnO/clay nanocomposites. Thus, to date, the synthesis and application of heterogeneous catalysts immobilized on clay are still being awaited. TiO_2/ZnO was anchored on Tunisia clay for the photocatalytic degradation of methylene green in water (Bel Hadjltaief *et al.*, 2016). The heterogeneous nanocomposites were characterized by SEM, HRTEM and zero-point charge of pH (pHzpc). The working operations of the experimental set-up were evaluated under the effects of catalyst dosage, pH, initial dye concentration and UV irradiation intensity. They found that almost complete mineralization occurred at 30 min in the presence of the nanocomposites under UV irradiation, demonstrating a positive effect of ZnO nanoparticles in the catalytic process. In the study reported by Vaizoğullar (2017), the photocatalytic activities of TiO_2, ZnO, TiO_2/ZnO and TiO_2/ZnO/sepiolite catalysts were determined. The composites were synthesized for the degradation of flumequine antibiotic. The photocatalysts were characterized by SEM, XRD, FTIR, and zero-point charge for their photocatalytic performance. The operating conditions which included pH, initial sorbate concentration and dosage were investigated. It was reported that sepiolite and ZnO played a vital role in the adsorption and degradation of flumequine on the surface of the catalyst.

As reported by Huanhuan *et al.* (2018), a novel clay nano-based catalyst of ZnO/TiO_2/rectorite was synthesized and characterized for photodegradation and adsorption of methylene blue from the aqueous phase. The experiment was conducted by varying the conditions of the solution pH, catalyst dosage and TiO_2 mass ratio. The study showed that the degradation kinetics of methylene blue obeyed the Langmuir-Hinshelwood model. They found that TiO_2 enhanced the photocatalytic activity of the nanocomposites in the removal

of the dye while ZnO/rectorite was responsible for both the photodegradation and adsorption processes.

2.14 The need for Stringent of Applications of Nanoparticles and Nanocomposites in Water Treatment

One of the principal difficulties of the focused nanoparticles, TiO_2 and ZnO, is the large bandgap energy of the nanoadsorbents which make them need excitation by UV on applications during photodegradation of the contaminants in wastewater (Khaki *et al.*, 2017). In most literature, these nanoparticles are not classified as pollutants but their stability in water is paramount in assessing their potential risks. Considering their application in water, another crucial problem is regeneration. These nanoparticles in suspension are difficult to recover, therefore effort need to be devoted to overcoming these problems. To achieve this, incorporating nanoparticles in clay has attracted much attention. Thus, filtration techniques may become paramount for the removal of pollutants in wastewater. This technology can be improved through the production of nano-based filters. This nano-based filtration technology as shown will allow for regeneration, reduce toxicity and cost thus giving room for industrial-scale production. In order to materialize this goal, research needs to focus on developing nano-based filters which will require less energy, intensive synthesis techniques and cheap feedstock. This can be accomplished by examining the compositions of clay minerals and their mechanical properties before employing them for applications.

2.14.1 Water filters

The filters for water purification have become instrumental tools where access to safe drinking water is inadequate. International organizations have dedicated their efforts towards making sure that humans gain access to safe drinking water by establishing clay water filters. However, the workability of clay water filters is affected by filtration mechanism flow and porosity.

2.14.1.1 Filtration mechanism

Filtration is a physical, chemical as well as biological process which depends largely on the water being treated. The performance of filters is relied upon to acquire removal mechanism efficiencies. As shown in Figure 2.13, these pollutants removal mechanisms are sedimentation on media, adsorption, absorption, biological action, mechanical screening, diffusion and straining (Adekeye *et al.,* 2019).

During straining, the liquid passes through the filter whose pores are smaller than the particles of the contaminants. The major disadvantage of this mechanism is the clog formed by these particles. This tends to reduce the filtration cycle when the pores are clogged. However, this can be overcome by proper backwashing in order to remove the entrapped solids. This can be achieved via the application of water alone, air and water separately and subsequently, air and water simultaneously (Missengue, 2012).

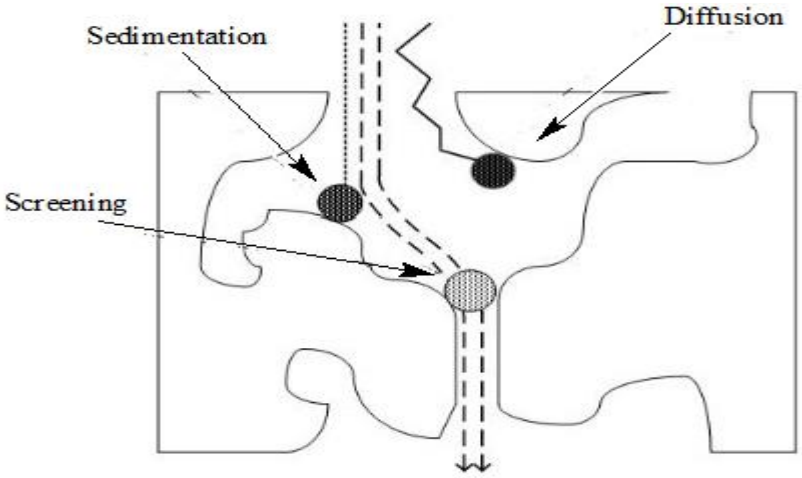

Figure 2.13: Mechanism of Filtration (Missengue, 2012)

2.14.1.2 Porosity and flow

Porosity is measure of the volume of empty space in a solid. Water filters produced at high temperatures burn off the organic waste materials in the composite filter materials. This helps to create pores which allow more water to pass through the water filter body during

filtration. In general, there are three (3) types of pores namely; isolated, interconnected or effective and dead-end pores as seen in Figure 2.14 (Missengue, 2012).

Figure 2.14: Types of Pores in the Pot Filter

The dead-end pores alongside with interconnected pores are connected but the isolated and dead-end pores do not contribute to the flux across the water filter pores. When pores in the water filter are filled with water, a delay occurs after which a steady-state filter out is reached Wang *et al.*, 2019).

2.15 Research Summary and Gap Analysis

The use of nanomaterials such as carbon nanotubes, zeolite, TiO_2 and ZnO nanoparticles for wastewater treatment has been proposed by different scholars but availability of adequate and separation techniques of the nanomaterials and treated wastewater has caused the fouling of so-called treated water. Therefore, it is important to take measures aimed at reducing the level of these harmful and foul smelling substances accomplish the free level generated after treatment with nanoparticles. Clay has proved to be a promising natural material for removing pollutants and microorganisms from water due to its physicochemical characteristics. Among the recent works reported by Olubayode *et al.* (2016); Zereffa and Bekalo (2017); Ekpunobi *et al.* (2018); Shivaraju *et al.* (2018) and Bulta and Micheal (2019), the use of clay nanocomposites as filters for wastewater treatment is still lacking. This chapter highlights the synthesis, characteristics and applications of TiO_2 and ZnO nanoparticles. It also gives insight into the importance and literature on different clays, clay/TiO_2 and clay/ZnO blends used for adsorption studies but integrated methods like adsorption and filtration techniques for wastewater treatment is still lacking. More so, there is little or no information available in previous research on the fabrication of nanofilters

from the combination of kaolin with TiO_2 and ZnO nanoparticles (nanocomposites) for the removal of pollutants from tannery wastewater. Therefore, the research gaps that need to be filled in this research include: synthesis and characterization of nano-kaolin, kaolin/TiO_2, kaolin/ZnO nanocomposites and the combined nanocomposites of kaolin, TiO_2 and ZnO nanoparticles at different ratios, the use of the aforementioned nanoadsorbents for the treatment of tannery wastewater, the design of nanofilters from the synthesized adsorbents and performance evaluation of the designed nanofilters for the removal of bacteria and some physicochemical parameters from tannery wastewater.

CHAPTER THREE

3.0 MATERIALS AND METHODS

3.1 Materials

The chemicals used in this study were of analytical grade with percentage purity and manufacturers as shown in Table 3.1, while Table 3.2 shows the list of equipment used in this study. Similarly, the Figure 3.1 represents the flow chart of different steps of anchoring TiO_2 and ZnO nanoparticles onto clay including the characterization tools utilized.

Table 3.1: List of Reagents/Chemicals

S/N	Item	Formula	% Purity	Manufacturer
1.	Titanium isopropoxide	$(Ti(OCH(CH_3)_2)_4)$	98	Sigma Aldrich
2.	Sodium hydroxide	NaOH	97	Merck,
3.	Ethanol	C_2H_5OH	96	BDH Chemicals England
4.	Tetraoxosulphate (VI) acid	H_2SO_4	98	BDH Chemicals England
5.	Mercury(II) tetratoxosulphate (VI)	Hg_2SO_4	98	BDH Chemicals England
6.	Ammonium sulphate	$(NH_4)_2SO_4$	99.5	BDH Chemicals England
7.	Manganese(II) tetraoxosulphate (VI)	$MnSO_4$	99	BDH Chemicals England
8.	Potassium iodide	KI	99.5	BDH Chemicals England
9.	Sodium thiosulphate	$Na_2S_2O_3$	99	BDH Chemicals England
10.	Hydrochloric acid	HCl	34-37	BDH Chemicals England
11.	Tin(II) chloride	$SnCl_2$	97	BDH Chemicals England
12.	Potassium sulphate	K_2SO_4	99	BDH Chemicals England
13.	Boric acid	H_2BO_3	99.5	BDH Chemicals England
14.	Hydrogen peroxide	H_2O_2	30-32	BDH Chemicals England
15.	Trioxonitrate (V) acid	HNO_3	67-70	BDH Chemicals England
16.	Sodium trioxocarbonate (IV)	Na_2CO_3	99.5	BDH Chemicals England
17.	Copper(II) chloride	$CuCl_2$	98	BDH Chemicals England
18.	Zinc acetate dihydrate	$Zn(CH_3COO)_2.2H_2O$	98	BDH Chemicals England

Table 3.2: List of Equipment

Instrument	Model	Manufacturer
Muffle furnace	FSE-621-010L	Gallenkamp, England
Digital weighing balance	Scout Pro SPU	Ohaus Cooperation, China
pH Meter	EIL 7045/46	Kent, England
Magnetic Stirrer	78HW-1	Gallenkamp, England
X-ray diffractometer	XRD 6000	Shimadzu Scientific Instrument
High-resolution transmission electron microscope	Zeiss Auriga	FEI, Netherland
High resolution scanning electron microscope	Zeiss Auriga	FEI, Netherland
Fourier Transform Infra-red		Thermo Scientific Nicolet iS5 instrument with iD5 ATR spectrometer
Atomic absorption spectroscopy		
Brauner Emmetter Teller		Novawin Quantachrome instrument
Conductometer	EIL 5013	Kent, England
UV-visible spectrophotometer	JENWAY 6310	Barloworld Scientific LTD, UK

\

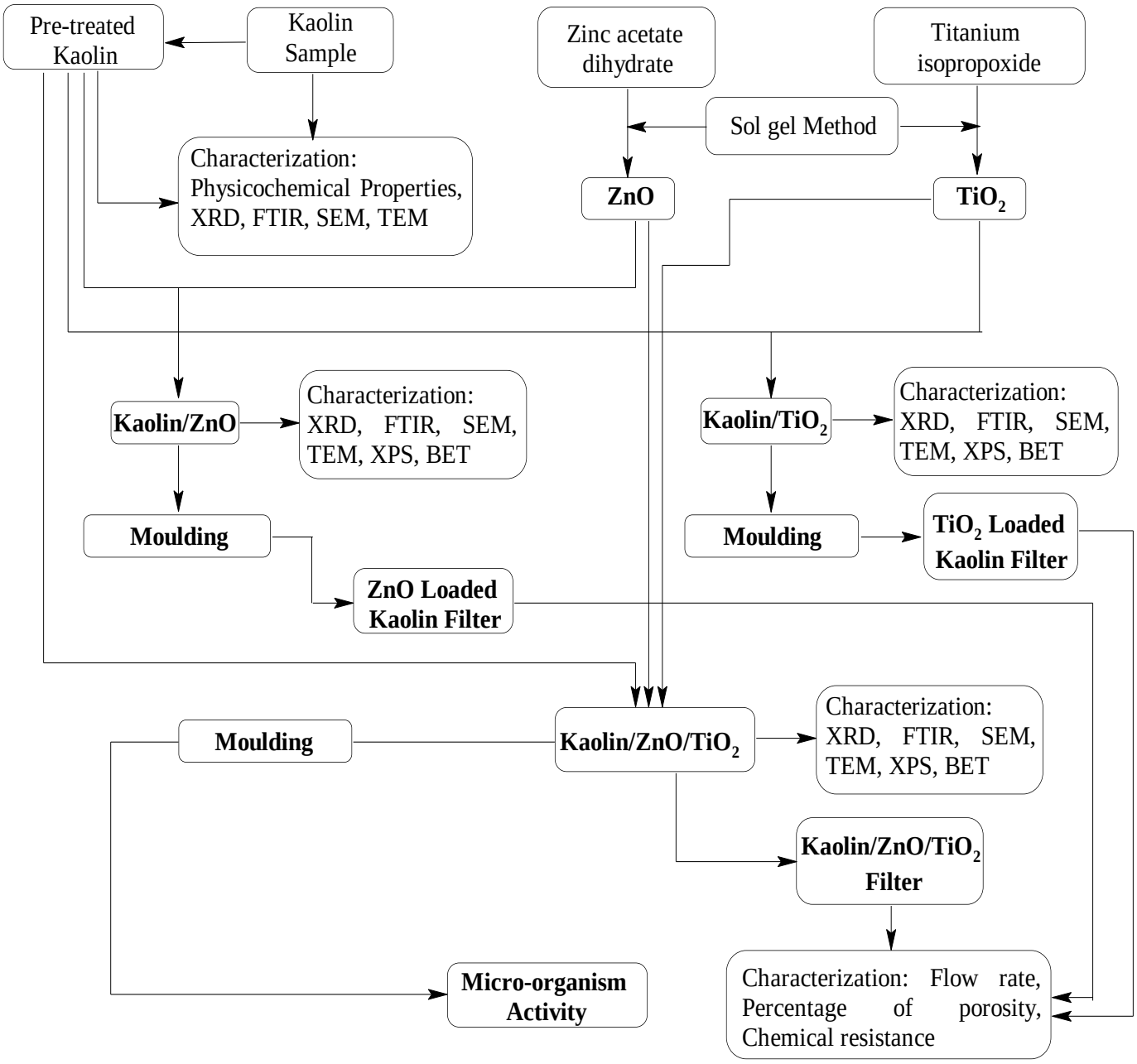

Figure 3.1: Flow Chart of Different Steps of TiO_2 and ZnO Nanoparticles Loaded on Kaolin

3.2 Sample Collection and Pre-treatment

The clay sample used in this study was obtained from a clay deposit in Gbako Local Government Area in Niger State, Nigeria located longitude and latitude at 9°24′00″N 6°02′00″E respectively as shown in Figure 3.2, with the image of collected clay sample presented in Plate II.

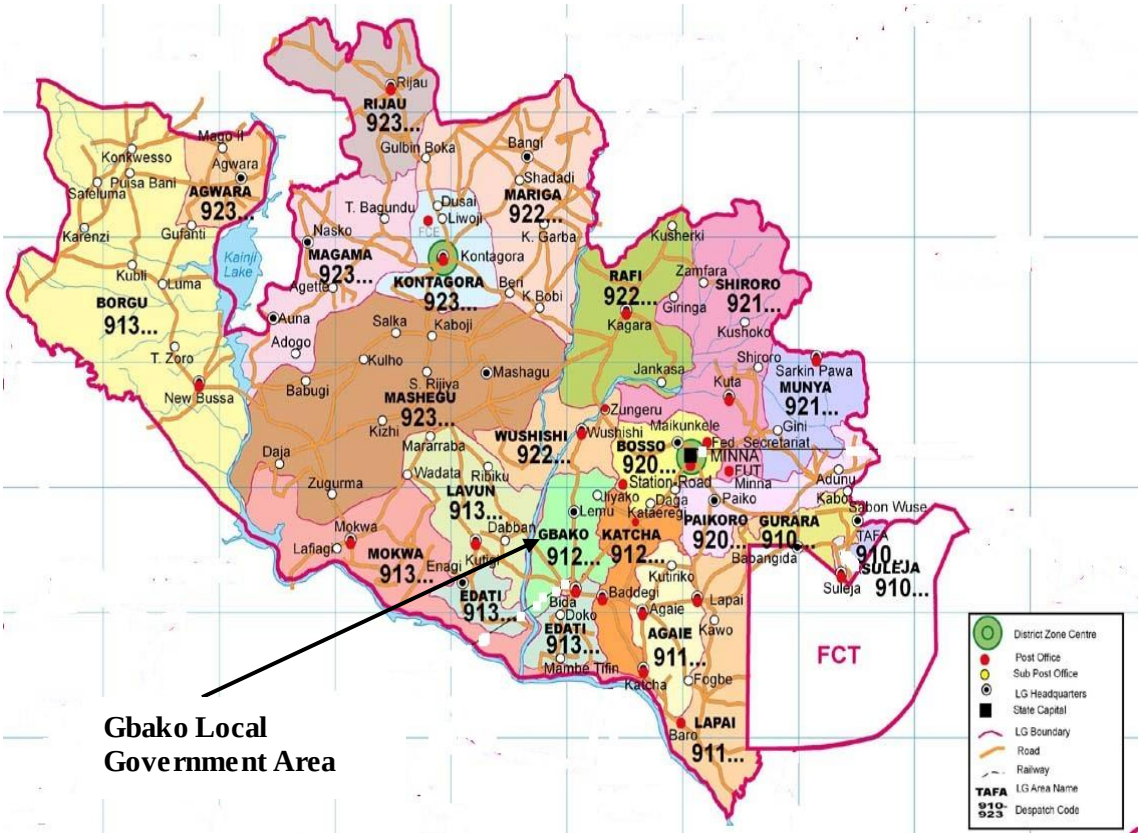

Figure 3.2: Map of Showing the Collection Site

Plate II: Image of Kaolin

The tannery wastewater sample was collected from Majema Tannery industry, Manuri Road, Tudun Wada Area, Sokoto State and put in a fifty (50) litre galloon rinsed with diluted hydrogen trioxonitrate (V) acid. The wastewater samples was transported to the laboratory for the determination of some physicochemical parameters and the bacteria contents.

3.2.1 Preparation and beneficiation of clay

The collected clay samples were pre-treated to remove debris and thereafter air-dried at ambient temperature for three (3) days. The samples were crushed with a mortar and pestle, then passed through a 250 µm mesh sieve to obtain very fine particle and subsequently stored in a plastic container prior to analysis.

The removal of impurities from the sieved clay was done by physical separation of dirt followed by wet/soaking method as described by Aroke *et al.* (2013). 100 g of powdered bulk clay sample was soaked in a plastic container with 1000 cm^3 of de-ionized water for 48 h. The resultant slurry was plunged and screened through a 250 µm sieve and then allowed to settle. The mixture was soaked with deionized water and later the water was decanted and deionized water was added to the slurry for further treatment.

3.2.1.1 Oxidation of organic matters

About 100.0 cm^3 of 0.5 M sodium oxochlorite (I) solution was added to the 200 cm^3 prepared slurry (clay and de-ionized water) in a 500 cm^3 beaker. The mixture was stirred with a magnetic stirrer, covered and allowed to settle for 2 days. The supernatant was decanted and the treatment was done for two consecutive times.

3.2.1.2 Washing and dispersing of clay

The resultant mixture was decanted into a 200 cm^3 beaker and 10.0 cm^3 of 0.5 M H_2O_2 was added for the further bleaching process. The mixture was stirred using a magnetic stirrer and allowed to settle for 2 days. The water was decanted and the residue was washed with de-ionized water copiously, oven-dried, crushed and then stored for further analysis.

3.3 Elemental Analysis of Clay Samples

Approximately 0.1 g of powdered beneficiated and raw clay samples each was weighed and transferred into two separate 100 cm^3 beakers. To each, 10.0 cm^3 of nitric acid was added, heated to 80 ^oC for 5 min and allowed to cool. Thereafter, 5.0 cm^3 each of H_2O_2 and conc. HNO_3 was added. The mixture was gently warmed on a hot plate until effervescence subsided and then allowed to cool for 1 hr. To the digest, the solution was diluted with 40 cm^3 of deionized water. The particulate matter was removed by filtration using Whatman filter paper No 41 in 100 cm^3 volumetric flask and made up to mark with de-ionized water. The filtrate was analyzed using AAS for Al, Fe, Pb and Cd. A blank reagent was prepared following a similar approach without the samples (Alsaleh *et al.*, 2018).

3.4 Physicochemical Properties of Beneficiated Clay

3.4.1 Measurement of pH

About 2.0 g of the sample was weighed into a 50 cm^3 beaker and 20 cm^3 of de-ionized water was added. This was transferred into a 100 cm^3 sample bottle. The sample bottle was placed on a mechanical shaker and shaken for 1h at 150 rpm and then allowed to settle for 15 min. The electrode of the calibrated pH meter using buffer tablets of 4, 7 and 11 was inserted into the solution and the pH reading was taken.

3.4.2 Measurement of electrical conductivity

About 5.0 g of the sample was weighed into a 50 cm^3 beaker and 20 cm^3 of de-ionized water was added and placed on a mechanical shaker for 1 h and the supernatant was decanted into a beaker where the electrical conductivity value was recorded using conductometer (Kent EIL 7045/46).

3.4.3 Determination of organic carbon content

A mixture of 1.0 g of the sample and 10.0 cm^3 of 0.5 M $K_2Cr_2O_7$ solution was prepared in a 250 cm^3 conical flask. About 20.0 cm^3 of conc. H_2SO_4 was added to the mixture, shaken

vigorously and allowed to remain for 30 min until it cooled. 100 cm^3 of de-ionized water was added followed by drops of ferroin indicator and titration was done with ammonium iron (II) sulphate solution until the colour changed to maroon. The percentage organic carbon was obtained using Equation 3.2 (Enang *et al.*, 2018).

$$\% \text{ Organic carbon} = \frac{(B - S) \times 0.4N \times 0.003 \times 100 \times F}{\text{Mass of dried sample}} \quad (3.1)$$

where;

B is a constant called the blank = 28.1

S is the titration value

N is the normality of the solution

F is the correction factor = 1.33

$$\% \text{ Organic matter of the sample} = \% \text{ organic carbon} \times 1.729 \quad (3.2)$$

3.4.4 Determination of the cation exchange capacity (CEC)

Copper bisethylenediamine $[Cu(EDA)_2]^{2+}$ cation method was used to determine the cation exchange capacity (CEC) as described by Hamadneh *et al.* (2019).

Cation Exchange

About 0.5 g of raw and beneficiated clay was weighed into 250 cm^3 volumetric flasks. 5 cm^3 of the complex solution was diluted with 25 cm^3 de-ionized water and then added to the clay sample. The resultant mixture was shaken for 30 min at 150 rpm and then centrifuged. The concentration of the complex remaining in the supernatant was determined by iodometry method as follows:

15.0 cm^3 of the supernatant was mixed with 15 cm^3 of 0.1 M HCl to deactivate the $[Cu(EDA)_2]^{2+}$ complex. Approximately 2 cm^3 of 0.5 cm^3 KI solution was added, and the solution was titrated with 0.02 M $Na_2S_2O_3$ solution with starch as an indicator. The CEC result was expressed as milliequivalents per gramme of dried clay as shown in eq. 3.2 to 3.5.

$$2Cu^{2+} + 4I^- \rightarrow 2CuI + I_2 \quad (3.3)$$

$$I_2 + 2S_2O_3^{2-} \rightarrow 2I^- + S_4O_6^{2-} \quad (3.4)$$

$$2Cu^{2+} + 2I^- + 2S_2O_3^{2-} \rightarrow S_4O_6^{2-} + 2CuI \quad (3.5)$$

$$\text{CEC} = \frac{(\text{Simple titre value} - \text{Blank}) \times \text{Normality of acid}}{\text{Weight of sample}} \times 100 \quad (3.6)$$

3.5 Synthesis of Nanoparticles and Nanocomposites

3.5.1 Synthesis of zinc oxide nanoparticles via sol-gel method

The zinc oxide nanoparticles were synthesized using a modified sol-gel method as described by Manikandan *et al.* (2018). A known mass (50 g) of zinc acetate dihydrate [$Zn(C_2H_3O_2)_2 \cdot 2H_2O$] powder was measured into a 250 cm^3 beaker and about 100.0 cm^3 of de-ionized water was added. The solution was stirred using a magnetic stirrer for 30 min at 150 rpm. 0.5 M sodium hydroxide (NaOH) was added drop-wise to the solution to obtain the desired pH of 6, 8, 10 and 12. The mixture was stirred for 5 min and a precipitate was obtained and later filtered by Whatman No. 1 filter paper. The precipitate obtained was washed with deionized water and ethanol to eliminate traces of the unreacted precursors. The final product was oven-dried at 105 ^oC for 24 h and finally calcined in the furnace at 450 ^oC to obtain ZnO nanoparticles.

3.5.2 Synthesis of titanium oxide nanoparticles (sol-gel method)

The sol-gel method which involves the variation of stirring time and solution pH was used for the synthesis of TiO_2 nanoparticles and are described as follows:

3.5.2.1 Effect of stirring time

With respect to effect of stirring time on synthesis of TiO_2 nanoparticles, five different solutions were prepared sequentially in this order: Approximately 30 cm^3 of titanium isopropoxide solution was measured individually into five separate 250 cm^3 beaker containing 120 cm^3 of de-ionized water. (Figure 3.3 A and B). The five separate solutions

were stirred for 20, 40, 60, 80 and 100 min, respectively using a magnetic stirrer at 250 rpm. A gel was formed in each of the five solutions at pH 5.62 and washed with de-ionized water and ethanol several times and thereafter, oven-dried at 105 ^{o}C for 24 h (Figure 3.3 D). The obtained yellow xerogel was pulverized in a mortar to a fine powder and further calcined in the furnace at 450 ^{o}C for 3 h (Figure 3.3 E). Figure 3.3 shows the steps involved in the synthesis of TiO_2 nanoparticles via sol-gel method without (Figure 3.3 C)

3.5.2.2 Effect of pH solution

Scheme 1 shows the pictorial representation of the synthesis protocol of TiO_2 nanoparticles via sol-gel method. Another set of five different solutions were prepared as follows: Firstly, 30 cm^3 of the titanium isopropoxide solution was measured into five separate 250 cm^3 beaker containing 120 cm^3 of de-ionized water (see Figure 3.3 A and B). To each of the five solutions, the pH of the solution was adjusted to 4, 6, 8, 10 and 12 respectively, using 0.5 M nitric acid or 0.5 M sodium hydroxide, followed by vigorous stirring on a magnetic stirrer at 250 rpm for optimum stirring time (smallest crystallite size) (Figure 3.3 C). A gel was formed and were allowed to age for 2 h, later washed with de-ionized water and ethanol several times and thereafter, oven-dried at 105 ^{o}C for 24 h (Figure 3.3 D). The obtained yellow xerogel was pulverized in a mortar to a fine powder and further calcined in the furnace at 450 ^{o}C for 3 h (Figure 3.3 E).

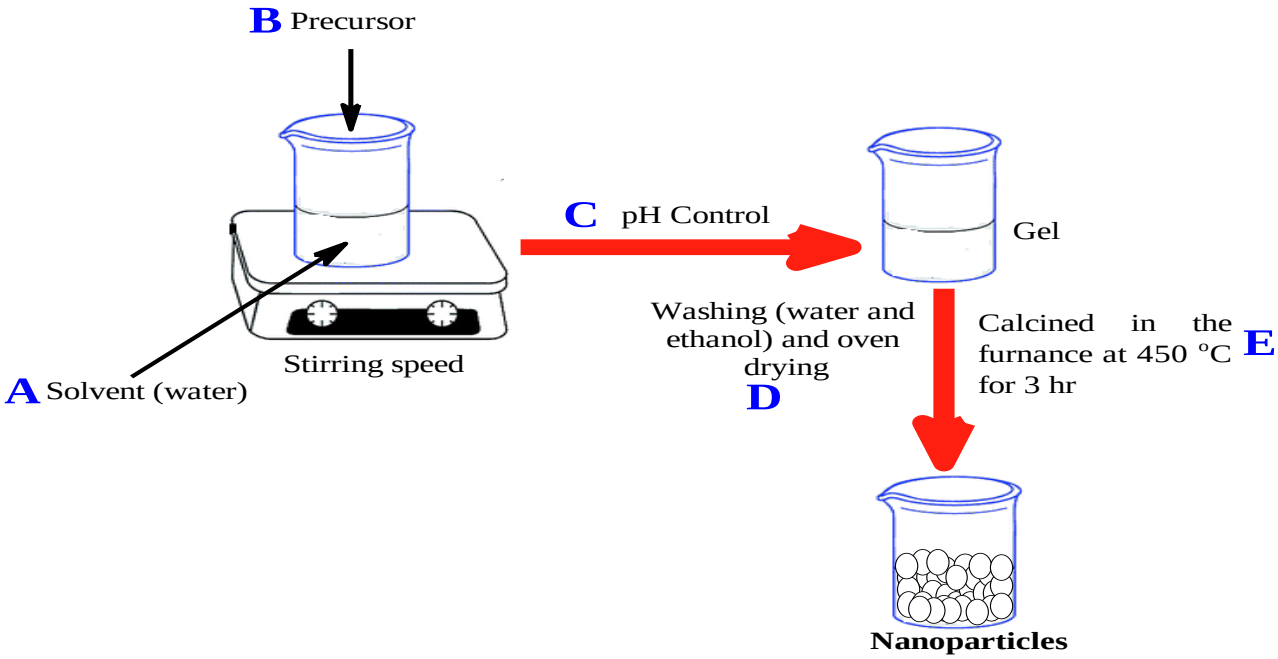

Figure 3.3: Pictorial representation of the steps involved in the preparation of TiO_2 nanoparticles using the sol-gel technique

3.5.3 Synthesis of kaolin/TiO_2 nanocomposites

The kaolin/TiO_2 nanocomposite was prepared using a wet impregnation method. Firstly, 5.0 cm^3 of titanium isopropoxide was measured into a 250 cm^3 beaker containing 50.0 cm^3 of de-ionized water and then the optimum solution pH was adjusted using 0.5 M NaOH, followed by stirring for 1 h at 150 rpm. Secondly, 5.0 g of the beneficiated clay was mixed with the gel and the mixture was homogeneously shaken for 2 h. The resulting mixture was washed severally with deionized water and ethanol. The final slurry was dried in an oven at 105 °C for a day and calcined at 450 °C for 3 h.

3.5.4 Synthesis of kaolin/ZnO nanocomposites

For the preparation of kaolin/ZnO, 5.0 g of $[Zn(C_2H_3O_2)_2{\cdot}2H_2O]$ was firstly dissolved in 50.0 cm^3 de-ionized water and stirred to get a precursor, then 0.5 M sodium hydroxide was added in drops into the precursor solution until the desired optimum pH was obtained. To the white suspension formed, 0.5 g of the beneficiated clay was dispersed under vigorous stirring for 1 hr at 150 rpm. A clay/ZnO homogeneous gel was formed and the product was

washed with de-ionized water. The dispersion was further dried in an oven for 24 h and finally calcined at 450 ^{o}C for 3 h in the furnace.

3.5.5 Synthesis of kaolin/TiO_2/ZnO nanocomposites

The kaolin/TiO_2/ZnO composite was prepared via a sol-gel method. 5.0 cm^3 of titanium isopropoxide was dissolved in 100 cm^3 of de-ionized water and stirred for 1 h. To the gel, 5.0 g of zinc acetate dehydrate was added and was further stirred for 1 h. The mixture was adjusted to the optimum pH value obtained during the synthesis of TiO_2 and ZnO nanoparticles. Subsequently, 5 g of beneficiated clay was added to this mixture and the following weight ratios of clay/TiO_2/ZnO (1:1:1), (1:2:1) and (1:1:2) were used. The samples were coded KTZ11, KTZ21 and KTZ12. The suspensions were further agitated, rinsed with de-ionized water and ethanol and calcined for 3 h in a muffle furnace at 450 ^{o}C.

3.6 Characterization of Kaolin, Kaolin/Nanoparticles and the Nanocomposites

3.6.1 XRD analysis

The identification of phases and the crystallite sizes of the synthesized nanoparticles and nanocomposites were determined using Bruker AXS D8 Advance X-ray diffractometer with Cu Kα radiation. The powdered samples were sprinkled in each case, on a de-greased glass slide and the diffraction pattern recorded between diffraction angles of 20^{o} and 90^{o}. The phase identifications were done by comparison with available d-spacing information and peaks from the Joint Committee on Powder Diffraction Standard (JCPDS).

3.6.2 HRSEM analysis

The morphologies of the synthesized samples were examined using Zeiss Auriga HRSEM. About 0.05 mg was sprinkled onto carbon adhesives tape and sputter-coated with Au-Pd using Quorum T15OT Analyzer for 5 min. The microscope was operated with electron high tension at 5 kV for imaging. High resolution scanning electron microscope (HRSEM)

equipped with energy dispersive spectroscopy (EDS) was further used to determine the elemental composition of the synthesized nanoparticles and nanocomposites.

3.6.3 HRTEM analysis

The particle size and distribution pattern were analysed by Zeiss Auriga High-resolution transmission electron microscopy (HRTEM) coupled with energy dispersive spectroscopy (EDS). About 0.02 g each of the synthesized samples was suspended in 10 cm^3 of methanol and thereafter subjected to ultra-sonication until complete dispersion was achieved. Two drops of the slurry were dropped onto a holey carbon grid with the aid of a micropipette and subsequently dried by exposure to photo light prior to imaging. The imaging was done on HRTEM model.

3.6.4 Branauer-Emmett-Teller technique N_2 adsorption

About 0.1 g each of the dry powdered samples in a sample tube was first degassed at 95 ^oC for 5 h to remove residual water and volatile compounds that could block the pores. The BET surface area and average pore volume distributions were obtained from the plot of the volume adsorbed (cm^3/g STP) against relative pressure. The N_2 adsorption-desorption isotherms were poised at -196 ^oC using a micromeritics ASAP 2020 accelerated surface area and porosimetry analyser.

3.6.5 FTIR analysis

Fourier transform infrared spectra (FTIR) of the synthesized samples were recorded using Perkin-Elmer 2000 FTIR spectrometer fitted with a deuterated triglycine sulphate (DTGS) detector covering the frequency range of 500-4000 cm^{-1}. The sample cell was purged with nitrogen gas throughout data collection to exclude carbon(IV) oxide and water vapour. Ten milligrams (0.01 g) each, of the dried samples was evenly dispersed in 200 mg of

spectroscopic grade KBr to record the spectra. The sample was recorded in the range of 500 to 4000 cm^{-1} wavelength, the baseline was corrected and spectra were smoothened.

3.7 Determination of Physicochemical Properties of Tannery Wastewater

The physicochemical characterization of the wastewater was done using standard procedures as described by the American Public Health Association (APHA) (2017).

3.7.1 Chemical oxygen demand (COD) (closed reflux method)

For this determination, 15.0 cm^3 of conc. tetraoxosulphate (VI) acid with 0.3 g of mercuric tetraoxosulphate (VI) and a pinch of silver tetraoxosulphate (VI) along with 5.0 cm^3 of 0.025 M potassium heptaoxodichromate (VI) were measured into a Nessler's tube. Thereafter, 10.0 cm^3 of the tannery wastewater was added to the mixture and kept for about 90 minutes on a hot plate for digestion. About 40.0 cm^3 of de-ionized water was added to the cooled mixture (to make up to 50 cm^3) and titrated against 0.25 M ammonium iron(II) sulphate using ferroin indicator. The appearance of wine red colour from blue-green indicated the endpoint. A blank experiment was also carried out using 10 cm^3 of distilled water. The formulae used for the estimation of the COD level is shown in equation 3.7 to 3.8.

$$\text{COD}\left(\frac{\text{mg}}{\text{dm}^3}\right) = \frac{(\text{B} - \text{A}) \times \text{N} \times \text{F} \times 1000}{\text{Volume of the sample taken}} \tag{3.7}$$

$$\text{Normality of FAS} = \frac{\text{V}_\text{A} \times 0.25}{\text{V}_\text{F}} \tag{3.8}$$

$$\text{F} = \frac{1000}{\text{Titrant value of blank}} \tag{3.9}$$

where A = Volume of titrant used against the sample (cm^3), B = Volume of titrant used against blank (cm^3), N = Normality of titrant (N), V_A = Volume of FAS (cm^3) and V_F = Volume of reagent used (cm^3).

3.7.2 Determination of dissolved oxygen (DO)

The level of DO in the wastewater was determined by Winkler's method. Tannery wastewater was collected into BOD bottles, to each of which 2.0 cm^3 of manganese(II) tetraoxosulphate (VI) and 2.0 cm^3 of potassium iodide were added. They were then filled up to 250 cm^3 (to the brim) with the wastewater. This was corked and thoroughly mixed for some time for precipitation and the precipitate was allowed to settle down. At this stage, 2.0 cm^3 of conc. hydrogen tetraoxosulphate (VI) acid was added and mixed well until all the precipitate dissolved. 203 cm^3 of the wastewater was measured into a conical flask and titrated against 0.025 M sodium thiosulphate using starch as an indicator. The colour changed from blue to colourless. The level of DO was determined using equation 3.10.

$$\text{Dissolved Oxygen } \left(\frac{\text{mg}}{\text{dm}^3}\right) = \frac{(0.2 \times 1000) \times (0.025 \text{ M} \times \text{vol.}) \text{ of } Na_2S_2O_3}{203} \qquad (3.10)$$

Determination of biological oxygen demand

About 50 cm^3 of tannery wastewater sample was analysed for the first day DO and incubated at 20 ^oC for 5 days and the 5^{th} day DO was noted (APHA, 2017). A blank was prepared in a similar manner and the level of BOD was determined by equation 3.11.

$$\text{BOD } \left(\frac{\text{mg}}{\text{dm}^3}\right) = \frac{(D_1 - D_2) - (B_1 - B_2) \times 100}{\%\text{ dilution}} \qquad (3.11)$$

where D_1= DO of the sample immediately after preparation (mg/dm^3), D_2= DO of the sample after the incubation period (mg/dm^3), B_1= DO of blank (seeded dilution water) before incubation (mg/dm^3) and B_2= DO of blank (seeded dilution water) after incubation (mg/dm^3).

3.7.3 Determination of free carbon dioxide (CO_2)

A known volume (50.0 cm^3) of the wastewater sample was measured into a conical flask. Approximately, 2-3 drops of phenolphthalein indicator were added and titrated against 0.2

M sodium hydroxide till the pink colour persisted indicating the endpoint and the amount of free carbon dioxide was determined using equation 3.12.

$$\text{Free } CO_2(mg/dm^3) = \frac{V_t \times 1000}{V_s} \qquad (3.12)$$

where V_t= Volume of titrant (cm^3) and V_s= Volume of the sample (cm^3)

3.7.4 Determination of chlorides

A known volume of filtered water sample (50.0 cm^3) was measured in a conical flask, to which about 0.5 cm^3 of potassium chromate indicator was added and titrated against standard (0.014 M) silver trioxonitrate (V) till silver dichromate ($AgCrO_4$) started precipitating and the level of chloride was determined using equation 3.13.

$$\text{Chloride } (mg/dm^3) = \frac{(A - B) \times 35.457 \times N}{S} \qquad (3.13)$$

where A = Volume of silver trioxonitrate (V) consumed by the sample (cm^3), B = Volume of silver nitrate consumed by the blank, N = Normality of titrant and S = Volume of the sample (cm^3).

The salinity of water on the basis of its empirical relationship with chloride content was calculated as follows:

$$\text{Salinity } (g/dm^3) = 0.03 + 1.805 \left(\text{Chloride in} \frac{mg}{dm^3}\right) \qquad (3.14)$$

3.7.5 Determination of nitrate (NO_3^-)

A known volume (50.0 cm^3) of the water sample was pipetted into a porcelain dish and evaporated to dryness on a hot water bath. To this, 2.0 cm^3 of phenol disulphonic acid was added to dissolve the residue by constant stirring with a glass rod. A concentrated solution of sodium hydroxide and distilled water was added under continuous stirring to make the solution alkaline. The mixture was filtered into a Nessler's tube and the filtrate was made up to 50 cm^3 with de-ionized water. The absorbance was read at 410 nm using a

spectrophotometer after the development of colour. A standard graph was plotted by taking the concentration along X-axis and the spectrophotometric readings (absorbance) along Y-axis. The level of nitrate was found by comparing absorbance of the sample with the standard curve and expressed in mg/dm^3 and determined using equation 3.15.

$$\text{Nitrates} = \frac{\text{Absorbance of sample} \times \text{Conc. of Standard} \times 1000}{\text{Absorbance of Standard} \times \text{sample taken}} \qquad (3.15)$$

3.7.6 Determination of sulphate

About 250 cm^3 of the tannery wastewater sample was evaporated to dryness using an evaporating dish on a steam bath. The residue was moistened with a few drops of conc. HCl and 30 cm^3 de-ionized water was added, boiled for 30 min and then filtered using Whatman filter paper No 42. The dish was rinsed and the Whatman filter paper was washed with several portions of de-ionized water, both filtrate and washings were added together. This was heated to boiling and then 10 cm^3 of 10 % $BaCl_2$ solution was added, drop by drop with constant stirring at 150 rpm. The mixture was digested for about 30 minutes, filtered, and then the filter paper was washed with warm deionized water. It was then ignited, cooled and weighed in an already weighed crucible. Equation 3.16 was used to determine sulphate.

$$SO_4^{2-}\left(\frac{\text{mg}}{\text{dm}^3}\right) = \frac{\text{mg } BaSO_4 \times 411.5}{\text{volume of water sample}} \qquad (3.16)$$

3.7.7 Determination of alkalinity

About 20 cm^3 of the tannery wastewater sample was pipetted into a 250 cm^3 conical flask and 20 cm^3 of de-ionized water into another flask. Three drops of phenolphthalein indicator were added to each and the solution became pink. 0.01 M H_2SO_4 was added from the burette until the pink colour disappeared and the volume of acid was recorded. The alkalinity level was determined using eq. 3.16.

$$\text{Total alkanility}\left(\frac{\text{mg}}{\text{dm}^3}\right) = \frac{\text{volume of standard acid} \times \text{Molarity} \times 1000}{\text{volume of sample}} \qquad (3.16)$$

3.7.8 Determination of total hardness

About 2.0 cm^3 of 0.5 M NaOH solution was added to 50 cm^3 wastewater followed by 0.2 g of the indicator mixture (ammonium purperate) and then stirred for 1 hr at 150 rpm. 0.01 M EDTA was used to titrate the mixture until the colour changed from pink to purple. Then 2 drops of the titrant were added to ensure that there was no further colour change. The total hardness was determined using the relationship presented in equation 3.18 and 3.19.

where:

$$\text{Ca Hardness as } CaCO_3 \left(\frac{\text{mg}}{\text{dm}^3}\right) = A \times B \times 1000 \qquad (3.18)$$

A = volume of titrant used

B = mg $CaCO_3$ equivalent to 1 cm^3

$$\text{Total hardness } \left(\frac{\text{mg}}{\text{dm}^3}\right) = \text{Ca hardness} + \text{Mg hardness} \qquad (3.19)$$

3.7.9 Determination of nitrite (NO_2^-)

About 50.0 cm^3 of the tannery wastewater was measured into a 50 cm^3 volumetric flask. 1.0 cm^3 of sulphanilamide solution was added to the sample and after 3 min, 1 cm^3 of N-1 naphthyl ethylene diamine (NED) hydrochloride solution was added and mixed thoroughly. The absorbance was measured on the spectrophotometer at 543 nm. The nitrite value was deduced by comparing its absorbance with a standard curve and expressed in mg/dm^3.

3.7.10 Determination of phosphates

About 50.0 cm^3 of the filtered wastewater sample, 4 cm^3 of ammonium molybdate reagent and about 4-5 drops of stannous chloride reagent were mixed together in a 250 cm^3 beaker. After 10 to 12 min, the colour developed was measured on the spectrophotometer at 690 nm. A blank was run with the same treatment with de-ionized water as a sample. The value of phosphate was obtained by comparing absorbance of wastewater sample with the standard curve and expressed in mg/dm^3 using equation 3.20.

$$\text{Phosphate } \left(\frac{\text{mg}}{\text{dm}^3}\right) = \frac{\text{Absorbance of sample } \times \text{Conc. of Standard} \times 100}{\text{Absorbance of Standard} \times \text{Sample taken}} \quad (3.20)$$

3.8 Heavy Metal Determination

About 50 cm^3 of the tannery wastewater sample was measured into a 100 cm^3 beaker with the addition of 15 cm^3 concentrated trioxonitrate (V) solution and 10 cm^3 of 50 % concentrated hydrochloric acid. The contents were heated on a hot plate and 7 cm^3 of 50 % concentrated hydrochloric acid added and heated for 10 minutes. The solution was allowed to cool, and then deionized water was added and filtered into a 100 cm^3 Pyrex volumetric flask using Whatman No 42 filter paper. This was then made up to the mark with deionized water and stored for further analysis of heavy metals such as Zn, Pb, Cd and Cr using AAS (Perkin Elmer 200 Atomic Absorption Spectrophotometer) (Ali *et al.,* 2016).

3.9 Batch Adsorption Processes

Batch equilibrium adsorption experiments were performed in order to evaluate the equilibrium time, obtain adsorption kinetics, adsorption isotherm and adsorption thermodynamic data. The removal efficiency (% removal) and the adsorption capacity, q_e (mg/g) of some physical and chemical indicators from tannery wastewater solution by clay, clay/TiO_2, clay/ZnO and clay/TiO_2/ZnO (KTZ11, KTZ21 and KTZ12) at different conditions were calculated using equations 3.21 and 3.22.

The adsorption capacities of the differently prepared adsorbents were determined as follows:

$$\% \text{ removal} = \frac{C_0 - C_e}{C_e} \times 100 \quad (3.21)$$

$$q_e = \frac{(C_0 - C_e)}{M} V \quad (3.22)$$

where $\mathbf{C_0}$ (mg/dm^3) and $\mathbf{C_e}$ (mg/dm^3) are the initial and equilibrium liquid phase concentration, respectively; **V** (dm^3) the volume of the solution and **M** (g) the mass of the adsorbent.

The adsorption experiments were designed to carry out the adsorption characteristics of the beneficiated clay and nanocomposites under various conditions. The effects of parameters such as contact time, mass ratio of adsorbent to the volume of adsorbate and temperature on some indicator parameters were determined.

3.9.1 Effect of contact time

The effects of contact time on the physical and chemical indicators analysed in this research using the beneficiated clay, nanoparticles and nanocomposites were investigated by contacting 0.20 g of the adsorbents in each case, with 40 cm^3 of the wastewater in a corked 250 cm^3 conical flask, agitated at 150 rotations per min (rpm) for 0, 5, 10, 15, 20, 25 and 30 min on an orbital shaker. The samples were analysed after filtration by Whatman No. 42 filter paper. The final concentrations of chloride, BOD, COD, sulphate, nitrate and metal ions (Zn, Pb, Cd and Cr) were analysed using APHA Methods (2017) and atomic absorption spectrometer (AAS) for the heavy metals. The optimum contact time, especially for the adsorbents for metal ions sorption from tannery wastewater were also determined.

3.9.2 Effect of adsorbent dose

The effects of adsorbent dosage on the equilibrium uptake of physical and chemical indicators from wastewater using beneficiated clay, nanoparticle and nanocomposites were investigated with adsorbent doses of 0.4, 0.6, 0.8, 1.0, 1.2 and 1.4 g, respectively. The experiments were performed by adding the known weights of the adsorbents into 250 cm^3 flasks containing 40 cm^3 of the wastewater each. The flasks were shaken at 150 rpm at the optimum contact time of each adsorbent. The samples were filtered using Whatman paper No. 42 and the concentrations of the chloride, BOD, COD, sulphate, nitrate and metal ions (Zn, Pb, Cd and Cr) were measured using APHA Methods (2017) and atomic absorption spectrometer (AAS), respectively.

3.9.3 Effect of temperature

The effects of temperature on the equilibrium uptake of the indicator parameters from tannery wastewater by beneficiated clay and nanocomposites at the temperature values of 30, 40, 50, 60, 70 and 80 ^{o}C were investigated. The experiments were performed by adding 0.2 g of the adsorbent to 40 cm^3 of wastewater in 250 cm^3 conical flasks. The corked flasks were shaken in a water bath at respective temperature for the optimum contact time. The samples were filtered using Whatman paper No. 42 and the concentrations of chloride, BOD, COD, sulphate, nitrate and metal ions (Zn, Pb, Cd and Cr) were measured using APHA Method (2017) and atomic absorption spectrometer (AAS) respectively.

3.10 Studies on the Adsorption Isotherms

Halsey model was employed in order to evaluate the multilayer adsorption at a relatively large distance from the surface of the adsorbents. The equation of the adsorption isotherm is given as follows:

$$q_e = \frac{1}{n_H} I_n K_H - \frac{1}{n_H} \ln C_e \qquad (3.23)$$

where $\mathbf{n_H}$ and $\mathbf{I_n K_H}$ are Halsey isotherm constants and these were determined from the slopes and intercepts of the linear plots of $\mathbf{q_e}$ as the ordinates and $\mathbf{\ln C_e}$ as the abscissa at the temperature range of 30 to 80 ^{o}C, constant pH and adsorbent dosage of 0.2 g.

Jovanovic model was established on the assumption of the Langmuir model and also to the possibility of some mechanical contacts between the sorbate and adsorbents. The linear form of the adsorption model given in equation 3.24 was employed for this study.

$$\ln q_e = \ln q_{e(max)} - K_j C_e \qquad (3.24)$$

A plot of $\mathbf{\ln q_e}$ against $\mathbf{C_e}$ was used to determine the Jovanovic constant ($\mathbf{K_j}$) and the maximum adsorption capacity ($\mathbf{q_{e(max)}}$), where $\mathbf{K_j}$, the slope and $\mathbf{q_{e(max)}}$, the intercept were also determined.

The Redlich-Peterson (R-P) isotherm which is the combination of the Langmuir and Freundlich adsorption models with its linearized expression as defined in equation 3.25 was employed in the study.

$$\ln\frac{C_e}{q_e} = \beta \ln C_e - \ln A \qquad (3.25)$$

where the isotherm constants **β** and **A** were determined from the slope and intercept of the plot of $\mathbf{ln}\frac{\mathbf{C_e}}{\mathbf{q_e}}$ as the abscissa and $\mathbf{lnC_e}$ as the ordinate.

The Flory-Huggins isotherm model which evaluates the degree of surface coverage properties of a sorbate on the sorbent was also studied. The Flory-Huggins model defined by the equations 3.36 and 3.27 were also employed.

$$\ln\frac{\theta}{C_o} = \ln K_{FH} + n\ln(1-\theta) \qquad (3.26)$$

$$\theta = \left(1 - \frac{C_e}{C_o}\right) \qquad (3.27)$$

The adsorption data at different temperatures were plotted as a function of $\mathbf{ln}\frac{\boldsymbol{\theta}}{\mathbf{C_o}}$ against $\mathbf{ln}(\mathbf{1}-\boldsymbol{\theta})$. Where n is number of adsorbates occupying adsorption site, θ is the degree of surface coverage and $\mathbf{K_{FH}}$ is the Flory-Hugging constants.

3.11 Kinetic Models Study

The adsorption mechanism, as well as rate controlling steps, can be established on the removal of the studied pollutants with respect to contact time (0-30 min) via kinetic models. The kinetic data were analysed using the Bangham, fractional power and Avrami equation models. The Boyd kinetic and Weber-Morris intraparticle diffusion models were used to check the mechanism of adsorption.

Bangham's model equation is expressed as:

$$\log\left[\log\left(\frac{C_o}{C_o - q_t M}\right)\right] = \log\left(\frac{K_o M}{2.303V}\right) + \alpha \log t \qquad (3.28)$$

where $\mathbf{C_o}$ is the initial concentration of the pollutant in wastewater (mg/dm^3), **V** is the volume of wastewater (dm^3), **M** is the weight of adsorbent (g/dm^3), $\mathbf{q_t}$ is the amount of pollutant adsorbed at time, **t** (mg/g) and $\mathbf{K_o}$ and $\boldsymbol{\alpha}$ (less than 1) are constant which are calculated from the intercept and slope of the linear plot of $\mathbf{log}\left[\mathbf{log}\left(\frac{\mathbf{C_o}}{\mathbf{C_o - q_t M}}\right)\right]$ against $\mathbf{logt}$.

The Avrami equation is used to evaluate the kinetic parameter as a function of time (0-30 min) was also employed in the study. The linear form of the Avrami kinetic model is expressed as:

$$\ln\left[\ln\left(\frac{q_e}{q_e - q_t}\right)\right] = n_{AV}\ln K_{AV} + n_{AV}\ln t \qquad (3.29)$$

where $\mathbf{K_{AV}}$ is the Avrami kinetic constant and $\mathbf{n_{AV}}$ is the Avrami model constant related to the adsorption mechanism. The values of $\mathbf{K_{AV}}$ and $\mathbf{n_{AV}}$ are obtained for the intercept and slope, respectively, from the plot of $\mathbf{ln}\left[\mathbf{ln}\left(\frac{\mathbf{q_e}}{\mathbf{q_e - q_t}}\right)\right]$ versus $\mathbf{lnt}$.

Equation 3.30 which depicts the linear form of the model represented as follows was also employed in the study.

$$\log q_t = \log K + V\log t \qquad (3.30)$$

where **V** and **K** are constants with **V** less than 1. The values of **V** and **K** are slope and intercept obtained from the plot of $\mathbf{logq_t}$ against $\mathbf{logt}$, respectively.

3.11.1 Determination of the mechanisms of adsorption

The adsorption mechanism of the pollutant removal using kaolin, kaolin/TiO_2, kaolin/ZnO and kaolin/TiO_2/ZnO nanocomposites were investigated using the intraparticle diffusion model by Weber-Morris equation and Boyd model. The Weber-Morris equation proposed for modelling adsorption kinetic is expressed as:

$$q_t = K_d t^{1/2} + I \qquad (3.31)$$

where $\mathbf{K_d}$ (mgg^{-1}min$^{-1/2}$) is the intraparticle diffusion rate constant, **I** is a constant that shows the thickness of boundary and the greater the intercept, the greater the rate-controlling step

on the adsorption surface. The **I** and $\mathbf{K_d}$ are the intercept and slope, respectively, which are evaluated from the linear plot of $\mathbf{q_t}$ against $\mathbf{t^{1/2}}$.

Boyd model was used to analyse the rate-controlling step in the adsorption of the studied pollutant by kaolin, kaolin/TiO_2, kaolin/ZnO and kaolin/TiO_2/ZnO nanocomposites. The Boyd kinetic equation is presented as

$$F = 1 - \frac{6}{\pi}\exp(-B_t) \tag{3.32}$$

$$F = \frac{q_t}{q_e} \tag{3.33}$$

where $\mathbf{q_t}$ and $\mathbf{q_e}$ in (mg/g) are the amount of adsorbate uptake at a time and maximum equilibrium uptake. **F** is the fraction of pollutant adsorbed at any time, **t**.

$$B_t = -0.4977 - \ln(1 - F) \tag{3.34}$$

$\mathbf{B_t}$ is the time constant and is a function of **F**. The linear plot of $\mathbf{B_t}$ against time, t is employed for the experimental data.

3.12 Bacteriological Analysis of Wastewater

The counting was done using microbial colony counter and the result was recorded as cfu (colony forming count) which is the S.I unit of microbial counts. After counting the microbial cells, the pure culture was made by sub-culturing a single colony into a fresh nutrient Agar plate for bacteria and suborned dextrose Agar for microbes so as to obtain a pure isolate. After sub-culturing, the plates were incubated accordingly. These were used for characterization (identification) of the isolates and finally naming of the organisms.

A smear was made on a clean grease-free glass slide. The smear was flooded with crystal violet and allowed to stay for 30 s. It was then diluted with Gram's of iodine after the 30 sec which acted as a mordant on the smear and left for another 30 sec. This was then drained and decolourized with 95 % ethyl alcohol for 1 minute. After decolonization, the smear was counterstained with safranine and left for 1 min. This was finally washed with distilled and

moped with 40 Whatman filter paper and finally viewed at x 100 (objective lens) using a binocular microscope. This gave the evolutionary trend of bacteria. The Grain's positive retained the colour of wastewater dye of crystal violet. The Gram negative retained the colour and the cell shape was either cylindrical (rod) or spherical (cocci), the argent of the cells only 0.2 connected (pain), scattered (clusters), or connected in long rod (chain) are noted and recorded.

3.13 Characterization of Moulded Beneficiated Kaolin

3.13.1 Moulding of the trial bars

The kaolin was molded into shapes via wooden moulds. The lubricant was applied to the surface of the moulds in order to prevent the kaolin from sticking to their surfaces. The initial shape was spherical with a width of 3.5 and the second shape was a rectangular bar with length 6 cm.

3.13.2 Shrinkage test

The original lengths of the molded spherical and rectangular bars were recorded immediately after molding and they were recorded as $\mathbf{L_1}$ (cm). The pieces of the bar were then air-dried for 3 days and subsequently, oven-dried for 3 days at 105 ^{o}C to attain constant weights. The shrinkage from the marks on the bars were determined and recorded as $\mathbf{L_2}$ (cm). The bars were further calcined at 900 ^{o}C. The shrinkage of the bars from the marks after firing was recorded as $\mathbf{L_3}$ (cm) and was expressed as:

$$\text{Linear shrinkage } (\%) = \frac{L_1 - L_3}{L_2} \times 100 \qquad (3.35)$$

$$\text{Total shrinkage } (\%) = \frac{L_1 - L_3}{L_1} \times 100 \qquad (3.36)$$

3.13.3 Determination of water absorption

The calcined test bars were weighed and the known weights of the dried samples were recorded as $\mathbf{M_1}$ (g). Afterwards, the bars were soaked in de-ionized water for 24 h, then

removed, cleaned and weighed immediately. The weights of the samples were recorded as M_2 (g). The percentage water absorption was calculated as follows:

$$\text{Water absorption } (\%) = \frac{M_2 - M_1}{M_1} \times 100 \qquad (3.36)$$

3.13.4 Determination of porosity

The fired bars and filter pots at 910 °C were weighed and soaked in water for 24 h. The apparent porosity of samples was calculated using equation. 7.

$$\text{Apparent porosity } (\%) = \frac{M_w - M_f}{\rho_e V_f} \qquad (3.37)$$

where $\mathbf{M_f}$ is the weight of the fired sample (g), $\mathbf{M_w}$ is the weight of soaked sample in water for 24 h (g), $\mathbf{V_f}$ and $\boldsymbol{\rho_e}$ is the volume of fired sample (cm^3) and volumic mass of water (g/cm^3), respectively.

3.14 Clay Filter Pot Production

A laboratory-scale test was used for the fabrication of ceramic pot filter. The production techniques were carried out at the Industrial Design Department of the Federal University of Technology, Akure, Nigeria. Different rations of kaolin and sawdust were sieved using 250 µm mesh sieve. The kaolin was molded into shapes via wooden moulds. The lubricant was applied to the surface of the moulds in order to prevent the kaolin sample from sticking to their surfaces. The initial shape was spherical with a width of 3.5 and the second shape was a rectangular bar with length 6 cm as shown in Plate III.

The mixed kaolin and sawdust were hydrated by the addition of de-ionized water and homogenously mixed and kneaded with friable material. The resultant mixture was allowed to age for 72 hr. The ageing of the mixture will cause plasticity, fermentation and some physical changes in the material. Plate 1 describes the kaolin bars calcined at 910 ^oC for determination of porosity, water absorption and shrinkage. The bars produced were designated as T1 to T10.

Plate III: (A) Trial bars from beneficiated kaolin and (B) Mould

The mixtures were moulded using giggle jolly machine as shown in Plate IV (a). The moulded filter materials were dried at ambient temperature for 7 days to avoid the manufacture pot filters from cracking when sintering in a kiln. Afterwards, the dried ceramic filters were placed inside a kiln as seen in Plate IV (b) and then fired in a kiln at 910 ^{o}C. The firing constitute different stages namely; dehydration (100-300 ^{o}C), oxidation (300-500 ^{o}C) and vitrification stage (500-900 ^{o}C). Firing allows the reduction in porosity, increase in strength and density of the material. Ten (10) ceramic pot filters at different kaolin to sawdust rations produced using a gas-fired temperature-controlled kiln as presented in Fig. 3.4. The fired ceramic pot filter samples labelled (T1-T10) were allowed to cool in the kiln and tested for water absorption, flow rate, porosity, microbial and some physicochemical parameters removal efficiency.

Plate IV: (A) A Pictorial representation of giggle jolly machine and (B) Kiln

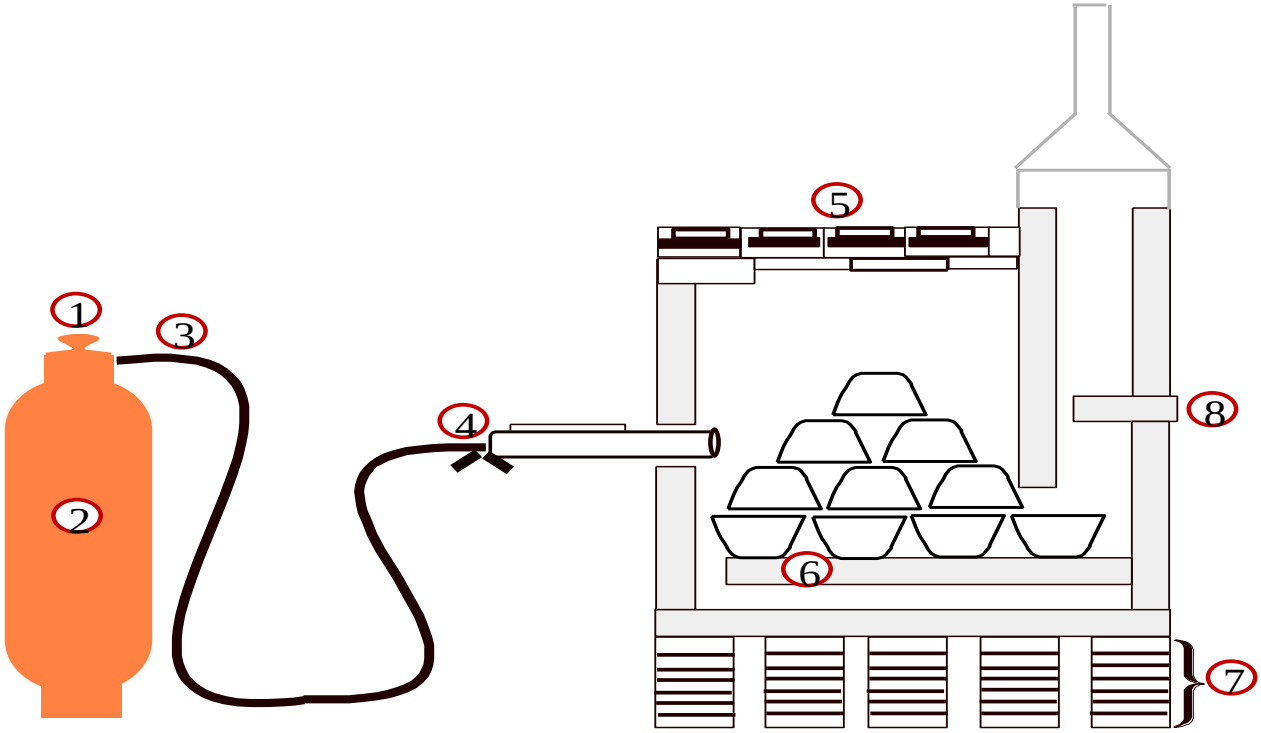

1. Tap
2. Gas cylinder
3. Nozzle
4. Burner
5. Roof parts
6. Internal floor
7. Pillars
8. Chimney

Figure 3.4: A Gas Fixed Temperature-Controlled Kiln for the Production of Pot Filters

Table 3.3: Various Trails of Filter Pots at Different Proportions of Clay/Sawdust

Sample	Percentage (%)		Total
	Clay	Saw dust	
T1	40	60	100
T2	44	56	100
T3	33	67	100
T4	50	50	100
T5	46	54	100
T6	60	40	100
T7	56	44	100
T8	67	33	100
T9	60	40	100
T10	54	46	100

3.15 Chemical Resistance Analysis

The chemical resistance was performed on the optimum filter fired at 910 ^{o}C. The flat bar and ceramic filter were immersed in solution and pH of the solution was varied from 1-12 and adjusted to the desired value using either 0.5 M H_2SO_4 and 0.5 M NaOH and after the adjustment the flat bars were left in the solution for 48 h. Thereafter, the bars and ceramic pot filter were removed from the solution weighed and the chemical resistance was computed as follows:

$$\% \, R = \frac{M_1 - M_2}{M_1} \times 100 \qquad (3.38)$$

where $\mathbf{M_1}$ and $\mathbf{M_2}$ are the mass of the sample before pH attach and mass after removing from acidic/basic solution (**g**).

CHAPTER FOUR

4.0 RESULTS AND DISCUSSION

4.1 Raw and Beneficiated Kaolin

4.1.1 Physicochemical properties of raw and beneficiated kaolin

Table 4.1 shows the physicochemical properties of the raw and beneficiated kaolin. The pH values of the raw and beneficiated clay were 5.47 and 6.97, respectively. The pH value of the beneficiated clay is slight neutral and this will help to promote pollutants such as heavy metals precipitation and adsorption. The cation exchange capacity (CEC) of the clay was between 8.50 and 12.15 meq/100 g and could be attributed to the presence of inorganic/organic matter; thus, making the beneficiated kaolin play an important role in the adsorption of metal ions. The EC of the beneficiated clay was higher than that of the raw sample. The higher electrical conductivity (EC) of the beneficiated kaolin than that of the raw sample implies that the beneficiated clay probably has dissolved salts which could allow for the removal of some toxic metal ions. Also, its high porosity could provide interlayer spacing making it as a good adsorbent for the removal of pollutants. From all the results of the samples (raw and beneficiated), the beneficiated kaolin had more enhanced properties than the raw one.

Table 4.1: Some Physicochemical Properties of Raw and Beneficiated Kaolin

Parameter	Raw	Beneficiated
Colour/Texture	White/Fine	White/Finer
pH	5.47	6.97
Organic carbon (%)	0.05	0.00
Cation Exchange Capacity (CEC) (meq/100 g)	8.50	12.15
Electrical Conductivity (EC) (µS/cm)	198	298
Aluminum (Al) (mg/kg)	2606	2700
Iron (Fe) (mg/kg)	3972	9788
Cadmium (Cd) (mg/kg)	0.00	0.00
Lead (Pb) (mg/kg)	0.002	0.00

4.1.2 XRD analysis

The mineralogical composition of the beneficiated clay was determined by XRD. The diffractogram was between 2θ is 10 to 90°. The XRD pattern of the beneficiated clay was shown in Figure 4.1. It could be noted that the peak of quartz is highly intense and well-pronounced which indicate aggregates of kaolinite.

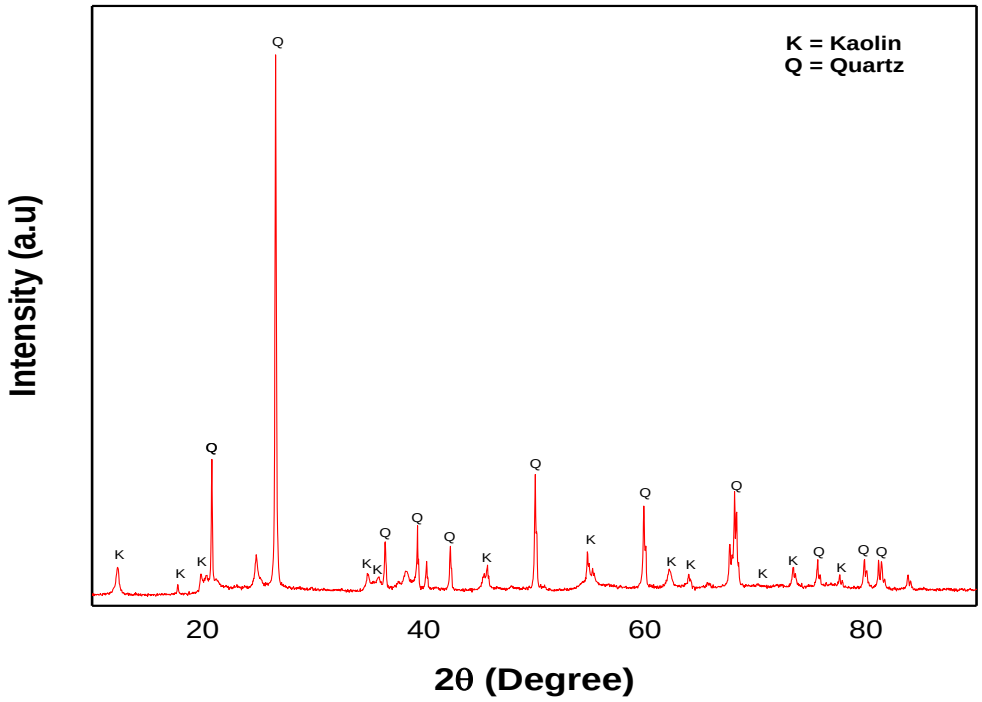

Figure: 4.1: XRD Pattern of the Beneficiated Kaolin

The JCPDS file revealed the presence of main diffraction peaks at 2θ: 12.40°, 19.85°, 24.95°, 36.07°, 46.59°, 54.61° and 73.77° which correspond to the crystallographic orientation of (001), (020), (002), (200), (221), (150) and (-402), respectively. Similar diffraction peaks were also reported by Zen *et al.* (2018). This indicates that the sample contains quartz (predominate phase) which are commonly found in kaolin as constituent of kaolinite.

4.1.3 FTIR analysis

Figure 4.2 shows the infra-red spectrum of the beneficiated kaolin measured from 500 to 4000 cm^{-1}.

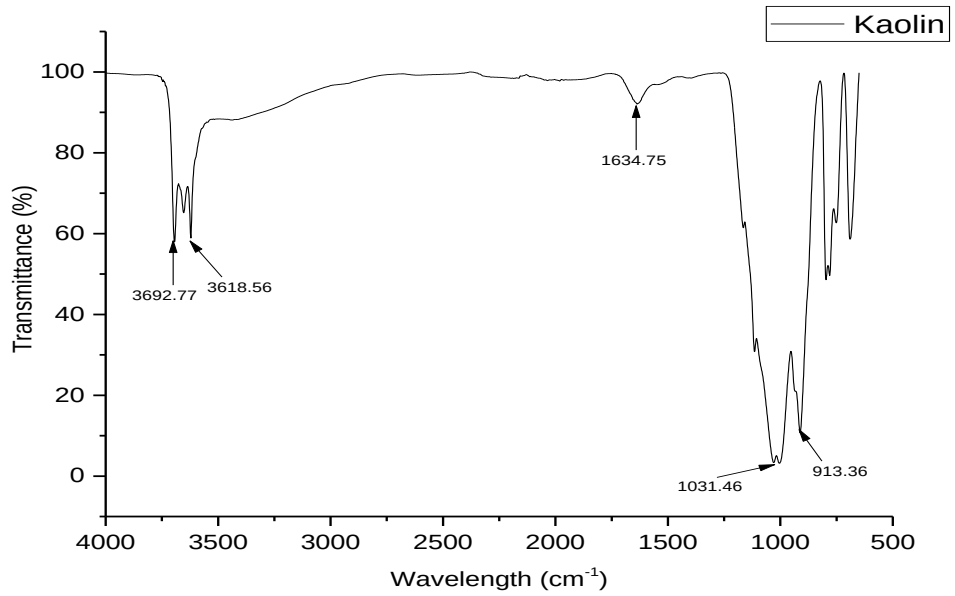

Figure 4.2: FTIR Analysis of the Beneficiated Kaolin

The FTIR spectrum of the beneficiated kaolin revealed the absorption bands 3692 and 3618 cm^{-1} assigned to be OH stretching vibrations while the absorption bands at 1634 cm^{-1}, 1031 cm^{-1}, 1050 cm^{-1} and 913 cm^{-1} are H-O-H interlayer, Si-O-Si group of the tetrahedral sheet, Si-O stretching vibration and Al-OH, respectively (Yu *et al.*, 2019). These functional groups are common to kaolinite minerals. The peaks at 750 and 467 cm^{-1} correspond to quartz while the band at 430 cm^{-1} in the kaolin correspond to stretching vibration modes of Si-O, Al-O and Si-O-Si bonds (da Silva Lopes *et al.*, 2019). This information provides the surface functional groups that took place during the adsorption process on the surface site of kaolin.

4.1.3 HRSEM analysis

The surface morphology of raw and beneficiated clays was determined using HRSEM as presented in Plate V. The SEM images reveal significant changes in the surface morphology of the beneficiated clay after treatment with it surface morphology showed more kaolinite crystals.

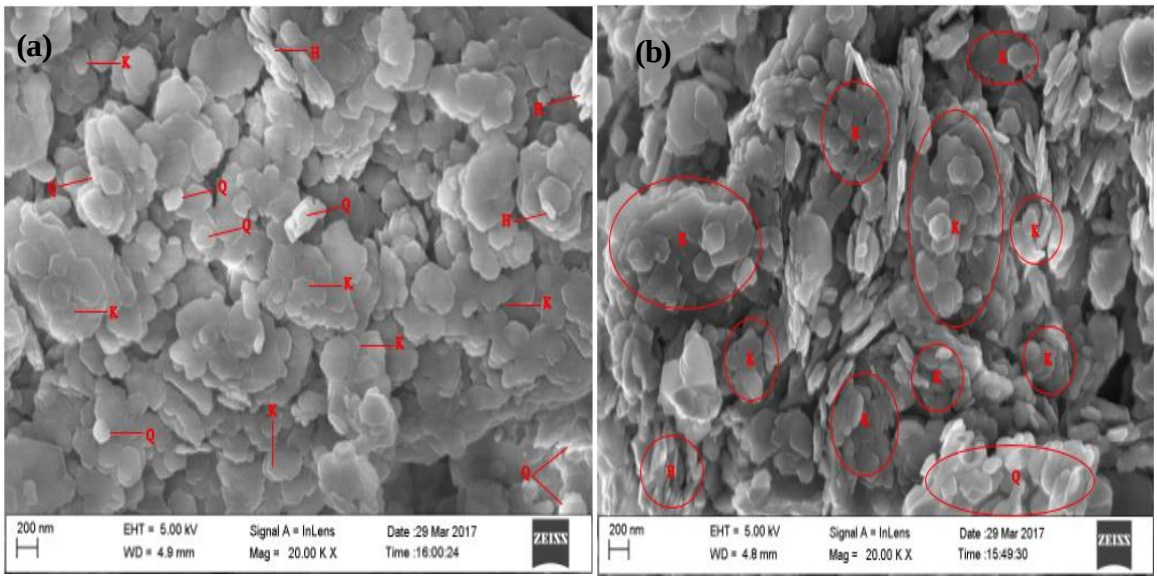

Plate V: SEM Analysis: (a) Raw and (b) Beneficiated Kaolin

The results of the surface morphologies of these samples as depicted in Plate V (a) and (b) indicate that the raw kaolin contains a mixture of halloysite, quartz and kaolin forming dense aggregate texture. The long tubes in it could be identified as halloysite and these tubes are not randomly oriented but roughly packed on the surface of the clay. It was observed that a smaller number of small flakes with the hexagonal structure were arranged in face-to-face patterns compared to the well crystalline pseudo-hexagonal edges of kaolinite as well as plate-like edged as well as plate-like edged kaolinite particles as seen in Plate V (a). In Plate V (b), kaolin particles are quite established with more distribution, fragmentation and fewer aggregations. This could be due to the treatment methods like washing and calcination (450 ^{o}C), leading to the removal of impurities such as colour, organic carbon and matter. At this stage, more of the stable phase of kaolinite instead of silicate was formed. This result gives more defined the existence of more porosity of the kaolinite lattice. Therefore, the occurrence of negative charges on the basal surface will be responsible for the adsorption of cations.

4.1.5 HRTEM and EDX analysis

The nanostructures of the raw and beneficiated kaolin from HRTEM and SAED results revealed a pseudo-hexagonal structures of kaolinite as presented in Plate VI.

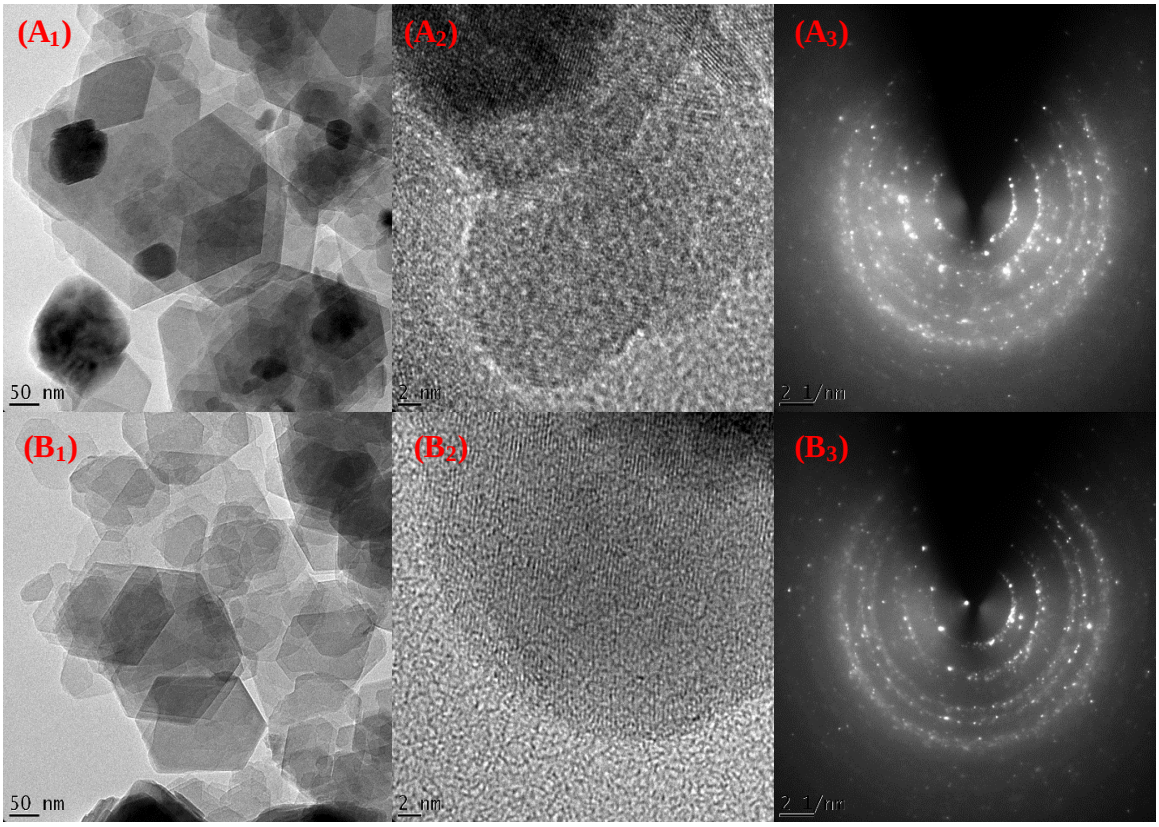

Plate VI: HRTEM and SAED Patterns: (A_{1-3}) Raw and (B_{1-3}) Beneficiated Kaolin

The purification of kaolin confirmed the improvement in the crystallinity of kaolinite from the HRTEM analysis obtained as presented in Plate VI (B_1). The presence of cross-fringes indicates the edge observation that the inter-network layers are coherently stacked and the stacking is more orderly within those domains as displayed in Plate V. Based on the SAED investigation on the kaolin samples in this study, turbostratic patterns were observed over the aggregation of amorphous structures that were randomly oriented. This indicates that the particles are kaolinite phase with crystallinity with dotted concentric rings assigned to quartz and halloysite forms as shown in Plate VI. The EDX spectra revealed the existence of the following elements: O, Al, Si, K, Ti and Fe (Figure 4.3). Although, both samples

exhibited similar morphologies based on EDX results, their elemental constituent differed. As it can be seen, the major difference may be attributed to the percentage reduction of Fe, total removal of Ti and additional presence of K. These results suggest that there is the possibility of cation exchange between exchangeable cation in the kaolin samples and metal ions during treatments. Thus, this could enhance high adsorption capacity and removal efficiency of metal ion on the kaolinite samples. These results are consistent with the XRD and FTIR results as earlier stated in this study.

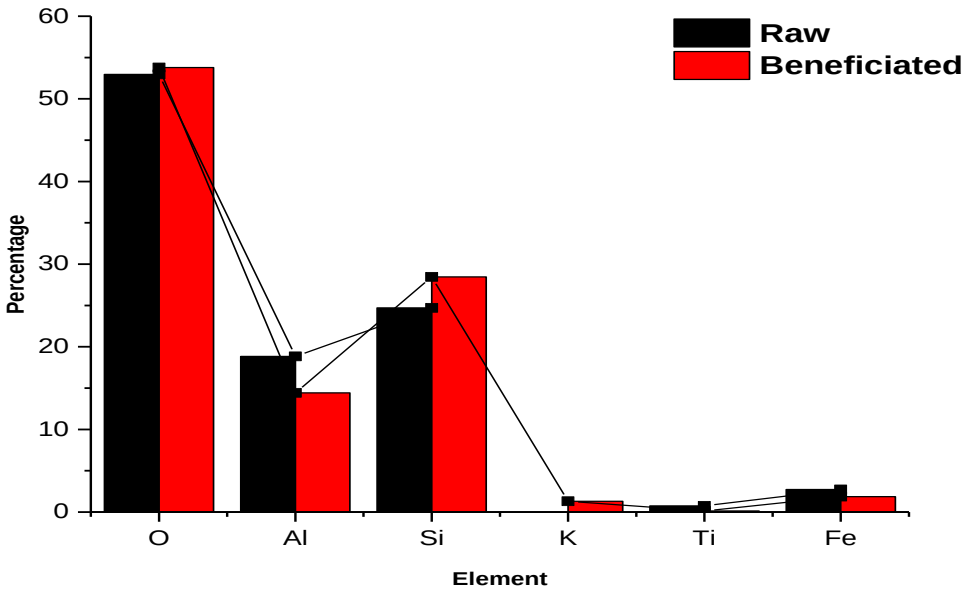

Figure 4.3: EDX Analysis of Raw and Beneficiated Kaolin

4.1.6 BET analysis

The N_2 adsorption-desorption isotherm and pore size distribution of the beneficiated kaolin are displayed in Figure 4.4. As the relative pressure, $\frac{P}{P_o}$, increased, especially at values > 0.44, the adsorption-desorption isotherms began to rise and showed typical H3 features which could be ascribed to mesoporous structures.

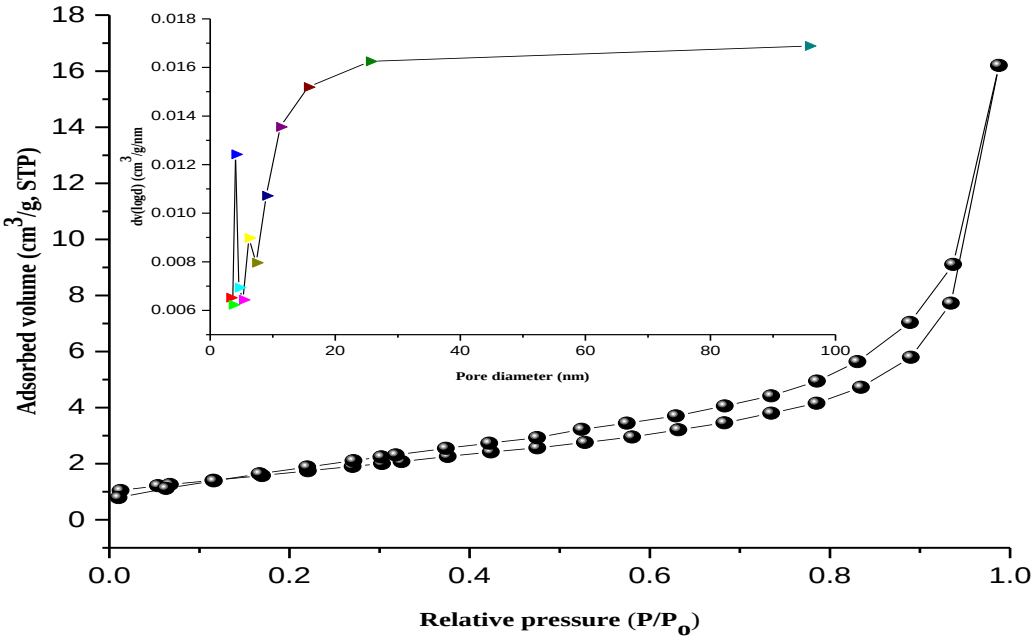

Figure 4.4: BET Analysis for Beneficiated Kaolin

The quasi-overlapping adsorption-desorption curves and the pore size distribution of the beneficiated kaolin as presented in Figure 4.4 indicate that the N_2 adsorption-desorption isotherm curve of the sample can be classified as Type IV, which belongs to a Type H3 hysteresis loop indicating a purely mesoporous material with small pore size (Yu *et al.*, 2020). The BET surface area of the beneficiated kaolin in this study according to Barrette-Joyner-Halenda method was 17 m^2/g with a sharp pore distribution peak of 3.26 nm. This was thus considered to be consistent with a mesoporous material.

4.2 Synthesis of TiO_2 Nanoparticles

4.2.1 XRD analysis

Figure 4.5 and 4.6 show the XRD patterns of the TiO_2 nanoparticles prepared at different stirring time and pH values, respectively. The obtained spectra are made up of several peaks related to anatase materials.

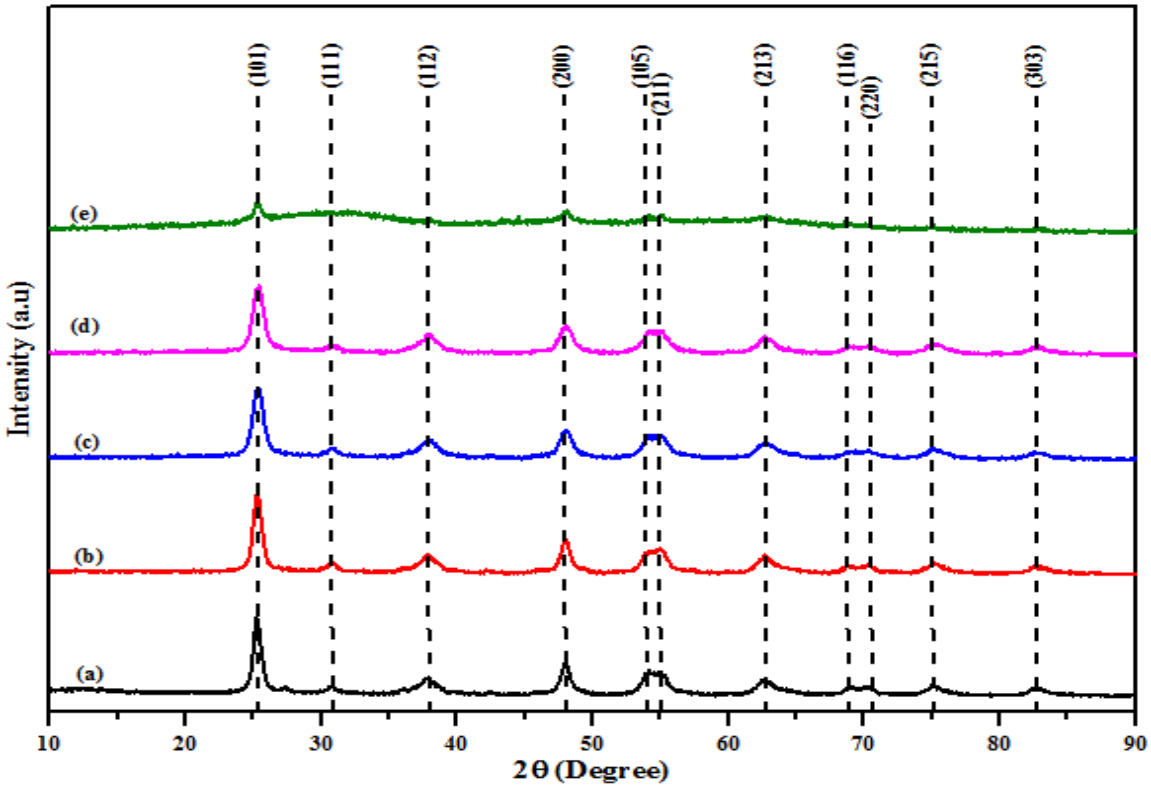

Figure 4.5: Effect of Stirring time on the XRD Patterns of TiO_2 Nanoparticles at (a) 20 min (b) 40 min (c) 60 min (d) 80 min (e) 100 Calcined at 450 °C.

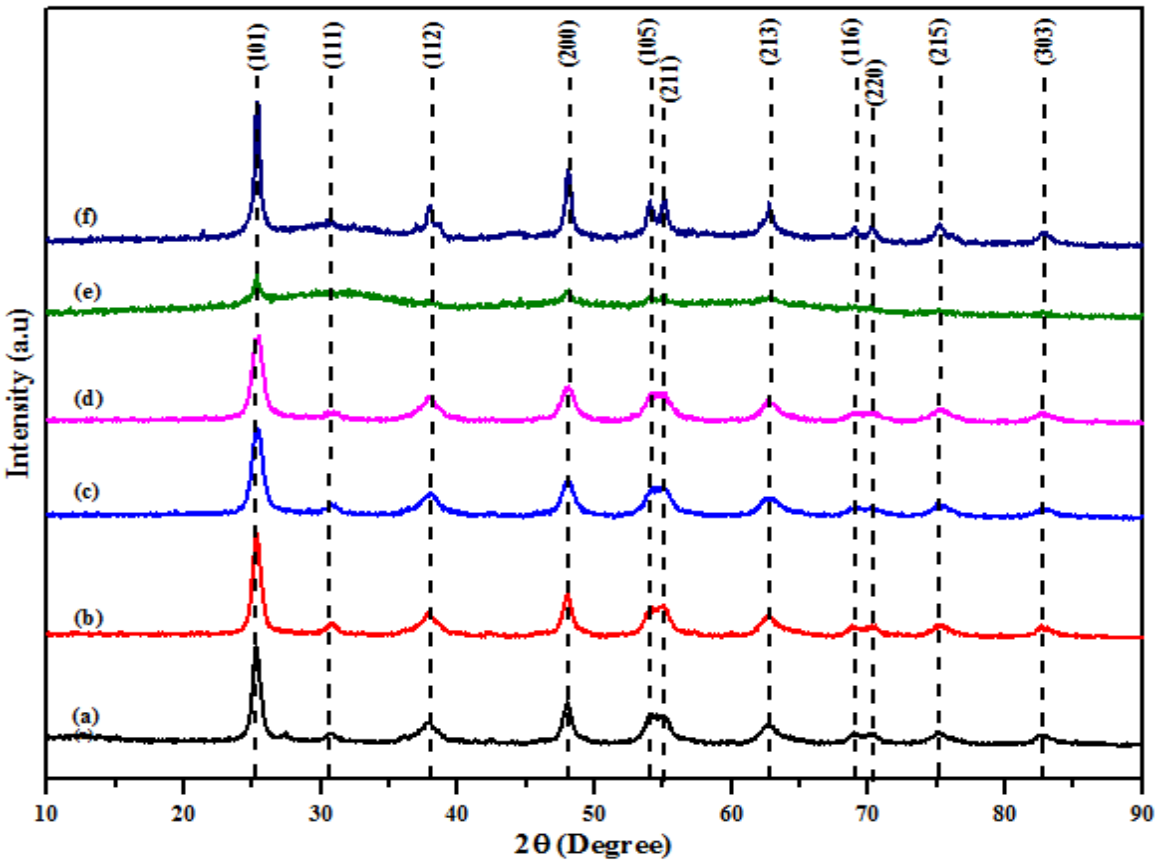

Figure 4.6: Effect of pH on the XRD Patterns of TiO_2 Nanoparticles at (a) 2 (b) 4 (c) 6 (d) 8 (e) 10 and (f) 12 Calcined at 450 °C.

The relationship between full width at half maximum (FWHM) and lattice strain, **ε** of the materials according to Williamson-Hall equation were calculated and presented in Tables 4.2 and 4.3 from the XRD results of effect of stirring time and pH.

Table 4.2: Average Crystallite Size of TiO_2 at Different Stirring Time from Scherrer Formula and Williamson-Hall (W-H) Analysis

Parameter		**Stirring time (min)**				
		20	**40**	**60**	**80**	**100**
Phase		Anatase	Anatase	Anatase	Anatase	Anatase
Scherrer	D (nm)	5.48	6.00	6.52	5.38	6.37
	$\frac{1}{D}$ (nm^{-2})	3.30	2.80	2.40	3.50	2.50
Williamson-Hall	D (nm)	5.82	5.05	4.46	4.93	6.16
	$\frac{1}{D}$ (nm^{-2})	3.00	3.90	5.00	4.10	2.60
	$\varepsilon \times 10^{-2}$	-11.15	-30.27	-36.91	-26.69	-7.62
Lattice parameter	a	3.79	3.79	3.79	3.79	3.79
	c	9.51	9.51	9.51	9.51	9.51
	$\frac{a}{c}$	0.40	0.40	0.40	0.40	0.40
Lattice structure		Tetragonal	Tetragonal	Tetragonal	Tetragonal	Tetragonal

Table 4.3: Average Crystallite Size of TiO_2 at Different pH from Scherrer Formula and Williamson-Hall (W-H) Analysis

Parameter		pH					
		2	**4**	**6**	**8**	**10**	**12**
Phase		Anatase	Anatase	Anatase	Anatase	Anatase	Anatase
Scherrer	D (nm)	6.20	5.67	4.71	4.671	15.02	11.27
	$\frac{1}{D}$ (nm^{-2})	2.60	3.10	4.50	4.60	4.40	0.79
Williamson-Hall	D (nm)	7.54	7.27	6.10	5.91	8.47	6.16
	$\frac{1}{D}$ (nm^{-2})	1.80	1.90	2.70	2.90	1.40	2.60
	$\varepsilon \times 10^{-2}$	2.28	5.03	5.38	5.79	-8.83	-23.71
Lattice parameter	a	3.79	3.79	3.79	3.79	3.79	3.79
	c	9.51	9.51	9.51	9.51	9.51	9.51
	$\frac{a}{c}$	0.40	0.40	0.40	0.40	0.40	0.40
Lattice structure		Tetragonal	Tetragonal	Tetragonal	Tetragonal	Tetragonal	Tetragonal

The XRD patterns of TiO_2 nanoparticles at different stirring times and pH values were investigated in this study as shown in Figuress 4.6 and 4.7 respectively. The production of different phases of titania depends on calcination temperatures and it has been reported that formation of anatase occurs at low temperature that is less than 600 ^oC (Pavel and Radovan, 2015; EL-Mekkawi *et al.,* 2017). The choice of calcination temperature (450 ^oC) based on adsorption properties corroborated the formation of titania with anatase phase. For the TiO_2 powder at various stirring times between 20 and 100 min, different peaks with crystal planes (101), (111), (004), (200), (211), (204), (220), (215) and (224) were found at 2θ value of $25.28^o, 30.79^o, 37.80^o, 48.05^o, 55.06^o, 62.69^o, 70.31^o, 75.03^o$ and 82.66^o respectively. No trace of brookite or rutile phase was detected, signifying high purity of synthesized TiO_2 powder. This information is in agreement with Joint Committee on Powder Diffraction Standard

(JCPDS) No. 00-021-1272 of TiO_2, anatase with parameters a = b= 3.79 Å, c = 9.51 Å, $\frac{a}{c}$ = 2.51, cell volume = 136.31 Å, density = 3.89 and all the peaks correspond to tetragonal lattice structure. The XRD patterns of the TiO_2 nanoparticles irrespective of stirring time and pH exhibited similar anatase phase as displayed in Figure 4.6. Crystallite sizes were computed in comparison using Dybe-Scherrer and Williamson-Hall equations (equations 4.1 and 4.2):

$$D = \frac{k\lambda}{\beta\cos\theta} \tag{4.1}$$

where D is the crystallite size (nm), k is a constant (0.94 for spherical particles), λ is the wavelength of the X-ray radiation (CuKα = 0.1541 nm), β is the full width at half maximum (FWHM) of the intense and broad peaks and θ is the Bragg's or diffraction angle.

$$\beta\cos\theta = \frac{k\lambda}{D} + 4\varepsilon\sin\theta \tag{4.2}$$

The crystalline sizes were obtained using Eq. 4.2 at stirring times 20, 40, 60, 80 and 100 min as shown in Table 4.6. These values were 5.48, 6.00, 6.62, 5.38 and 6.39 nm for anatase TiO_2 calcined at 450 ^oC. It can be noticed that crystallite size increased with increasing stirring time except at 80 min. At this point, 80 min, it was clearly shown that an optimum stirring time of the smallest nanocrystallite size was obtained.

Figure 4.6, it was observed that Bragg's peaks were more intense at (101) an indication of large particle size while broad peaks depict small particle size. This could be as a result of growth or nucleation of the titanium crystals during stirring. The dislocation density (δ) as shown in Table 4.2 which indicates the deficiency in the nanoparticles was calculated using equation 4.3:

$$\delta = \frac{1}{D^2} \tag{4.3}$$

It can be seen that the dislocation density is inversely proportional to the grain size/crystallite size of TiO_2 nanoparticles according to Scherrer's formula. The dislocation

density decreased with increase in stirring time except at optimum stirring time (80 min) where sudden increment was noticed. This increment may be due to decrease and rearrangement in the crystallite size of TiO_2 (Koutu *et al.*, 2020). The optimum stirring time gave the highest value of dislocation density which is an indication of inverse proportionality of both parameters as seen in Figure 4.7.

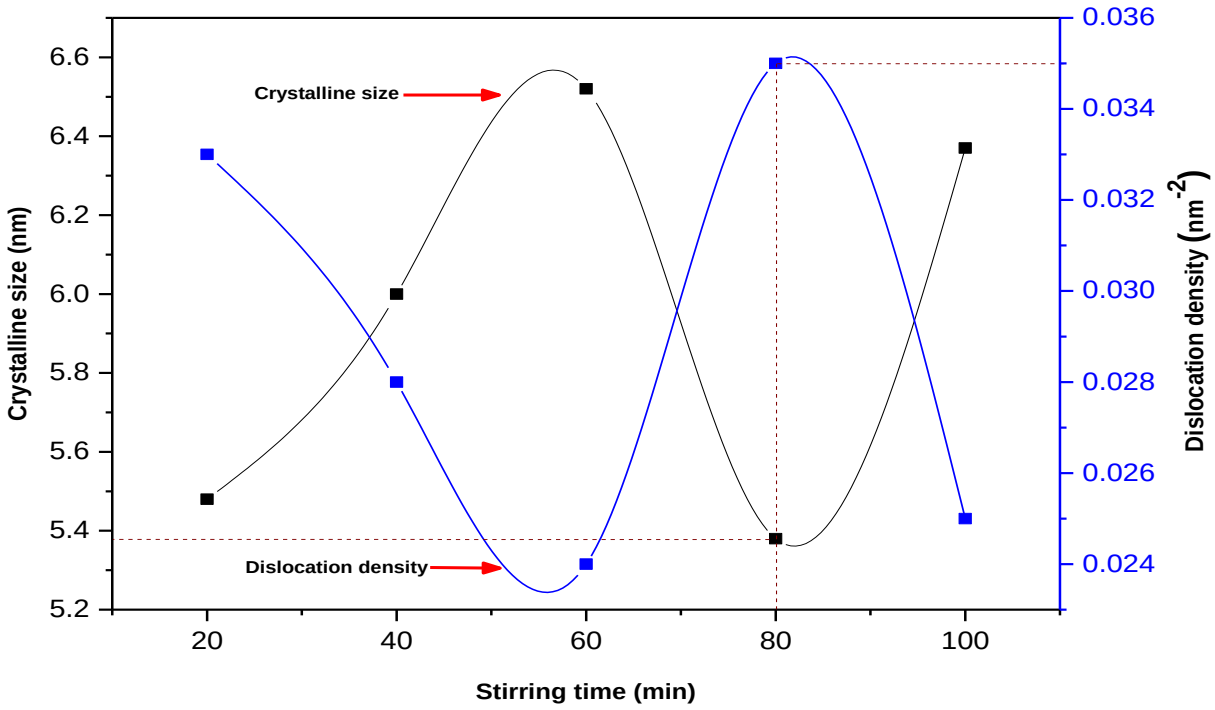

Figure 4.7: Plot of Crystalline Size and Dislocation against Stirring Time of TiO_2 Nanoparticles using Dybe-Scherrer Analysis

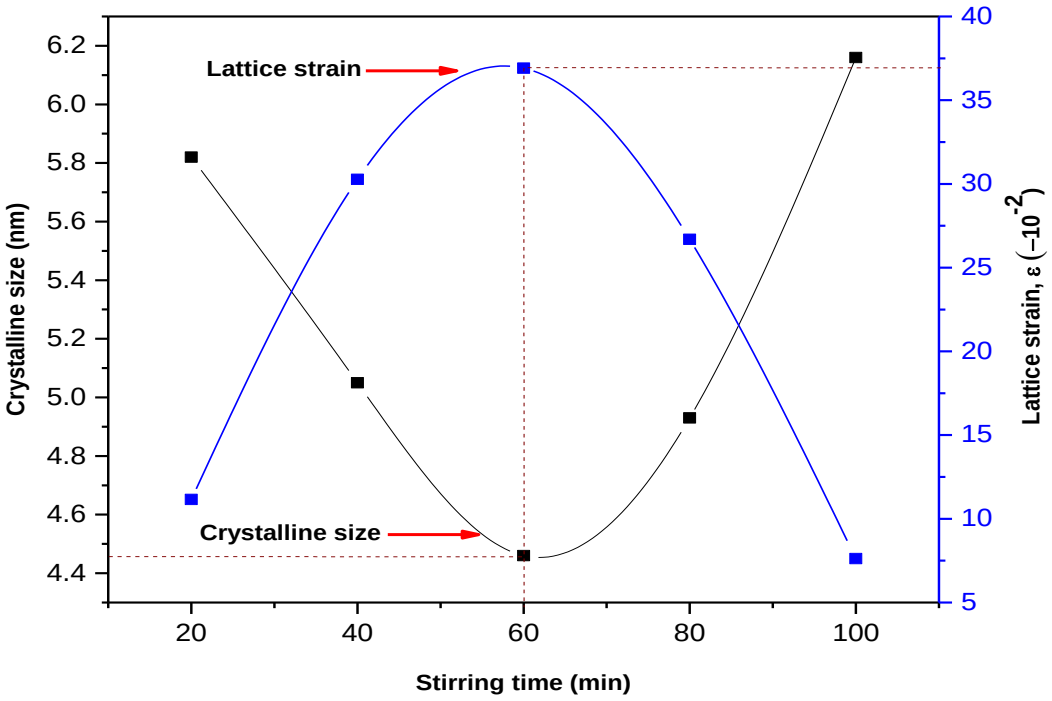

Figure 4.8: Plot of Crystalline Size and Lattice Strain against Stirring Time of TiO_2 Nanoparticles using Williamson-Hall Analysis

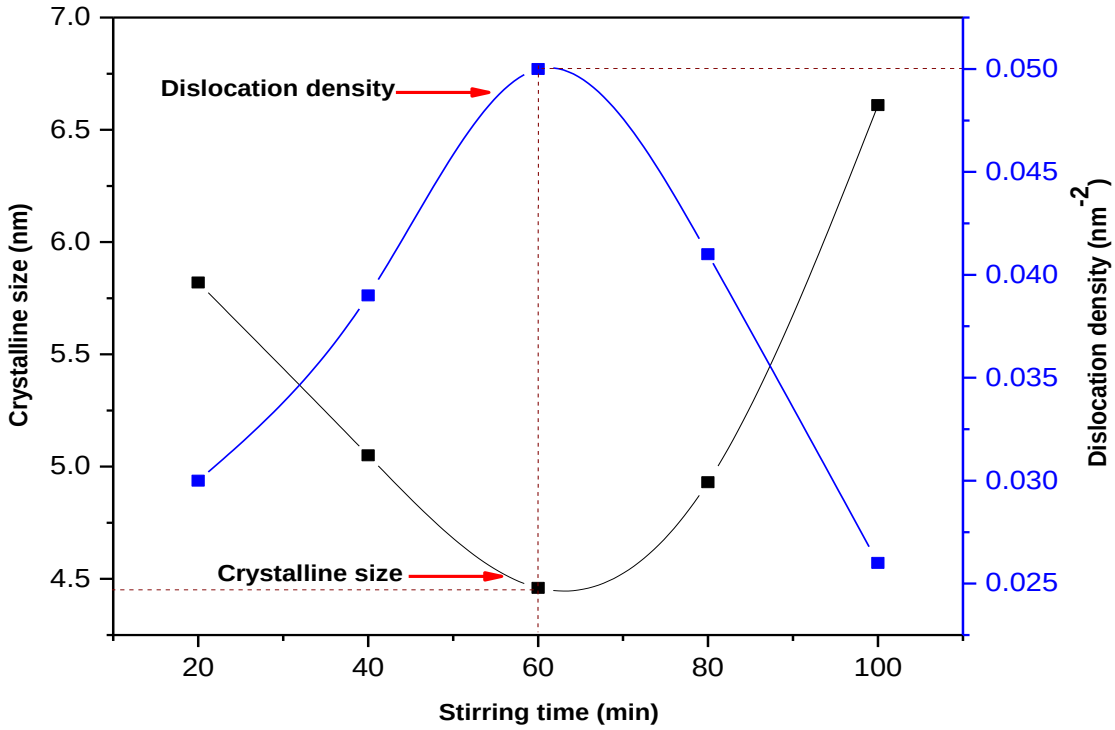

Figure 4.9: Plot of Crystalline Size and Dislocation against Stirring Time of TiO_2 Nanoparticles using Williamson-Hall Analysis

The plots of $\beta\cos\theta$ against $4\sin\theta$ give a straight line and the respective values of lattice strains and average crystalline sizes were calculated from the slopes and intercepts. The plots of W-H for anatase samples as shown in Figures 4.8 and 4.9 gave grain sizes of the stirring times that are in close agreement with the results obtained from Scherrer's equation. Thus, both equations employed for average particle size determination fitted well for the TiO_2 nanoparticles.

The effect of pH was studied using the optimum stirring time (80 min) and calcination temperature of 450 ^oC on the formation of TiO_2 nanoparticles. As shown in Table 4.2, Scherrer and Williamson-Hall equations were employed in the evaluation of average crystallite sizes and dislocation densities. The change in pH led to the formation of anatase TiO_2 of varied crystallite sizes. This shows that at basic medium, deoxolation occurs and further condensation led to the formation of anatase (Kumar and Rao, 2014; Mirjalili *et al.*, 2017). This strongly proves that the crystalline structure is affected by adjusting the pH. Peaks were observed at diffraction angles similar to the effect of stirring time, showing the basic medium (pH 8) with the smallest crystallite size of 4.67 nm. Importantly, it was noted that the effect of pH on the production of TiO_2 as a significant effect, giving rise to nanoparticle smaller than the stirring time. The sharp and intense diffraction peaks observed at pH 12 in the XRD patterns could be attributed to nucleation which increases the crystallinity and average crystallite size of the sample. Thus, this is quite different from the broad diffractograms obtained for lower pH values.

The plots of crystalline sizes, dislocation densities and lattice strains from the effect of pH on TiO_2 nanoparticles given in Table 4.3 calculated using the formulae of Debye-Scherrer and Williamson-Hall are presented in Figures 4.10, 4.11 and 4.12.

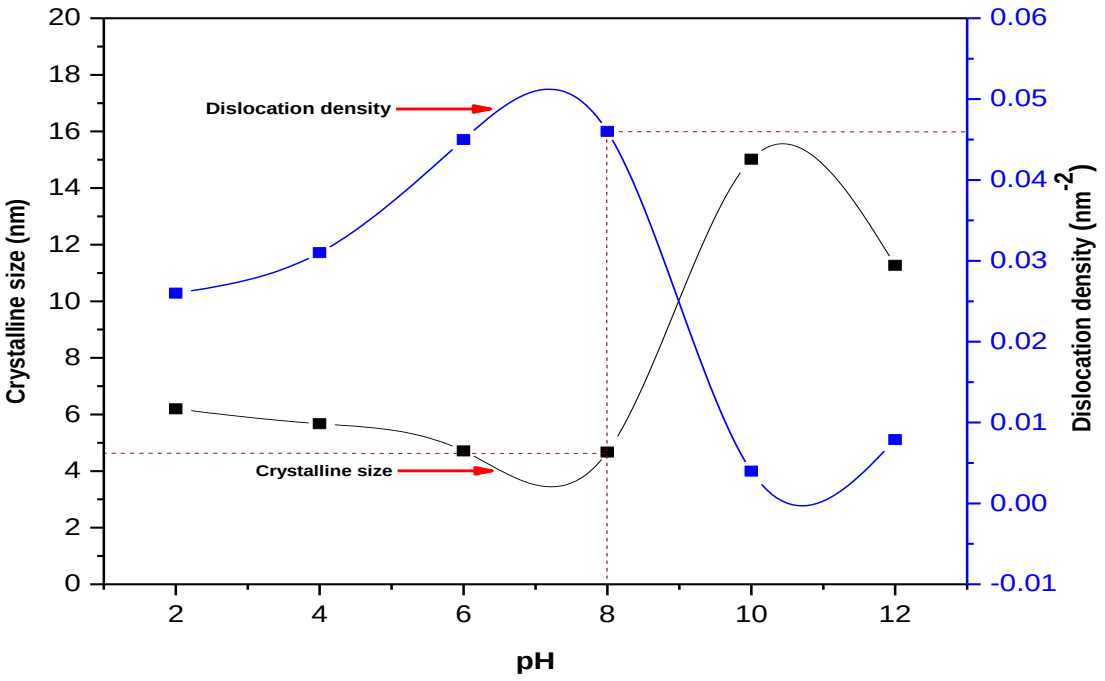

Figure 4.10: Plot of Crystalline Size and Dislocation against pH of TiO_2 Nanoparticles using Debye-Scherrer Analysis

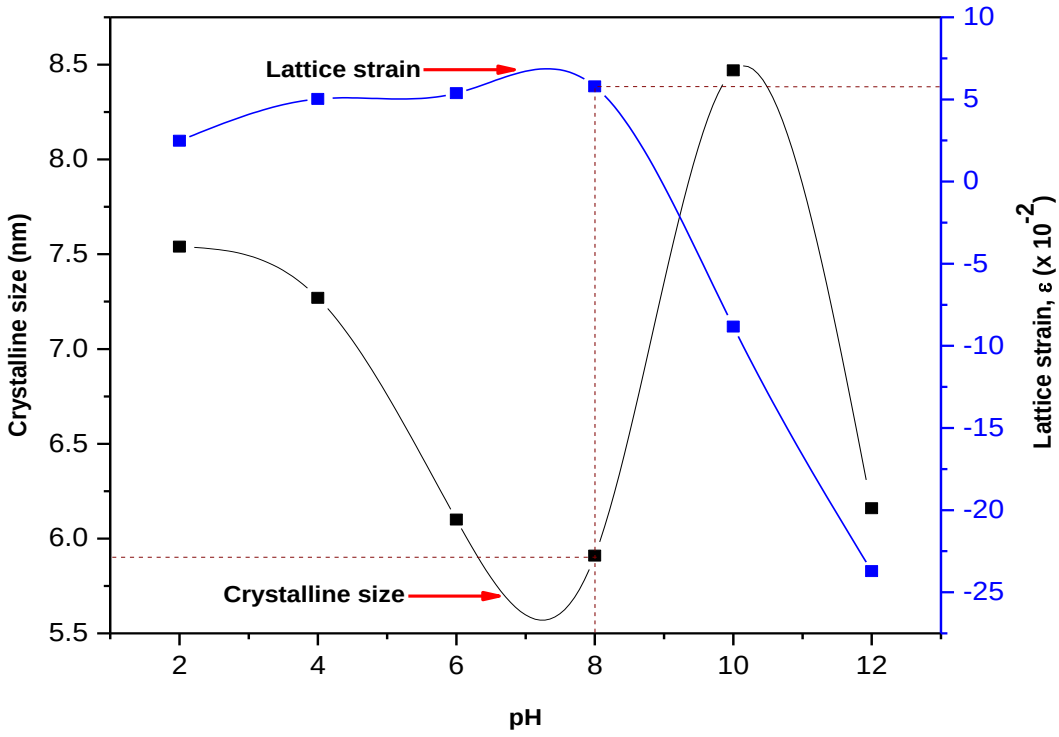

Figure 4.11: Plot of Crystalline Size and Lattice Strain against pH of TiO_2 Nanoparticles using Williamson-Hall Analysis

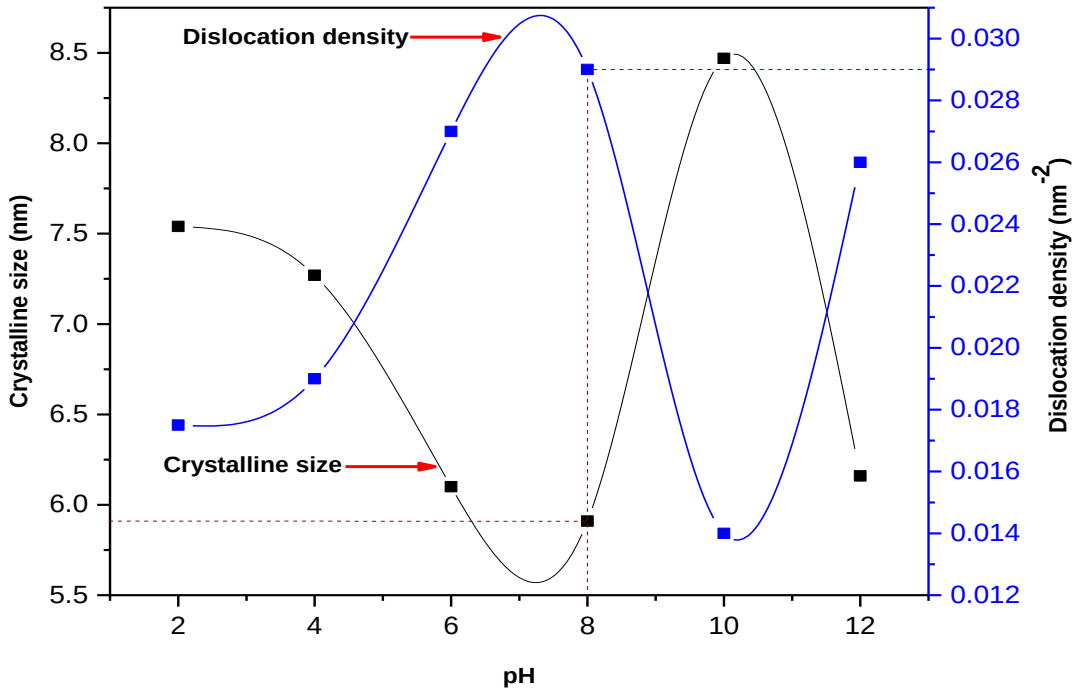

Figure 4.12: Plot of Crystalline Size and Dislocation against pH of TiO_2 Nanoparticles using Williamson-Hall Analysis

Williamson-Hall analysis of TiO_2 at different pH gives the average crystalline size and strain estimated from linear fit data. The results provide coherent values of lattice strains which range from 0.0228 to -0.0237. The small values obtained for the lattice parameters could lead to larger surface areas giving rise to more active sites (Hajjaji *et al.*, 2016). It was observed that with increase in pH from 2 to 12, the strains associated with the TiO_2 samples decreased, as shown in Table 4.3 which is an evidence of high surface area and more active sites.

4.2.2 FTIR analysis

Figures 4.13 and 4.14 present the FTIR spectra of the anatase nanoparticles at different stirring times and pH values calcined at 450 ^{o}C investigated in the region 500-4000 cm^{-1}.

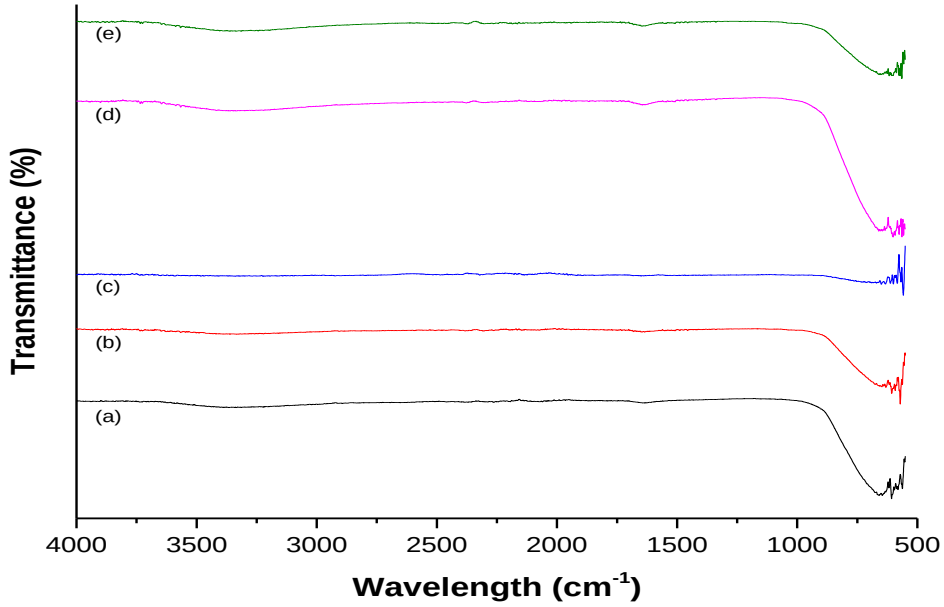

Figure 4.13: FTIR of the TiO_2 calcined at 450 °C at stirring time of (a) 20 min (b) 40 min (c) 60 min (d) 80 min and (e) 100 min.

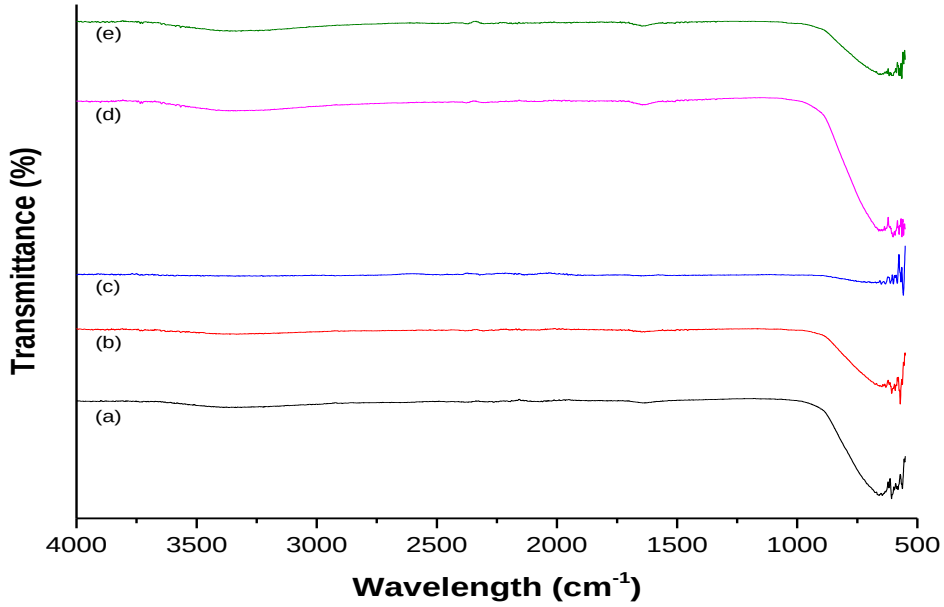

Figure 4.14: The FTIR spectra of TiO_2 nanoparticles calcined at 450 °C at pH (a) 2 (b) 4 (c) 6 (d) 8 (e) 10 and (f) 12.

The FTIR spectra of TiO_2 calcined 450 °C for stirring time of (a) 20 min (b) 40 min (c) 60 min (d) 80 min and (e) 100 min are shown comparatively in Figure 4.13. The band belonging to 1623 cm^{-1} at stirring time of 80 min was assigned to H-O-H bending of adsorbed water. At stirring time of 60 min, it was noted that the intensity bands between

535 and 600 cm^{-1} decreased. Only these strong absorption peaks appeared at 20, 40, 80 and 100 min and they are associated with vibrational modes of Ti-O-Ti bonds (León *et al.*, 2017). This is an indication that the intensities of the bands promote the Ti-O network resulting in the formation of TiO_2 phase.

The FTIR spectra of TiO_2 nanoparticles calcined at 450 ^oC at pH (a) 2 (b) 4 (c) 6 (d) 8 (e) 10 and (f) 12 are given in Figure 4.14. The TiO_2 sample showed main peaks in the range 520-630 $cm^{-1,}$ the peaks at this region are assigned to Ti-O stretching modes (Shehap and Akil, 2016). At pH 8, a broader band was observed at 630 cm^{-1} which could be linked to O-Ti-O and Ti-O-Ti of the TiO_2 framework, indicating the existence of the energetically bonded -OH group from NaOH.

4.2.3 HRSEM and EDX analysis

The surface morphologies of the as-prepared TiO_2 nanoparticles at different pH (a) 2 (b) 4 (c) 6 (d) 8 (e) 10 (f) 12 and calcined at 450 ^oC were as presented in Plate VII. The displayed images show that the particles were cluster and randomly distributed.

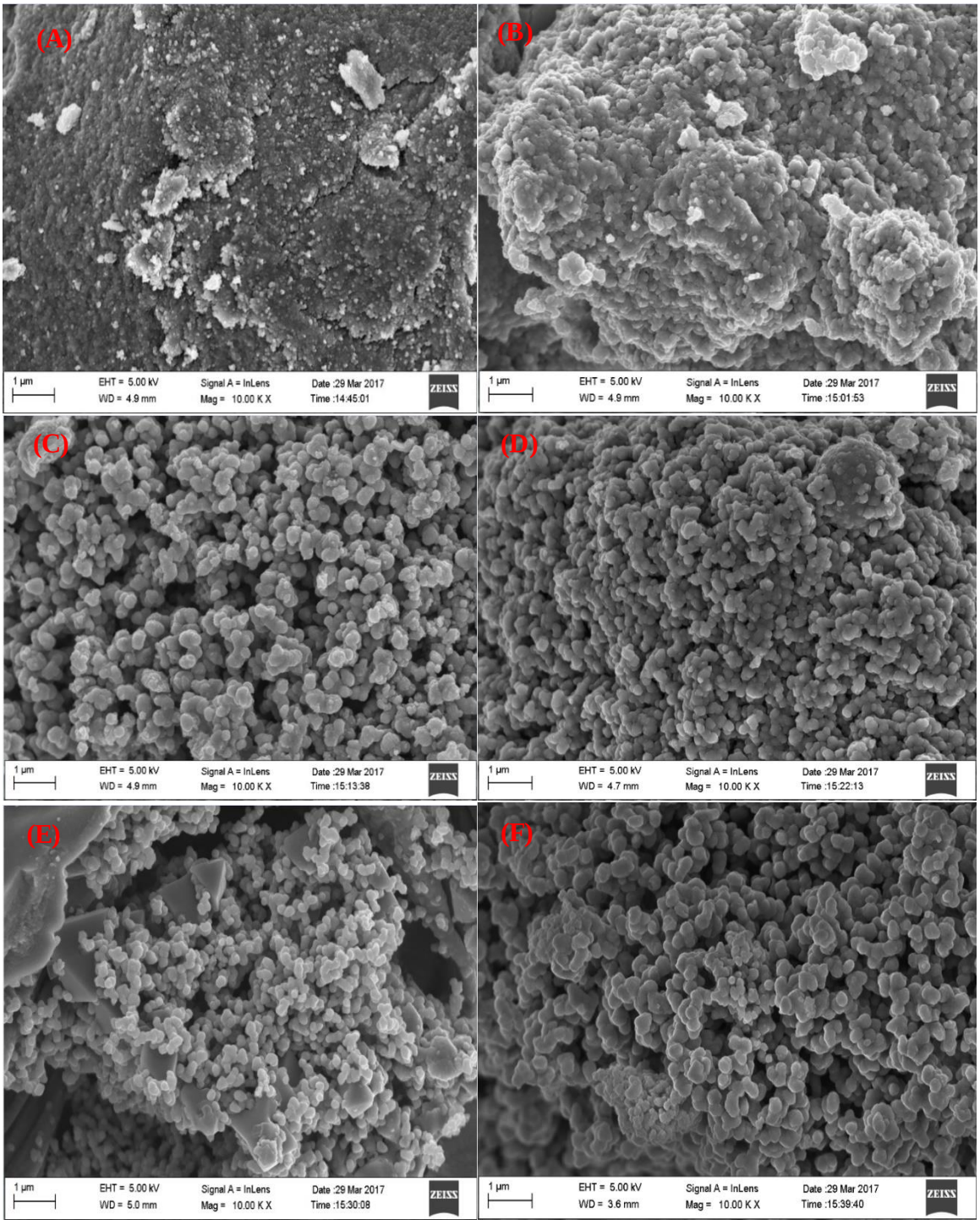

Plate VII: HRSEM Analysis of TiO_2 Nanoparticles at different pH (A) 2 (B) 4 (C) 6 (D) 8 (E) 10 and (F) 12 Calcined at 450 °C.

These micrographs reveal that the sizes of the particles were influenced by the experimental pH condition, indicating randomly and cluster distribution of TiO_2 nanoparticles. During this condition, hydrolysis of titanium cation occurred at acidic medium and oxolation takes place. At higher pH values, deoxolation due to condensation takes place, leading to the

formation of anatase materials (Soni *et al.*, 2016). Therefore, the nano-crystalline structure produced is pH-dependent and promote the yield of anatase phase of TiO_2. The aggregation of TiO_2 nanoparticles at lower and higher pH conditions are as follows:

Acidic condition: $TiO_2 + nH^+ \rightarrow TiO_2H_n^{+n}$

Basic condition: $TiO_2 + nOH^- \rightarrow TiO_2(OH)_n^{-n}$

With increasing pH values, the shapes of TiO_2 samples become more defined (spherical) due to the addition of the precipitating agent (NaOH). This shows that the precipitating agent used in this study completely controlled and improved dispersivity of TiO_2 nanoparticles. The micrographs of the nanostructures of all the samples were analysed by Image-J Processing analytical software to obtain the average grain sizes. The average grain sizes ranged from 8.38 to 13.50 nm. As it can be seen from the HRSEM images (Plate VII C, D, E and F), the inter-particle porosity of the mesoporous TiO_2 nanocrystal was observed in between the space of the nanoparticles. The spheroidal spherical crystal morphologies of TiO_2 samples were clearly evident at basic medium and well dispersed, spherical, homogeneous and less agglomerated nanocrystal of TiO_2 can be seen.

4.2.4 HRTEM analysis

The HRTEM images of TiO_2 calcined at 450 ^oC at pH (a) 2 (b) 4 (c) 6 (d) 8 (e) 10 and (f) 12 were as shown in Plate VIII. It was clearly seen that the samples consist of anomalistic spherical crystalline sizes of TiO_2.

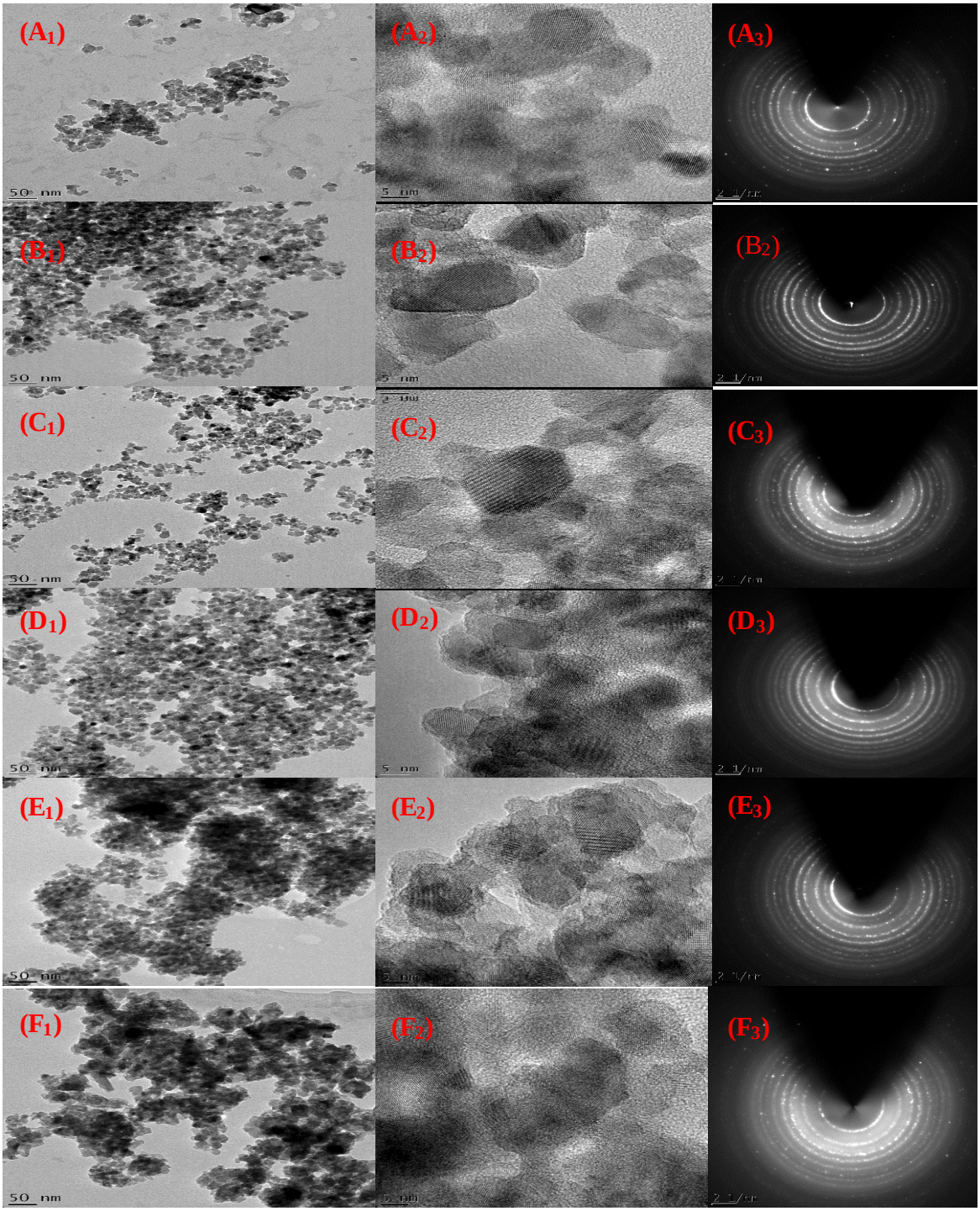

Plate VIII: HRTEM Micrographs of TiO_2 at high and Low Magnification including their corresponding SAED patterns at pH (A) 2 (B) 4 (C) 6 (D) 8 (E) 10 and (F) 12

Plate VIII shows the HRTEM images of TiO_2 calcined at 450 °C and prepared at pH (a) 2 (b) 4 (c) 6 (d) 8 (e) 10 and (f) 12 values. It was clearly seen that the samples consist of anomalistic spherical crystalline sizes of TiO_2. The average particle sizes ranged from 10 to 14.30 nm, which is in good harmony with the XRD results. Lattice fringes were observed

in HRTEM shown in Plate VIII, with the d-spacing for TiO_2 planes, corresponding to the results obtained from the XRD and SAED patterns.

The EDX spectrum recorded for elemental composition of TiO_2 nanoparticles revealed the presence of Ti, O, C, and Ni for the as-synthesized TiO_2 in acidic medium while Na was detected in the synthesized TiO_2 at pH > 7. The presence of oxygen was due to the interaction of Ti with air during synthesis (washing with ethanol and water) and calcination process. The observed peaks of Na and Ni could be related to impurities while the spectrum of C is from the carbon holey grid used for the HRTEM analysis. The selected area of electron diffraction (SAED) analysis as shown in Plate VIII indicates that the TiO_2 nanoparticles are polycrystalline in nature with the dotted concentric rings, indicating that the as-synthesized TiO_2 nanoparticles are crystal-like in shape.

4.2.5 BET analysis

The surface area and pore size distribution of the optimum TiO_2 at pH 8 was studied using the nitrogen gas adsorption isotherm shown in Figure 4.15.

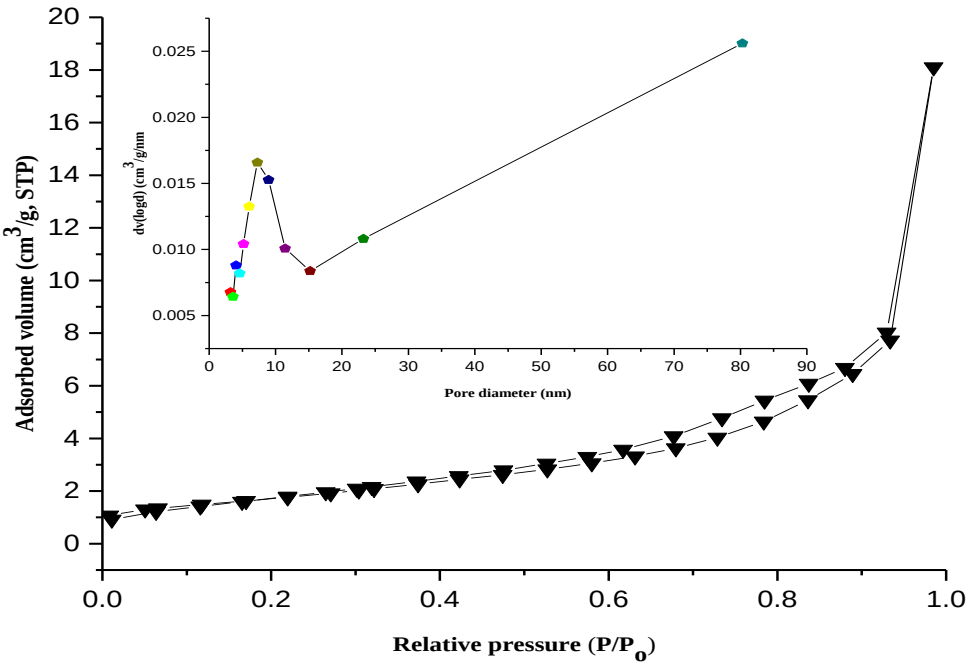

Figure 4.15: BET Analysis for TiO_2 at pH 8

Figure 4.15 shows the specific area and pore size distribution of the synthesized TiO_2 sample characterized using nitrogen adsorption-desorption isotherm measurements. The BET and BJH methods were used to analyse the surface areas and pore size distribution. According to the International Union of Pure and Applied Chemistry (IUPAC), the N_2 adsorption-desorption isotherm exhibits Type IV hysteresis isotherm at pH 8, showing that the nanoparticles are mesoporous (IUPAC, 2015). The adsorption hysteresis approached the region of relative pressure (P/P_o) above 0.9 with the BET of the mesoporous TiO_2 being 53.8 m^2/g and pore volume of 0.106 cm^3/g with smaller pores of 3.614 nm. The distribution shows that the porosity of the TiO_2 was probably contributed by pH adjustment.

4.3 Synthesis of ZnO Nanoparticles

4.3.1 XRD analysis

The XRD patterns of the ZnO nanoparticles at different pH values were as shown in Figure 4.16. It was observed that the peaks correspond to zincite.

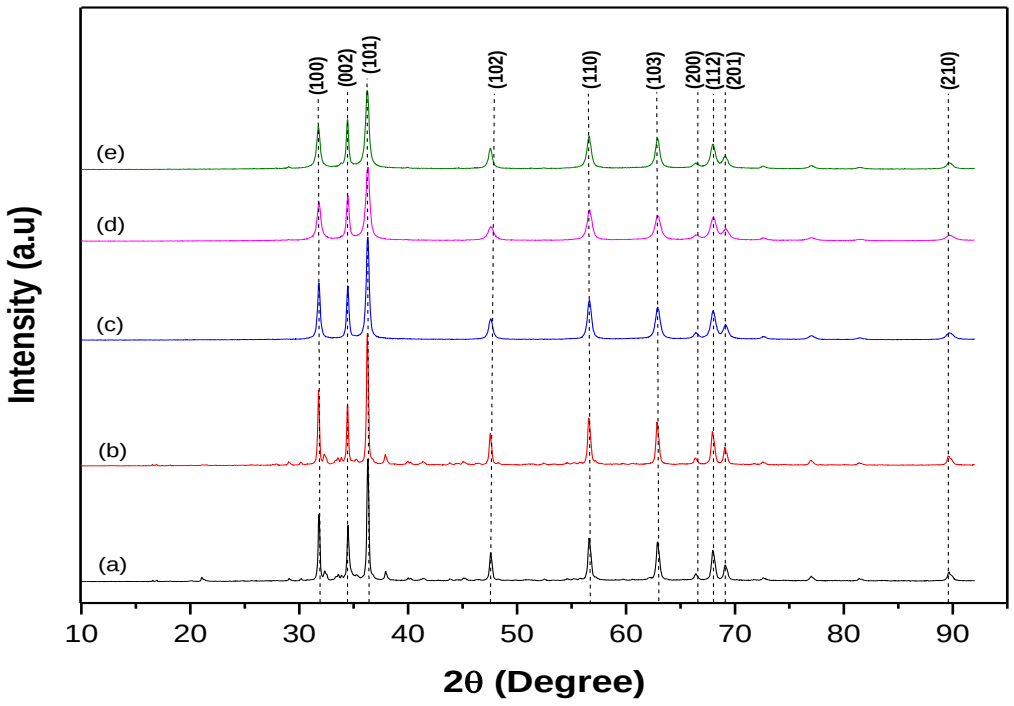

Figure 4.16: XRD patterns for ZnO prepared at pH (a) 4 (b) 6 (c) 8 (d) 10 and (e) 12 and calcined at 450 °C.

The relationship between FWHM and lattice strain, ε according to the Williamson-Hall equation and the determination of crystallite sizes of ZnO nanoparticles at different pH values using Scherrer equation were calculated and presented in Table 4.4.

Table 4.4: Average Crystallite Size of ZnO at Different pH for the Scherrer Formula and the Williamson-Hall (W-H) Analysis

Parameter		**pH**				
		4	**6**	**8**	**10**	**12**
Phase		Zincite	Zincite	Zincite	Zincite	Zincite
Scherrer	D (nm)	22.58	24.82	16.10	11.84	14.10
	$\frac{1}{D}$ (nm^{-2})	0.20	0.16	0.39	0.71	0.50
Williamson-Hall	D (nm)	61.70	75.52	46.77	28.32	29.71
	$\frac{1}{D}$ (nm^{-2})	0.26	0.18	0.46	1.30	1.10
	$\varepsilon \times 10^{-2}$	8.82	7.26	13.84	23.73	11.88
Lattice parameter	a	3.25	3.25	3.25	3.25	3.25
	c	5.21	5.21	5.21	5.21	5.21
	$\frac{a}{c}$	0.62	0.62	0.62	0.62	0.62
Lattice structure		Hexagonal	Hexagonal	Hexagonal	Hexagonal	Hexagonal

In the case of ZnO nanoparticles prepared at different solution pH values and at the constant stirring time of 80 min as shown in Figure 4.16, diffraction peaks were noticed at 2θ values of 31.77°, 34.42°, 36.25°, 47.54°, 56.60°, 62.85°, 66.38°, 67.96°, 69.10° and 89.61° corresponding to the following crystal planes at diffraction lines (110), (002), (101), (102), (110), (103), (200), (112), (203) and (201) respectively. These diffraction peaks matched well with the standard card file JCPDS-00-036-1451 of hexagonal zincite structure. In the

study, the solubility of synthesized ZnO at low below was high. This is because of the presence of a high and low concentration of H^+ and OH^- in the sol, respectively. At high pH (greater than 7) conditions, the amount of OH^- ion from the base reacting with H^+ ions in the sol is higher. Thus, the use of alkali favoured the formation of ZnO.

The presence of diffraction peaks with the highest at pH 6 and 8 may be due to excessive amounts of OH^- ions available for the formation of $Zn(OH)_2$ which later transformed to ZnO after calcination. No other peaks were detected for the ZnO samples at all other pH values, suggesting that the zinc precursors were completely decomposed at the calcination temperature of 450 ^oC. All the ZnO samples with diffraction line (101), (002) and (101) were narrower than the other diffraction lines. It was observed that in the basic medium, the diffraction lines were broadened, an indication of the formation of particles with smaller sizes. Thus, smaller nanoparticles were formed at high pH. The average crystallite size of 11.84 to 24.82 nm of as-prepared ZnO nanoparticles was calculated using the Scherrer's equation and other values of parameters such as wavelength and shape factor remained constant. The plot of crystalline size and dislocation against pH is shown in Figure 4.17.

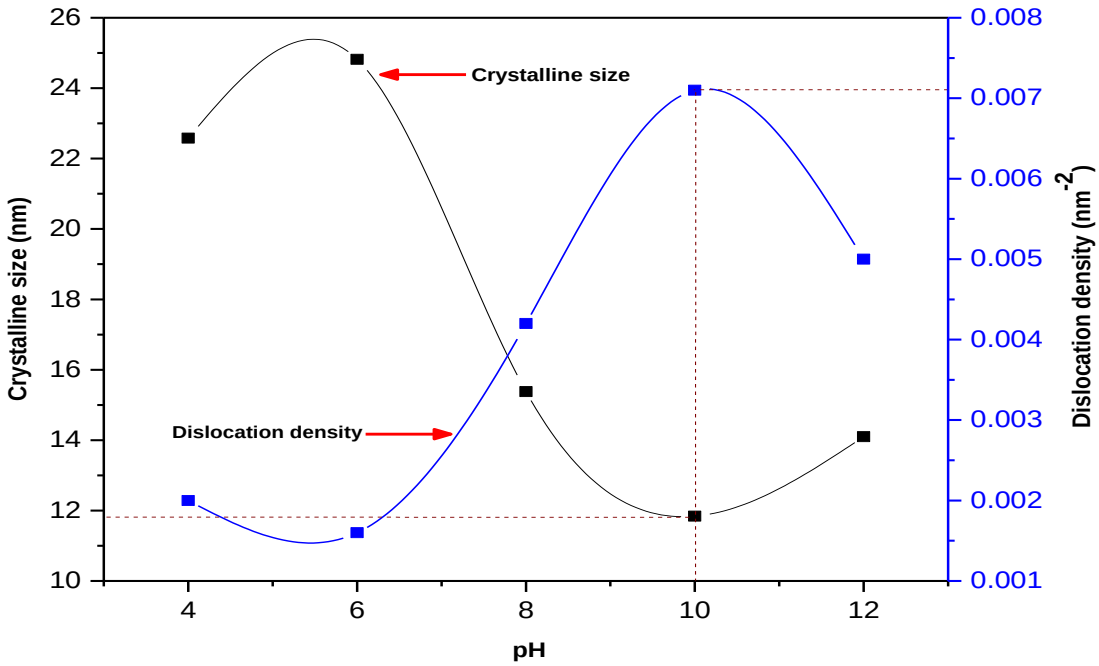

Figure 4.17: Plot of Crystalline Size and Dislocation against pH of ZnO Nanoparticles using Dybe-Scherrer Analysis

As shown in Table 4.4, the results of the calculated crystallite size using OriginPro 2015 software were summarized. Generally, the average particle sizes were larger at low pH with a general decrease at high pH values. This could be as a result of fine particles of ZnO produced at high pH value and the augmentation in precursor-to-volume of sodium hydroxide ratio (Mrad *et al.*, 2018). The dislocation density, δ, measures the number of defects and vacancies in the crystal that is determined from the crystallite size using Scherrer's formula (Leila *et al.*, 2018). From Table 4.4, it is noted that there was an increase in dislocation density in basic medium. The highest δ of 0.71 nm^{-2} was recorded at pH 10, with the crystallite size of 11.84 nm. It is evident that the decrease in crystallite size causes an increase in the dislocation density.

Table 4.4 presents the parameters of ZnO nanoparticles obtained from Scherrer's and Williamson-Hall formulae. In comparison from the table, the values of the average crystallite size obtained for W-H analysis show large variation; this variation was due to

differences in the average particle distribution. The crystalline sizes recorded for W-H were between 28.32 and 75.52 nm which are not in agreement with those of Scherrer's equation whose values ranged from 11.84 to 24.82 nm. The plots of crystalline sizes, lattice strain and dislocation against pH were depicted in Figures 4.18 and 4.19. This implies that Scherrer's formula fitted well for the determination of grain size of ZnO in this study. It was found that there was variation and increased in lattice strain at basic medium. Thus, the variation in strain could be due to the change in size and microstructure of the particles.

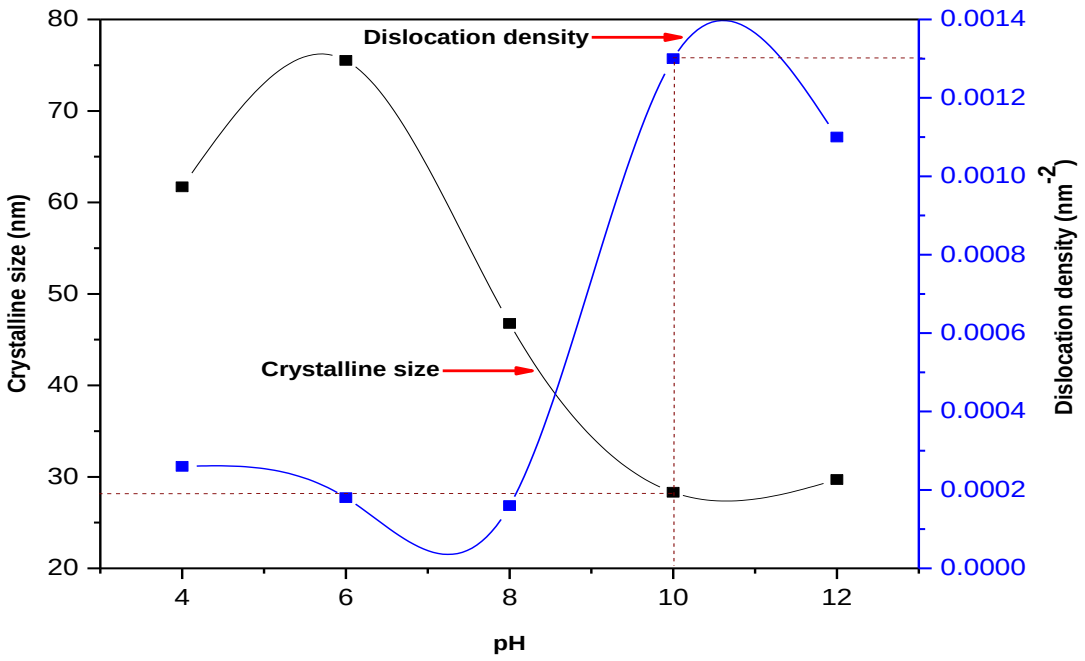

Figure 4.18: Plot of Crystalline Size and Dislocation against pH of ZnO Nanoparticles using Williamson-Hall Analysis

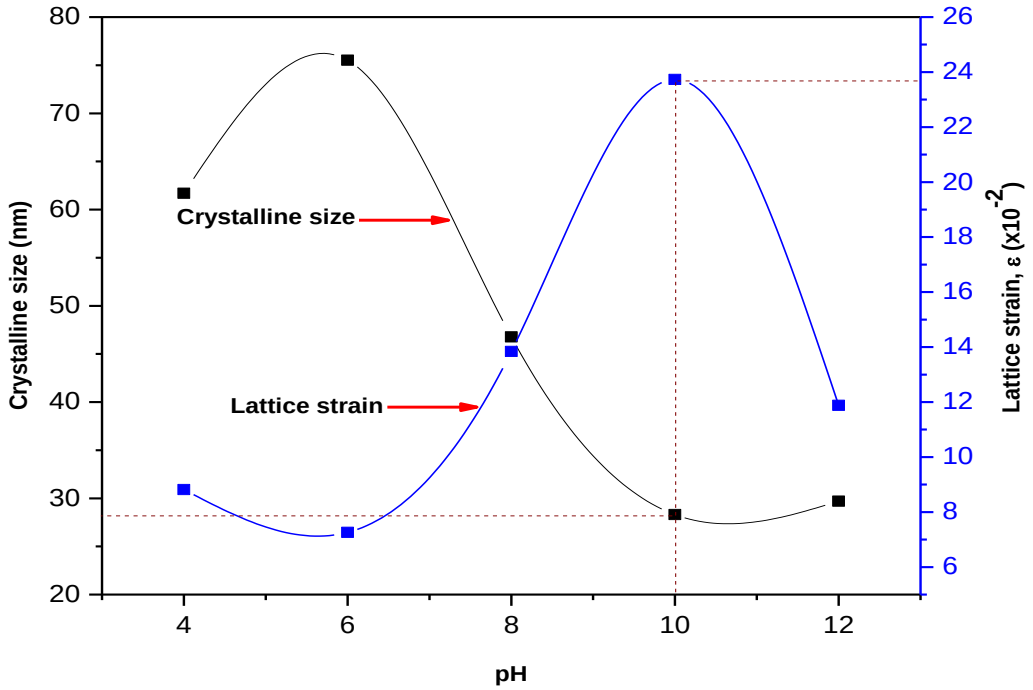

Figure 4.19: Plot of Crystalline Size and Lattice Strain against pH of ZnO Nanoparticles using Williamson-Hall Analysis

4.3.2 FTIR analysis

Fig. 4.20 presents FTIR spectra of the zincite nanoparticles at different pH calcined at 450 ^{o}C are investigated in the region 500-4000 cm^{-1}.

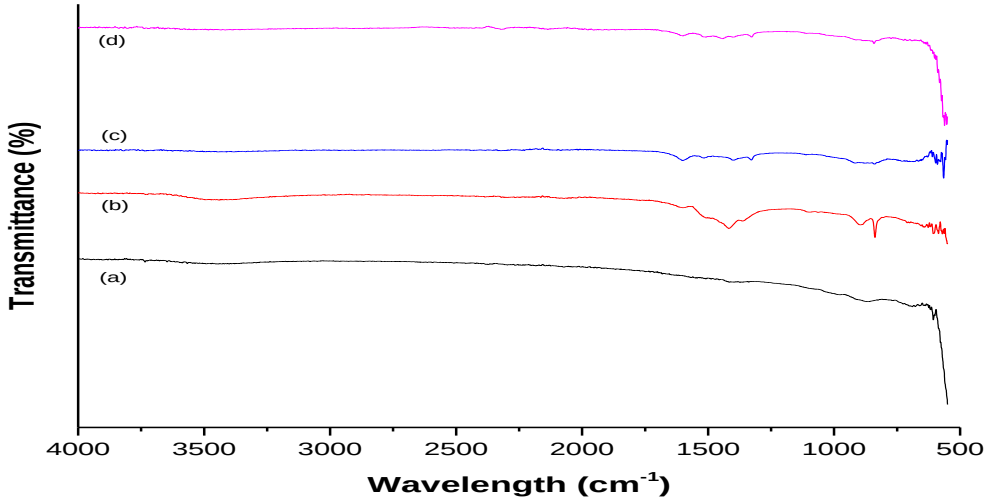

Figure 4.20: FTIR spectra of synthesized ZnO nanoparticles calcined at 450 ^{o}C at pH (a) 6 (b) 8 (c) 10 and (d) 12.

Figure 4.20 shows the FTIR spectra of synthesized ZnO nanoparticles, pH at (a) 6 (b) 8 (c) 10 (d) 12, calcined at 450 ^{o}C. At pH of 6 and 8, the absorption wavenumber at 3300-3600 cm^{-1} which measured as the pH increased from 10 to 12 is assigned to the OH moiety which emanated from water and ethanol. The band appearing at 1456 and 1540 cm^{-1} correspond to symmetric C=O and C-O stretching vibrations respectively while the peaks at 1630 cm^{-1} are assigned to COONa bond. The presence of peaks between 900 and 780 cm^{-1} indicate that there are C-H groups emanating from the precursor used for ZnO synthesis. The ZnO moiety gave absorption bands at 513-710 cm^{-1} at the fingerprint region, indicating the complete transformation of $Zn(OH)_2$ to ZnO. At pH of 6 and 12 when compared to pH of 8 and 10 in this study, the peak shift between 1640 and 550 cm^{-1} may be attributed to the change in average particle size distribution as a function of pH and this also caused a shift in the wavelength. This observation is supported by the XRD results of this material.

4.3.3 HRSEM and EDX analysis

The morphologies of the synthesized ZnO nanoparticles at different pH (a) 6 (b) 8 (c) 10 (d) 12 calcined at 450 ^{o}C were as presented in Plate IX. The displayed images show that the particles were spherically distributed.

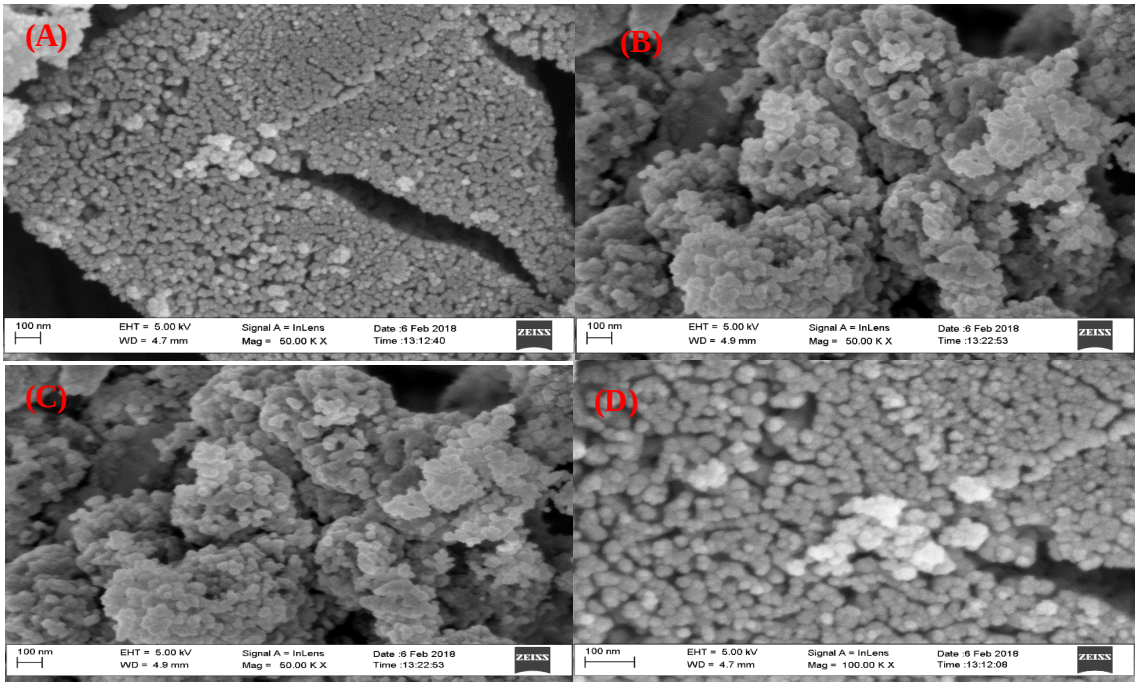

Plate IX: HRSEM Images of ZnO Nanoparticles calcined at 450 oC at pH (a) 6 (b) 8 (c) 10 and (d) 12.

The HRSEM images of ZnO nanoparticles prepared by sol-gel method at pH (a) 6 (b) 8 (c) 10 and (d) 12 are presented in Plate IX. The synthesized ZnO nanoparticles were spherical and not uniformly distributed. At low pH, agglomeration of the ZnO nanoparticles became more evident. However, there was a decrease in the aggregation during the nucleation process upon the addition of NaOH. It was found that the surface morphology significantly depends on this experimental parameter (pH). The effect of pH on ZnO could also exhibit the complexation of the Zn^{2+} ion, thus resulting in a complete reaction between the precursors leading to the formation of less agglomerated nanoparticles (Shaban *et al.*, 2018). The particle sizes of 26.10, 17.23, 14.90 and 16.38 nm for ZnO at pH 6, 8 10 and 12 were obtained respectively. Figure 4.21 shows the EDX spectra of ZnO nanoparticles. The strong peaks of Zn and O were detected in the EDX spectra, which confirmed the formation of ZnO while C and Na were present as impurities. The weights and atomic percentages of these elemental compositions are presented in Table 4.5. From the Table, synthesized ZnO

nanoparticles have atomic percentages of approximately stoichiometric ratio of Zn (2): O (1).

Figure 4.21 shows the results obtained from the EDX characterization which suggest that the ZnO nanoparticles have good percentage purity with little impurities. Experimentally, the stoichiometric mass percentage of Zn and O in the samples are presented in Table 4.5.

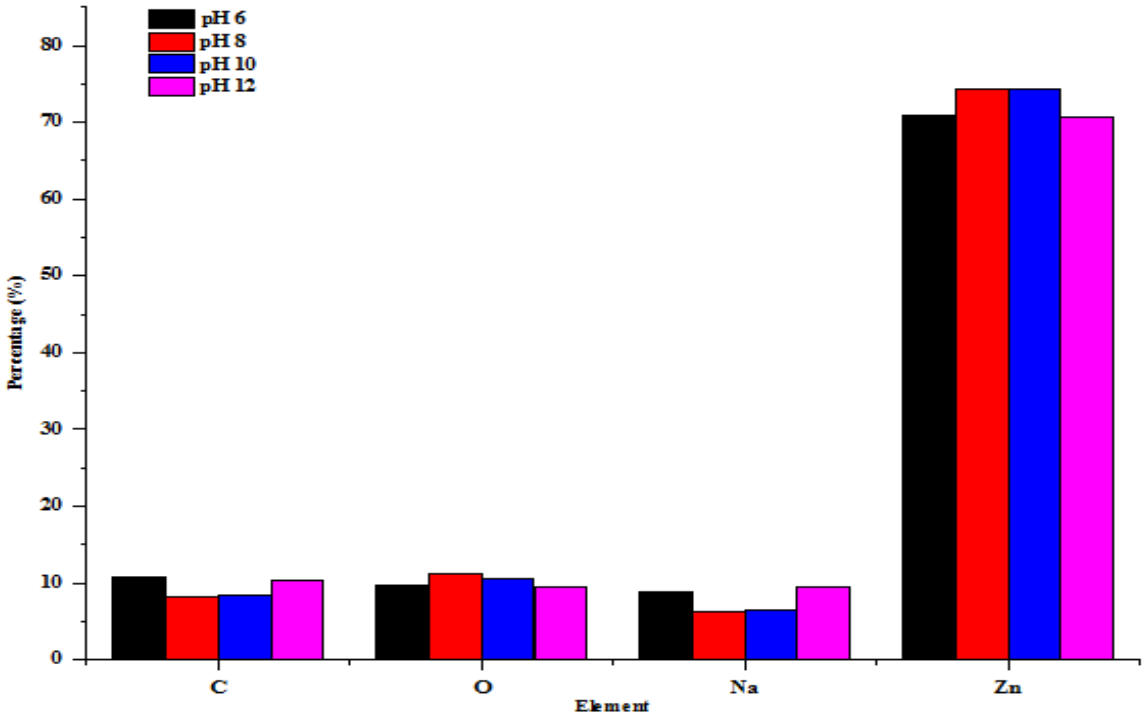

Figure 4.21: EDX Analysis of ZnO nanoparticles at different pH

Table 4.5: EDX Results of ZnO Nanoparticles at pH 6, 8, 10 and 12

Element	pH							
	6		8		10		12	
	% Wt	% At	% Wt	% At	% Wt	% At	% Wt	% At
Carbon	8.08	24.01	10.80	30.30	8.42	25.00	10.28	29.05
Oxygen	11.19	25.00	9.64	20.20	10.59	23.57	9.58	20.27
Sodium	6.31	9.68	8.78	12.80	6.55	10.36	9.50	13.85
Zinc	74.42	41.22	70.78	36.70	74.43	41.07	70.64	36.82

4.3.4 BET analysis

The specific surface areas and pore size distribution of the optimum ZnO nanoparticles prepared at pH 10 was studied using the nitrogen gas adsorption isotherm as shown in Figure 4.22.

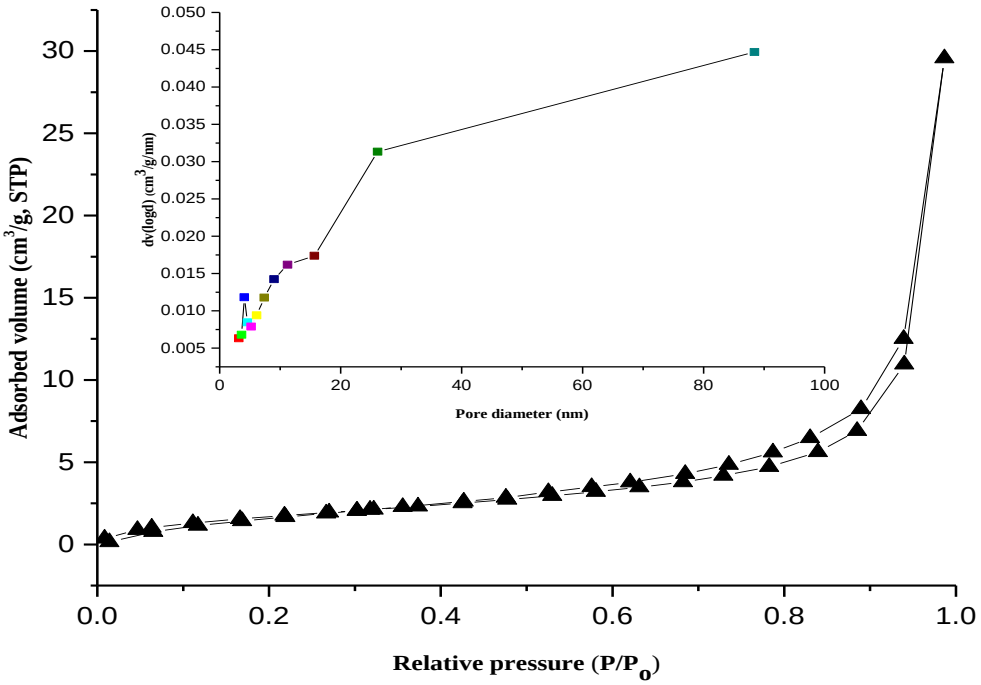

Figure 4.22: BET Analysis of ZnO at pH 10

The N_2 adsorption-desorption isotherm of ZnO nanoparticles synthesized at pH 10 and calcined at 450 °C is shown in Figure 4.22. The obtained isotherm is Type IV according to

IUPAC and corresponds to capillary condensation of gases as the relative pressure (P/P_o) approaches unity. The hysteresis loop is Type H3 and this describes the synthesized ZnO to be a mesoporous material. The BET and BJH analysis show that the surface area is 31.8 m^2/g and the pore size distribution is maximum at 3.81 nm. The pore size value strongly supports the fact that ZnO nanoparticles are mesoporous.

4.4 Synthesis of kaolin/TiO_2 Nanocomposites

4.4.1 XRD Studies

The phase structure and degree of crystallinity of the synthesis kaolin/TiO_2 nanocomposites were analyzed by XRD. Figure 4.23 shows the XRD pattern of kaolin and anatase TiO_2 (kaolin/TiO_2) prepared by the calcination process at 450 °C.

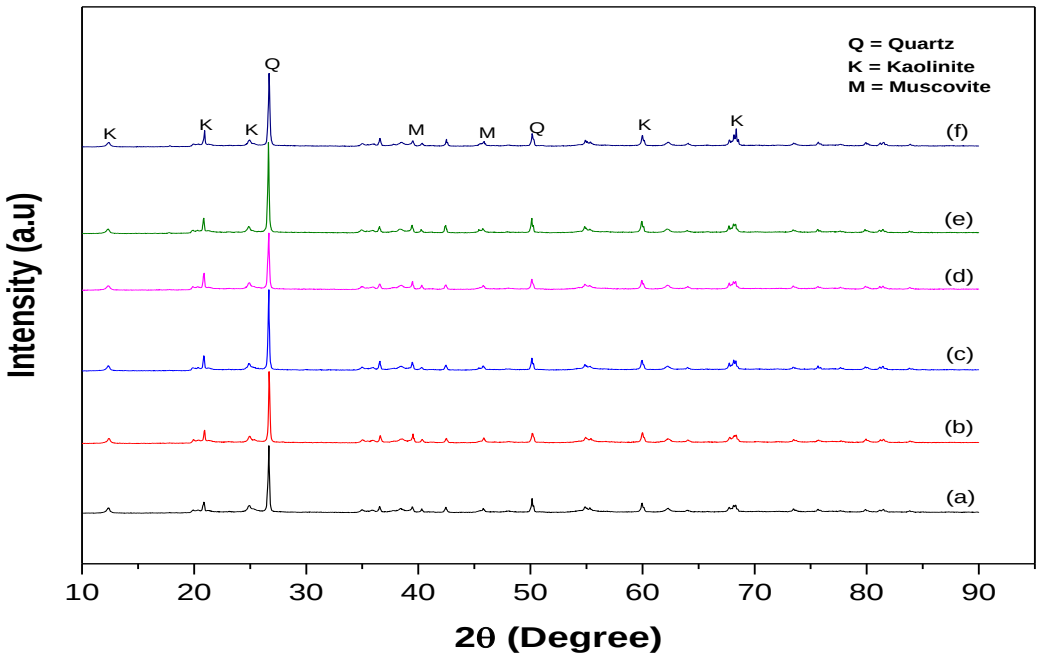

Figure 4.23: Diffractogram of Kaolin/TiO_2 at pH (a) 2 (b) 4 (c) 6 (d) 8 (e) 10 and (d) 12 at Calcination Temperature of 450 °C for 3 hr.

The diffractogram of the nanocomposites of TiO_2 at pH (a) 2 (b) 4 (c) 6 (d) 8 (e) 10 and (d) 12 anchored on kaolin calcined at 450 °C as shown in Figure 4.23 indicated that the diffraction pattern of kaolin overshadowed that of TiO_2 reflections, leaving the 2θ

reflections of kaolinite phase unchanged. The observed peaks of anatase TiO_2 disappeared while the peaks of kaolinite were still retained which may be due to: (i) the closeness of peaks of anatase to kaolin, making the TiO_2 phase to be difficult to identify (ii) the weakness and low-strength peaks of TiO_2 leading to non-generation of new peaks and non-aggregation of the nanocomposites and (iii) the amount of TiO_2 nanoparticles were too low to be detected by XRD.

However, the low-strength peaks of calcined kaolin is an indication that the calcined kaolin was decorated with well-crystallized TiO_2 nanoparticles. After calcination at 450 ^oC, this broad peak disappeared and the crystallization of TiO_2 began, while all the characteristic peaks of kaolinite were maintained, suggesting that the structure of the clay was maintained. It may be remarked that the characteristic peaks of anatase are very close to those of kaolinite, which make it difficult to analyse.

4.4.2 FTIR analysis

FTIR studies of the kaolin/TiO_2 nanocomposites as presented in Figure 4.24 were carried out in the region of 500-4000 cm^{-1} in order to observe the changes involved when the pH values of the media were changed.

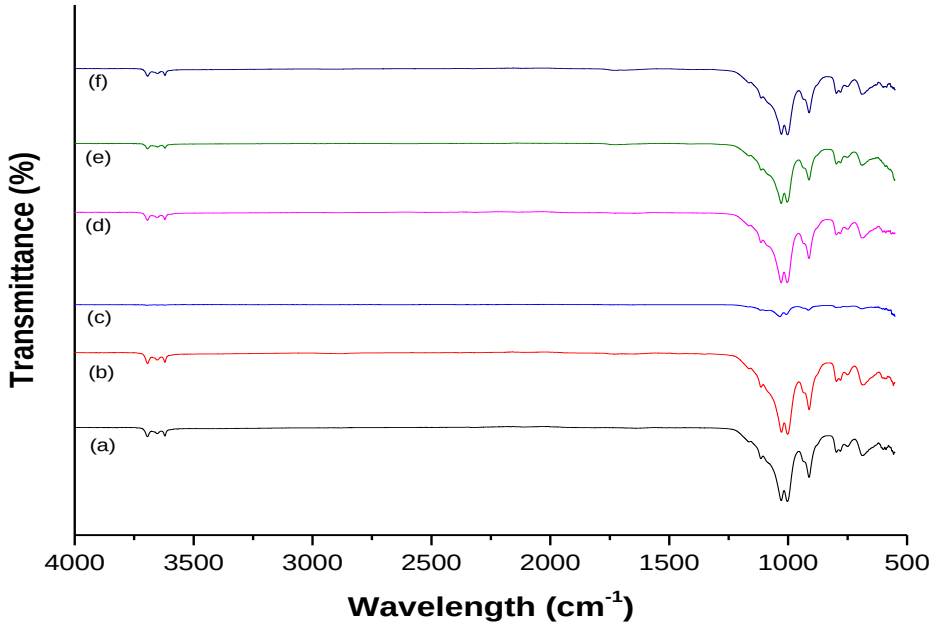

Figure 4.24: FTIR of Spectra of the Beneficiated Kaolin with its TiO_2 Nanocomposites at pH (a) 2 (b) 4 (c) 6 (d) 8 (e) 10 and (f) 12 Calcined at 450 °C.

The functional groups in kaolin/TiO_2 nanocomposites were investigated using FTIR spectroscopy. Figure 4.24 describes the FTIR spectra of the beneficiated kaolin and TiO_2 nanocomposites at pH (a) 2 (b) 4 (c) 6 (d) 8 (e) 10 and (f) 12. From the figure, it was observed that the nanocomposites calcined at 450 °C exhibited similar spectra properties except for pH 6. The absorption bands at 3696, 3663 and 3626 cm^{-1} correspond to hydroxyl groups and Al-OH. Compared to the FTIR of beneficiated kaolin alone, the hydroxyl bands were not affected, indicating that the TiO_2 interact laterally with Al and Si. The intense bands at 1034, 914-951, 789, and 594 cm^{-1} could be attributed to the Si-O, Ti-O-Si, Al-O and Ti-O bonds respectively. The stretching vibration of Ti-O-Si in the samples may be due to the incorporation of Ti into the kaolin structure. However, it was found that the amount of Ti in the kaolin-TiO_2 nanocomposites was higher than the ordinary kaolin proving that the TiO_2 crystallites are anchored onto the kaolin framework in reference to the EDX result.

4.4.3 HRSEM analysis

The results of the surface morphologies of the optimum kaolin/TiO_2 nanocomposites were analysed by HRSEM as depicted in Plate X and their EDX analysis is presented in Figure 4.25.

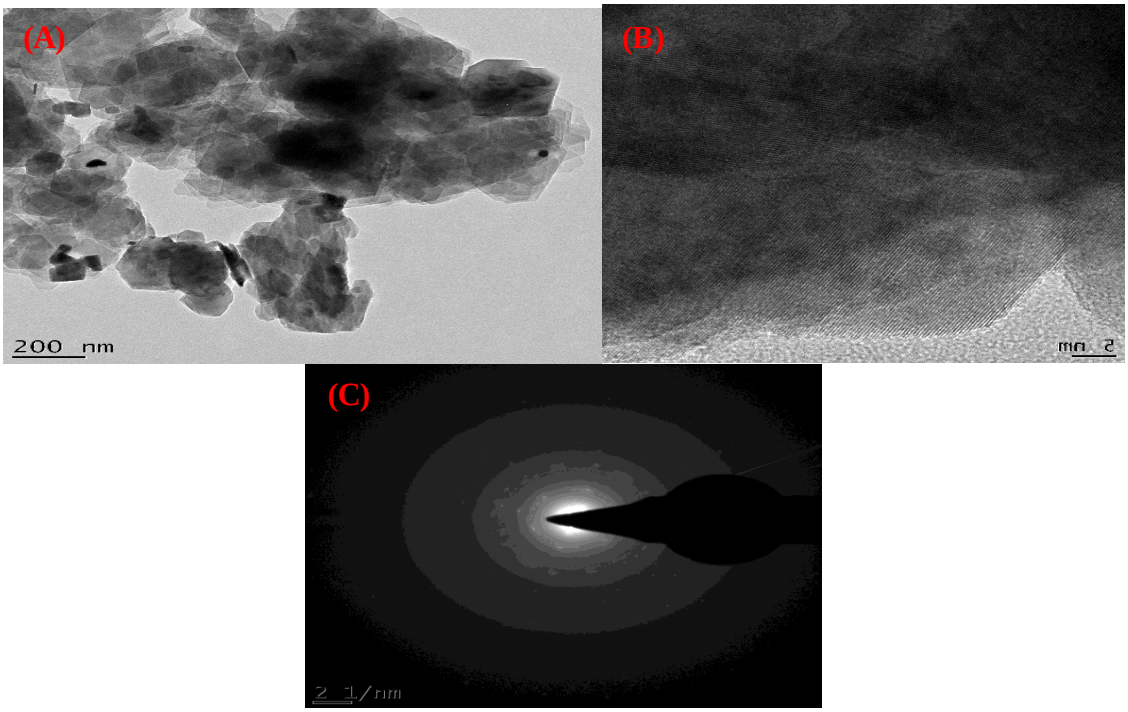

Plate X: HRTEM and SAED Analysis of TiO_2 Nanoparticles support on Kaolin at pH 8

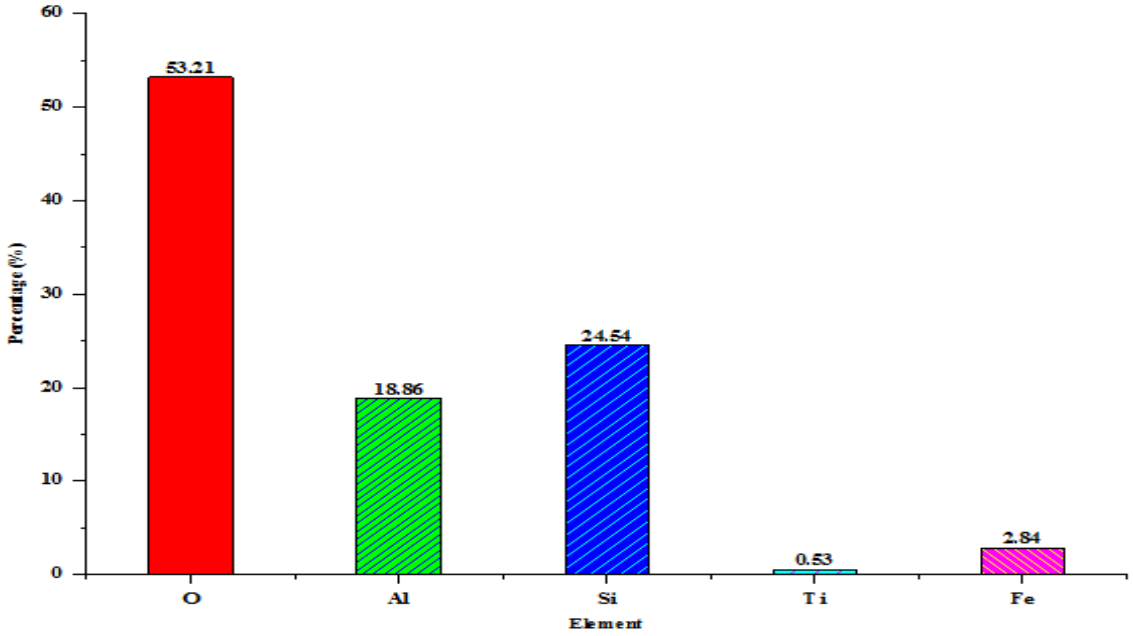

Figure 4.25: EDX analysis of Kaolin/TiO_2 Nanocomposites

The TiO_2/kaolin nanocomposites characterized by HRTEM microscopy as shown in Plate X. HRTEM had kaolin layer ratio which the spherical TiO_2 nanoparticles were dispersed with a lattice spacing of 0.24 nm, a characteristic of (111) crystal plane of anatase (Sun *et al.*, 2018). The HRTEM analysis further confirmed that the TIO_2 nanoparticles were both in the internal and external surfaces of the kaolin which may increase the active surface sites of the nanoadsorbent. Additionally, EDX measurements analysis as presented in Figure 4.25 showed the existence of some elements which may help in improving the adsorption capacity of the adsorbent.

4.5 Synthesis of Kaolin/ZnO Nanocomposites

4.5.1 XRD analysis

The structures of kaolin/ZnO nanocomposites were determined by XRD. The results plotted in Figure 4.26 shows that the composites are a mixture of kaolinite and zincite phases.

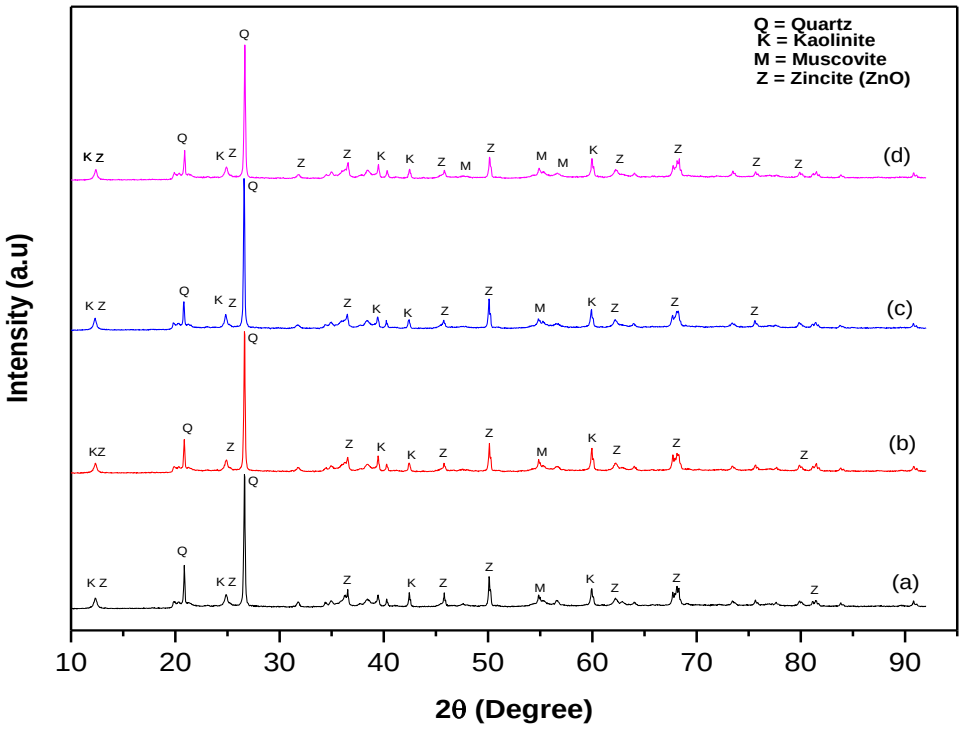

Figure 4.26: Diffractogram of Kaolin/ZnO Nanocomposites at pH (a) 6 (b) 8 (c) 10 and (d) 12 at Calcination Temperature of 450 °C for 3 hr.

As illustrated in Figure 4.26, the XRD analysis of the ZnO/kaolin nanocomposites calcined at 450 °C for 3 h, prepared at pH (a) 6 (b) 8 (c) 10 and (d) 12, the XRD patterns showed the presence of diffractions related to the zincite hexagonal structure. The high-intensity peak at 26.8° indicates the presence of quartz in the various nanocomposite samples. On the other hand, small intensity of ZnO nanoparticles were still observed in the spectra. The diffractogram showed the 2θ peaks at 24.7°, 31.67°, 34.28°, 36.61° and 50.16° which correspond to (101), (110), (002), (101) and (110) crystal plane. All reflections of ZnO nanoparticles were evident in the kaolin nanocomposite samples, indicating the successful formation of kaolin/ZnO nanocomposites.

4.5.1 FTIR analysis

Figure 4.27 shows the FTIR results of kaolin/ZnO nanocomposites in the region of 400-4000 cm^{-1}.

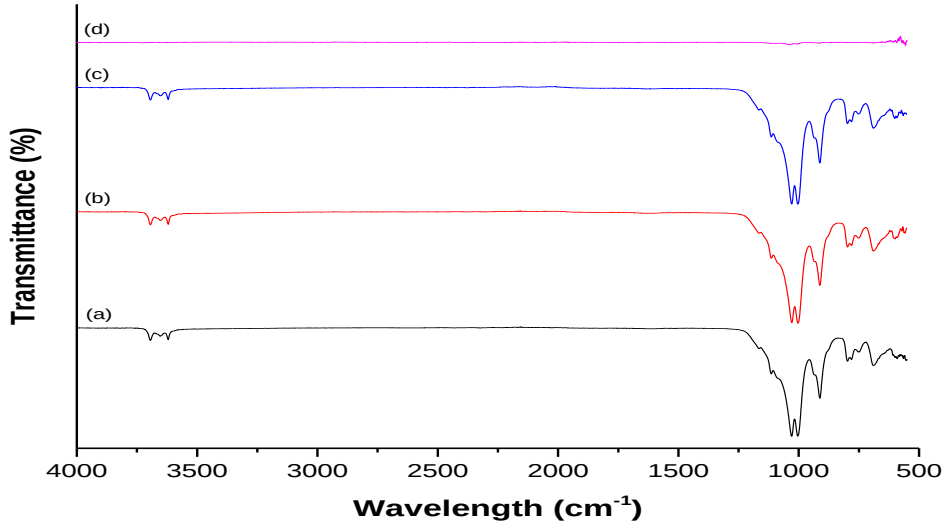

Figure 4.27: FTIR Nanocomposites Spectra of Kaolin/ZnO at pH (a) 6 (b) 8 (c) 10 and (d) 12 Calcined at 450 °C.

The characteristic peaks of the nanocomposites of ZnO at different ratios immobilized on kaolin at different ratios were found at 3486 and 3673 cm^{-1}, 2910 and 2964 cm^{-1} (symmetric vibration of C-H), 1726 cm^{-1} (Ti-O) ,1470 cm^{-1} (stretching of Ti-O-Ti), 947 cm^{-1} (Ti-O-Si)

and 914 cm^{-1} (Zn-O-H). The band at 1560 cm^{-1} in the nanocomposites is due to C=O bond. The absorption peaks around 513 and 881 cm^{-1} could be ascribed to the vibration mode of Zn-O, Ti-O-Ti and Zn-O-Ti bonds. Therefore, according to the appeared peaks at this region, the FTIR spectra confirm that $ZnTiO_3$ nanocomposites were formed. The bands between 1247 and 1449 cm^{-1}. The resultant vibration of T-O-C could be due to the interaction between the asymmetric and symmetric COO^- groups from zinc precursor and Ti-O network.

4.5.2 HRTEM and EDX analysis

The HRTEM micrographs and SAED analysis of the nanocomposites in Plate XI show the presence of ZnO nanocomposites homogeneously dispersed on the surface of kaolin with low agglomeration.

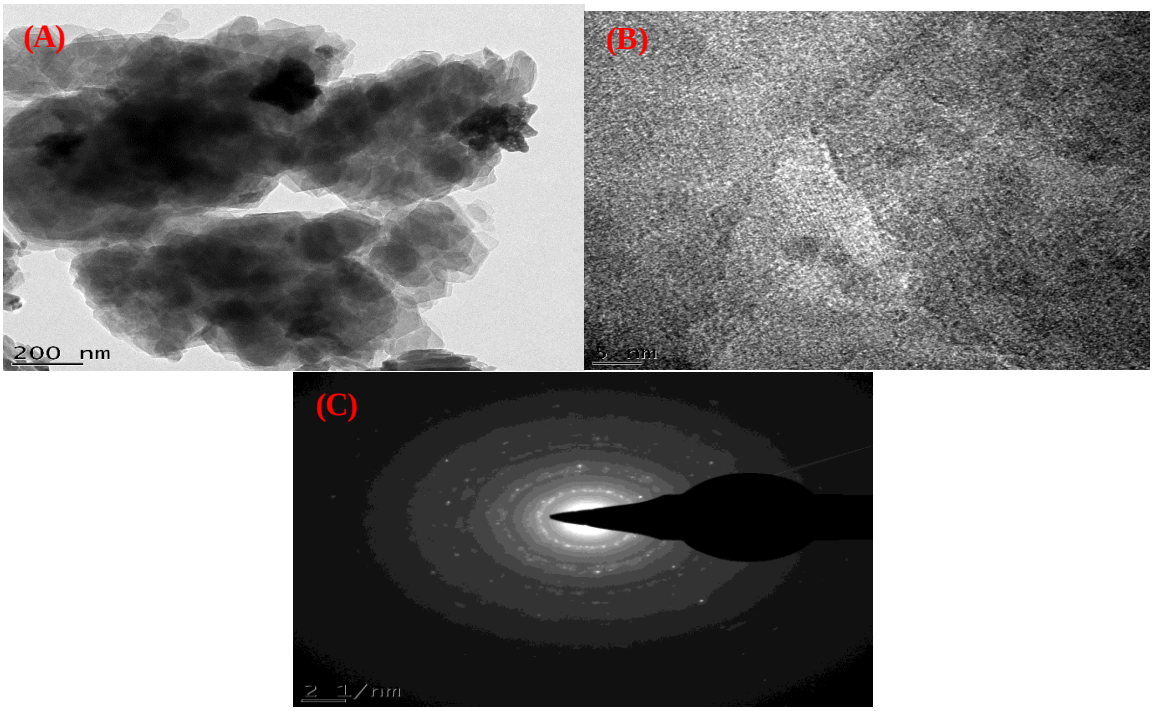

Plate XI: HRTEM and SAED Analysis of ZnO Nanoparticles at pH 10 supported on Kaolin

The EDX result of kaolin/ZnO nanocomposites at pH 10 as presented in Figure 4.28 shows elemental distribution that includes Zn which confirms the assembly of the element in the kaolin.

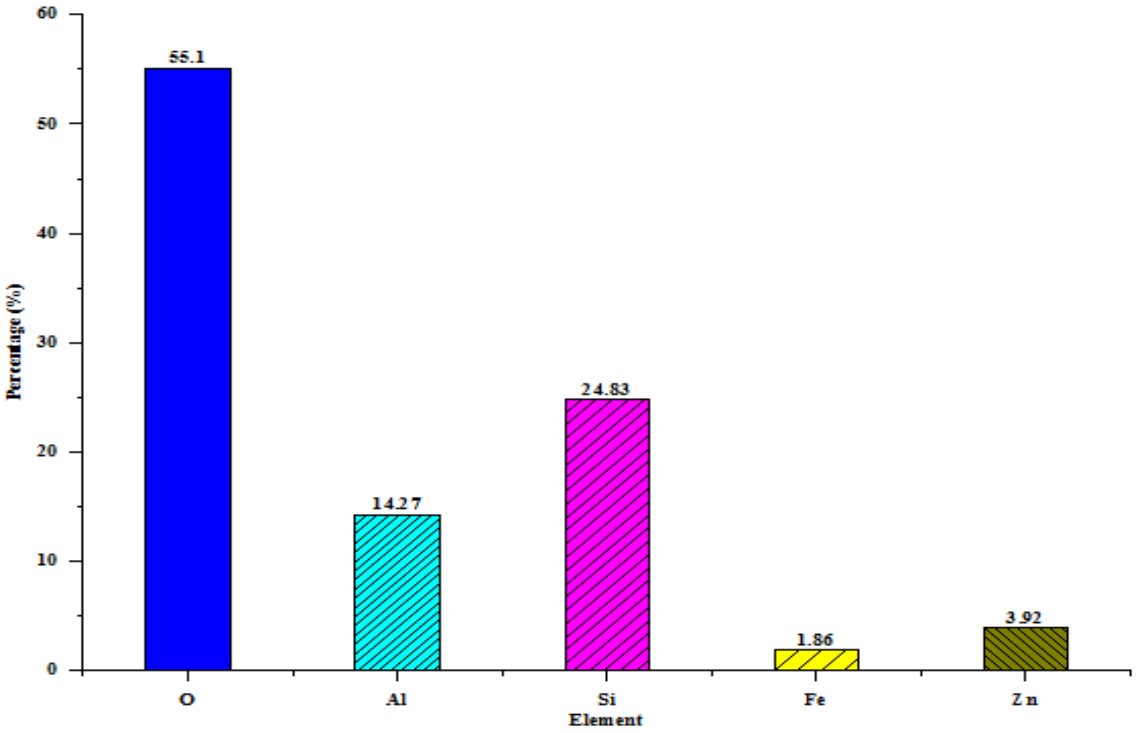

Figure 4.28: EDX Analysis of Kaolin/ZnO Nanocomposites

The HRTEM micrograph of ZnO/kaolin in Plate XI shows the presence of less agglomerated ZnO nanoparticles homogeneously dispersed on the surface of the kaolin. The EDX image shows the presence of C, O, Na and Zn elements (Figure 4.28). The HRTEM exhibits clear lattice fringes with a d-spacing of 0.26 nm indexed (002) plane of the zincite ZnO crystal and the diffraction pattern shows evident rings. From the spectrum, sharp peaks corresponding to Zn were observed at 1.06, 8.64 and 9.63 keV, respectively. Thus, immobilization of ZnO nanoparticles on kaolin matrix prevents agglomeration of the nanoparticles leading to large and active surface sites of the nanocomposite. The HRTEM images indicate spherically shaped ZnO nanoparticles (dark spots) surrounded by the light shapes silicate layer, showing the formation of ZnO nanoparticles in the interlayer spaces of kaolinites. The size distribution of ZnO nanoparticles was within 21.34 nm for ZnO/kaolin nanocomposites.

4.6 Synthesis of Kaolin/TiO_2/ZnO Nanocomposites

4.6.1 XRD studies

The mineralogical compositions of the kaolin/TiO_2/ZnO nanocomposites were determined by XRD. The diffractogram angle, 2θ was between 10 and 90° as shown in Figure 4.29. It was noted that the peak of zincite is highly intense when compared to titania in the nanocomposites materials.

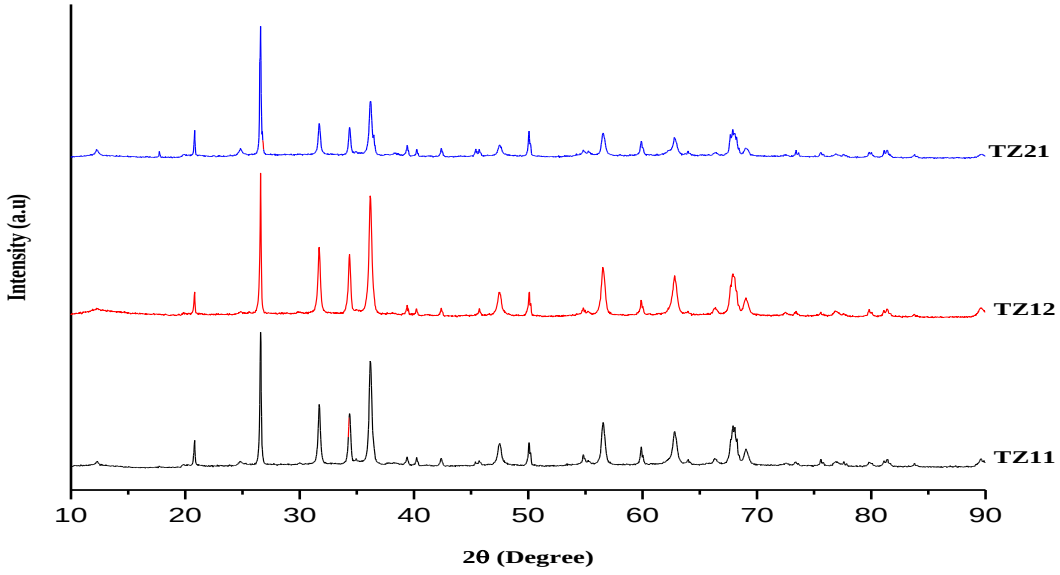

Figure 4.29: XRD Patterns of Kaolin/TiO_2/ZnO Nanocomposites Calcined at 450 °C.

The crystal structures of kaolin/TiO_2/ZnO nanocomposites calcined at 450 °C were investigated using the XRD pattern. The XRD results as shown in Figure 4.29 represent those of kaolin/TiO_2/ZnO nanocomposites: KTZ11, KTZ12 and KTZ21. The XRD pattern of the samples revealed sharp diffraction peaks of zincite phase while KTZ11 and KTZ12 samples showed broader and intense peaks of mainly ZnO. This may be due to the incorporated ZnO in the TiO_2 lattice and the broadness of the diffraction peaks, could be as a result of the overlap of TiO_2 lattice planes. Moreover, this observation in this study is supported by the FTIR analysis and the intensity of the diffraction peaks which indicate the dominant peaks of ZnO. The obtained ZnO structures have proved to have stronger

adsorption properties and the XRD patterns clearly points to the presence of kaolinite, quartz and ZnO as the main crystalline phases.

The average crystallite sizes of KTZ11, KTZ12 and KTZ21 nanocomposites were calculated using the Debye-Scherrer formula. The XRD patterns of the nanocomposites at different ratios showed the appearance of peaks at 2θ angle of 26.03, 31.67, 34.60, 36.83, 55.38, 63.01 and 68.1°. The average crystallite sizes of the KTZ11, KTZ12 and KTZ21 were 12.05, 8.23 and 9.31 nm, respectively using the ZnO peaks.

4.6.2 FTIR analysis

Figure 4.30 shows the FTIR results of kaolin/ZnO/TiO_2 nanocomposites in the region of 500-4000 cm^{-1} used to find out the changes involved when different ratios of nanoparticles were used.

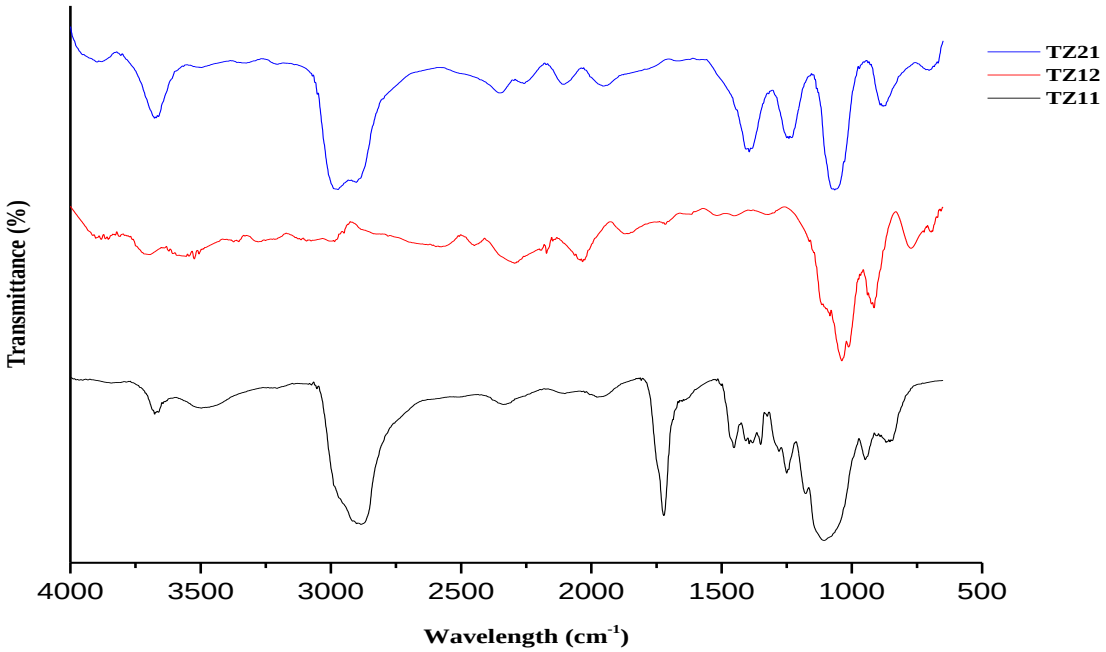

Figure 4.30: FTIR Spectra of Kaolin/TiO_2/ZnO Nanocomposites Calcined at 450 °C

Figure 4.30 represents FTIR characteristic peaks of the nanocomposites of TiO_2 and ZnO immobilized in kaolin at different ratios. The absorption bands were found at 3486 and 3673 cm^{-1} (OH stretching vibration), 2910 and 2964 cm^{-1} (symmetric and asymmetric stretching

vibration of C-H), 1726 cm^{-1} (Ti-O) ,1470 cm^{-1} (stretching of Ti-O-Ti), 947 cm^{-1} (Ti-O-Si) and 914 cm^{-1} (Zn-O-H). The appearance of the hydroxyl bond could be from ethanol and water during the hydrolysis of the titanium precursor. The band at 1560 cm^{-1} in KTZ12 could be due to C=O bond. The absorption peaks around 513 and 881 cm^{-1} could be ascribed to the vibration mode of Zn-O, Ti-O-Ti and Zn-O-Ti bonds. The bands between 1247 and 1449 cm^{-1} can be denoted as Ti-O and Ti-O-C vibration modes. The resultant vibration of T-O-C could be due to the interactions between asymmetric and symmetric COO^- groups from zinc precursor and Ti-O network. Therefore, according to the obtained peaks in the above stated region (500 to 4000 cm^{-1}), the FTIR spectra confirm that $ZnTiO_3$ nanocomposites were formed.

4.6.3 HRTEM and EDX analysis

The HRTEM images of the kaolin/ZnO/TiO_2 nanocomposites as shown in Plate XII show the presence of ZnO and TiO_2 nanoparticles dispersed on the surface of kaolin with less agglomeration in A_1 and C_1.

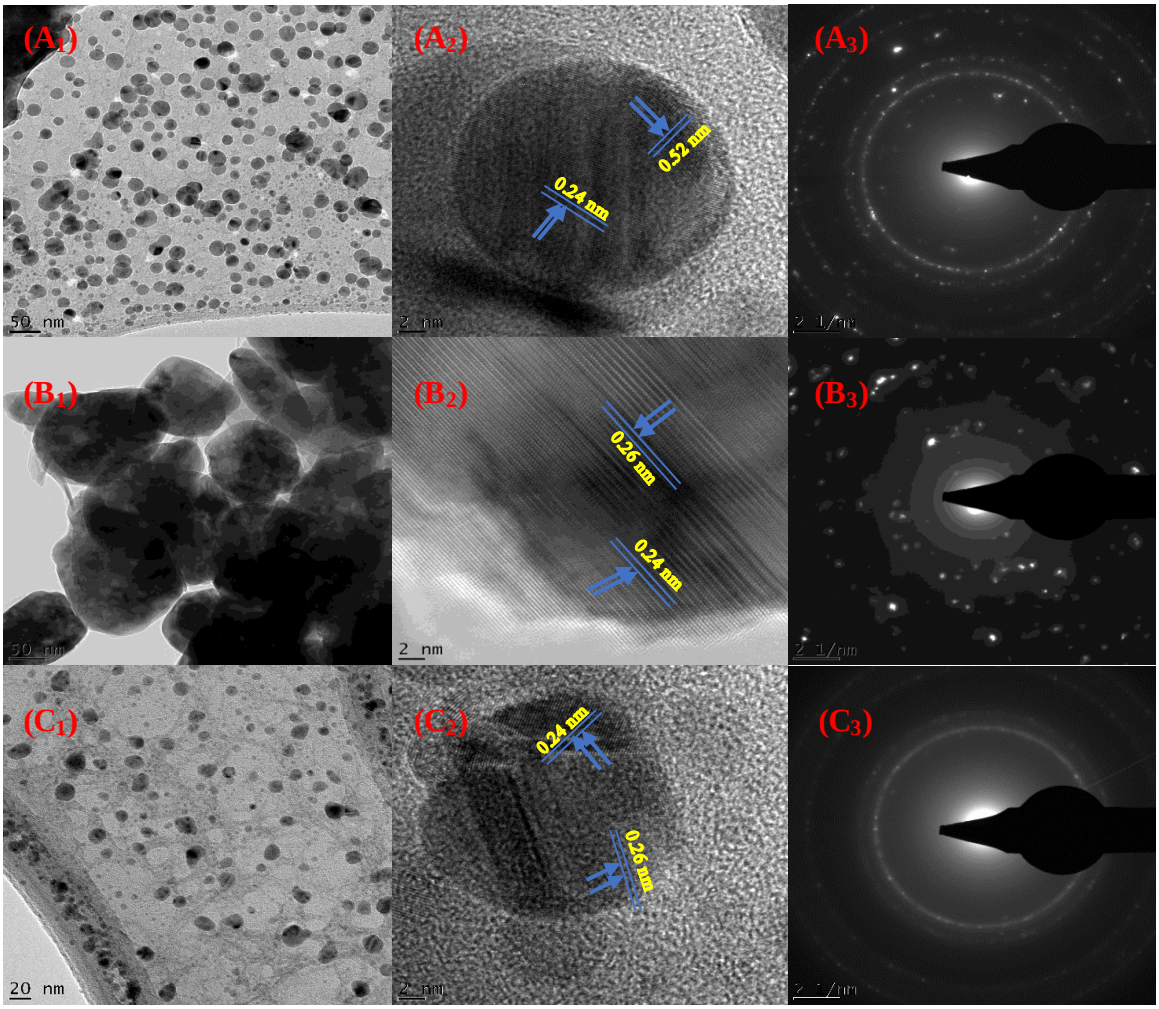

Plate XII: HRTEM and SAED Analysis of Kaolin/TiO_2/ZnO Nanocomposites: (A_{1-3}) KTZ11 (B_{1-3}) KTZ21 and (C_{1-3}) KTZ12.

The EDX results of kaolin/ZnO/TiO_2 nanocomposites as presented in Figure 4.31 show a distribution of Zn and Ti elements in the composites which confirms the assembling of both elements on the kaolin.

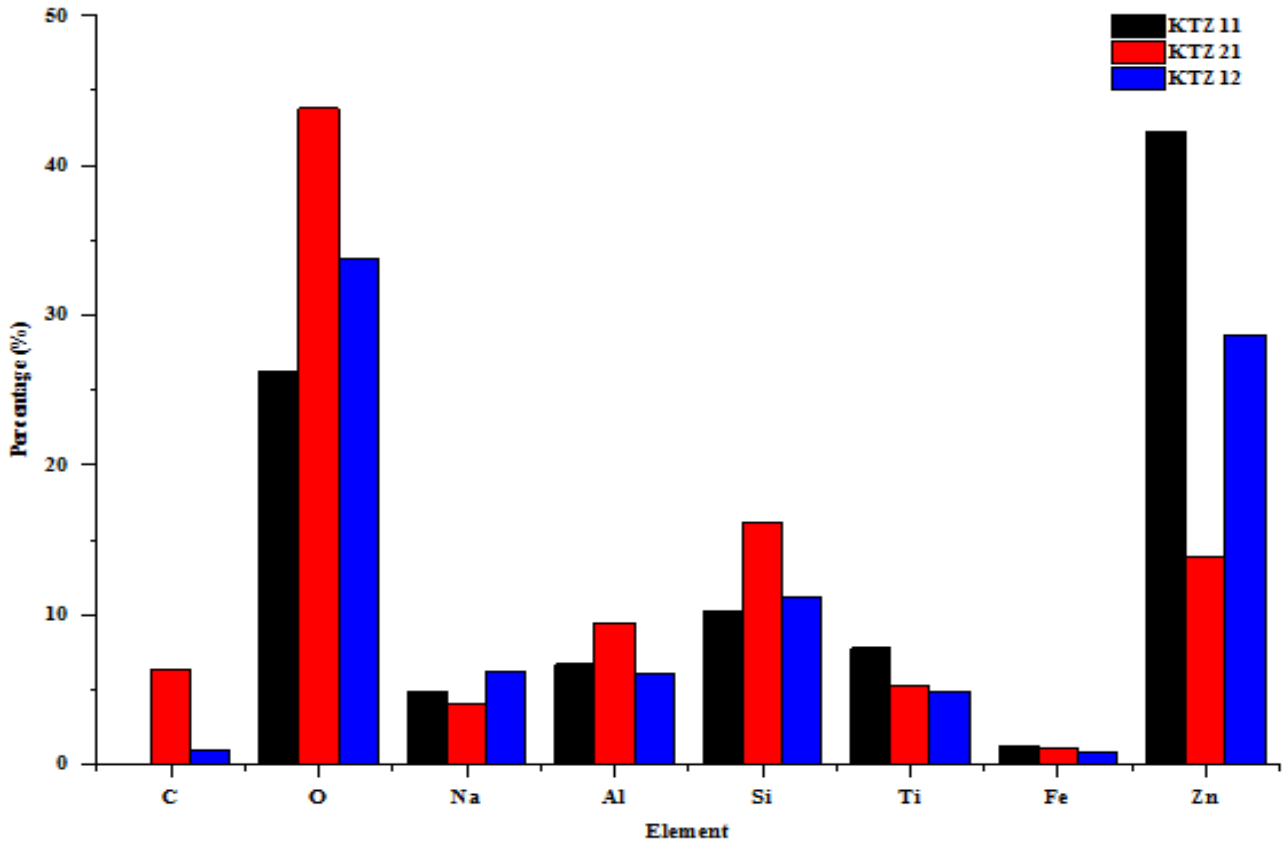

Figure 4.31: EDX Analysis of Kaolin/TiO_2/ZnO Nanocomposites

HRTEM micrographs of kaolin/TiO_2/ZnO nanocomposites at different ratios of KTZ11, KTZ21 and KTZ12 are shown in Plate XI. From Plate XII, It is seen that the TiO_2 and ZnO nanoparticles were immobilized on the kaolin. The size distributions of the anchored TiO_2 and ZnO nanoparticles were measured, which show lattice spacing of 0.24 and 0.26 nm corresponding to (111) and (002) lattice planes of anatase and zincite phases. The primary particle sizes of ZnO and TiO_2 estimated by XRD were reduced due to the elimination of agglomeration in the nanocomposites and hence, formed monodispersed/evenly distributed composited nanocomposites were obtained. Figure 4.31 depicts the results of EDX analysis for the synthesized nanocomposite, which shows the presence of C, O, Na, Al, Si, Ti, Fe and Zn in the kaolin/TiO_2/ZnO structures.

4.6.4 BET analysis

The N_2 adsorption-desorption isotherms and pore size distribution of kaolin/ZnO/TiO_2 nanocomposites at different ratios are displayed in Figures 4.32 and 4.33 (a and b), respectively. In Figure 4.32, the relative feature obtained could be ascribed to mesoporous material while the pressure $\frac{P}{P_o} > 0.44$, indicates that adsorption-desorption isotherm starts to rise and showed a typical H3 hysteresis loop.

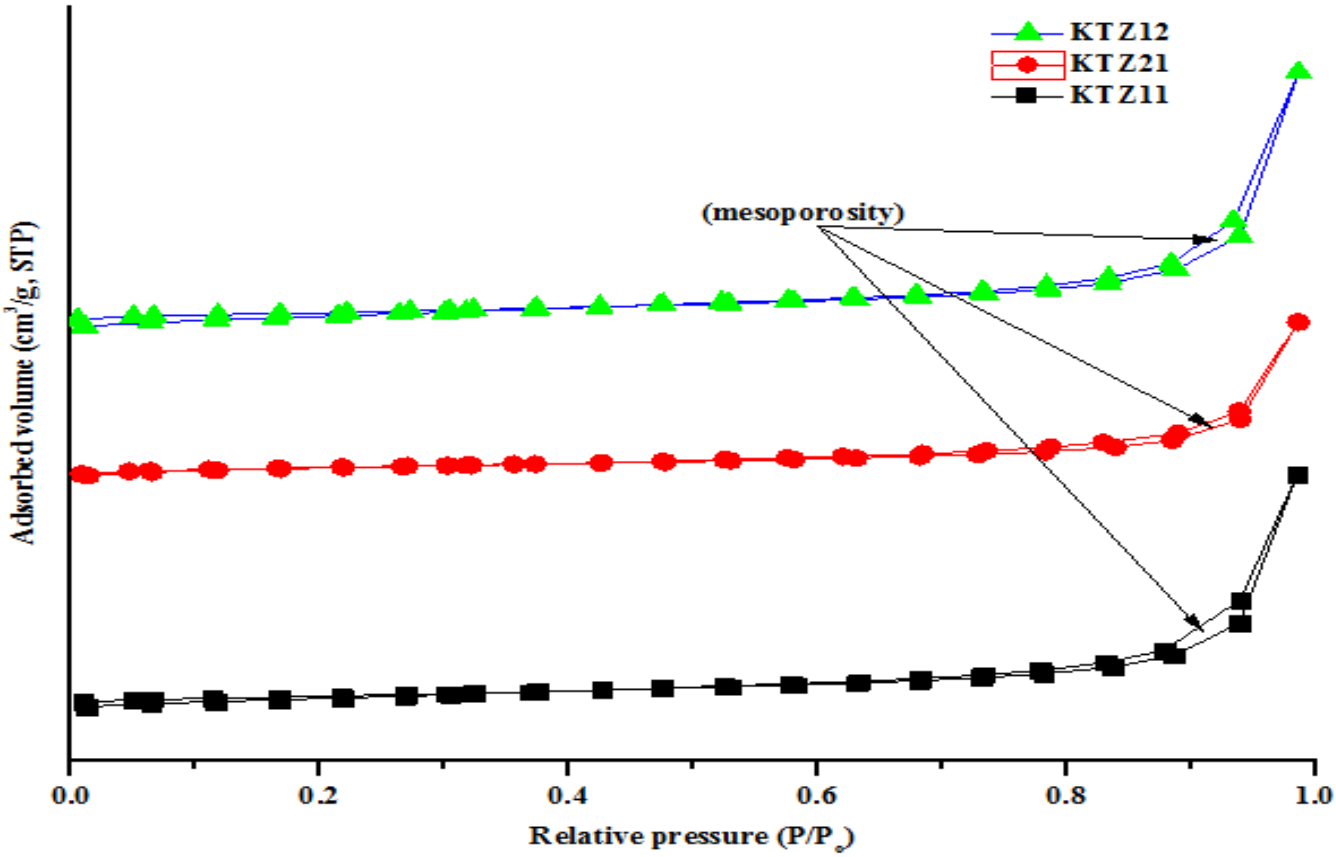

Figure 4.32: BET Analysis of Kaolin/ZnO/TiO_2 Nanocomposites at different Nanoparticles ratios

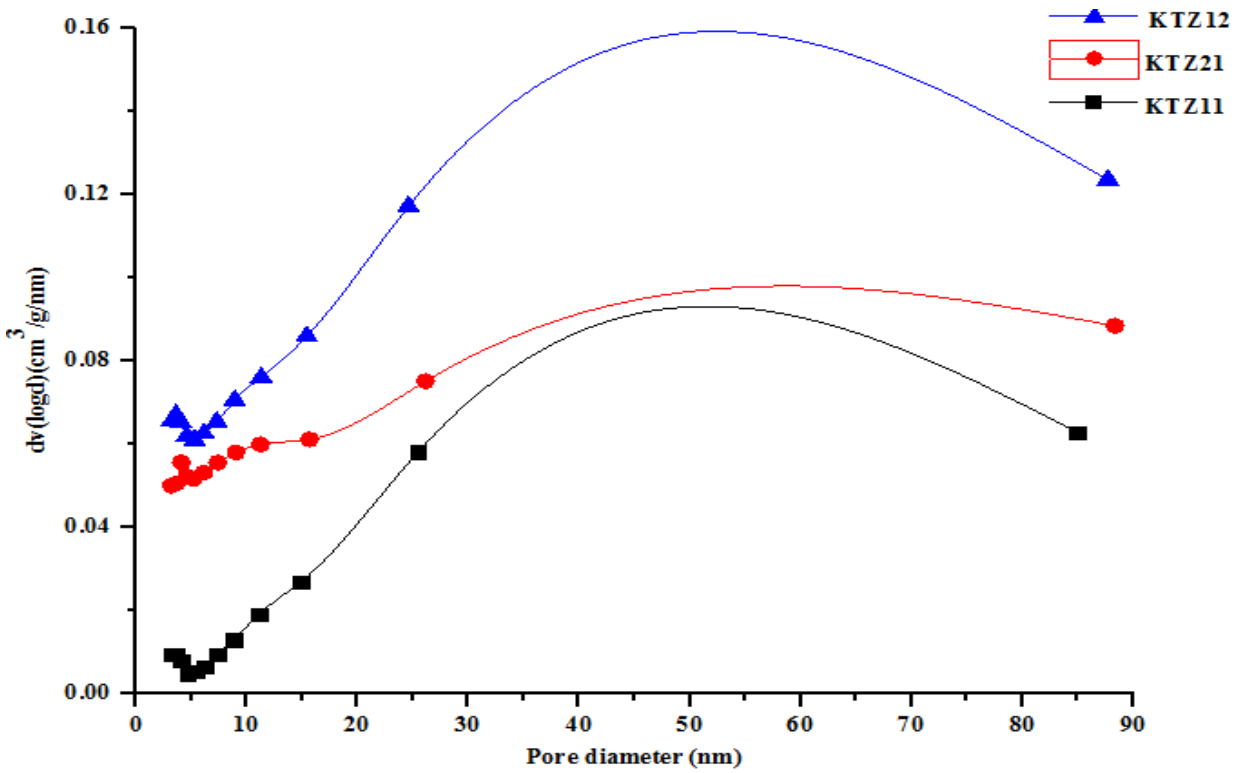

Figure 4.33 (a): Pore Diameter Analysis of Kaolin/ZnO/TiO_2 Nanocomposites at different Nanoparticles ratios using Barret-Joyner-Halenda (BJH) Methods.

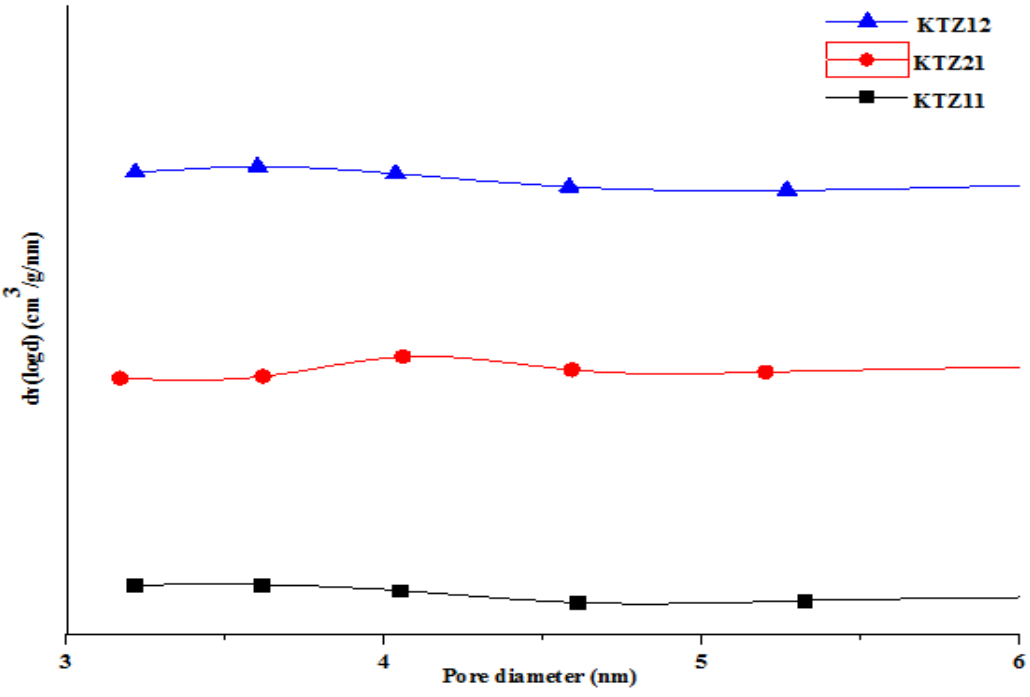

Figure 4.33 (b): Pore Diameter Analysis of Kaolin/ZnO/TiO_2 Nanocomposites at different Nanoparticles ratios using BJH Methods.

Figure 4.32 describes the N_2 adsorption-desorption isotherm of the TiO_2/ZnO/kaolin nanocomposites labelled KTZ11, KTZ21 and KTZ12. The nanocomposites samples

exhibited Type IV isotherm with H3 hysteresis loops, an indication of mesoporosity according to the IUPAC classification. Interestingly, all the nanocomposites samples exhibited similar isotherms. The BET and BJH pore size distributions correspond to mesoporous materials that are in the range of 3.93 to 4.24 nm. The nanocomposites result show the BET specific surface areas, and pore volumes of 58.10 to 73.80 m^2/g and 0.201 to 0.224 cm^3/g, respectively. It was noted that the mesoporous nanocomposites had more enhanced BET values than the beneficiated clay, indicating that some molecules had been incorporated in the interlayers of the clay. The mesoporosity could allow different molecules of different sizes into their pores of the composites, making them highly suitable for adsorption purposes. This effect can also be related to the internetwork connection of metal during synthesis forming multi metallic nanoparticles. The formation of metal to oxygen bonds also increases the porous structure of the kaolin, thus increasing the active surface area. The addition of basic solution promoted the release of OH^- ions resulting in deprotonation followed by hydrogen bonding and polymetallic formation. Furthermore, the specific surface areas of all the samples were greater than that of the beneficiated kaolin. The high BET values are attributable to the increase in pore volumes and pore sizes.

4.7 XPS Analysis

The XPS analysis was performed to determine the surface chemical states of Zn and O on the prepared ZnO nanoparticles. Figure 4.34(a) shows the high XPS survey of Zn in the nanoparticle showed strong signals of Zn (2p), O LLM, O (1s), Zn (LMM), C (1s), Zn (3s), Zn (3p) and Zn (3d). The Zn (2p) core level region of ZnO nanoparticles exhibited a sharp singlet peak at a binding energy of 1021.30 eV which was attributed to the Zn ($2p_{3/2}$) line. The binding energy of Zn $2p_{3/2}$ revealed that the Zn element exists in the Zn^{2+} chemical state which corroborates the findings of Soyekwo *et al.* (2019). The quantitative analysis

shows that the atomic percentage of Zn and O are 79.24 and 18.90 %, respectively, which agrees with the theoretical values of Zn and O of ZnO.

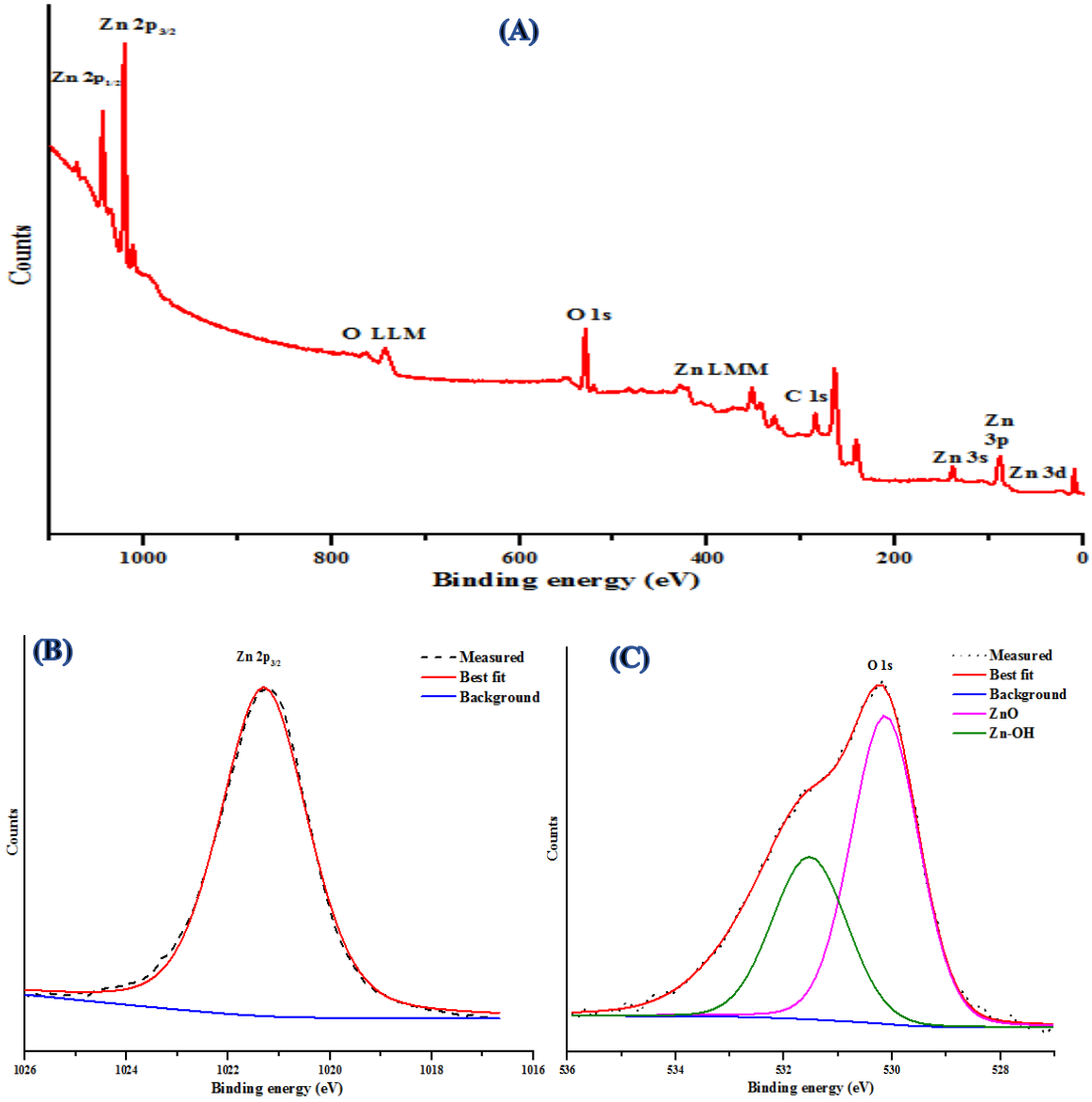

Figure 4.34: XPS Profiles of ZnO Nanoparticles for (A) Zn and (B) O 1s

As shown in Figure 4.34 (b), the binding energy of the O (1s) region for the ZnO nanoparticles revealed the presence of two sharp and intense peaks at around 530.2 and 531.8 eV, indicating lattice oxygen. These peak could be attributed to adsorbed oxygen and existence of oxygen in the ZnO nanoparticles. The Auger electron peak of Zn LMM at binding energy of 287 eV also confirmed the presence of Zn^{2+} in the ZnO nanoparticles, confirming that Zn of the nanoparticles is in the environment of the Zn^{2+} oxidation state.

Figure 4.35 represents the XPS spectra of synthesized TiO_2 nanoparticles at an optimum pH of 8 by sol-gel method. The figure shows the high XPS survey of Ti in the nanoparticle showing strong signals of Ti LMM, O KLL, O (1s), Ti (2s), C (1s), Ti (2p), Ti (3s) and Ti (3p). The spectra for Ti with line shapes of Ti ($2p_{1/2}$) and Ti ($2p_{3/2}$) corresponds to 32.8 and 67.2 %, respectively. This indicates that Ti exist in +4 oxidation state and was obtained from the spin-orbit splitting of Ti ($2p_{1/2}$) and Ti ($2p_{3/2}$) electron bands (Pal *et al.*, 2019). The energy difference between the doublet peaks is approximately 6 eV, thus confirming the presence of Ti in +4 and oxidation number of +3. The Ti LMM Auger transition exhibited a sharp peak in the region of 880 eV which corroborate to the crystal TiO_2.

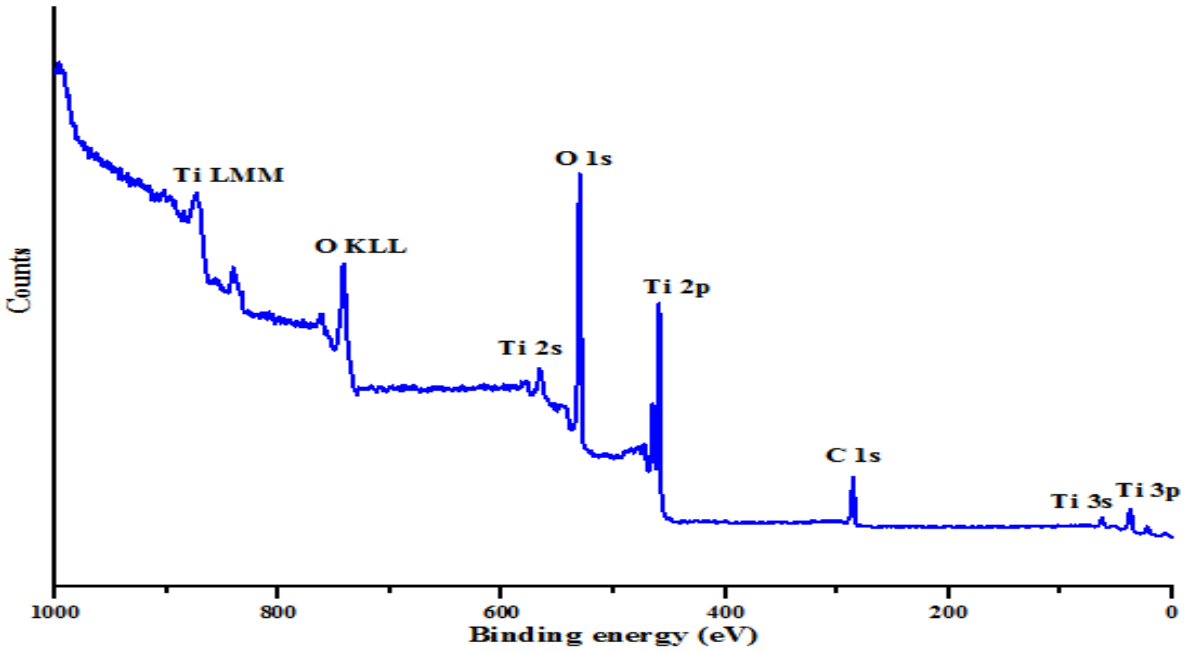

Figure 4.35: Survey Spectra of TiO_2 Nanoparticles

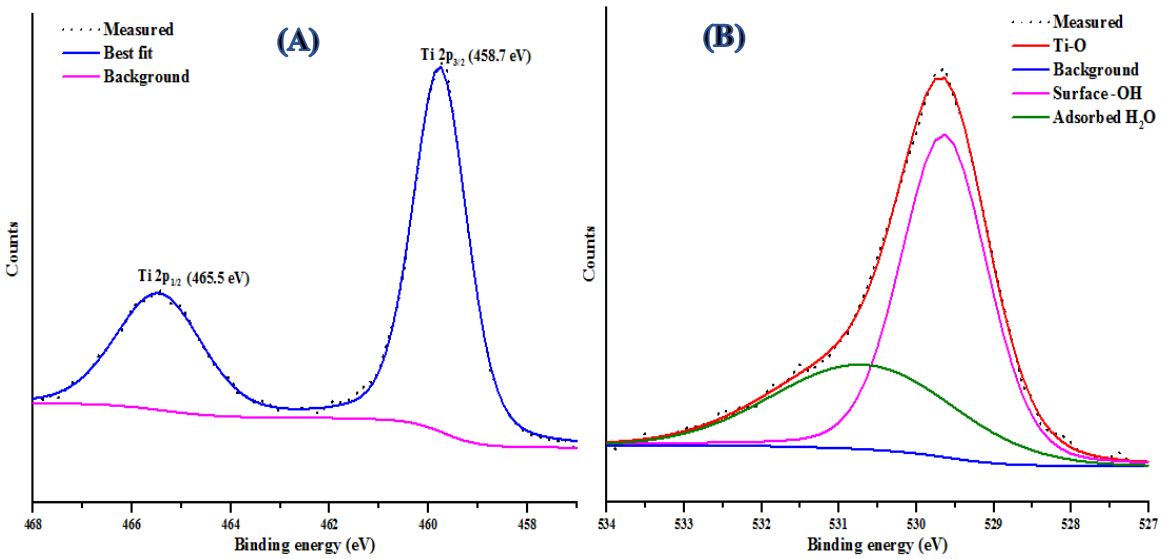

Figure 4.36: XPS Profiles of TiO_2 Nanoparticles for (A) Ti and (B) O 1s

These two identified peaks at 464.9 eV (Ti $2p_{1/2}$) and 458.8 eV (Ti $2p_{3/2}$) in Figure 4.36 (a) are similar to the published work reported by Krishnan *et al.* (2017) who found that peaks for Ti^{4+} were located at 459.3 and 465 eV, respectively. The two major peaks in O (1s) lies between the binding energy of 529.5 eV and 530.9 eV. The hump shape of the O 1s spectrum shows the presence of embedded surface species which were ascribed to four peaks at 530.7, 531.9, 532.9 and 534 eV as represented in Fig. 4.36 (b) The initial peak at 530.7 eV represents lattice O band to Ti^{4+} and the other three peaks are from water molecules on the surface of the sample (Cook *et al.*, 2019). The order of OH group with oxygen at the bridging oxygen site (531.9 eV), OH group as a terminal group and oxygen attached to the five coordinated Ti^{4+} (O-Ti^{4+}) covalent bond at 533 eV and formation of a water molecule at 534 eV.

The ZnO/kaolin, TiO_2/kaolin and ZnO/TiO_2/kaolin nanocomposites calcined at 450 ^oC were analyzed by XPS. Figure 4.37 (a) showed the spectra for Si 2p. The Si (2p) spectra of the nanocomposites as seen in Figure 4.37 (a) shows a single peak around 102.51 eV (ZnO/kaolin), 102.27 eV (TiO_2/kaolin) and 101.81 eV (ZnO/TiO_2/kaolin) samples. The evident shift in peaks could be due to the different compositions. The Ti LMM Auger signal showed blunt peak with no significant difference in binding energy when compared to the

TiO_2/kaolin nanocomposites. The Si (2p) spectra are attributed to silicon bounded to carbon and oxygen in the samples. The binding energy at 531.48 eV and 531.61 eV corresponds to (Zn-O and Ti-O) and Zn-O-Ti, respectively (Fig. 4.37 c). The samples also demonstrated a single peak around 532.6 eV which corresponds to the oxygen bonded with silicon (Si-O-Si). In comparison, the O 1s in the nanoparticles (ZnO and TiO_2) show that the binding energy did not change significantly. This suggest that incorporation of kaolin has no clear effect on the bonding of oxygen with silicon. However, the peak corresponding to silicon oxide still remains intact.

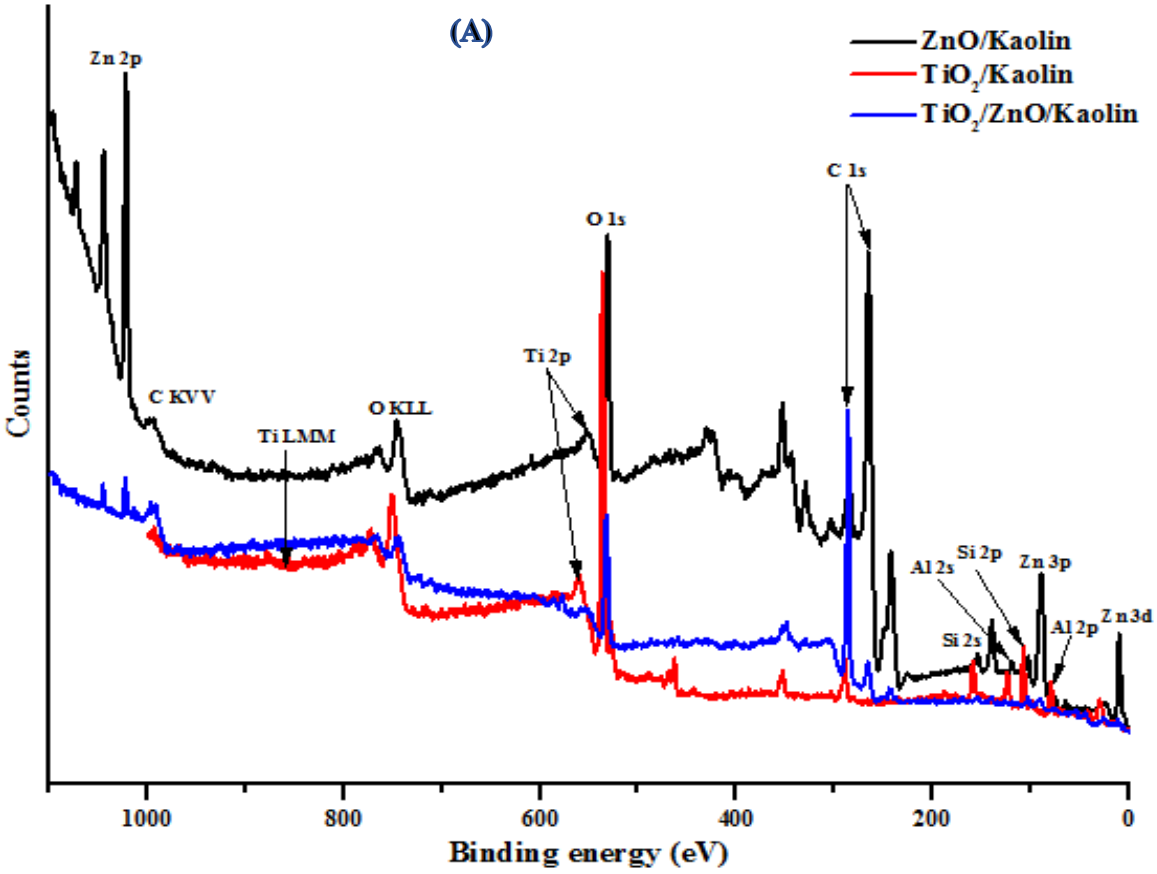

Figure 4.37: Survey Spectra of ZnO/kaolin, TiO_2/kaolin and ZnO/TiO_2/kaolin Nanocomposites

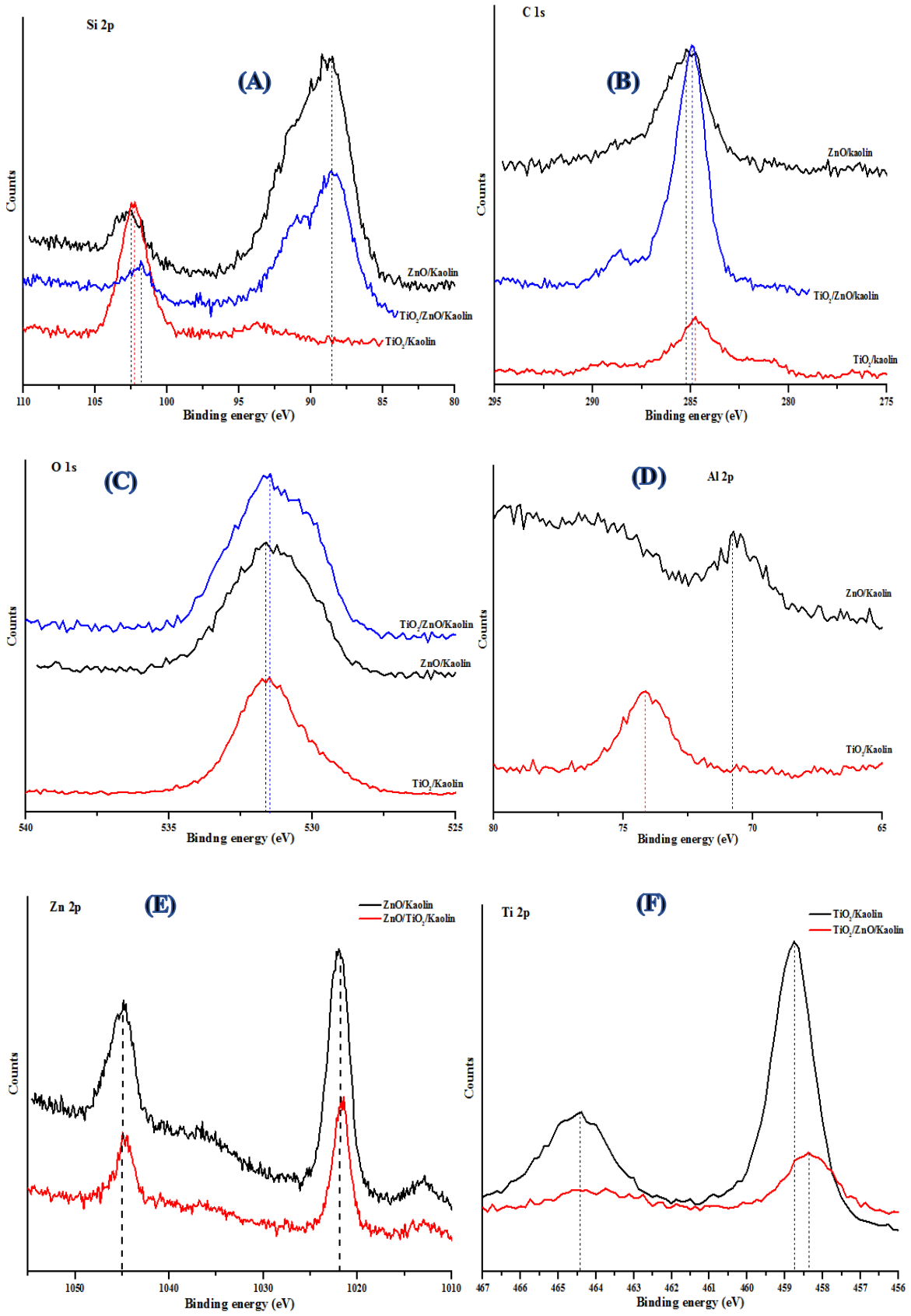

Figure 4.38: High Resolution of XPS Spectra of (A) Si 2p (B) C 1s (C) O 1s (D) Al 2p (E) Zn 2p and (F) Ti 2p for the Synthesized ZnO/kaolin, TiO_2/kaolin, and ZnO/TiO_2/kaolin Nanocomposites.

The surface composition of the nanocomposites displays the spectra of the C 1s regions as shown in Figure 4.38 (c). The peaks located at 284.92 and 285.27 eV indicate oxygen bonded species, C-O for the nanocomposites. The presence of carbon is assigned to the catalytic evaluation of nanoparticles during the carbonization technique. Figure 4.37 describes the survey XPS spectra from the nanocomposites. The elements detected are mainly constituted in the samples and no other forms of contamination were present in the samples. Thus, the presence of carbon could be a result of sample exposure to air.

XPS spectra of Zn core electrons are presented in Fig… It is worthy of note that the binding energy of Zn (2p) spectra in the nanocomposites (ZnO/kaolin and TiO_2/ZnO/kaolin) which appeared at binding energy 1021.85 eV has been observed to be increased by 0.55 eV as compared to ZnO nanoparticles. The XPS spectra of Ti (2p) core electron as represented in Figure 4.38 (f) for TiO_2/kaolin and TiO_2/ZnO/kaolin samples show no significant difference in the binding energy compared to TiO_2 nanoparticles. However, there was no formation of peak at Ti $2p_{1/2}$ for ZnO/TiO_2/kaolin nanocomposites. This observation indicates the effect of the nanoparticles on the surface of kaolin influenced the valence and core electron differently.

The peak intensity helps to quantify the amount of nanoparticles on the surface of the supported material. This also depend on the X-ray emission, resolution, charge neutralization and sample itself (Bergman *et al.,* 2017). It is interesting to note that the peak intensity of nanocomposites that contain ZnO nanoparticles appear to be high. This could be as a result of rapid diffusion of Al, Si and Ti into the Zn. The Zn (2p) core level spectra of the nanocomposites showed doublet whose energies were 1021.85 and 1045.02 eV, identified as Zn $2p_{3/2}$ and Zn $2p_{1/2}$ level regions. The difference in binding energy between the two regions are 23.17 eV, which satisfactorily relates to the standard reference value of ZnO (Iaiche and Djelloul, 2015).

The XPS spectra of the Al 2p level region of the nanocomposites are shown in Figure 4.38 (d). The Al 2p for ZnO/kaolin and TiO_2/ZnO/kaolin whose binding energies were 70.81 and 74.16 eV, respectively are related to the presence of Al^{3+} state. Also, there was a significant shift in Al 2p binding energy, indicating a decrease in intensity and a slight difference in its environment. The Al core level was observed on the surface of ZnO/kaolin and TiO_2/kaolin nanocomposites but not detectable in TiO_2/ZnO/kaolin, as seen in Figure 4.38 (d). Al ions dissolved in ZnO and TiO_2 by forming bond electrons wit Zn and Ti which will contribute to conductivity. From periodic table, the following elements present in the nanocomposites have the ionic radii; Al (0.0535 nm), Si (0.04 nm), Zn (0.074 nm) and Ti (0.064 nm). It can be deduced that Al and Si diffuse fast into Ti and Zn to form bi-metallic (Zn_3Si_2, Ti_3Si_2, Zn_3Al, Ti_3Al), ter-metallic ($TiSi_2Al$) and quad-metallic (Ti-Al-Si-Zn) nanoparticles. Thus, it can be concluded that Al and Si will capture oxygen in competition with Zn and Ti which led to more oxygen vacancies. Thus, the observed elemental compositions of the samples are in good agreement with the EDX analysis of the crystalline phase of the nanocomposites.

4.8 Physicochemical Properties of Tannery Wastewater

The physicochemical properties of tannery wastewater samples were determined according to standard methods for the examination of water and wastewater (APHA, 2017) as presented in Table 4.6. The results were compared to the references of WHO (2002) and NESREA (2009).

Table 4.6: Physicochemical Properties of Tannery Wastewater

Parameter	Recorded value	WHO (2002)	NESREA (2009)
Colour	Dark brown		
Odour	Objectionable		
pH	5.84±0.02	5-5.9	
Chemical oxygen demand (COD) (mg/dm^3)	1988.60±0.23	250	60
Biological oxygen demand (BOD) (mg/dm^3)	625.30±0.10	30	30
Electrical conductivity (µS/cm)	1647.00±0.20	1200	
Chloride (mg/dm^3)	7580.50±0.42	1000	250
Nitrate (mg/dm^3)	118.30±0.16		
Sulphate (mg/dm^3)	2944.00±0.22		
Total suspended solids (TSS) (mg/dm^3)	438.00±0.30	60	
Total dissolved solids (TDS) (mg/dm^3)	724.00±0.10		
Nitrite (mg/dm^3)	16.5±0.19	3	0.5
Total hardness (TH) (mg/dm^3)	1500.00±0.61		
Total alkalinity (TA) (mg/dm^3)	2200.00±0.91		
Total organic carbon (TOC) (%)	1.41±0.25		
Carbon(IV) oxide (mg/dm^3)	48.27±0.15		
Zinc (mg/dm^3)	2.15±0.10	1.0	
Lead (mg/dm^3)	1.70±0.13	0.1	
Cadmium (mg/dm^3)	1.23±0.50	2.0	
Copper (mg/dm^3)	0.71±0.20	0.1	
Nickel (mg/dm^3)	0.67±0.33	3	
Chromium (mg/dm^3)	8.30±0.28	2	1.5-2.0
Manganese (mg/dm^3)	0.22±0.10		
Aluminium (mg/dm^3)	2.98±0.14		
Iron (mg/dm^3)	7.20±0.60	10	

World Health Organization (**WHO**); The National Environmental Standards and Regulations Enforcement Agency (**NESREA**).

The physical and chemical properties of the analysed tannery wastewater with respect to BOD, COD, colour, odour, pH, electrical conductivity, chloride, nitrate, nitrite, sulphate, TSS, TDS, total hardness, total alkalinity, total organic carbon and carbon(IV oxide are presented in Table 4.6.

4.8.1 pH

pH influences other physicochemical parameters especially the metal ions present in the wastewater. The pH of the tannery wastewater was found to be 5.84 which is slightly acidic, which may be as a result of sulphate and chloride used during the tanning process. The pH value is slightly lower than the permissible value for industrial wastewater set by WHO (2002) which is 5-5.9. The discharge of this untreated wastewater into water bodies may be detrimental to zooplankton and fishes, thus affecting their physiology.

4.8.2 COD

According to Table 4.6, it can be seen that the amount of COD in the tannery wastewater was 1988.60 mg/dm^3 which is above the respective permissible levels given by WHO (2002) and NESREA (2009). This indicates that high amounts of chemicals were used during different tanning processes. COD is the amount of oxygen used by the oxidizable matter or organic impurities in the wastewater and the high COD content from the wastewater could affect the survival of gill breathing of aquatic organisms.

4.8.3 BOD

The level of BOD in the wastewater was recorded as 625.30 mg/dm^3 which is above the permissible limit of 60 mg/dm^3 set by NESREA (2009) for effluent discharged as depicted in Table 4.6. The high BOD content could be due to the presence of organic substances responsible for the consumption of oxygen in the wastewater. Furthermore, the presence of organic matter could promote anaerobic action when discharged into water bodies. The high

level of BOD could also be related to the unabsorbed organic chemicals in the tanning process.

4.8.4 EC

The EC value in the wastewater was obtained as 1647 µS/cm as shown in Table 4.6. The EC analysis measures the number of dissolved ions in wastewater. The obtained EC value is greater than the 1200 µS/cm standard value by WHO (2002). This indicates that the high level of EC might be attributed to various soluble salts used during the tanning process.

4.8.5 Chloride

The concentration of chloride in the tannery wastewater was found to be 7580.50 mg/dm^3 as shown in Table 4.6. The value exceeds the permissible limits of 1000 and 250 mg/dm^3 of WHO (2002) and NESREA (2009), respectively. The chloride level gives insight into the salinity of the wastewater sample. The high level of chloride in the wastewater could be due to sodium chloride used during the soaking and pickling stages of tanning. On discharge of this wastewater into water bodies, the water bodies become polluted, limiting the amount of water available for drinking and irrigation. This water could also cause harm to zooplankton.

4.8.6 TSS

The obtained TSS value in the wastewater sample was 438 mg/dm^3 and this is higher than the permissible TSS level of 60 mg/dm^3 set by WHO (2002). According to different scholars, TSS in wastewater (100 mg/dm3 is weak, > 100 mg/dm^3 but < 220 mg/dm^3 is medium and > 220 mg/dm^3 is strong. The result of this study shows that the tannery wastewater could be categorized as a strong wastewater. The level of TSS in the tannery wastewater solely depends on the quality of hides and skins (Chowdhury *et al.*, 2015). The level of TSS might be attributed to the presence or accumulated of residues from the discharged chemicals and fine leather particles during processing (Barman *et al.*, 2017).

Thus, the presence of this TSS in water bodies could lead to high turbidity which might cause low photosynthesis and respiration in aquatic systems.

4.8.7 TDS

In this study, the level of TDS in the tannery wastewater is 724 mg/dm^3 as presented in Table 4.6 and this level may affect the aesthetic content of water due to increased turbidity. The high content of TDS could be due to the presence of chemical compounds such as carbonate, chloride and sulphate in the wastewater. This indicates that the direct discharged of this tannery wastewater could limit the provision of good water for drinking and other purposes.

4.8.8 Some heavy metal ions

The concentration of heavy metals in tannery wastewater varies depending on the tanning process used in various industries. As shown in Table 4.6, tannery waste water contains higher levels of metals such as chromium, zinc, iron, iron, nickel, cadmium, manganese, and copper. When compared to WHO (2002) and NESREA (2009) standards, the tannery wastewater contained higher levels of chromium, zinc, and lead. Continuous chromium discharge, even at low concentrations, has been reported to be toxic to aquatic life and to disrupt the aquatic food chain (Mitra *et al.*, 2017). High levels of copper in humans cause a variety of negative health effects, whereas acute zinc toxicity causes throat dryness, cough, weakness, generalized aching, chills, fever, nausea, and vomiting (Hall, 2020).

4.9 Adsorption Studies

4.9.1 Effect of contact time

Fig. 4.39 to 4.47 describe the effects of contact time on the adsorption of COD, BOD, chloride, sulphate, nitrate, zinc, cadmium, lead and chromium onto kaolin, clay/TiO_2, kaolin/ZnO, and different ratios of TiO_2 and ZnO embedded in kaolin (KTZ11, KTZ21 and KTZ12) nanocomposites. The effects of contact time on the adsorption of the toxic

pollutants in wastewater onto the adsorbents is important in order to achieve equilibrium adsorption. The rates of adsorption were faster initially but became slow on reaching the equilibrium. Different equilibrium times were observed for all the parameters on the adsorbents. The equilibrium percentage adsorption of Zn, Cd, Pb, Cr, nitrate, sulphate, chloride, BOD and COD onto the nanoadsorbents at various contact times were as recorded in Appendix A (Table 1 to 9). The rates of adsorption which were faster at the initial time but became slow on reaching the equilibrium could be as a result of the availability of vacant sites for adsorption at the first stage which decreased with the course of adsorption. The phenomenon of adsorption process in the reduction of pollutants in the wastewater by these mesoporous nanoadsorbents involved film diffusion, pore diffusion and the mass transport of wastewater to the active sites of the adsorbents.

From the recorded values in Table 1 to 9 (Appendix A) for pollutants removal, it was observed that rapid adsorption rates were obtained, with different optimum times for different adsorbents usage. This could be attributed to the availability of the active/binding sites on the adsorbents. These indicate that differences in removal efficiencies using different nanoadsorbents could be as a result of differences in their porosity and specific surface areas.

From Figure 4.39 to 4.47, it was found that on reaching the optimum time/equilibrium, the rate of adsorption equals the rate of desorption. At these points, slow uptake of pollutants was observed and at these stages, it might be as a result of attachment-controlled process caused by less available active sites for adsorption, while the slight decrease in percentage removal with further increase in contact time may be due to the saturation of the surface of the adsorbent with pollutants. Afterwards, there is almost no further increase in the adsorption, therefore, leading to desorption. At this stage, the adsorption diminished which was likely due to less available adsorption sites. In addition, the desorption occurred due to

slow pore diffusion of the pollutants into the adsorbents and longer diffusion in the inner cavities in exiguous adsorbate (Zou *et al.*, 2019).

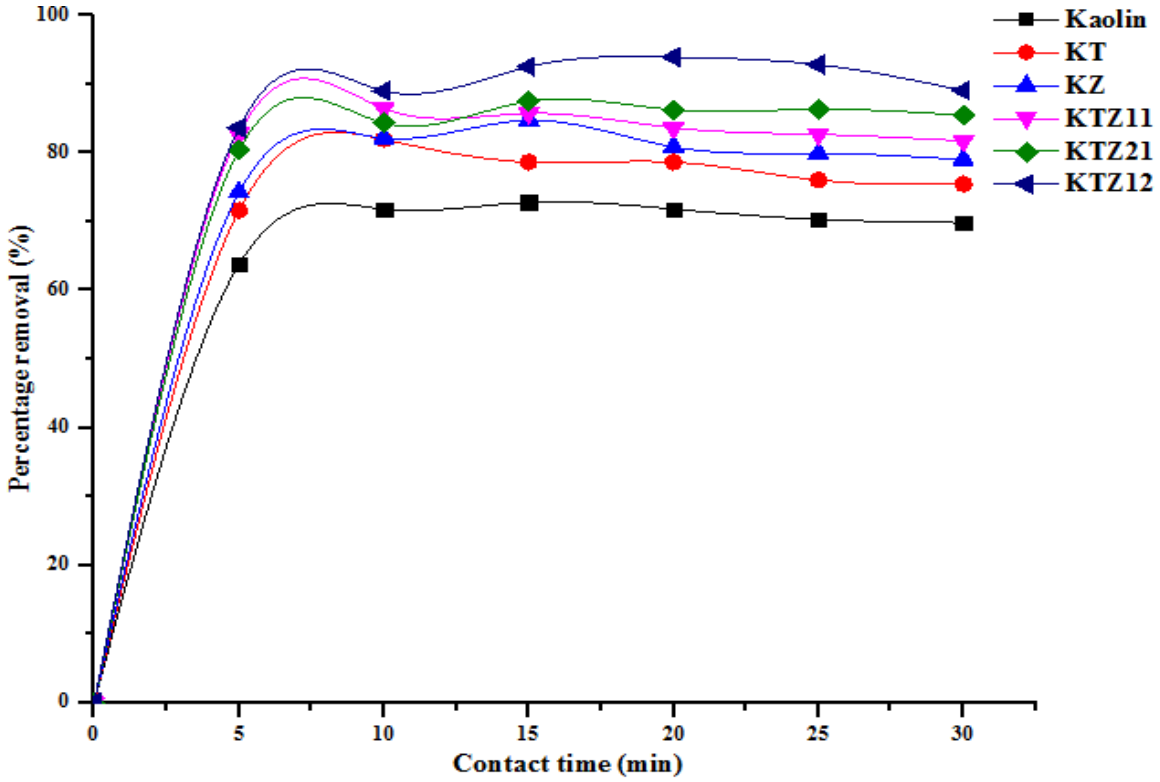

Figure 4.39: Effect of Contact Time on the Removal of COD, dosage 0.2 g, pH 5.84 and Temperature 26±2 ºC

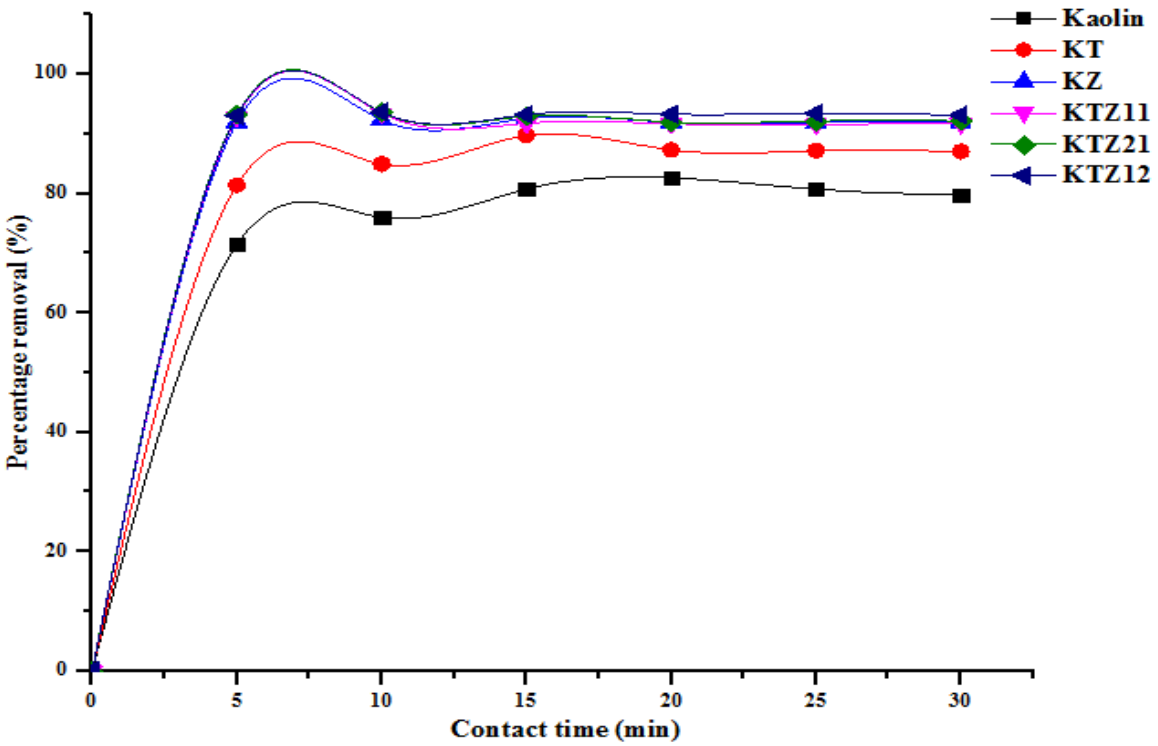

Figure 4.40: Effect of Contact Time on the Removal of BOD, Dosage 0.2 g, pH 5.84 and Temperature 26±2 °C

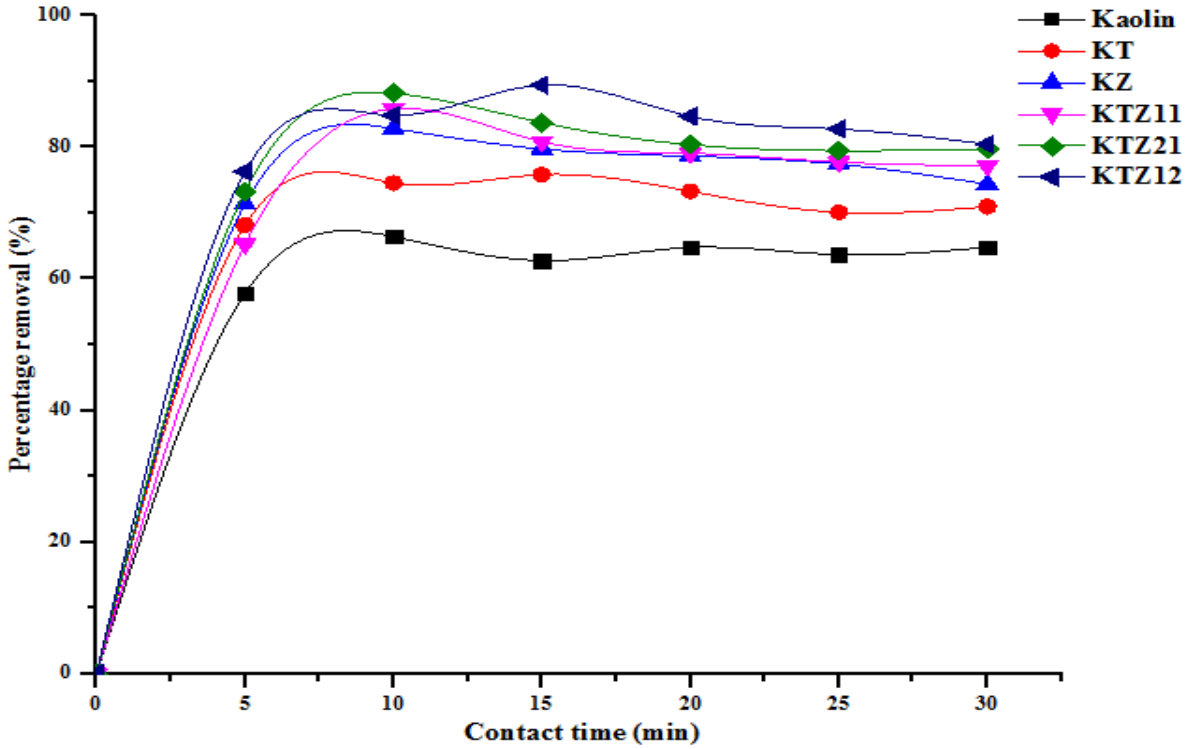

Figure 4.41: Effect of Contact Time on the Removal of Chloride, Dosage 0.2 g, pH 5.84 and Temperature 26±2 °C

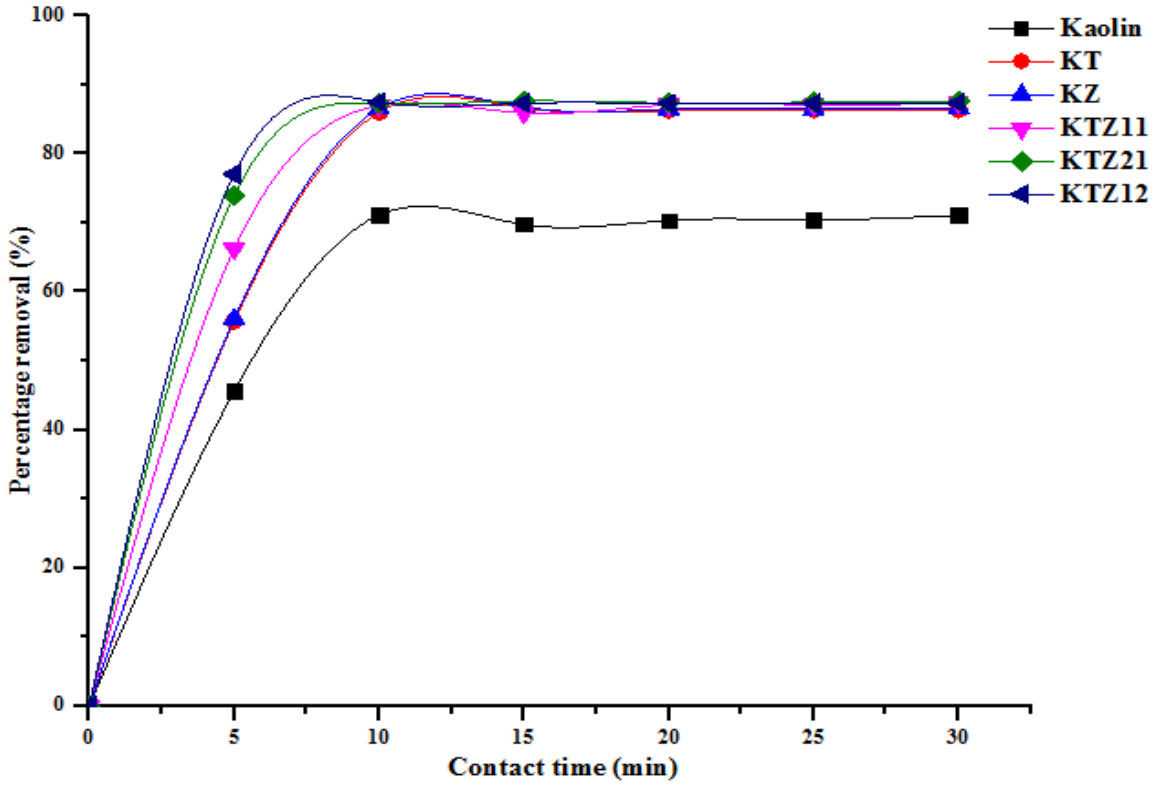

Figure 4.42: Effect of Contact Time on the Removal of Sulphate, Dosage 0.2 g, pH 5.84 and Temperature 26±2 °C

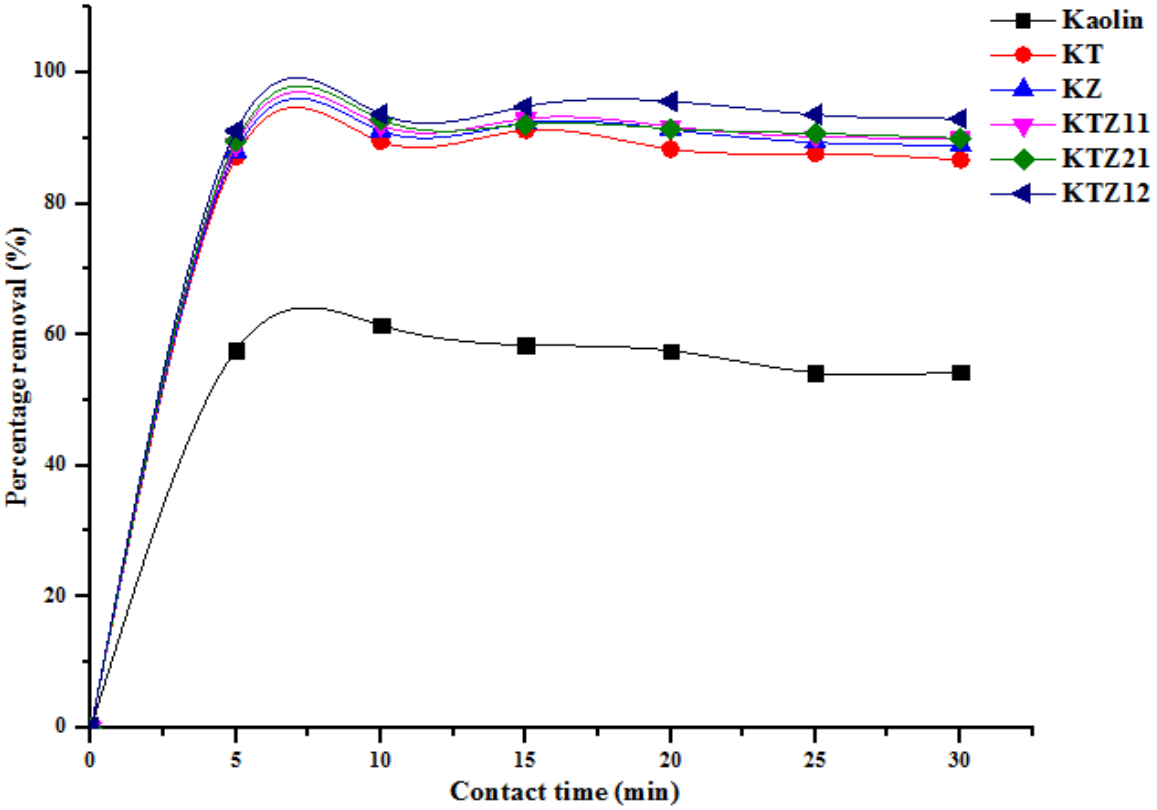

Figure 4.43: Effect of Contact Time on the Removal of Nitrate, Dosage 0.2 g, pH 5.84 and Temperature 26±2 °C

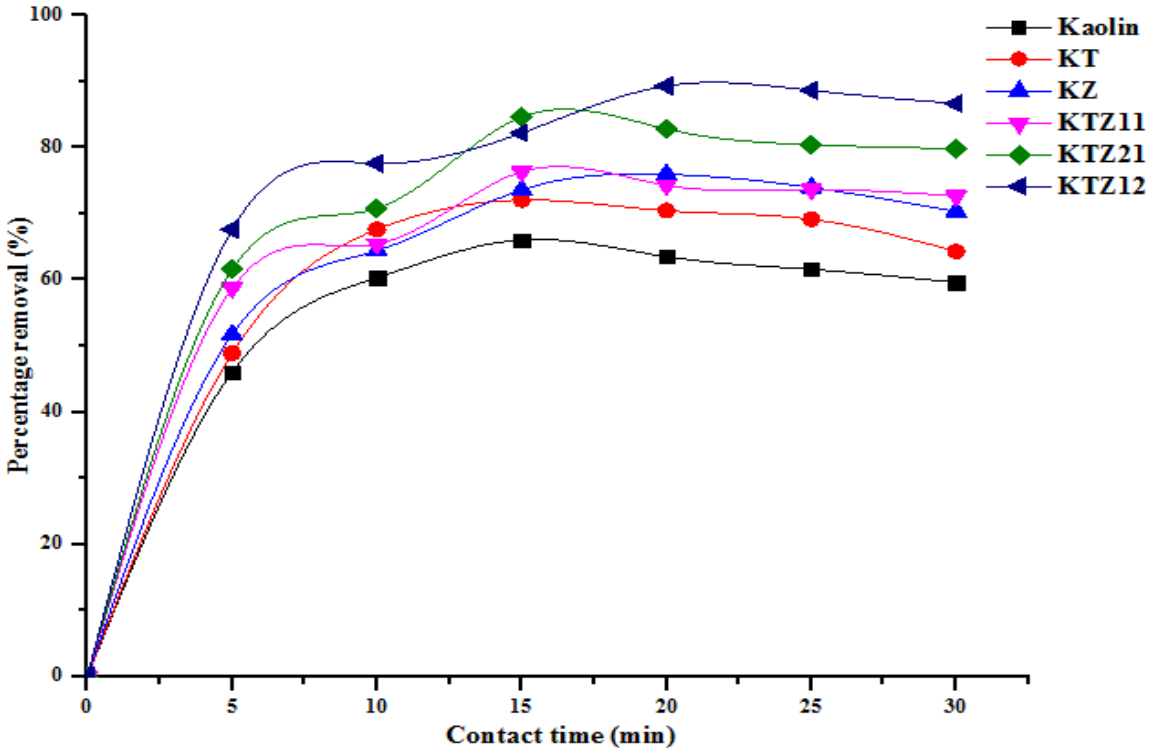

Figure 4.44: Effect of Contact Time on the Removal of Zinc, Dosage 0.2 g, pH 5.84 and Temperature 26±2 °C

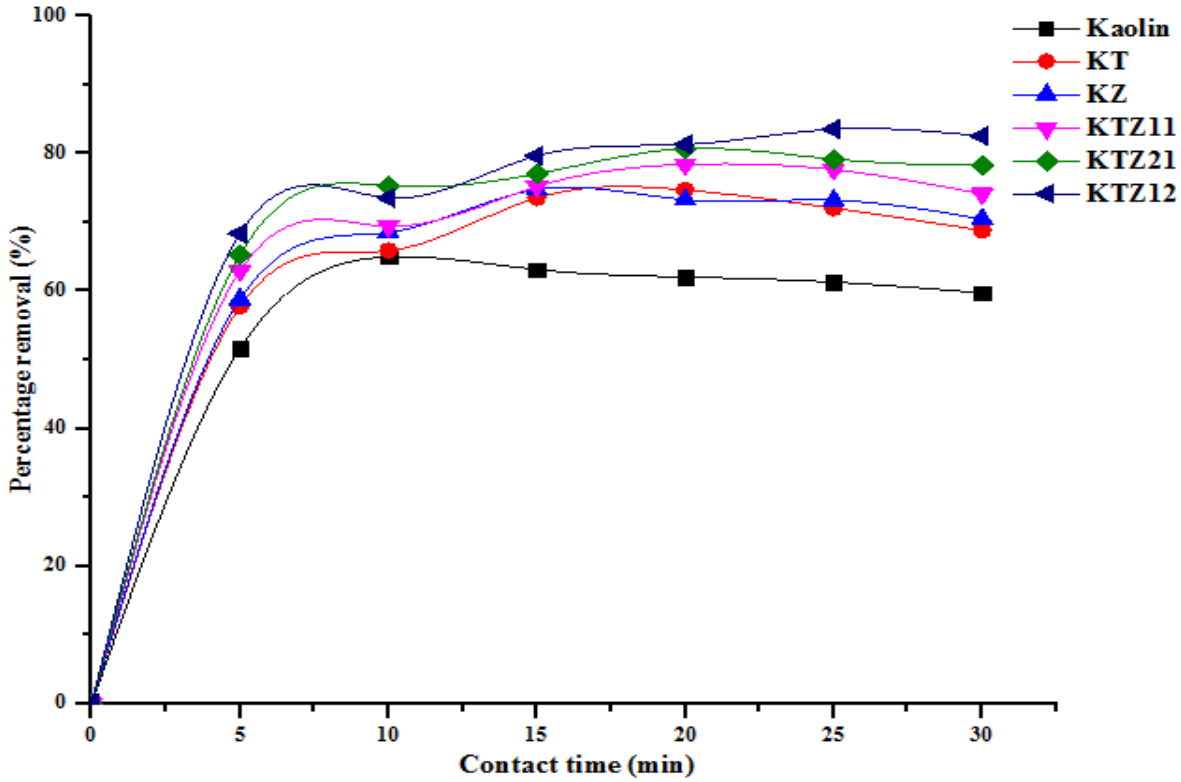

Figure 4.45: Effect of Contact Time on the Removal of Lead, Dosage 0.2 g, pH 5.84 and Temperature 26±2 °C

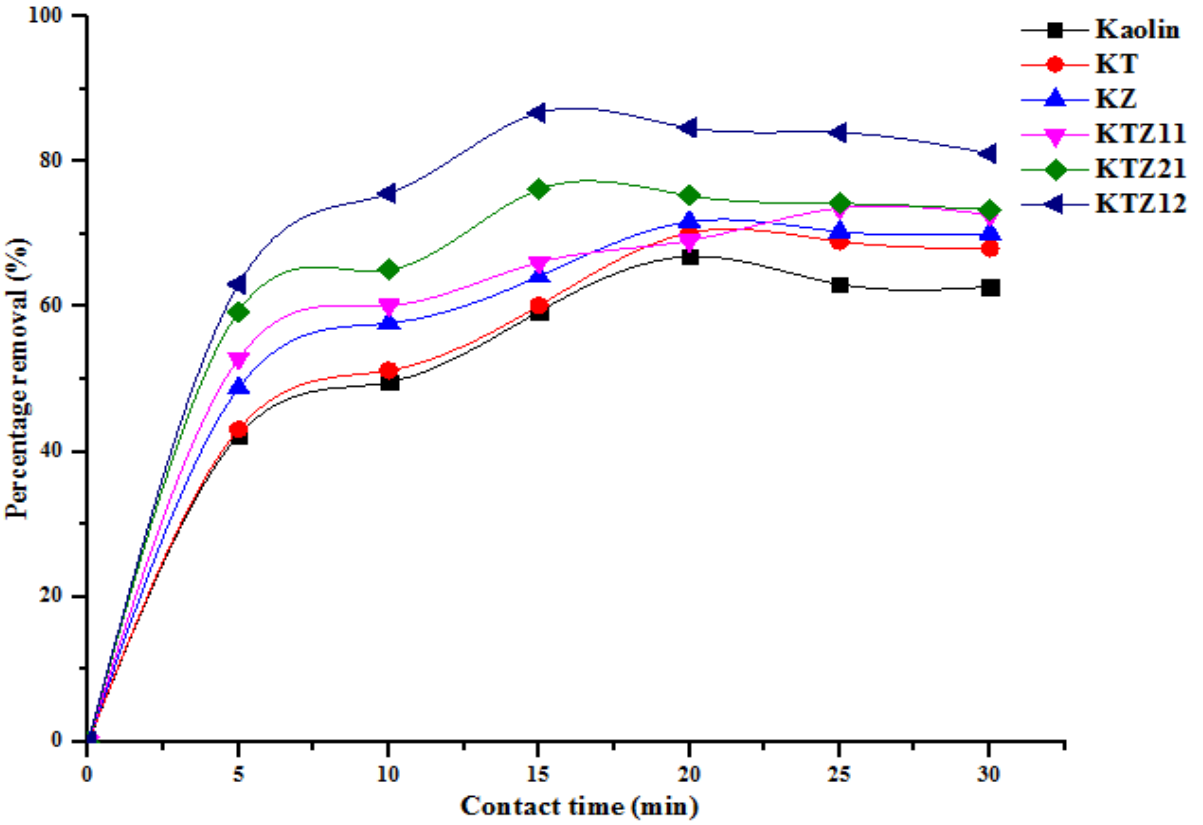

Figure 4.46: Effect of Contact Time on the Removal of Cadmium, Dosage 0.2 g, pH 5.84 and Temperature 26±2 °C

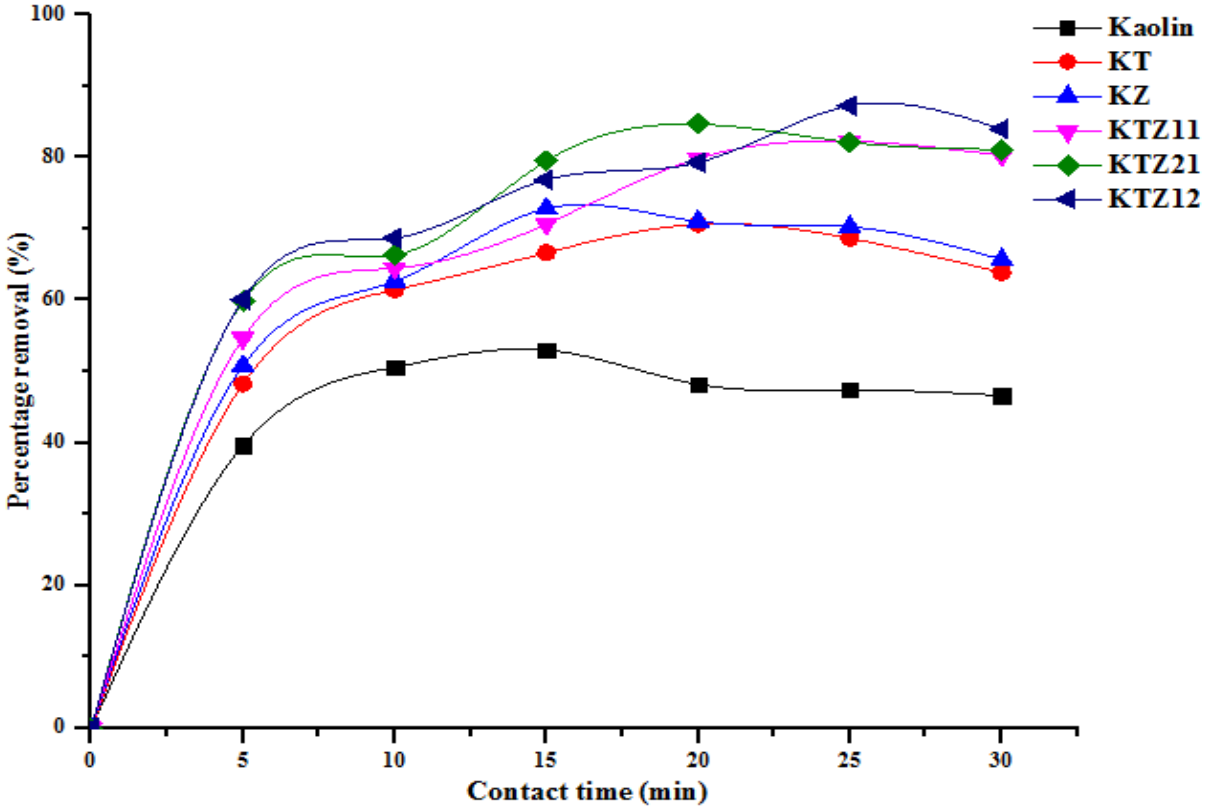

Figure 4.47: Effect of Contact Time on the Removal of Chromium, Dosage 0.2 g, pH 5.84 and Temperature 26±2 °C

4.9.2 Effect of dosage

The adsorbent dosage is a paramount parameter responsible for the adsorption of pollutants by the adsorbent. The effects of adsorbent dose on the percentage removal of chloride, COD, BOD, sulphate, nitrate, cadmium, lead, chromium and zinc from wastewater are presented in Figures 4.48 to 4.56. The removal efficiencies of these pollutants from wastewater onto the nanoadsorbents are presented in Appendix A (Table 10 to 18). It was observed that all the parameters followed similar trends. At a lower dosage, the rate of adsorption was influenced by inter ionic competition among the metal ions which is due to the presence of small surface area. At higher dosage, the adsorption process increased. This is as a result of an increase in the available active binding sites and large surface areas of the adsorbents. Thus, this affected the removal efficiency of the pollutants from the solution by the adsorbents. This could also be inferred to be due to the availability of vast exchangeable sites for adsorption.

The trend, in terms of heavy metals removal by the two materials was Cr > Cd > Pb > Zn. This behavioural pattern can be linked to the differences in the atomic weights and ionic radii of the concerned metal ions. At higher dosages, the adsorption increased due to the availability of more active binding exchangeable sites for adsorption of the target pollutants (Abukhadra and Mohamed, 2019). Thus, for every dose of nanomaterial used for the pollutant removal, it was found that kaolin/TiO_2/ZnO (1:2) performed best probably due to its high surface area and functional groups. Thus, the pollutants removal efficiency in the tannery wastewater strongly depends on the dosage of the nanoadsorbents.

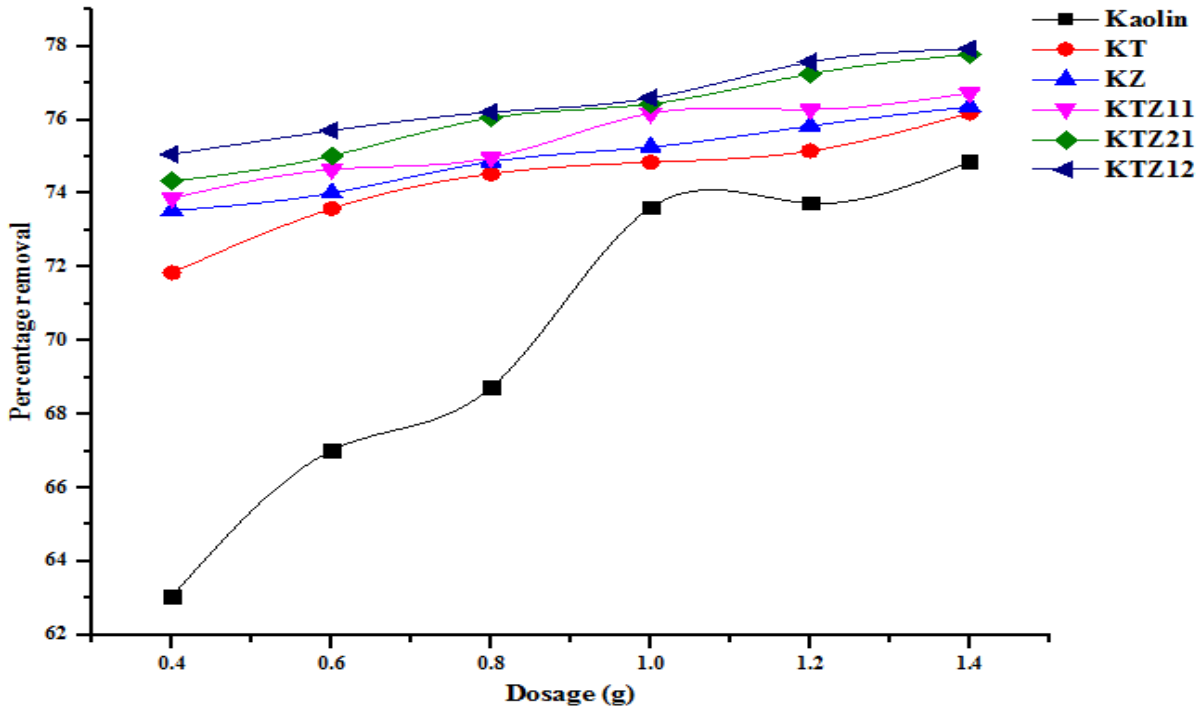

Figure 4.48: Effect of Dosage on the Removal of Chloride at pH 5.84 and Temperature 26±2 °C

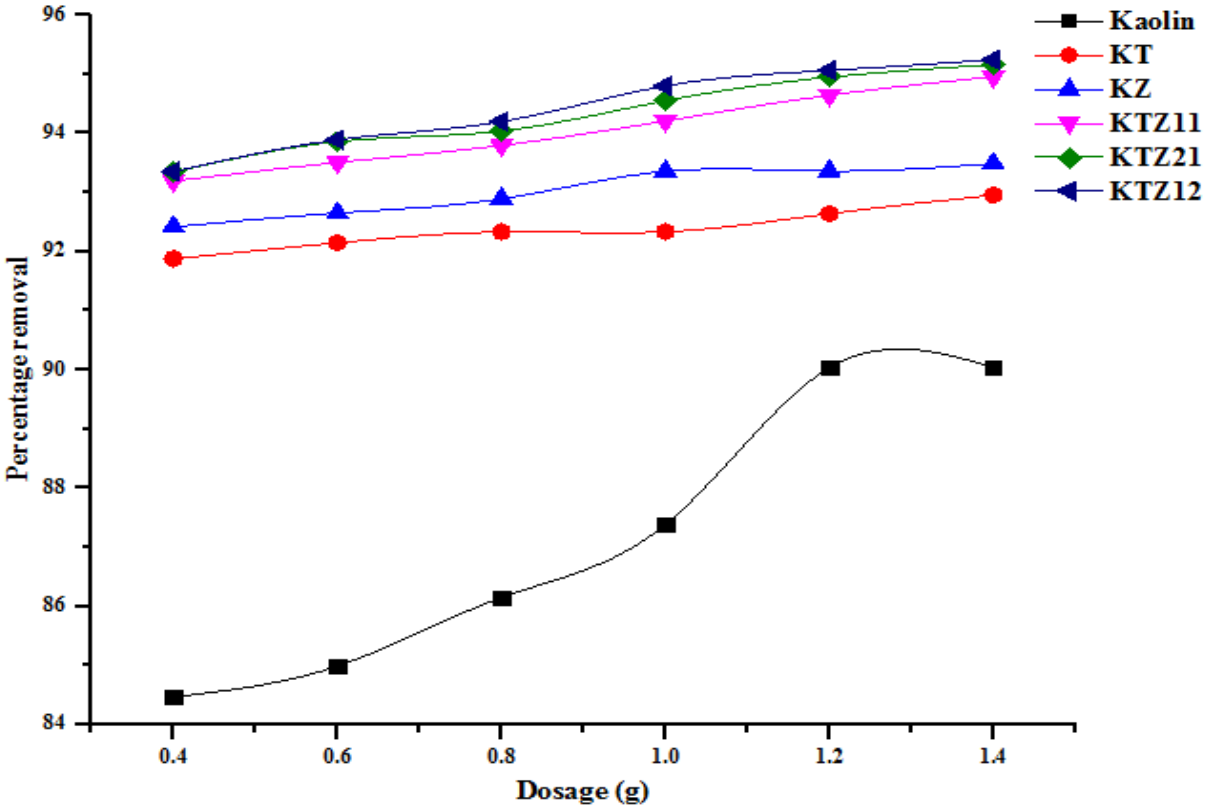

Figure 4.49: Effect of Dosage on the Removal of COD at pH 5.84 and Temperature 26±2 °C

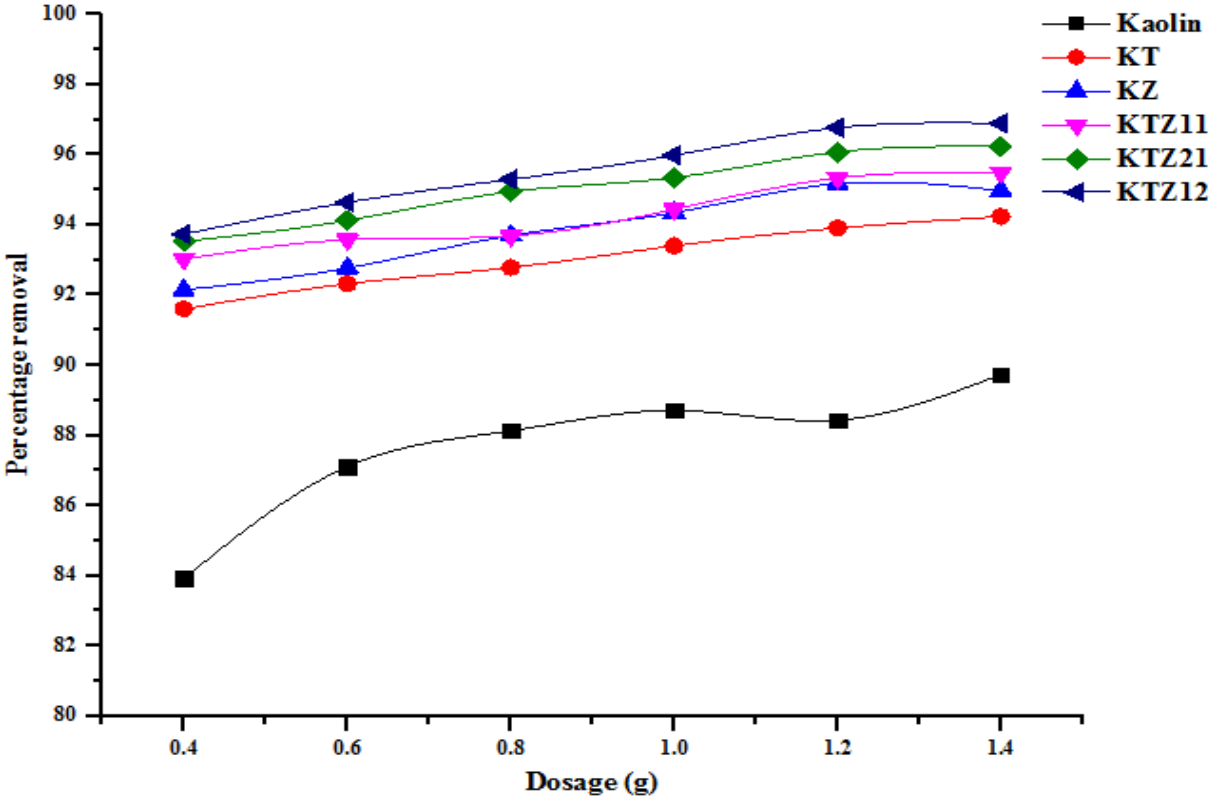

Figure 4.50: Effect of Dosage on the Removal of BOD at pH 5.84 and Temperature 26±2 °C.

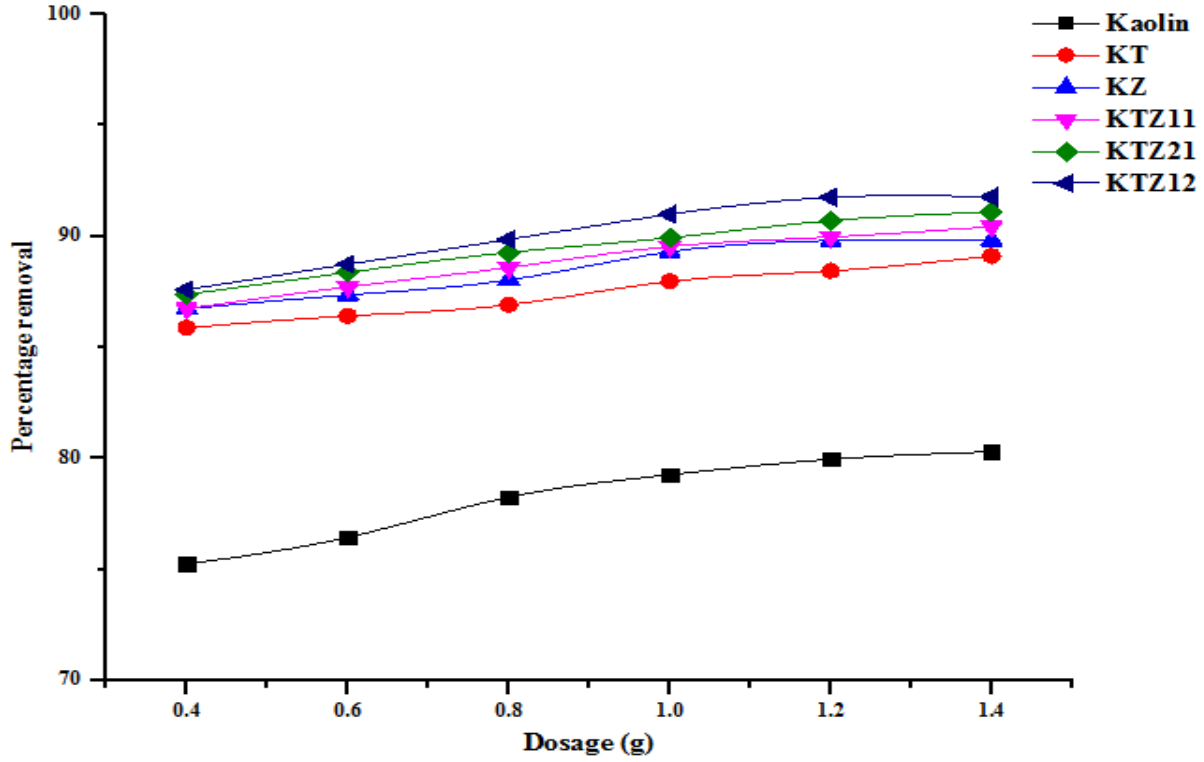

Figure 4.51: Effect of Dosage on the Removal of Sulphate at pH 5.84 and Temperature 26±2 °C

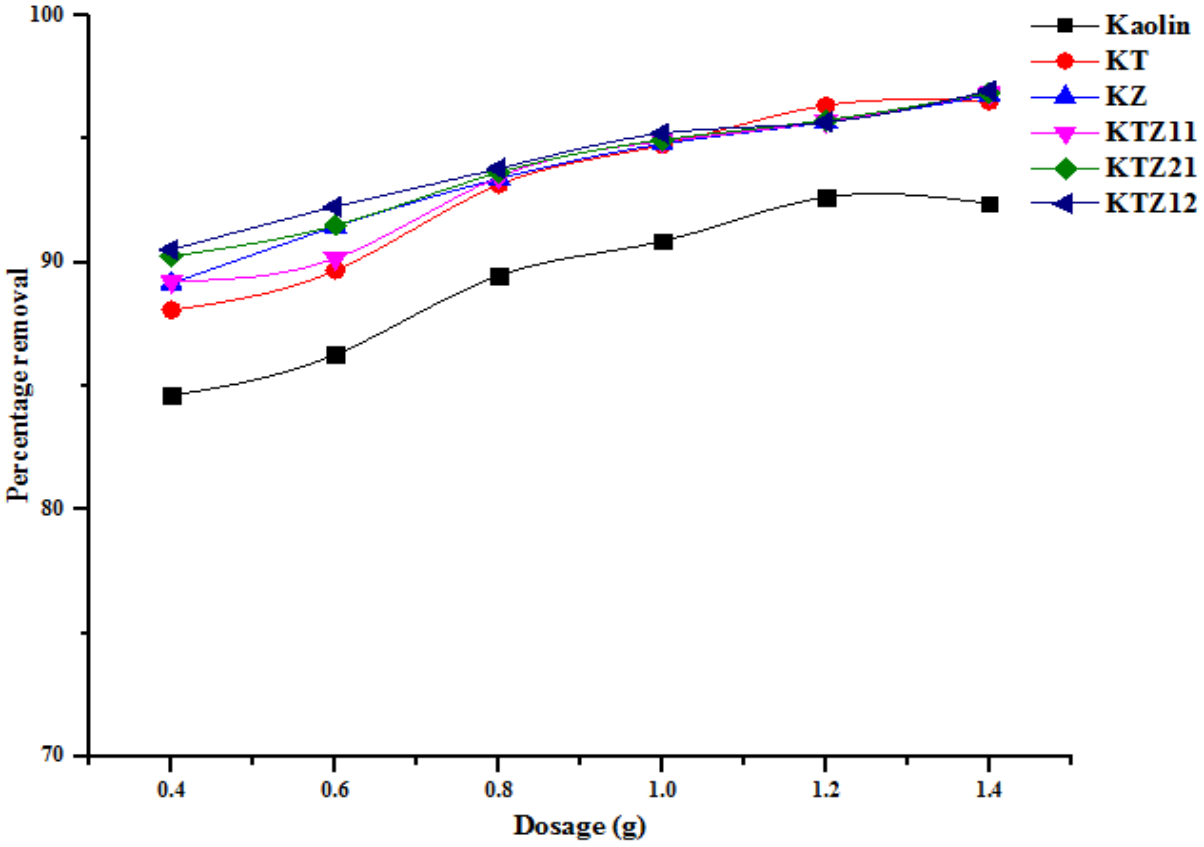

Figure 4.52: Effect of Dosage on the Removal of Nitrate at pH 5.84 and Temperature 26±2 °C

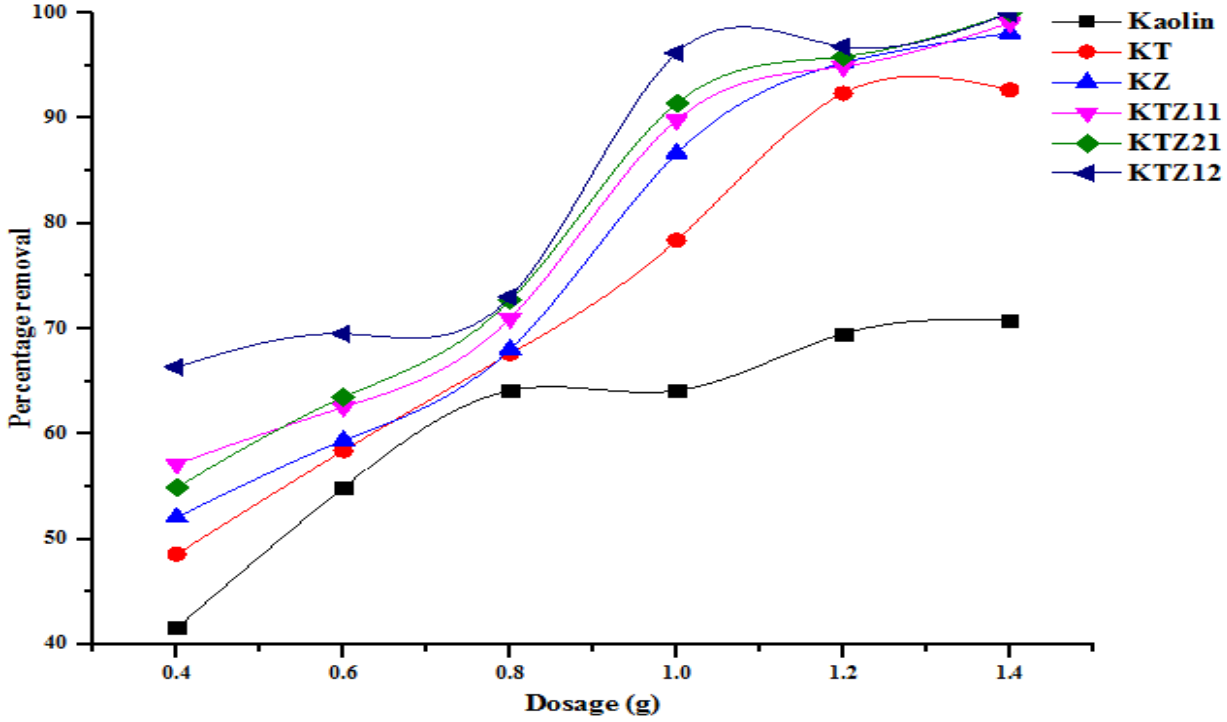

Figure 4.53: Effect of Dosage on the Removal of Cadmium at pH 5.84 and Temperature 26±2 °C

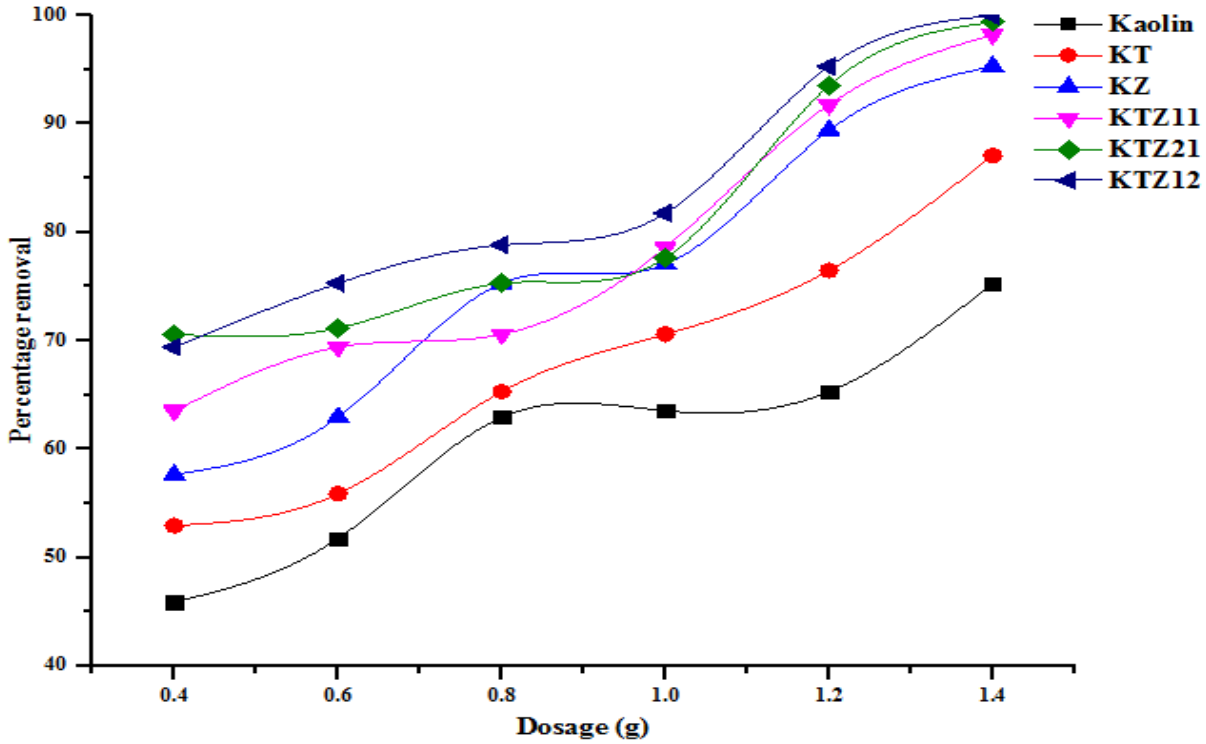

Figure 4.54: Effect of Dosage on the Removal of Lead at pH 5.84 and Temperature 26±2 ºC

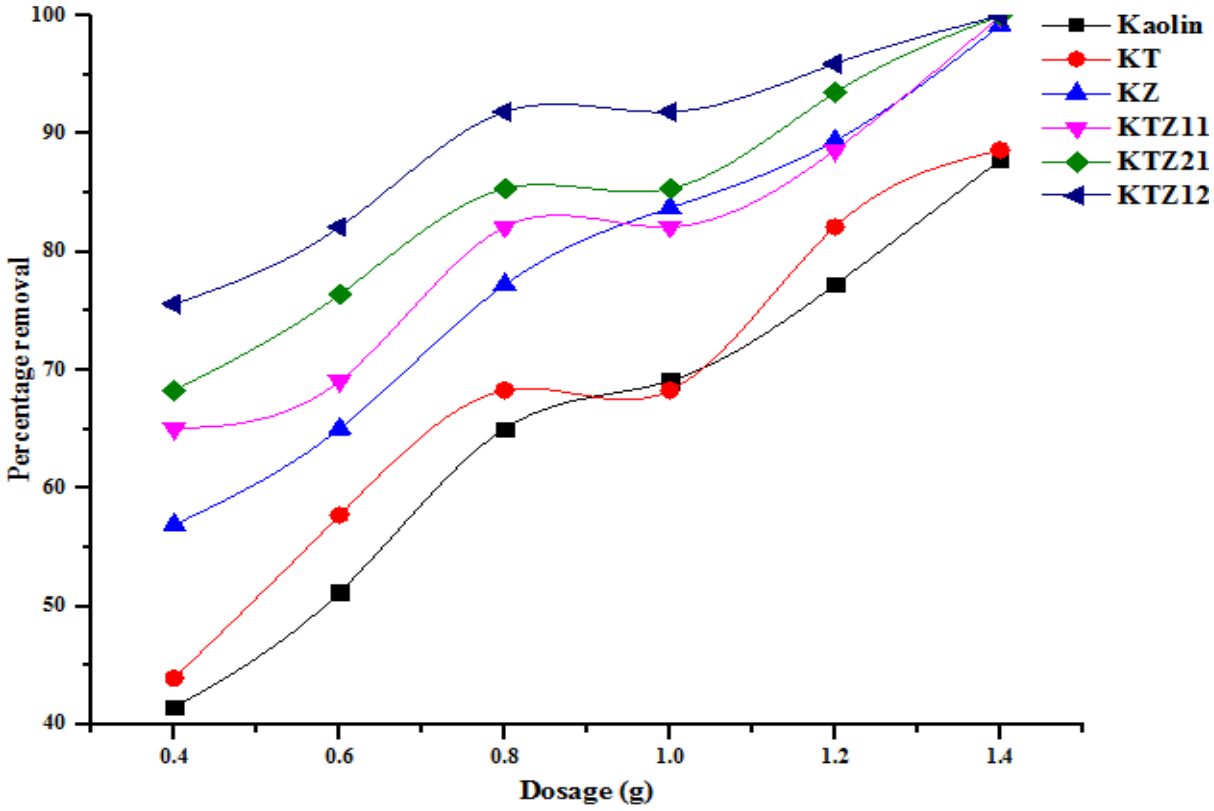

Figure 4.55: Effect of Dosage on the Removal of Chromium at pH 5.84 and Temperature 26±2 ºC

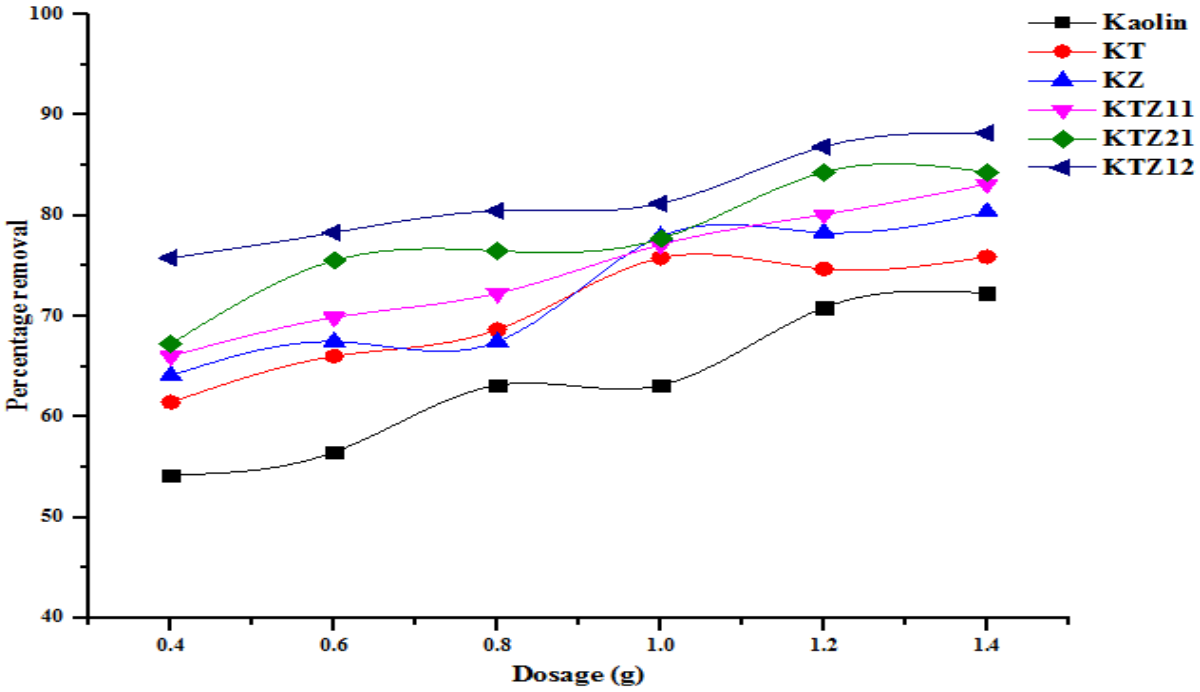

Figure 4.56: Effect of Dosage on the Removal of Zinc at pH 5.84 and Temperature 26±2 °C

4.9.3 Effect of temperature

The effects of temperature on the adsorption isotherms were investigated in the temperature range of 30 to 80 °C. Temperature is a highly important parameter in adsorption processes, influenced by the diffusion rates of adsorbate molecules and internal pores of the adsorbents. Increasing the temperature in an adsorption system brings about an increase in chemical reaction rate (Mekatel *et al.,* 2015). The influence of temperature on the removal of chloride, COD, BOD, sulphate, nitrate, zinc, lead, cadmium and chromium onto the nanoadsorbents are shown in Figures 4.57 to 4.65. While Table 19 to 26 (Appendix A) show the adsorption of the pollutants onto the nanoadsorbents at their various contact times. As can be seen from the figures, the increase in temperature (30-80 °C) corresponds to the increase in the removal efficiencies of the target pollutants. The increase in adsorption may be due to the kinetic energy acquired by the adsorption system at higher temperatures. This leads to an increase in the adsorption rates rather than desorption. Furthermore, at higher temperatures, the interaction between the pollutants and the active sites of the adsorbents

became stronger due to the increase in the dissolution or solubility of the pollutants in the solution with temperature.

The results of this study suggest that the adsorption of these pollutants was favoured at high temperatures. This could be as a result of the fact that interaction among the functional groups present in the nanoadsorbents with the adsorbate led to the formation of strong bonds with an increase in temperature (Taghlidabad *et al.*, 2020). Thus, the rate of adsorption increased with temperature and endothermic in nature.

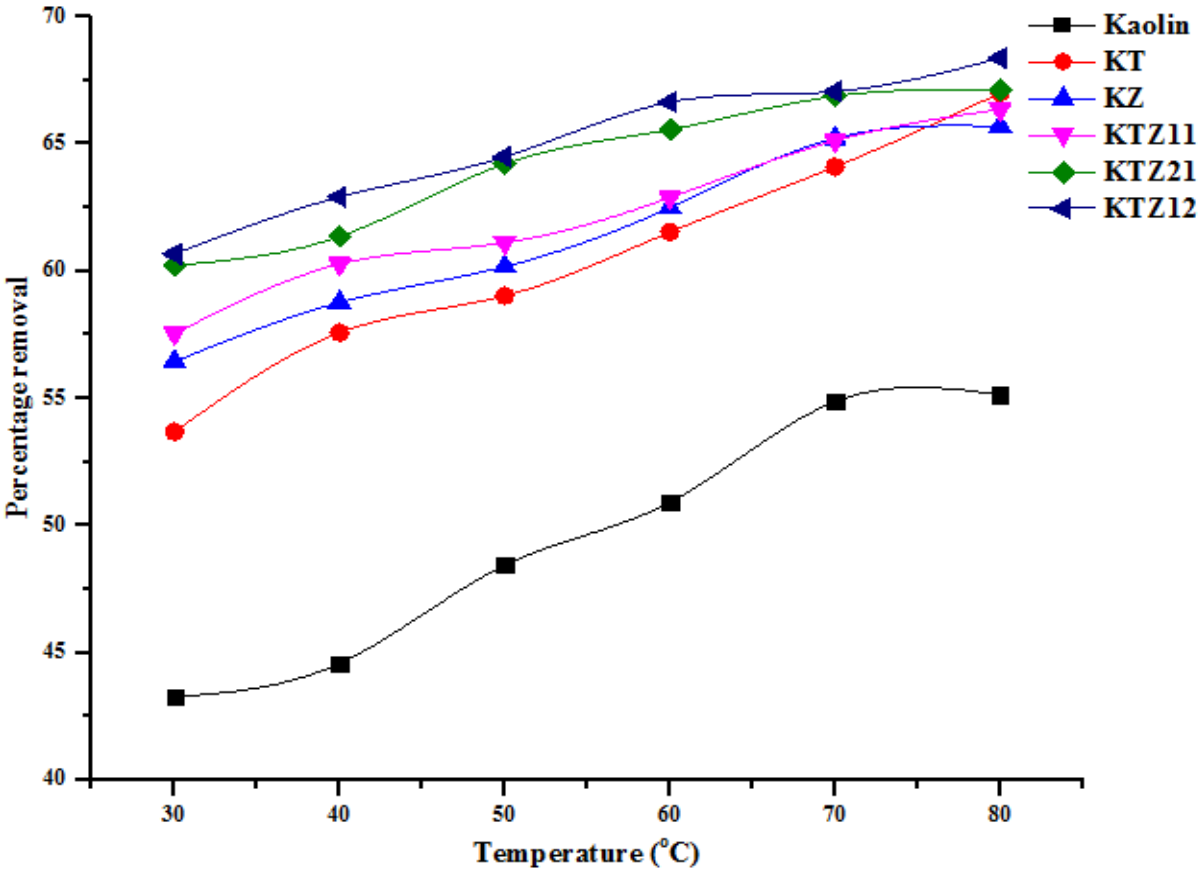

Figure 4.57: Effect of Temperature on the Removal of Chloride at Dosage 0.2 g and pH 5.84.

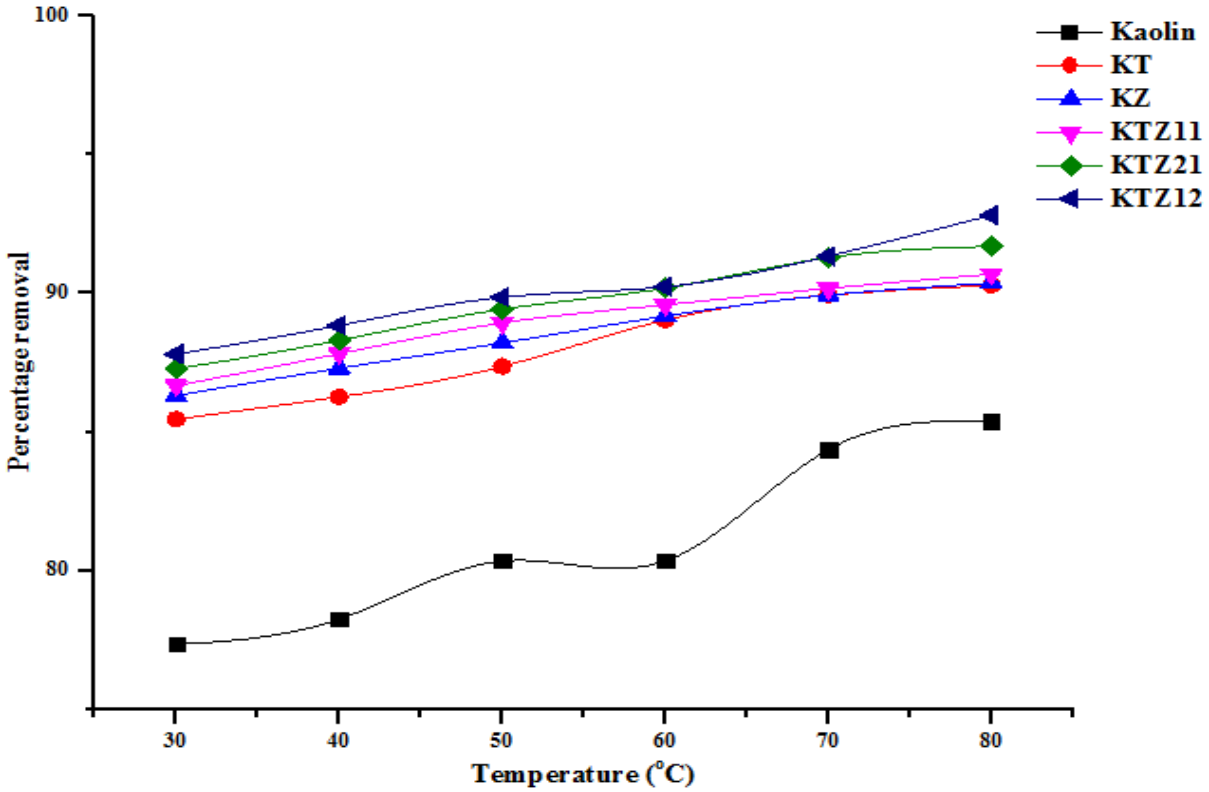

Figure 4.58: Effect of Temperature on the Removal of COD at Dosage 0.2 g and pH 5.84.

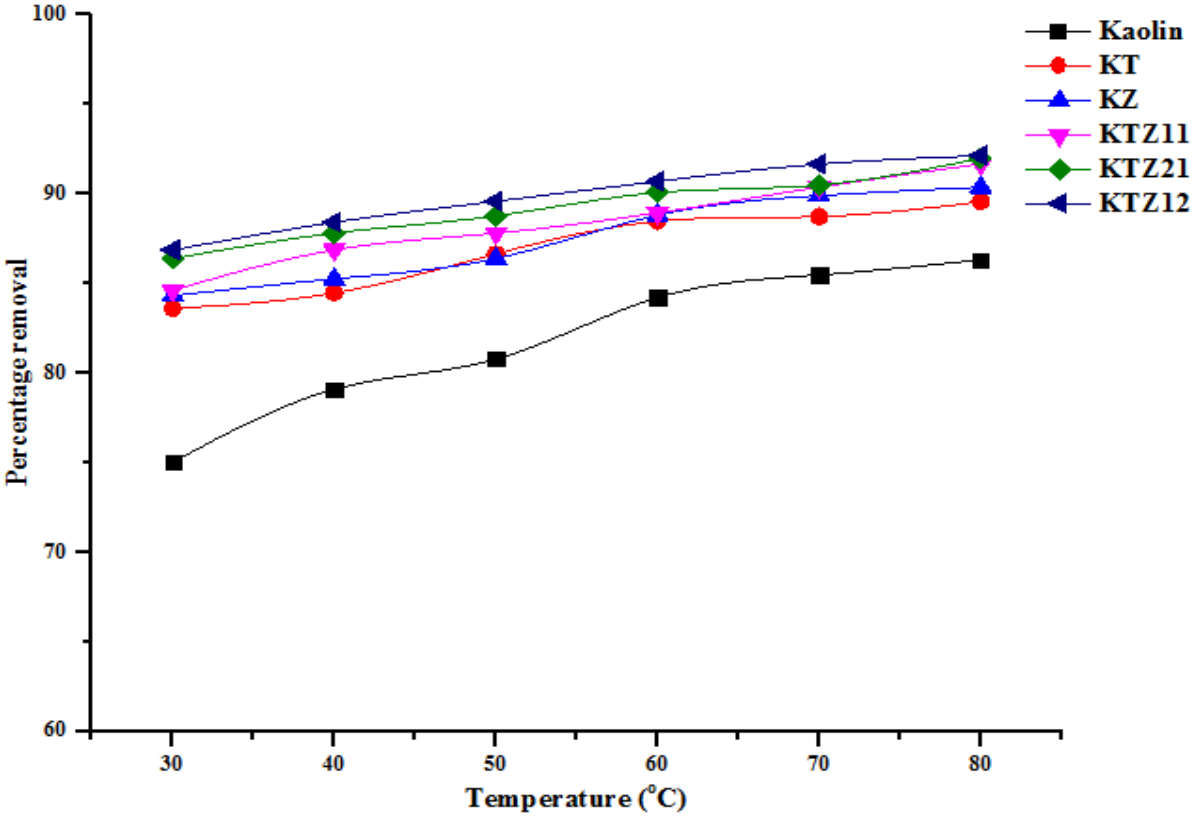

Figure 4.59: Effect of Temperature on the Removal of BOD at Dosage 0.2 g and pH 5.84.

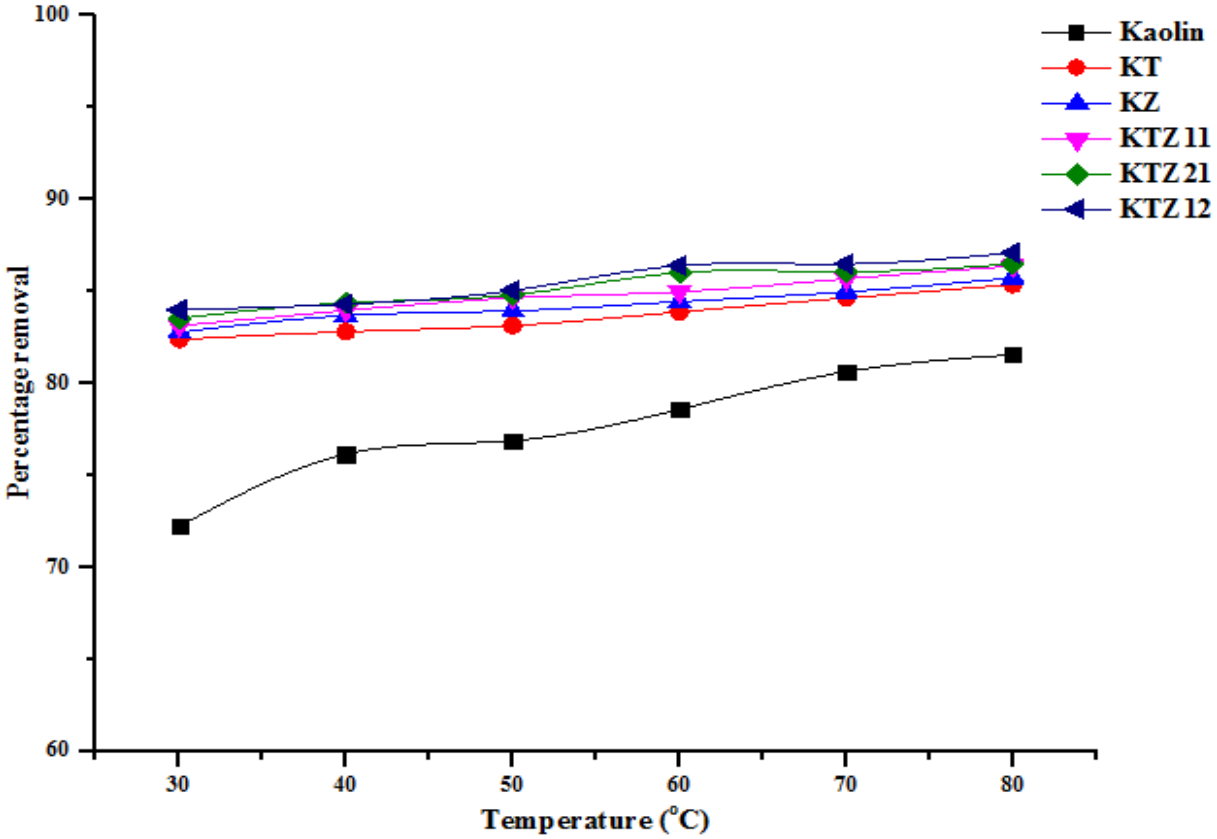

Figure 4.60: Effect of Temperature on the Removal of Sulphate at Dosage 0.2 g and pH 5.84.

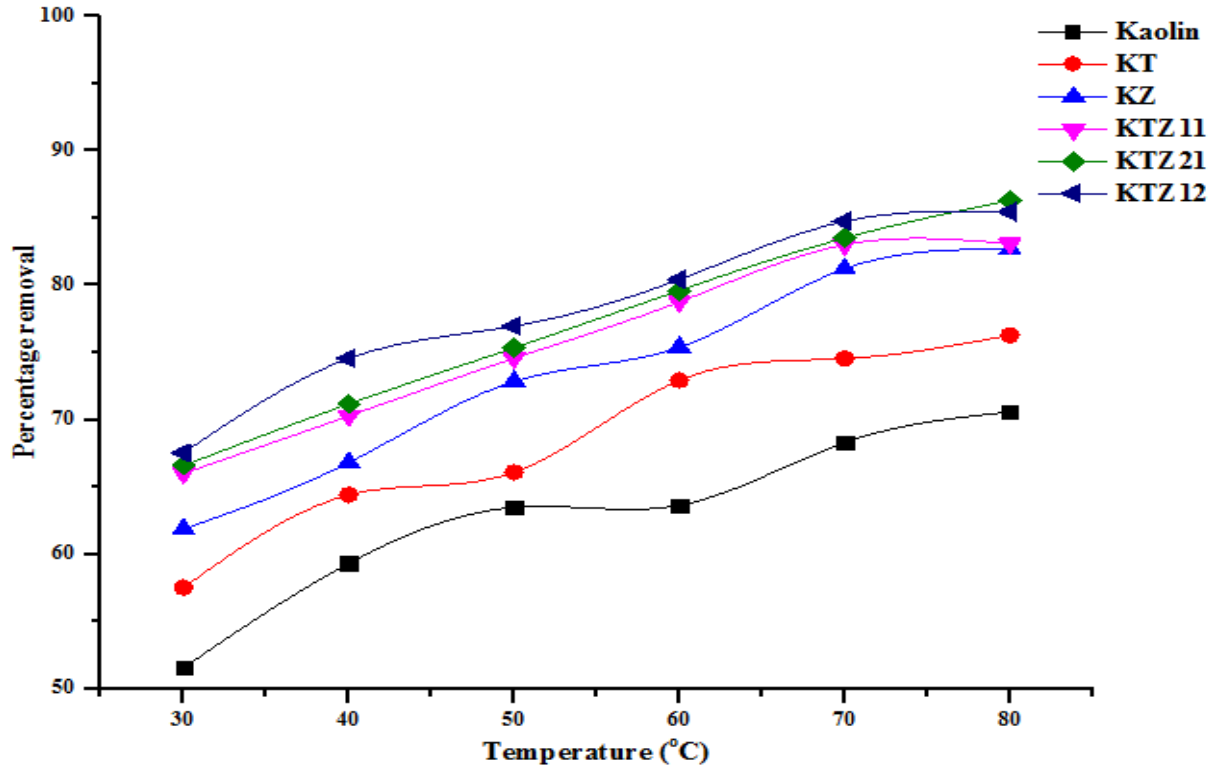

Figure 4.61: Effect of Temperature on the Removal of Nitrate at Dosage 0.2 g and pH 5.84

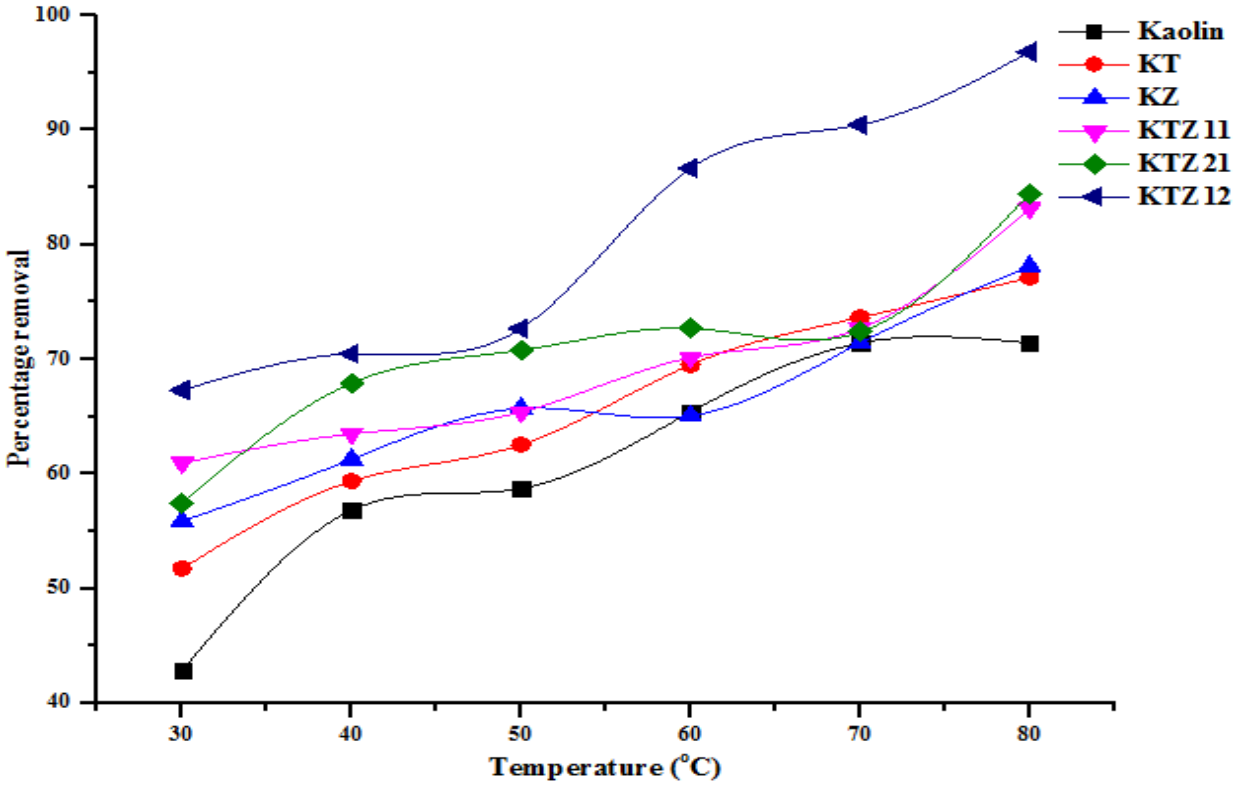

Figure 4.62: Effect of Temperature on the Removal of Zinc at Dosage 0.2 g and pH 5.84.

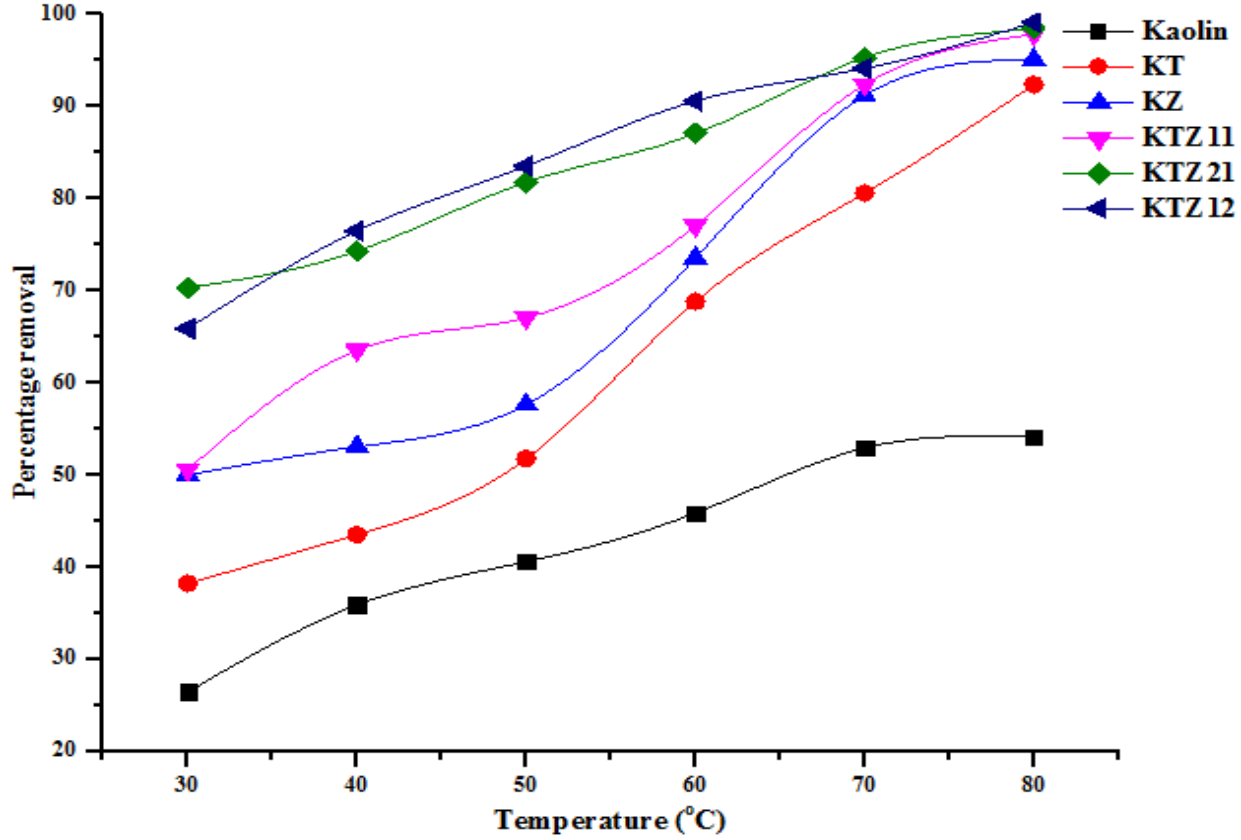

Figure 4.63: Effect of Temperature on the Removal of Lead at Dosage 0.2 g and pH 5.84.

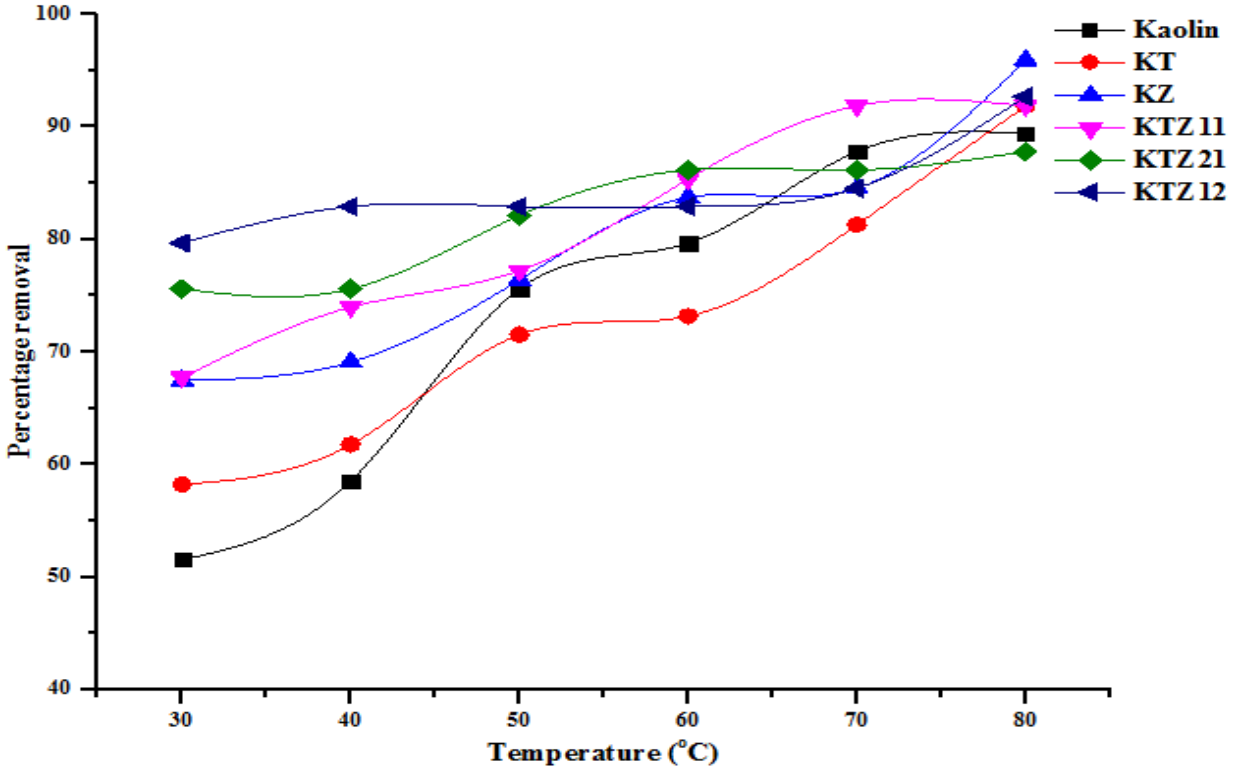

Figure 4.64: Effect of Temperature on the Removal of Cadmium at Dosage 0.2 g and pH 5.84.

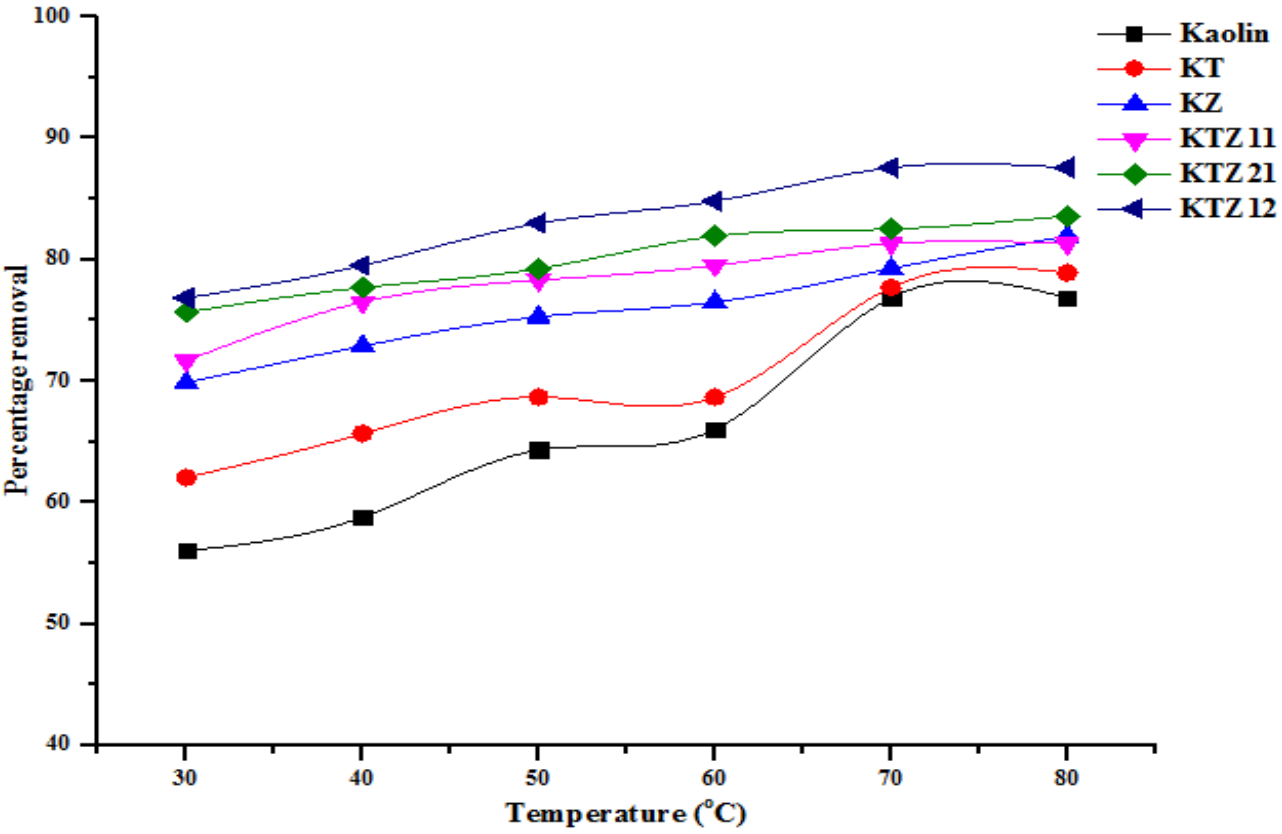

Figure 4.65: Effect of Temperature on the Removal of Chromium at Dosage 0.2 g and pH 5.84.

4.9.4 Effect of contact time on TOC and pH removal

The effects of contact time on the removal of total organic carbon and pH by kaolin, kaolin/TiO_2, kaolin/ZnO and kaolin/TiO_2/ZnO nanocomposites were carried out at contact time (0-30 min). Figure 4.66 and 4.67 display the time-dependence of the degradation of TOC and the increase in pH value from acidic to basic medium. The percentage TOC during the adsorption process was found to be directly proportional to the maximum time rate. It was observed that TOC removal is highest using KTZ12 which could be mainly ascribed to the functional groups and more active sites on the surface of adsorbent as a result of combination of the kaolin and anatase/zincite phases (Hasan *et al.*, 2020).

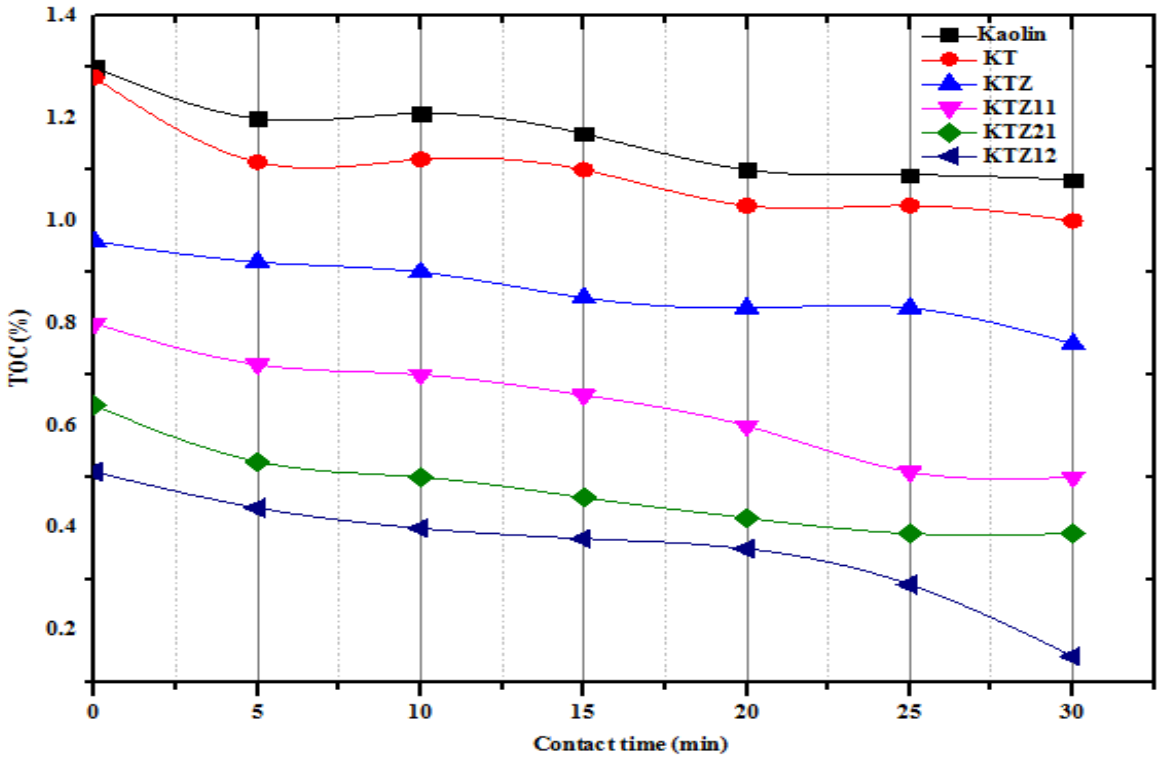

Figure 4.66: Effect of Contact Time on Total Organic Carbon Removal

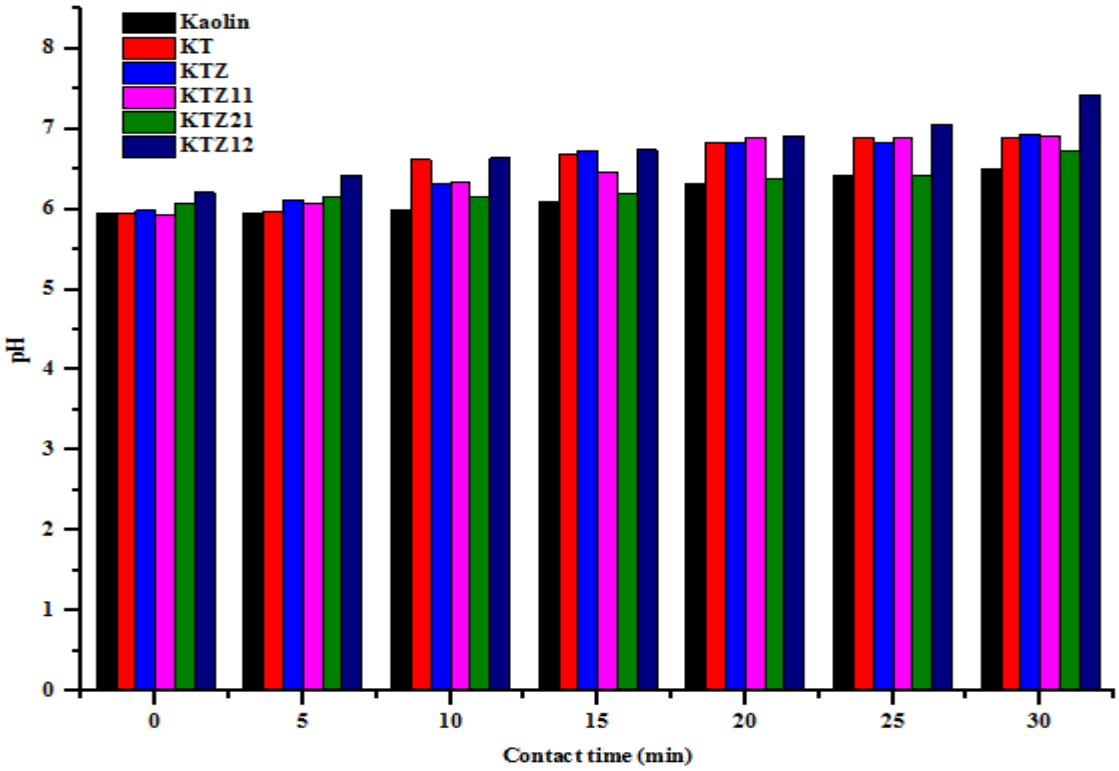

Figure 4.67: Effect of Contact Time on pH of Tannery wastewater

It can be seen that the adsorption rate followed the order: KTZ12 > KTZ21 > KTZ11 > KZ > KT > kaolin as depicted in Figure 4.68. The result shows that KTZ12 exhibited the best adsorption activity for TOC degradation. This suggests that the presence of functional groups in the adsorbent enhanced the interaction of the adsorbent with the pollutants leading to the formation of intermediates during the adsorption process (MiarAlipour *et al.*, 2018).

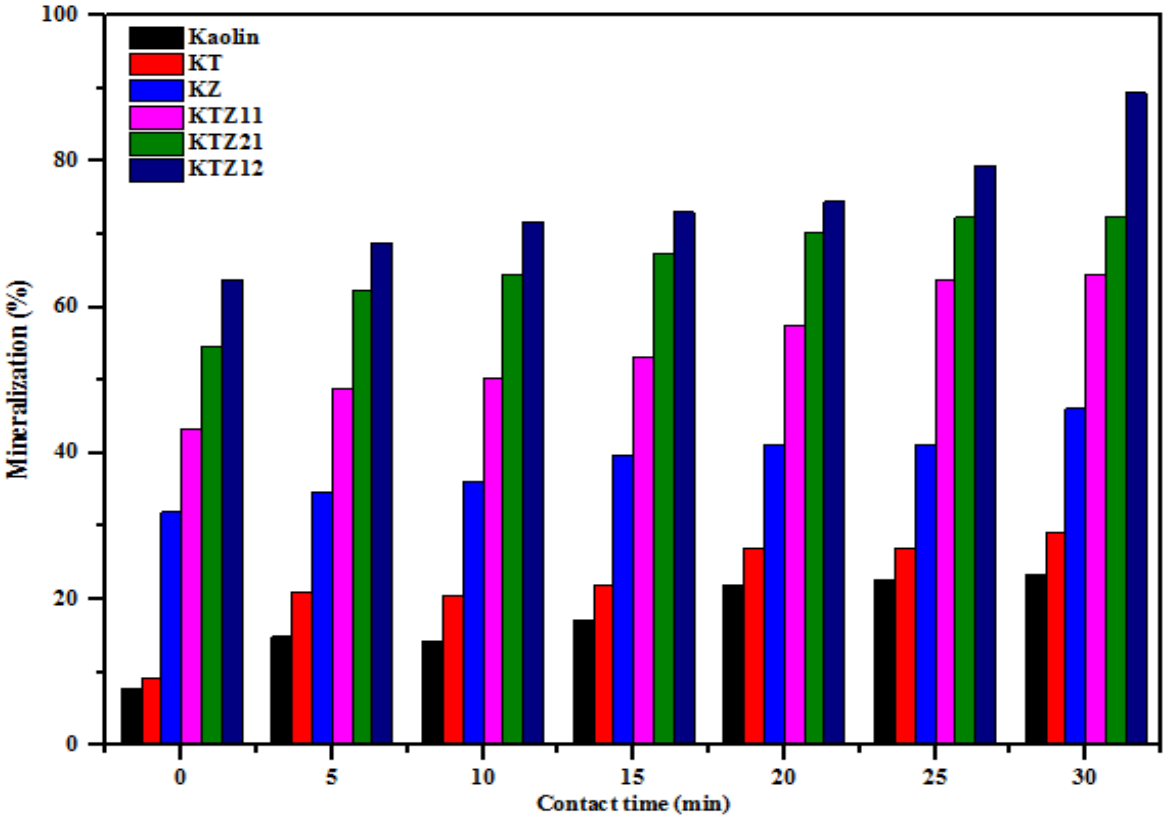

Figure 4.68: Removal of TOC by Kaolin, KT, KZ, KTZ11, KTZ21 and KTZ12 under various Contact Times.

4.10 Adsorption Isotherm Models

Tables 4.7 and 4.8 show Halsey model isotherm for the determination of $\mathbf{n_H}$ and $\mathbf{I_n K_H}$. From the slopes and intercepts of the plots for the removal of the studied pollutants in wastewater (Appendix C), the model showed to the multilayer adsorption patterns and the fitting to the heterosporous nature of kaolin and the nanocomposite materials. It is evident that the linear correlation coefficients ($\mathbf{R^2}$) for kaolin and the nanocomposites in the removal of parameters such chloride, BOD, COD, sulphate, nitrate, Zn, Pb, Cd and Cr were all greater than 0.98. This shows that the experimental data moderately fit Halsey and the adsorption of these pollutants onto the adsorbent materials could partially be based on multilayer adsorption (Ayawei *et al.*, 2017).

The values of Jovanovic constant ($\mathbf{K_j}$) and maximum adsorption capacity ($\mathbf{q_{e(max)}}$) for this adsorption system were evaluated from Appendix D and the experimental information are

provided in Tables 4.7 and 4.8. It is apparent that the correlation coefficient were > 0.99 and this confirms that the experimental data of kaolin and nanocomposites fitted well the Jovanovic's isotherm model. It is also showed that $\mathbf{R^2}$ values of Jovanovic isotherm model are higher than Halsey model which indicates that this model better describes the adsorption of the studied pollutants onto the adsorbents. The adsorption surface considers the system to be homogeneous with monolayer localized adsorption similar to that of Langmuir model due to the existence of some functional groups from kaolin, kaolin/TiO_2, kaolin/ZnO, kaolin/TiO_2/ZnO nanocomposites. It also shows high maximum adsorption capacity of these absorbents for the removal of the pollutants and the possibility of some mechanical contacts between liquid (adsorbate) and solid (adsorbent) phases interface (Talaiekhozani *et al.,* 2019). The comparison of pollutant adsorption capacities using the different adsorbents is presented in Table 4.9. Based on our findings, it was found that the maximum adsorption capacity of nanoadsorbents was higher than many adsorbents presented in Table 4.9.

The Redlich-Peterson model was used to determine the isotherm constants **β** and **A** from slopes and intercepts as plotted in Appendix B. The value of **A** presented in Table 4.7 and 4.8 show that the adsorption capacity of the adsorbents decreased from kaolin to KTZ12 and the values of **β** were slightly above 1 for the pollutant uptake onto the adsorbents. The Redlich-Peterson isotherm is described as three parameter empirical adsorption model to improve both the Langmuir and Freundlich equation (Ayawei *et al.,* 2017). The experimental data for the R-P isotherm followed the adsorption of the studied pollutants from the wastewater with corresponding correlation co-efficient ($\mathbf{R^2}$ > 0.999) as shown in Tables 4.7 and 4.8. The $\mathbf{R^2}$ values show the good fitting of the experimental data to the R-P adsorption model.

The linear form of the Flory-Huggins isotherm model (Appendix E) displays the Flory-Huggins equilibrium constant, $\mathbf{K_{FH}}$ as presented in Tables 4.7 and 4.8. The isotherm model expresses the feasibility and spontaneity of the adsorption process. The evaluated $\mathbf{K_{FH}}$ when used to calculate the spontaneity Gibb's free energy, showed that the $\Delta\mathbf{G}$ is negative. This indicates the influence of temperature during the adsorption system. Thus, adsorptivity of the adsorbents in this study is temperature-dependent. In addition, the obtained correlation coefficient for this isotherm model is related to that of Halsey isotherm. From the isotherms employed in this study, the descending order of the isotherms with respect to their correlation coefficient ($\mathbf{R^2}$) could be arranged in the order: Redlich > Jovanovic > Halsey = Flory-Huggins. This arrangement could therefore help in predicting the experimental behaviour of the adsorbent-adsorbate adsorption system in this study. Furthermore, the highest $\mathbf{R^2}$ values for the R-P isotherms suggest the applicability of the model to the adsorption of the studied pollutants uptake onto kaolin, kaolin/TiO_2, Kaolin/ZnO and kaolin/TiO_2/ZnO nanocomposites.

Tables 4.7 and 4.8 describe the parameters of some isotherm models of chloride, COD, BOD, sulphate, nitrate and some metal ions removal using kaolin, kaolin/TiO_2, kaolin/ZnO and kaolin/TiO_2/ZnO nanoadsorbents at the different optimum time, constant dosage 0.2 g and pH 5.84.

Table 4.7: The Jovanovic, Halsey, Flory-Huggins and Redlich Isotherms of some Physicochemical Parameters Removal in Tannery Wastewater

Parameter	Sample	Jovanovic			Halsey			Flory-H			Redlich-P		
		q_{max}	K_j	R^2	n_H	I_nK_H	R^2	n	K_{FH}	R^2	β	A	R^2
Chloride	Kaolin	1694.21	2.046	0.99871	0.917	14.712	0.99501	-1.023	$3.218x10^{-5}$	0.99501	2.023	$3.449x10^{6}$	0.99871
	KT	1706.16	2.072	0.99843	1.540	18.501	0.99013	-0.649	$4.339x10^{-5}$	0.99013	1.649	$1.647x10^{5}$	0.99843
	KZ	1715.4	2.128	0.99942	1.592	18.861	099629	-0.628	$4.938x10^{-5}$	0.99629	1.628	$1.393x10^{5}$	0.99942
	KTZ11	1733.68	2.155	0.99939	1.644	19.217	0.99589	-0.608	$4.527x10^{-5}$	0.99589	1.608	$1.191x10^{5}$	0.99939
	KTZ21	1745.86	2.191	0.99978	1.761	20.018	0.99832	-0.568	$4,715x10^{-5}$	0.99832	1.568	$3.654x10^{4}$	0.99978
	KTZ12	2085.99	2.683	0.99964	1.826	20.465	0.99717	-0.548	$4.814x10^{-5}$	0.99717	1.557	$8.215x10^{4}$	0.99964
COD	Kaolin	369.814	5.568	0.99979	4.474	31.756	0.99434	-0.224	$2.800x10^{-4}$	0.99434	1.224	$1.210x10^{3}$	0.99981
	KT	370.214	5.618	0.99995	7.386	48.726	0.99627	-0.135	$3.315x10^{-4}$	0.99627	1.135	$7.332x10^{2}$	0.99995
	KZ	380.615	5.672	0.9995	7.689	50.507	0.99625	-0.130	$3.350x10^{-4}$	0.99625	1.130	$7.126x10^{2}$	0.99995
	KTZ11	391.015	5.691	0.99950	7.923	57.883	0.99579	-0.126	$3.384x10^{-4}$	0.99579	1.126	$6.98x10^{2}$	0.99995
	KTZ21	401.016	5.720	0.99994	8.696	56.414	0.99431	-0.115	$3.468x10^{-4}$	0.99431	1.115	$6.570x10^{2}$	0.99994

	KTZ12	416.669	6.175	0.99999	9.598	61.717	0.98895	-0.104	$3.555x10^{-4}$	0.98895	1.104	$6.203x10^{2}$	0.99990
BOD	Kaolin	125.015	1.690	0.99949	4.360	24.885	0.98658	-0.229	$8.793x10^{-4}$	0.98658	1.229	$3.011x10^{2}$	0.99953
	KT	125.839	1.790	0.99992	6.528	34.996	0.99532	-0.153	$1.015x10^{-3}$	1.153	1.153	$2.129x10^{2}$	0.99992
	KZ	125.965	1.810	0.99992	7.176	37.563	0.99509	-0.141	$1.040x10^{-3}$	0.99509	1.141	$2.020x10^{2}$	0.99992
	KTZ11	126.217	1.830	0.99979	7.729	40.628	0.98495	-0.129	$1.067x10^{-3}$	0.98495	1.129	$1.919x10^{2}$	0.99980
	KTZ21	126.469	1.850	0.99988	8.445	44.011	0.98921	-0.118	$1.094x10^{-3}$	0.98921	1.112	$1.833x10^{2}$	0.99988
	KTZ12	127.996	1.980	0.9991	8.778	45.580	0.99175	-0.114	$1.105x10^{-3}$	0.99175	1.114	$1.800x10^{2}$	0.99991
Sulphate	Kaolin	596.453	3.973	0.99951	3.399	27.296	0.99079	-0.294	$1.691x10^{-4}$	0.99079	1.294	$3.074x10^{3}$	0.99952
	KT	597.050	3.995	0.99997	5.216	38.509	0.99888	-0.192	$2.006x10^{-4}$	0.99888	1.192	$1.609x10^{3}$	0.99997
	KZ	597.647	4.008	0.99996	5.374	39.492	0.99829	-0.186	$2.028x10^{-4}$	0.99829	1.186	$1.544x10^{3}$	0.99996
	KTZ11	598.245	4.031	0.99995	5.589	40.823	0.99799	-0.129	$2.055x10^{-4}$	0.99799	1.179	$1.488x10^{3}$	0.99995
	KTZ21	598.484	4.050	0.99997	5.704	41.542	0.99889	0.115	$2.059x10^{-4}$	0.99889	1.175	$1.445x10^{3}$	0.99998
	KTZ12	610.941	4.418	0.99998	5.918	42.813	0.99898	-0.169	$2.694x10^{-4}$	0.99898	1.169	$1.400x10^{3}$	0.99998
Nitrate	Kaolin	64.518	1.104	0.99679	1.598	8.076	0.99824	-0.626	$2.82x10^{-3}$	0.97824	1.626	$1.564x10^{2}$	0.99673
	KT	74.538	1.109	0.99795	2.108	9.458	0.98224	-0.424	3.29710^{-3}	0.98224	1.474	$8.885x10^{1}$	0.99814
	KZ	80.698	1.13	0.99781	1.359	11.356	0.97078	-0.359	3.78510^{-3}	0.97078	1.359	$5.867x10^{1}$	0.99790

	KTZ11	84.978	1.172	0.99871	3.144	12.385	0.97078	-0318	4.02110^{-3}	0.97987	1.318	$5.136x10^{1}$	0.99881
	KTZ21	95.834	1.264	0.99829	3.489	12.368	0.9676	-0.287	4.19810^{-3}	0.9676	1.287	$4.616x10^{1}$	0.99835
	KTZ12	107.322	1.396	0.99826	3.528	13.521	0.96805	-0.283	4.23610^{-3}	0.96805	1.283	$4.560x10^{1}$	0.99841

Table 4.8: The Jovanovic, Halsey, Flory-Huggins and Redlich Isotherms of some Heavy Metals Removal in Tannery Wastewater

Parameter	Sample	Jovanovic			Halsey			Flory-H			Redlich-P		
		q_{max}	K_j	R^2	n_H	I_nK_H	R^2	n	K_{FH}	R^2	β	A	R^2
Zinc	Kaolin	60.39	0.390	0.99169	1.424	2.070	0.95383	-0.702	$9.38x10^{-2}$	0.95383	1.702	4.282	0.99189
	KT	64.666	0.443	0.99569	1.911	2.740	0.96667	-0.523	$1.161x10^{-1}$	0.96667	1.523	4.199	0.99597
	KZ	67.719	0.453	0.99607	2.140	3.086	0.96475	-0.467	$1.245x10^{-1}$	0.96475	1.467	4.223	0.99634
	KTZ11	69.89	0.476	0.9971	2.773	4.003	0.96345	-0.361	$1.411x10^{-1}$	0.96345	1.361	3.899	0.99736
	KTZ21	72.015	0.496	0.99298	2.739	4.009	0.91472	-0.365	$1.404x10^{-1}$	0.91472	1.365	4.235	0.99349
	KTZ12	94.043	0.561	0.99806	6.340	9.492	0.86504	-0.158	$1.879x10^{-1}$	0.86504	1.157	4.469	0.99720
Lead	Kaolin	30.418	0.709	0.99085	0.642	0.170	0.97315	-1.558	$9.865x10^{-2}$	0.97315	2.558	1.303	0.9899
	KT	34.424	0.8	0.98481	2.446	1.059	0.83163	-0.409	$2.147x10^{-1}$	0.83163	1.409	1.542	0.98383
	KZ	35.493	0.847	0.99119	4.072	2.290	0.82487	-0.245	$2.665x10^{-1}$	0.82487	1.245	1.754	0.99214
	KTZ11	37.524	0.861	0.98736	6.482	4.540	0.70119	-0.154	$3.211x10^{-1}$	0.70119	1.154	2.015	0.99302
	KTZ21	39.712	0.955	0.9983	13.761	12.710	0.75543	-0.0727	$4.190x10^{-1}$	0.75543	1.073	2.518	0.99861
	KTZ12	61.341	1.553	0.99503	11.350	9.944	0.69529	-0.0885	$3.971x10^{-1}$	0.69529	1.649	1.175	0.96103
Cadmium	Kaolin	32.248	0.938	0.99671	3.155	-6.694	0.93381	-0.317	$3.709x10^{-1}$	0.93381	1.317	0.120	0.99596
	KT	34.251	1.002	0.98540	3.300	-6.998	0.83106	-0.303	$3.748x10^{-1}$	0.03106	1.303	0.121	0.98953

	KZ	37.251	1.013	0.99631	6.131	-11.612	0.84254	-0.163	4.808×10^{-1}	0.84254	1.163	0.151	0.99647
	KTZ11	38.255	1.094	0.99332	3.979	-8.098	0.87587	-0251	4.100×10^{-1}	0.87587	1.251	0.131	0.99447
	KTZ21	41.257	1.129	0.99969	4.509	-8.773	0.98948	-0.222	4.510×10^{-1}	0.98948	1.222	0.143	0.99965
	KTZ12	46.26	1.166	0.99935	7.201	-13.027	0.97354	-0.139	5.260×10^{-1}	0.97354	1.139	0.164	0.99960
Chromium	Kaolin	106.915	0.146	0.99760	2.129	4.258	0.98028	-0.470	4.689×10^{-2}	0.98028	1.470	17.46	0.99796
	KT	107.061	0.151	0.99861	2.535	7.098	0.98596	-0.395	5.180×10^{-2}	0.98596	1.395	16.450	0.99886
	KZ	107.253	0.157	0.99920	3.234	8.869	0.98602	-0.309	5.856×10^{-2}	0.98602	1.309	15.520	0.99921
	KTZ11	117.288	0.159	0.99953	3.334	9.126	0.99106	-0.300	5.942×10^{-2}	0.99106	1.300	15.450	0.99952
	KTZ21	127.678	0.170	0.99978	3.775	10.776	0.99479	-0.252	6.410×10^{-2}	0.99479	1.252	15.040	0.99979
	KTZ12	138.094	0.180	0.99958	4.888	13.131	0.98611	-0.205	6.912×10^{-2}	0.98611	1.205	14.680	0.99959

Table 4.9: Comparison of Adsorption Capacities of some Adsorbents

Adsorbent	Wastewater	Adsorption capacity (mg/g)	Reference
Kaolin/chitosan/TiO_2	Dye	88.496	Vardikar *et al.* (2018)
Kaolinite	Zinc salt solution	6.35	Chai *et al.* (2017)
Kaolinite	Dye	25.70 to 50.51	Sarma *et al.* (2019)
Kaolinite	Phosphate solution	17.61	Adeyi *et al.* (2019)
Chitosan-coated kaolinite	Arsenic solution	64.85	Futalan *et al.* (2018)
Raw clay	Methylene blue	23.13	Olusegun *e al.* (2018)
Montmorillonite/Graphene oxide	Crystal violet	348.43-74.27	Puri *et al.* (2018)
Clay/Polymer	Reactive Black 5	434.8-833.3	Erdem *et al.* (2016)
Fe_3O_4/Kaolin	Direct Red dye 23	22.88	Magdy *et al.* (2017)
Bentonite/γ-alumina	Magnesium solution	3.478	Pourshadlou *et al.* (2020)
Polyacrylamide/Bentonite	Lead and cadmium solution	84.16-164.87	Ayoub-khan *et al.* (2019)
Kaolin/TiO_2/ZnO	Chromium	138.09	This study
Kaolin/TiO_2/ZnO	Cadmium	46.26	This study
Kaolin/TiO_2/ZnO	Lead	61.34	This study
Kaolin/TiO_2/ZnO	Zinc	94.04	This study

4.11 Kinetic Models

In attempting to account for the adsorption kinetics of the studied pollutants using kaolin, kaolin/TiO_2, kaolin/ZnO and kaolin/TiO_2/ZnO nanocomposites, fractional power, Bangham and Avrami kinetic models were employed as depicted in Tables 4.9 and 4.10. The plots Bangham kinetic model (Appendix G) were used to observe the pore diffusion in the adsorption system and the **α** and Bangham constants are presented in Tables 4.9 and 4.10. The extrapolation of the double logarithm order kinetic model shows that multiple adsorption stages occurred and the correlation coefficients obtained for the model ranged between

0.6421 and 0.99248, showing that pore diffusion was involved in the pollutants removal using kaolin and the nanocomposites. On the other hand, the linearity of the Bangham plots (Appendix G) indicate that the sorbate pore diffusion is not the only rate-controlling step.

The Avrami kinetic parameters kinetic rate constant ($\mathbf{K_{AV}}$), Avrami exponent ($\mathbf{A_{AV}}$) and correlation coefficient ($\mathbf{R^2}$) are presented in Tables 4.9 and 4.10. The $\mathbf{A_{AV}}$ values were positive in all the pollutants uptake onto the adsorbent samples. This indicates that there is a possible change in the adsorption process. There is also an indication that during the contact of the sorbate with the adsorbents the rate of adsorption could allow multiple kinetic orders (Oladoja, 2016). The kinetic data suitably fitted well to the Avrami kinetic model which presented the highest $\mathbf{R^2}$ values for all the studied pollutants using kaolin, kaolin/TiO_2, kaolin/ZnO and kaolin/TiO_2/ZnO nanocomposites when compared to Bangham and fractional power kinetic models.

Tables 4.10 and 4.11 shows the values of kinetic constants and the characteristic parameter of the kinetic models on the chloride, BOD, COD, sulphate, nitrate and some metal ions uptake in tannery effluent onto kaolin, kaolin/TiO_2, kaolin/ZnO and kaolin/TiO_2/ZnO nanoadsorbents.

Table 4.10: Values of the Kinetic Model Parameters for some Physicochemical Properties Adsorption in Tannery Wastewater

Parameter	Sample	Fractional-P				Bangham			Avrami		
		K	V	KV	R^2	α	K_i	R^2	n_{AV}	K_{AV}	R^2
Conductivity	Kaolin	185.592	0.1453	26.967	0.76768	0.1473	4.562	0.7679	0.8076	-0.789	0.79173
	KT	211.592	0.1164	24.629	0.85837	0.1024	5.402	0.59457	0.6745	0.260	0.92081
	KZ	229.319	0.0912	20.914	0.82467	0.0799	5.820	0.56207	0.5981	0.836	0.95198
	KTZ11	231.542	0.08565	19.832	0.88111	0.0874	5.702	0.8895	0.5505	1.016	0.9545
	KTZ21	238.699	0.0791	18.881	0.7074	0.0860	5.808	0.8391	0.5671	1.180	0.90033
	KTZ12	238.402	0.08494	20.250	0.80069	0.0887	5.846	0.8559	0.6269	1.683	0.94185
Total Alkalinity	Kaolin	267.036	0.1135	30.309	0.87269	0.1157	4.916	0.87305	0.574	-0.145	0.91642
	KT	293.197	0.1131	33.161	0.73344	0.1117	5.444	0.68427	0.683	0.649	0.78048
	KZ	292.671	0.1161	33.979	0.74424	0.1178	5.423	0.74179	0.735	0.618	0.80967

	KTZ11	296.463	0.1116	33.085	0.73947	0.1133	5.466	0.73963	0.698	0.707	0.79663
	KTZ21	300.947	0.1089	32.773	0.70776	0.1086	5.576	0.67551	0.691	0.893	0.73351
	KTZ12	298.421	0.11014	32.868	0.76363	0.1038	5.607	0.62976	0.712	0.693	0.84273
COD	Kaolin	242.103	0.052	12.589	0.90404	0.0529	4.935	0.90401	0.2292	-0.119	0.90502
	KT	302.691	0.065	19.675	0.75652	0.0633	6.244	0.65422	0.470	2.216	0.80454
	KZ	305.492	0.063	19.246	0.71142	0.0630	6.270	0.67197	0.451	2.481	0.72991
	KTZ11	307.610	0.063	19.379	0.70289	0.0648	6.288	0.7029	0.469	2.492	0.71558
	KTZ21	307.610	0.061	18.764	069934	0.0629	6.302	0.06973	0.451	2.603	0.70842
	KTZ12	308.319	0.063	19.424	0.71258	0.0629	6.329	0.6775	0.474	2.490	0.73425
Total Hardness	Kaolin	179.920	0.0706	12.702	0.84848	0.0722	4.854	0.8672	0.323	-0.361	0.85913
	KT	237.290	0.04339	10.296	0.82001	0.0401	6.493	0.64211	0.392	3.531	0.86265
	KZ	240.066	0.04131	9.917	0.76956	0.0393	6.550	0.64796	0.303	4.216	0.80213

	KTZ11	241.841	0.04165	10.073	0.71598	0.0427	6.553	0.72933	0.396	4.218	0.74919
	KTZ21	243.377	0.03976	9.677	0.75324	0.0400	6.511	0.7222	0.309	4.429	0.77915
	KTZ12	245.484	0.03978	9.764	0.73349	0.0396	6.670	0.69301	0.322	4.439	0.75680
Chloride	Kaolin	764.452	0.0921	70.406	0.95722	0.0933	4.076	0.95698	0.496	-2.256	0.98299
	KT	881.049	0.0787	69.339	0.96461	0.0798	4.705	0.96475	0.356	-0.716	0.96583
	KZ	841.723	0.0890	72.510	0.57897	0.0902	4.346	0.57534	0.412	-1.484	0.55069
	KTZ11	84.355	0.0914	80.282	0.94222	0.0927	4.670	0.94189	0.425	0.646	0.91533
	KTZ21	902.090	0.0771	69.550	0.99242	0.0782	4.818	0.99248	0.345	0.411	0.99261
	KTZ12	957.547	1.0793	75.934	0.90434	0.0805	5.119	0.90461	0.375	0.324	0.92897
BOD	Kaolin	85.198	0.0534	4.550	0.88001	0.0543	5.527	0.88789	0.272	1.597	0.87159
	KT	103.455	0.0363	3.755	0.74321	0.0358	6.750	0.68402	0.305	4.896	0.76954
	KZ	104.064	0.0359	3.736	0.73413	0.0355	6.788	0.68264	0.310	4.956	0.75727
	KTZ11	105.642	0.0311	3.285	0.80944	0.0317	6.826	0.80953	0.294	5.464	0.84321

	KTZ21	106.204	1.0311	3.303	0.82183	0.0315	6.917	0.80759	0.307	5.364	0.86992
	KTZ12	107.248	0.0298	3.196	0.78374	0.0295	6.996	0.68809	0.380	5.837	0.76489
Nitrate	Kaolin	12.159	0.0409	0.497	0.75352	0.0680	3.852	0.94218	0.417	-1.919	0.95326
	KT	18.059	0.0588	1.062	0.86739	0.0598	6.203	0.8676	0.414	2.397	0.92549
	KZ	18.494	0.0547	1.072	0.87354	0.0556	6.355	0.87372	0.421	2.647	0.92911
	KTZ11	18.863	0.0500	0.943	0.82931	0.0519	6.469	0.86752	0.415	2.934	0.91737
	KTZ21	19.314	0.0444	0.858	0.8985	0.0452	6.641	0.89865	0.404	3.346	0.94735
	KTZ12	19.432	0.0491	0.954	0.90199	0.0500	6.682	0.90218	0.570	2.692	0.97410
Sulphate	Kaolin	352.063	0.056	19.716	0.94671	0.0568	4.843	0.94678	0.247	0.454	0.94758
	KT	423.448	0.0641	27.143	0.72763	0.0642	5.851	0.70353	0.356	2.088	0.74382
	KZ	426.138	0.0629	26.804	0.71929	0.0635	5.882	0.70853	0.352	2.205	0.73234
	KTZ11	425.736	0.0647	27.545	0.75715	0.0657	5.871	0.75727	0.369	2.065	0.78527

	KTZ21	429.883	0.0634	27.255	0.72064	0.0634	5.944	0.69114	0.366	2.245	0.73561
	KTZ12	432.803	0.0606	26.228	0.70611	0.0611	5.976	0.69395	0.350	2.446	0.71410

Table 4.11: Values of the Kinetic Model Parameters for some Metal Ions Adsorption in Tannery Wastewater

Parameter	Sample	Fractional-P				Bangham			Avrami		
		K	V	KV	R^2	α	K_i	R^2	n_{AV}	K_{AV}	R^2
Zinc	Kaolin	0.868	0.16133	0.140	0.92608	0.163	3.105	0.92607	0.278	-2.095	0.88306
	KT	0.255	07812	0.0462	0.93032	0.183	3.261	0.93006	0.325	-0.584	0.70481
	KZ	0.274	07564	0.0429	0.89879	0.158	3.514	0.89817	0.334	-0.487	0.76417
	KTZ11	0.305	07571	0.0462	0.83886	0.153	3.916	0.83793	0.162	-0.367	0.59218
	KTZ21	0.312	07315	0.0410	0.965	0.133	3.998	0.96573	0.282	0.160	0.92116
	KTZ12	0.352	0.0918	0.0324	0.94418	0.093	4.527	0.94429	0.159	1.994	0.70040
Lead	Kaolin	0.125	0.153	0.0191	0.80156	0.155	2.962	0.80144	0.381	-2.535	0.85199
	KT	0.134	0.1471	0.0197	0.76292	0.149	3.185	0.76265	0.424	-2.551	0.91171
	KZ	0.121	0.1056	0.0181	0.76981	0.111	4.016	0.84383	0.561	-1.949	0.88362
	KTZ11	0.176	0.1321	0.1232	0.77517	0.134	4.180	0.77378	0.724	-1.339	0.59887
	KTZ21	0.207	0.0882	0.0183	0.78810	0.0899	4.921	0.79603	0.447	-0.222	0.71121

	KTZ12	0.206	0.0988	0.0204	0.80222	0.1003	4.912	0.80128	0.553	-0.325	0.59477
Cadmium	Kaolin	0.0783	0.2319	0.0182	0.85008	0.234	2.563	0.84886	0.863	-1.981	0.77477
	KT	0.0868	0.1903	0.0165	0.58217	0.205	2.762	0.68486	0.684	-2.157	0.77294
	KZ	0.1005	0.1587	0.0180	0.77466	0.616	3.294	0.77365	0.548	-2.309	0.64615
	KTZ11	0.1151	0.1263	0.0145	0.67086	0.128	3.777	0.67013	0.667	-2.262	0.75957
	KTZ21	0.1227	0.1215	0.0149	0.72968	0.123	4.030	0.72873	0.606	-1.748	0.37021
	KTZ12	0.1476	0.1069	0.0158	0.84732	0.115	4.784	0.97998	0.581	0.406	0.94587
Chromium	Kaolin	0.797	0.02132	0.0169	071921	0.025	3.877	0.71904	0.520	-2.165	0.84700
	KT	0.881	0.0508	0.0445	0.81364	0.0514	4.292	0.81352	0.591	-1.332	0.89200
	KZ	0.904	0.0423	0.0391	0.93206	0.0428	4.506	0.93191	0.444	-0.599	0.72980
	KTZ11	0.975	0.0337	0.0329	0.93115	0.0341	4.757	0.93107	0.435	-0.418	0.76320
	KTZ21	0.988	0.0726	0.0717	0.6979	0.0737	4.817	0.69758	0.458	-0.367	0.82710

	KTZ12	0.980	0.093	0.0911	0.52477	0.0957	4.940	0.87554	0.508	0.280	0.73320

4.12 Adsorption Mechanism Models

Tables 4.12 and 4.13 describes the mechanisms of adsorption of some physicochemical properties of tannery wastewater onto kaolin, kaolin/TiO_2, kaolin/ZnO and kaolin/TiO_2/ZnO nanoadsorbents.

Table 4.12: Mechanism Adsorption Kinetic Parameters of some Physicochemical Properties in Tannery Wastewater

Parameter	Sample	Boyd Model	Intra-Particle Model		
		R^2	K_{id}	I	R^2
COD	Kaolin	0.81404	7.289	248.713	0.5551
	KT	0.87696	12.578	310.506	0.6427
	KZ	0.89255	12.065	313.406	0.57442
	KTZ11	0.87671	12.430	314.139	0.59435
	KTZ21	0.89325	12.075	315.096	0.59022
	KTZ12	0.89925	12.375	315.627	0.60525
BOD	Kaolin	0.71006	3.022	86.166	0.66822
	KT	0.87405	2.288	104.746	0.60812
	KZ	0.89446	2.220	105.524	0.56476
	KTZ11	0.81836	1.652	107.912	0.39124
	KTZ21	0.86573	1.685	108.414	0.41487
	KTZ12	0.84043	1.915	108.383	0.58885
Nitrate	Kaolin	0.75083	0.05834	13.183	0.17301
	KT	0.92246	0.68693	18.367	0.76476
	KZ	0.81174	0.64864	18.791	0.76069
	KTZ11	0.82556	0.60623	19.123	0.7377
	KTZ21	0.87751	0.53031	19.531	0.80626
	KTZ12	0.869982	0.61336	19.689	0.79982
Sulphate	Kaolin	0.74884	12.721	357.656	0.80789
	KT	0.86521	17.340	432.792	0.62526
	KZ	0.86456	17.039	435.580	0.61203
	KTZ11	0.86802	17.556	435.349	0.64409

	KTZ21	0.86471	17.422	439.194	0.62145
	KTZ12	0.86372	16.603	442.018	0.59977
Chloride	Kaolin	0.72019	16.701	537.002	0.89099
	KT	0.76501	18.120	540.119	0.90135
	KZ	0.80680	18.605	550.120	0.91305
	KTZ11	0.81305	18.920	552.402	0.92412
	KTZ21	0.84008	19.001	562.601	0.93503
	KTZ12	0.85110	19.821	570.201	0.94077

Table 4.13: Mechanism Adsorption Kinetic Parameters of some Heavy Metals in Tannery Wastewater

Parameter	Sample	Boyd Model	Intra-Particle Model		
		R^2	K_{id}	I	R^2
Zinc	Kaolin	0.86302	0.0301	0.254	0.73551
	KT	0.87886	0.0400	0.257	0.84147
	KZ	0.93544	0.0379	0.270	0.87694
	KTZ11	0.918877	0.0408	0.299	0.8011
	KTZ21	0.96133	0.0306	0.321	0.85657
	KTZ12	0.94824	0.0222	0.361	0.80915
Lead	Kaolin	0.82982	0.0107	0.144	0.21096
	KT	0.90455	0.0152	0.139	0.53946
	KZ	0.83635	0.0150	0.168	0.84067
	KTZ11	0.9337	0.0202	0.172	0.74439
	KTZ21	0.94069	0.0142	0.206	0.79411
	KTZ12	0.9080	0.0163	0.205	0.7952
Cadmium	Kaolin	0.8066	0.0197	0.0709	0.80749
	KT	0.90916	0.0184	0.0761	0.67984
	KZ	0.96065	0.0149	0.0965	0.76209
	KTZ11	0.92125	0.0128	0.112	0.69658
	KTZ21	0.95154	0.0128	0.120	0.71325
	KTZ12	0.92411	0.0127	0.147	0.93161
Chromium	Kaolin	0.77958	0.0268	0.846	0.15207
	KT	0.83948	0.0177	0.932	0.72089
	KZ	0.8715	0.0262	0.930	0.86996
	KTZ11	0.8577	0.0211	0.982	0.82552
	KTZ21	0.92982	0.0492	1.004	0.54531
	KTZ12	0.9818	0.0729	0.974	0.5732 0

The plots of the Boyd and intraparticle diffusion models did not pass through the origin, thus suggesting that some degree of boundary layer diffusion occurred in the removal of the studied pollutants onto the adsorbent materials (Ahmad *et al.*, 2014). The intercept, **I**, values in this study are > 0 for all the pollutants as presented in Table 4.12 and 4.13 indicating that the intraparticle diffusion is not the only controlling step (Abbas *et al.*, 2019). The result obtained implies that the rate of adsorption involves multi-kinetic stage. Also, the Boyd kinetic helps to identify whether the rate-determining step is an external transport or intraparticle transport during the adsorption process. The plots obtained showed linearity but did not pass through the origin, indicating that the initial concentrations of the pollutants and external mass transport control the rates of adsorption (Gong *et al.*, 2019).

Considering the intraparticle diffusion and Boyd models, the mechanism for the studied pollutants uptake onto the adsorbents may follow these assumptions: (i) bulk diffusion (ii) film diffusion (iii) intraparticle or pore diffusion (iv) ionic nature of the sorbate (chemical reaction through ion exchange).

4.13 Reaction Mechanism between Beneficiated Kaolin, TiO_2 and ZnO

The mechanistic reaction between kaolin, TiO_2 and ZnO were deduced from the elemental compositions and functional groups of the beneficiated kaolin together with the synthesized TiO_2 and ZnO nanoparticles. In this case, the calcined kaolin is transformed into metakaolin at high temperature, thus composed of octahedral alumina and tetrahedral silica.

In the first step, the calcinated kaolin is immersed in deionized water. Secondly, the addition of TiO_2 that is surface hydroxylated tends to hydroxylzed with the calcined kaolin via wet impregnation to form hydroxides. This step is fast. The surface comprises hydroxyl group, hydrogen bonding, electron donor-acceptor and dispersion interactions. The association of TiO_2 and ZnO results in Si-O-Ti, Ti-O-Ti, Ti-O-Zn, Al-O-Ti, Si-OH, Al-OH, Ti-OH and Zn-OH bonds as active groups as indicated in the FTIR spectra.

Figures 4.69, 4.70 and 4.71 show the mechanistic reactions that might have taken place when reacting the calcined kaolin/TiO_2, kaolin/ZnO and kaolin/TiO_2/ZnO, respectively.

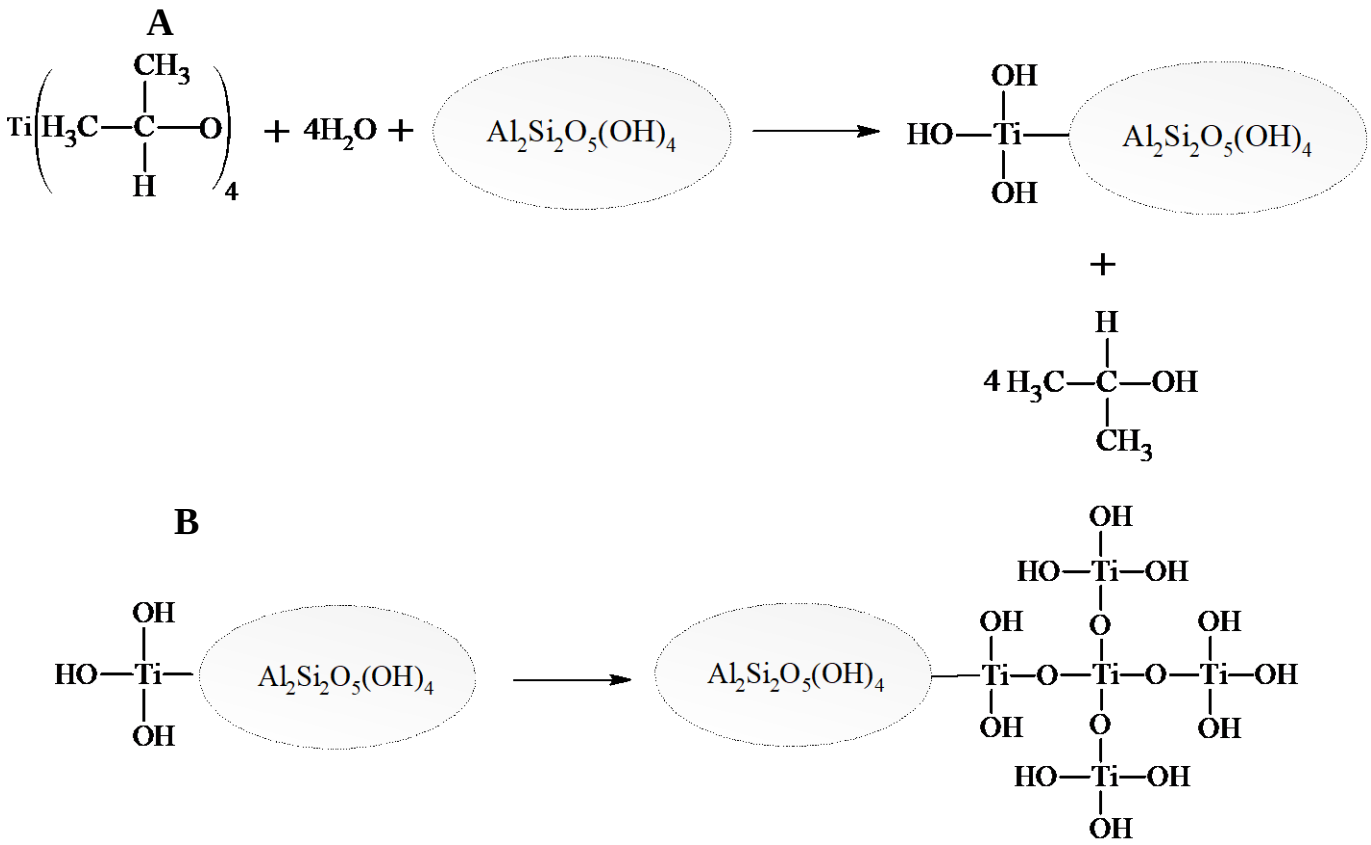

Figure 4.69: A and B Described Schematic Representation for Preparation of Kaolin/TiO_2 Nanocomposites

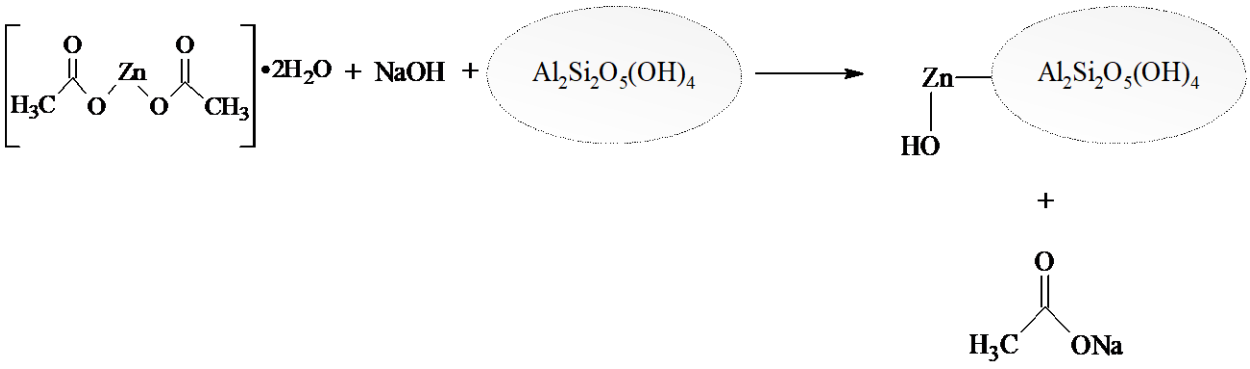

Figure 4.70: A Schematic Representation for Preparation of Kaolin/ZnO Nanocomposites

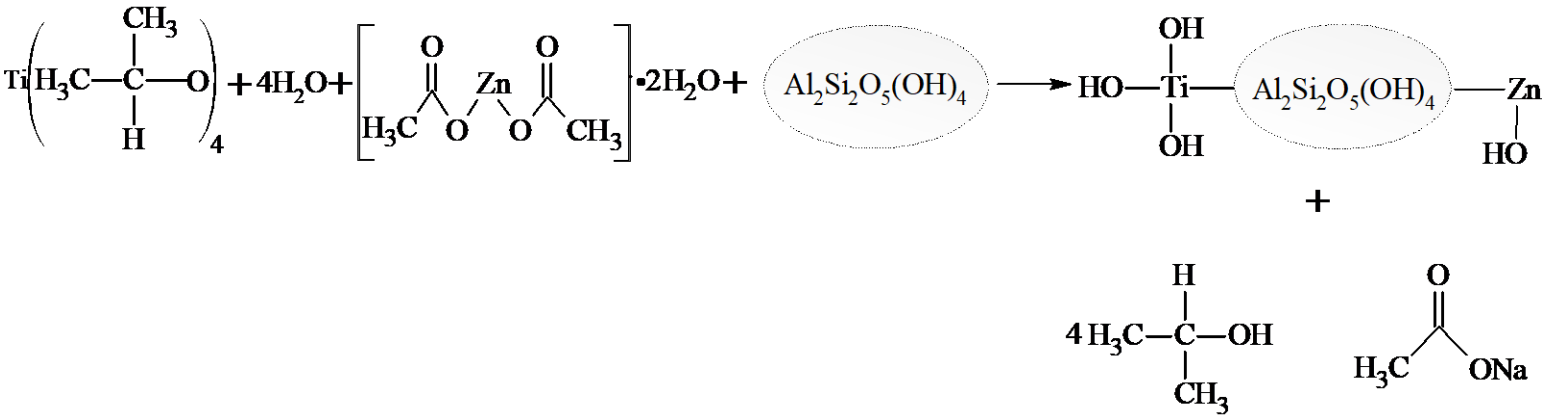

Figure 4.71: A Schematic Representation for Preparation of Kaolin/TiO_2/ZnO Nanocomposites

4.14 Thermodynamics Studies

The effects of temperature on the adsorption of some physicochemical properties onto kaolin, kaolin/TiO_2, kaolin/ZnO and kaolin/TiO_2/ZnO nanoadsorbents and their relatives' parameters are listed in Table 4.14 and 4.15.

Table 4.14: Thermodynamic Parameters of some Physicochemical Properties from Tannery Wastewater using Kaolin, Kaolin/TiO_2, Kaolin/ZnO and Kaolin/TiO_2/ZnO Nanoadsorbents

Parameter	Sample				ΔG (kJ/mol)					
		R^2	ΔH (kJ/mol)	ΔS (J/molK)	303K	313K	323K	333K	343K	353K
Chloride	Kaolin	0.96286	9.485	15.456	4.802	4.647	4.493	4.338	4.184	4.029
	KT	0.98356	9.465	19.122	3.671	3.48	3.289	3.097	2.906	2.715
	KZ	0.97805	7.312	12.878	3.410	3.281	3.152	3.024	2.800	2.766
	KTZ11	0.98213	6.54	10.775	3.275	3.167	3.060	2.952	2.844	2.736
	KTZ21	0.95259	5.818	9.287	3.004	2.911	2.818	2.725	2.633	2.54
	KTZ12	0.9763	5.951	9.985	2.926	2.826	2.723	2.626	2.526	2.426
COD	Kaolin	0.8856	9.827	28.816	1.096	0.808	0.519	0.231	0.0569	-0.345
	KT	0.9706	8.923	30.604	-0.350	-0.656	-0.962	-1.268	-1.574	-0.345
	KZ	0.99558	7.317	26.064	-0.580	-0.841	-1.102	-1.362	-1.623	-1.884
	KTZ11	0.9901	7.184	26.006	-0.696	-0.956	-1.216	-1.476	-1.736	-1.996
	KTZ21	0.99243	8.774	31.526	-0.778	-1.094	-1.409	-1.724	-2.039	-2.355

	KTZ12	0.93207	9.609	34.52	-0.851	-1.196	-1.541	-1.886	-2.231	-2.577
BOD	Kaolin	0.973	13.47	40.48	1.205	0.800	0.395	0.00984	-0.415	-0.819
	KT	0.95646	9.891	32.716	0.022	-0.349	-0.676	-1.003	-1.331	-1.658
	KZ	0.95733	10.931	36.357	0.0852	-0.449	-0.812	-1.176	-1.540	-1.903
	KTZ11	0.98207	11.714	39.467	-0.246	-0.639	-1.034	-1.429	-1.823	-2.218
	KTZ21	0.97559	9.985	34.869	-0.58	-0.929	-1.278	-1.626	-1.975	-2.324
	KTZ12	0.99524	10.385	36.658	-0.726	-1.093	-1.460	-1.826	-2.193	-2.559
Sulphate	Kaolin	0.96578	9.038	24.684	1.559	1.312	1.065	0.818	0.571	0.325
	KT	0.94717	3.931	12.255	0.218	0.0952	-0.0274	-0.150	-0.273	-0.501
	KZ	0.96791	3.672	11.806	0.0948	-0.0233	-0.141	-0.259	-0.378	-0.496
	KTZ11	0.98579	4.296	14.059	0.0361	-0.105	-0.245	-0.386	-0.526	-0.667
	KTZ21	0.9549	4.237	14.217	-0.0708	-0.213	-0.355	-0.497	-0.639	-0.782
	KTZ12	0.94274	4.814	16.146	-0.0782	-0.24	-0.401	-0.563	-0.724	-0.836
Nitrate	Kaolin	0.96578	13.398	32.007	3.700	3.380	3.060	2.740	2.420	2.100
	KT	0.94717	15.562	40.847	3.185	2.777	2.368	1.960	1.552	1.143
	KZ	0.98392	19.875	56.136	2.866	2.304	1.743	1.182	0.620	-0.059
	KTZ11	0.97198	17.97	51.381	2.402	1.888	1.374	0.860	0.346	-0.681

	KTZ21	0.99355	20.682	60.293	2.412	1.810	1.207	0.604	-0.0015	-0.601
	KTZ12	0.9747	18.654	54.611	2.107	1.561	1.015	0.0469	-0.0776	-0.624

Table 4.15: Thermodynamic Parameters of Zn, Pb, Cd and Cr from Tannery Wastewater using Kaolin, Kaolin/TiO_2, Kaolin/ZnO and Kaolin/TiO_2/ZnO Nanoadsorbents

Parameter	Sample				ΔG (kJ/mol)					
		R^2	ΔH (kJ/mol)	ΔS (J/molK)	303K	313K	323K	333K	343K	353K
Zinc	Kaolin	0.91998	21.096	74.153	-1.372	-2.114	-2.855	-3.597	-4.338	-5.080
	KT	0.99098	20.319	73.463	-1.940	-2.675	-3.410	-4.144	-4.879	-5.613
	KZ	0.89284	16.449	61.806	-2.278	-2.278	-3.514	-4.132	-4.751	-5.369
	KTZ11	0.79345	18.154	68.283	-2.536	-3.219	-3.901	-4.584	-5.267	-5.950
	KTZ21	0.78151	19.446	72.931	-2.652	-3.381	-4.114	-4.840	-5.569	-6.299
	KTZ12	0.84132	46.364	161.514	-2.575	-4.190	-5.805	-7.420	-9.035	-10.65
Lead	Kaolin	0.90400	24.631	77.825	1.053	0.272	-0.507	-1.285	-2.063	-2.841
	KT	0.90121	51.799	169.714	0.376	-1.322	-3.019	-4.716	-6.413	-8.110
	KZ	0.81706	63.838	235.159	-0.8415	-1.767	-12.118	-14.47	-16.822	-19.173
	KTZ11	0.79016	70.784	235.21	-0.485	-2.837	-5.189	-7.541	-9.893	-12.248
	KTZ21	0.71568	65.042	223.688	-2.736	-4.972	-7.209	-9.446	-11.683	-13.92
	KTZ12	0.96636	40.838	146.227	-3.469	-4.931	-6.393	-7.856	-9.318	-10.780
Cadmium	Kaolin	0.93850	35.713	105.904	3.624	2.588	1.506	0.447	-0.612	-0.1671
	KT	0.89801	37.629	110.452	4.162	3.058	1.953	0.849	-0.256	-1.361

	KZ	0.76465	38.273	116.388	3.007	1.844	0.68	-0.484	-1.648	-2.812
	KTZ11	0.95460	38.882	118.225	3.06	1.878	0.695	-0.487	-1.669	-2.851
	KTZ21	0.89956	16.877	57.272	1.341	0.829	0.316	-0.197	-0.090	-1.222
	KTZ12	0.52129	15.439	48.155	0.848	0.367	-0.115	-0.597	-1.0782	-1.560
Chromium	Kaolin	0.90041	18.725	68.898	-2.151	-2.840	-3.529	-4.218	-4.907	-5.596
	KT	0.87628	14.996	58.92	-2.857	-3.446	-4.035	-4.624	-5.214	-5.803
	KZ	0.97623	11.331	50.073	3.841	-4.342	-4.843	-5.343	-5.844	-6.345
	KTZ11	0.90386	9.407	45.178	-4.282	-4.734	-5.186	-5.639	-6.089	-6.541
	KTZ21	0.97864	9.074	45.164	-4.611	-5.062	-5.514	-5.966	-6.417	-6.869
	KTZ12	0.96831	14.531	63.727	-4.778	-5.416	-6.053	-6.690	-7.328	-7.965

In order to acquire an insight into the mechanisms involved in the adsorptivity process, the effects of temperature and thermodynamic parameters were established and evaluated from the adsorption system. The change in Gibbs free energy (Δ**G**), enthalpy (Δ**H**) and entropy (Δ**S**) at respective temperatures were computed using the following equations:

$$K_d = \frac{q_e}{C_e} \tag{4.5}$$

$$\Delta G = -RT\ln K_d \tag{4.6}$$

$$\Delta G = \Delta H - T\Delta S \tag{4.7}$$

where the values of Δ**G**, Δ**H** and Δ**S** were measured in kJ/mol, kJ/mol and J/molK respectively. T is the absolute temperature (**K**), **R** is the universal gas constant (8.314 J/molK). The Δ**H** and Δ**S** were evaluated from the slopes and the intercepts from the extrapolation of the distribution coefficient (K) against $\frac{\mathbf{1}}{\mathbf{T}}$ in Appendix I.

The values of Δ**H** and Δ**S** were found to be positive. The positive values of Δ**H** shows that the adsorption processes are endothermic in nature. While the positive values of Δ**S** indicate the affinity of the adsorbates with increasing randomness of the solid-liquid interface during the adsorption process (Harrache *et al.*, 2019). The Gibbs free energy on the other hands reduces with increase in temperature indicating a driving force that leads to higher adsorption capacity. Therefore, with high temperature, adsorption process increases as a result of increase in randomness and non-spontaneity of the process. The thermodynamic study on the removal of these pollutants suggests chemical adsorption due to strong interface where the sorbates adhere on the surfaces of the adsorbents through strong forces forming chemical bonds.

4.15 Microbial Analysis

The microbial activity of the tannery wastewater presented in Table 4.16 was performed to determine the type of bacteria that exists in the wastewater.

Table 4.16: Microbial Analysis of Wastewater before Treatment

Sample	TAC (cfu/mL)	TANC (cfu/mL)	TCC (cfu/mL)	TSC (cfu/mL)	TSPC (cfu/mL)		Macro-culture	S	GS	COUG	CT	SH	CIT	MR	IND	L	S	G	Name of the organism
Tannery wastewater	2.80×10^6	NIL	NIL	NIL	NIL	NIL	Mucoid, spherical, dull white raised or concave colonies	R	+	-	+	+	+	-	-	-	+	+	*Bacillus subtilis*
							Non-mucoid, spherical beads like in shape and aragant, whitish colonies	R	-	-	+	+	-	-	-	-	+	+	*Bacillus megaterium*

Key:
TAC = Total aerobic mesophilic count; TCC = Total coliform count; TSC = Total salmonella count; TSTC = Total streptococcus species count; TSPC = Total staphylococcus species count; TANC = Total anaerobic bacteria count; S = Shape of bacteria cells; GS = Grain's stain; COUG = Cougulase test; CT = Citrate utilization test; SH = Starch hydrolysis test; MR = Methyl res test; IND = Indole utilization test; L = Lactose sugar; S = Sucrose sugar; G = Glucose test; + = Positive (Has reaction); − = (No reaction); cfu = Colony forming unit (S.I unit of microbial count); mL = per one millimeter of sample.

4.15.1 Antibacterial study of nanoadsorbents

The antibacterial activities of kaolin, kaolin/TiO_2, kaolin/ZnO and kaolin/TiO_2/ZnO nanocomposites against *Bacillus subtilis* and *Bacillus megaterium* and Bacillus were observed for contact time of 5-30 min in the bacterial suspension of 1 cfu/cm^3. It was observed that bacteria inactivation increased at the constant adsorbent dosage of 0.2 g with increase in contact time. No bacteria cell was detected in the wastewater as depicted in Plate XIII. Thus, the clear pictures of the inhibition zones show the antibacterial effect of the kaolin and the other nanocomposites. This anti bactericidal effect of these adsorbents can be attributed to the mechanical and chemical properties of the nanoparticles in addition to the large surface area of kaolin. Therefore, the adsorbent materials used in this study were efficient in the treatment of the wastewater against the test organisms.

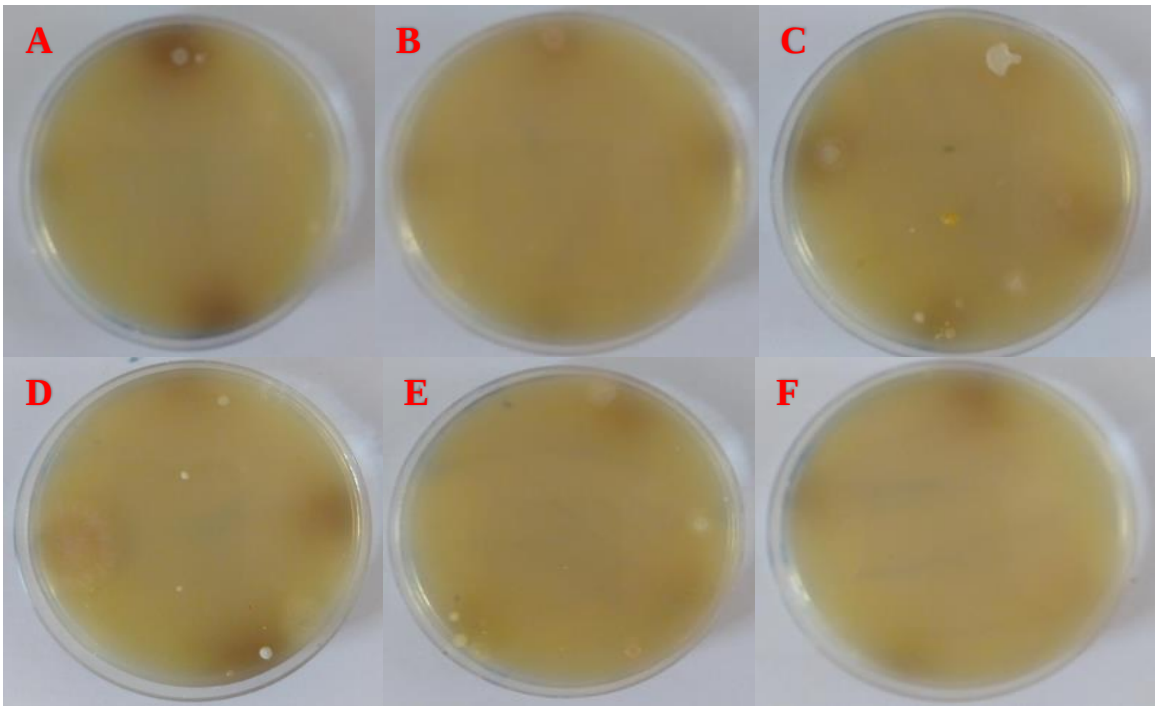

Plate XIII: Inhibition Growth of *Bacillus subtilis* and *Bacillus megaterium* using A) kaolin B) KT C) KZ D) KTZ11 E) KTZ21 F) KTZ12 Nanoadsorbents.

4.16 Fabrication of Filter Pots

The results from the percentage of porosity and correlation coefficient of kaolin filter pots without nanoparticles are presented in Table 4.17. It could be seen from the results that a reduction in the percentage of porosity from the composites (kaolin/sawdust) is due to the presence of higher amounts of kaolin in the mixture. The low percentage of porosity will lead to a low flow rate of liquid through the porous filter pots (permeability).

Table 4.17: Various Trials done on Pot Filters

Sample			**After firing**					**%**
	Kaolin/Sawdust	**Wt. before firing (g)**	**Line (mm)**	**Weight**	**Line**	**Weight**	**Weight after soaking**	**Porosity**
T1	40/60	36	54.00	26	10.00	58.07	41	54.07
T2	44/56	44	55.50	34	7.50	45.60	48	42.20
T3	33/67	34	53.00	24	11.67	61.29	40	64.72
T4	46/54	48	55.00	36	8.33	41.94	49	38.01
T5	50/50	46	56.00	37	6.67	42.85	50	36.49
T6	60/40	54	56.00	44	6.67	29.03	55.6	20.14
T7	54/46	50	58.00	40	3.33	35.48	52	26.19
T8	67/33	52	58.50	47	2.50	24.18	53	15.40
T9	65/35	54	56.00	46	6.67	32.25	54	17.82
T10	56/44	52	56.00	47	6.67	25.81	56	23.60

Initial line = 60 mm; **LOI of the beneficiated clay** = 5.03 %; **Refractoriness** = 910±5 ^{o}C; **Colour after firing** = light ash.

Table 4.17 shows the effects of temperature on different trials of filter pots. On the application of heat, the presence of oxides in the kaolin could act as fluxes, thereby combining with silica and alumina, thus reducing the refractoriness nature of the clay samples. As presented in Table 4.43, the loss in the ignition (LOI) is 5.03 % which is attributed to the dehydroxylation reaction in the kaolin mineral. This low LOI is an indication of low porosity of the product during kilning. The result obtained shows that the kaolin filter samples had fair refractory properties and did not rupture at 900 ^{o}C as displayed in Plate XIV. The shrinkage, plasticity and porosity are important physical factors to be considered after kilning of the product at 900 ^{o}C as shown in Table 4.17.

The shrinkage of after firing decreased and also the porosity either decreased or increased with respect to the blend ratio of kaolin/dust. It was seen that at a higher ratio of kaolin to sawdust, there were a low % porosity and shrinkage. This implies that on the application of temperature, the product tended to compress while the low shrinkage indicates a high level of non-fluxing impurities (sawdust) (Aboh *et al.,* 2014). The decrease in the shrinkage for the refractory material is attributed to the coming together and closure of the pores of the clay body. In this study, porosity is directly related to shrinkage. The higher the weight of the moulded clay pot, the more the porosity of the clay body. There were interstitial spaces between the kaolin after kilning the kaolin/dust. These small spaces are as a result of the burning off of the carbonaceous materials at high temperatures. Therefore, temperature, the ratio of kaolin and dust formulation are the principal factors governing the flow rate and percentage porosity of the filter pots.

In fact, a greater amount of sawdust over kaolin resulted in an increase in water absorption. While there was a decrease in water absorption on the addition of more kaolin and this was due to the reduction in porosity and making the kaolin/sawdust composite more plastic. The high plasticity tends to make the moulding of clay pot workable and easily moulded.

Plate XIV: Fabricated Kaolin Filter Pots at different Proportions of Sawdust and Kaolin

4.16.1 Performance evaluation of nano-filter pots

Figure 4.72 shows that the flow rate could be effectively used to check the amount of filtered wastewater. The flow rate was optimized by changing the proportion of kaolin and sawdust as shown in Table 4.17. The loaded amount of sawdust to the filter pot formulation served as the determinant of flow rate and percentage porosity of the filter pot. The flow rate was found to be varied with different ratios of kaolin to sawdust. The first four most porous filter pots studied at percentage ratio of kaolin to sawdust in descending order were: 33/67 (**T3**), 40/60 (**T1**), 44/56 (**T2**), 50/50 (**T4**) and 46/54 (**T5**). The slowest flow rate was associated with high amounts of loaded kaolin. It is noteworthy that the flow rate of the wastewater through the filter pots increased with porosity.

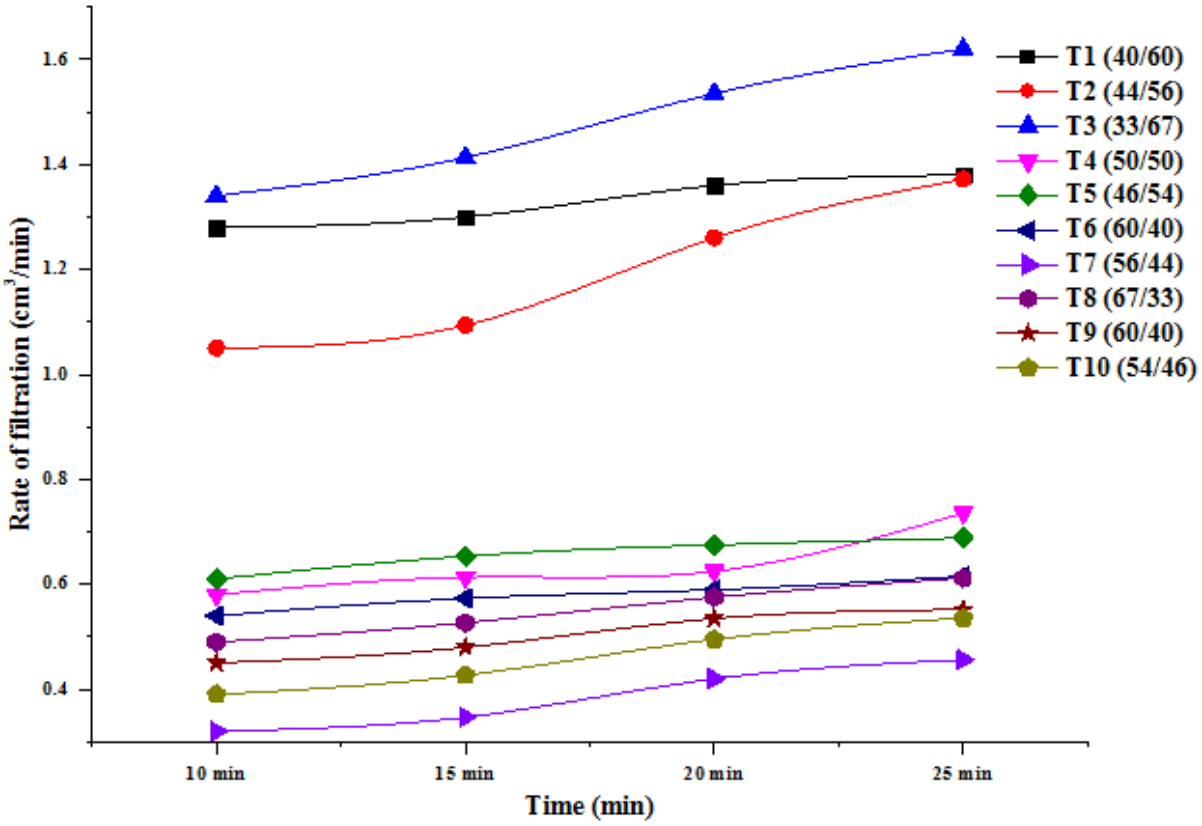

Figure 4.72: Rate of Filtration on Different Proportion of Sawdust and Kaolin Filter Pots

The rates of filtration of the tannery wastewater using the moulded filter pots were as presented in Figure 4.72. It was established that the direct use of wastewater on the filter pot is associated with a low flow rate. This could have been as a result of the suspended solids present in the wastewater. Therefore, a rapid estimation of the flow rate was performed firstly by removing particulates from the wastewater using Whatman filter paper. Finally, the discharged filtrate was filtered through the fabricated filter pot and a reasonable amounts of filtrate were obtained.

4.16.2 Chemical resistance behaviour of the filter

The resistance to acid/base corrosion performed on the optimal filter produced showed that significant weight loss was observed on soaking in acidic solution (pH 1-6). The produced filter exhibited slight weight loss in a weak acidic solution compared to the concentrated regions. Figure 4.73 shows the mass loss of optimal filter produced in acidic and basic solution at

constant time (48 h). This poor acid corrosion resistance of the filter may be as a result of the dissolution of some elements from kaolin that made the porous sample become fragile, suggesting that it is liable to a decrease in the fraction strength. The porous filter showed little or no significant weight loss in aqueous NaOH (8-14). This is due to strong interaction between hydroxide ions and the porous sample which provide sufficient mechanical strength. For porous kaolin starch/potassium phosphate supports with porosity, the mass loss during corrosion test showed a good chemical corrosion resistance for both acid and base (Sayehi *et al.*, 2018). This finding is not commensurable compared with kaolin/sawdust support in this study. The disparity in the studies could be attributed to different materials used as supports. However, the present study supported the findings reported in the literature (Mouiya *et al.*, 2018; Mouiya *et al.*, 2019). This shows that the porous sample (kaolin/sawdust) is alkali resistant and could not withstand acidic medium in term of chemical cleaning.

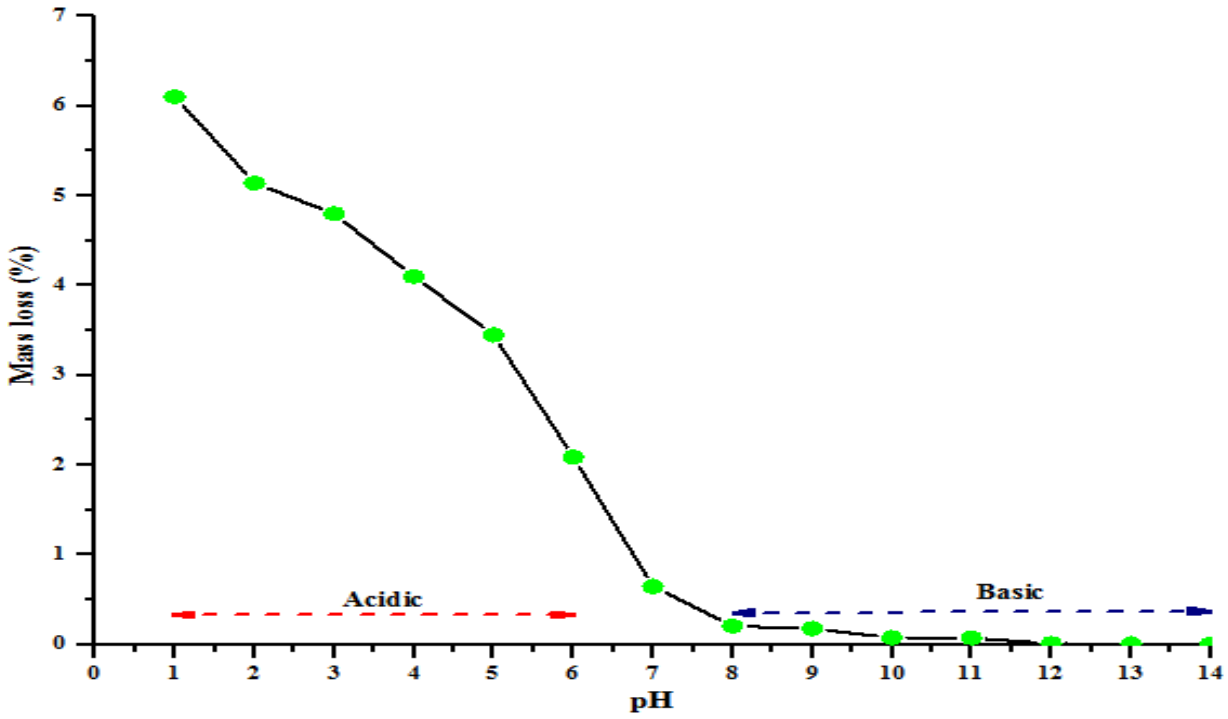

Figure 4.73: Weight loss (%) of optimal sintered kaolin/sawdust filter in acidic and basic medium at ambient temperature for 48 h.

4.16.3 Antibacterial and adsorption study on the prepared clay filter pots

The fungal strain, *Fusarium chlamydosporium* was detected in the tannery effluent by serial dilution method. The presence of this fungus mark its adaptation to and tolerance of heavy metals for a long time by various mechanisms like precipitation, complexation, oxidation-reduction reactions, adsorption to cell walls and transport across the cell membrane (Bahafid *et al.*, 2017).

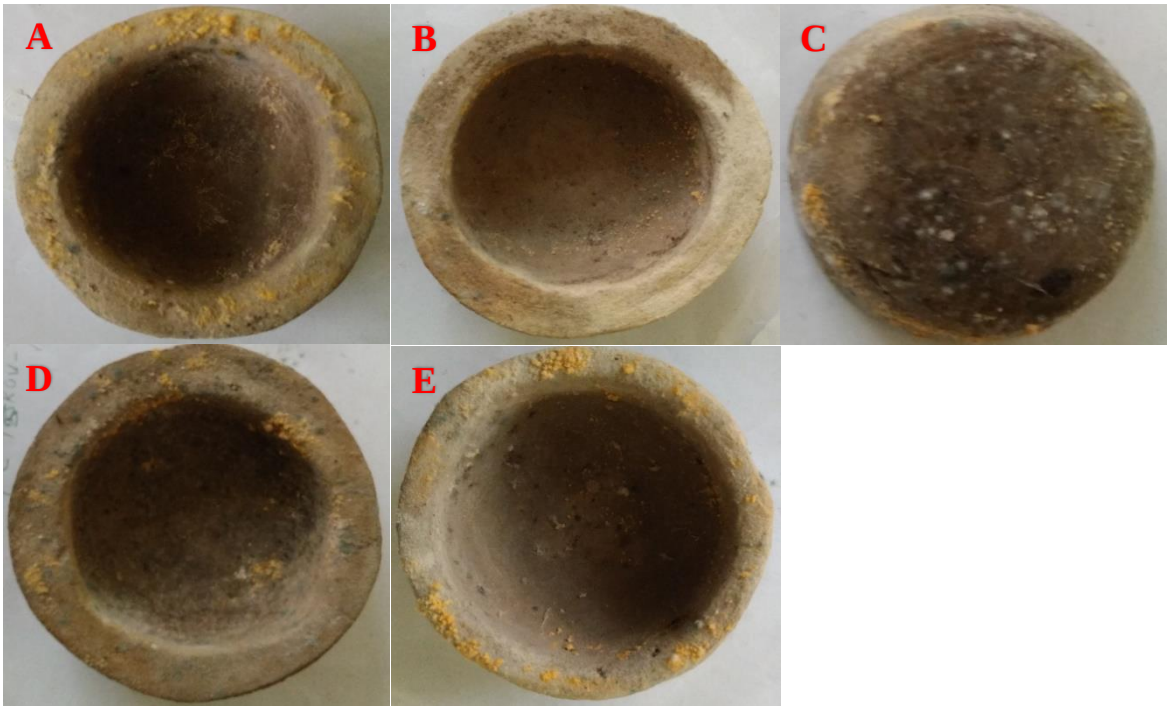

Plate XV: Nanocomposites Filer Pots of A) KT B) KZ C) KTZ11 D) KTZ21 E) KTZ12

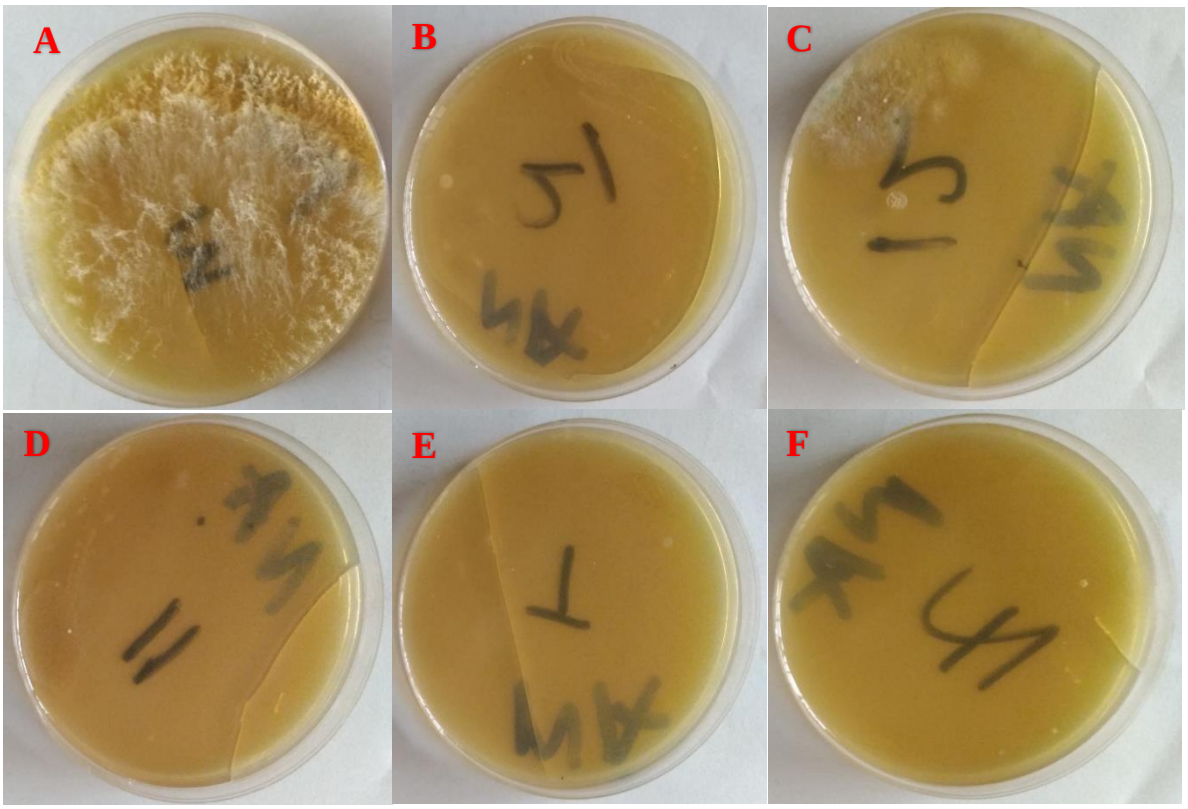

Plate XVI: Anti-microbial Test Results for A) Control (wastewater) B) KTZ12 C) KTZ21 D) KTZ11 E) KT and F) KZ

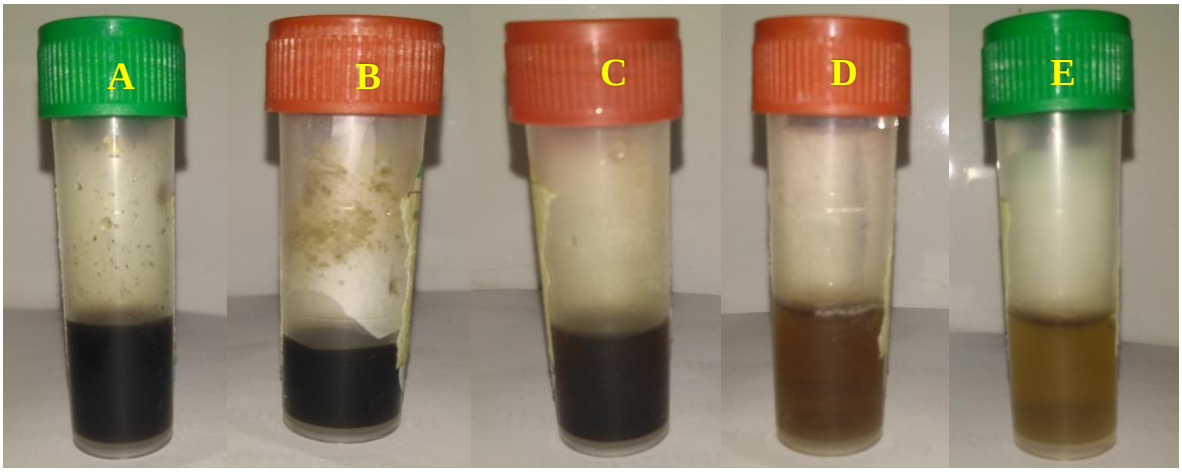

Plate XVII: Filtrates from Nanocomposites Filter Pots of A) KT B) KZ C) KTZ11 D) KTZ21 and E) KTZ12 in the Absence of Sunlight

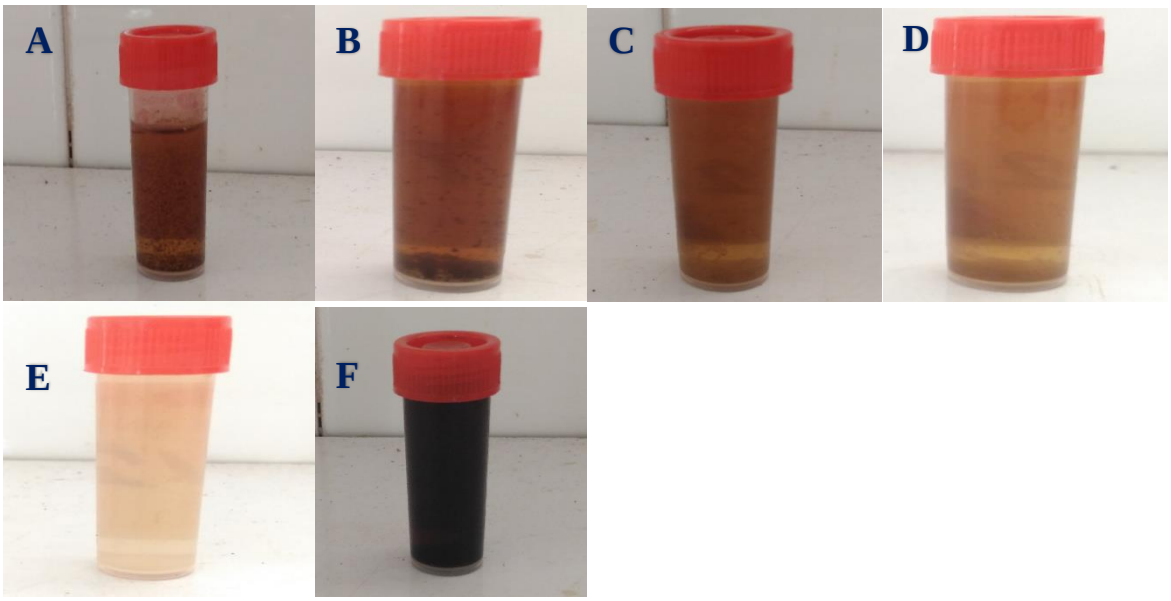

Plate XVIII: Filtrates from Nanocomposites Filter Pots of (A) KT (B) KZ (C) KTZ11 (D) KTZ21 (E) KTZ12 and (F) Kaolin in the Presence of Sunlight

The adsorption of some parameters at fixed volumes of tannery wastewater was determined in ambient temperature using the nanocomposites. The concentrations of parameter reduction were found to be significant as presented in Table 4.18.

Table 4.18: Adsorption of some Physicochemical Properties using different Nanocomposites Filters

Parameter	Control	KT	KZ	KTZ11	KTZ21	KTZ12
pH	5.84±0.02	7.12±0.15	7.05±0.10	7.64±0.03	7.49±0.52	7.70±0.17
COD (mg/dm^3)	1988.60±0.23	680±0.20	640±0.40	592±0.32	560±0.16	480±0.20
BOD (mg/dm^3)	625.30±0.10	44±0.27	39±0.12	38±0.02	30.5±0.05	27.8±0.28
Chloride (mg/dm^3)	7580.50±0.42	1020±0.02	848±0.015	741±0.024	725±0.04	710±0.01
Nitrate (mg/dm^3)	118.30±0.16	59.4±0.013	55.7±0.05	52.6±0.01	48.8±0.03	40.7±0.06
Sulphate (mg/dm^3)	2944.00±0.22	502±0.12	510±0.04	483±0.08	450±0.03	442±0.01
TDS (mg/dm^3)	724.00±0.10	104±0.09	92.5±0.15	80.2±0.15	74.1±0.07	70.2±0.19
TH (mg/dm^3)	1500.00±0.61	680±0.12	520±0.07	421±0.01	402±0.06	381±0.03
TA (mg/dm^3)	2200.00±0.91	360±0.15	280±0.01	260±0.10	243±0.02	200±0.03
TOC (%)	1.41±0.25	0.26±0.01	0.24±0.05	0.22±0.01	0.19±0.09	0.15±0.06

The treatment of tannery wastewater with kaolin, kaolin/TiO_2, kaolin/ZnO and kaolin/TiO_2/ZnO at different nanoparticles ratios at ambient temperature as seen in Plate XVII, reduced the COD, colour, TSS, turbidity, nitrate and other physicochemical parameters. The decolourization of tannery wastewater using kaolin/TiO_2/ZnO (KTZ12) could be attributed to the oxidation degradation of the organic molecules. Notably, the treated tannery wastewater also recorded a decrease in pH values for all the adsorbents due to breakdown of organic compounds. The reduction in TSS and turbidity could be ascribed to the entrapment of suspended solid particles by the wall of the filter pots. Whereas, the decrease in the concentrations of the ion; NO_3^-, Cl^- and SO_4^{2-} ions might be as a result of the utilization of these ions by the cationic species present in the filter pots (ion exchange).

CHAPTER FIVE

5.0 CONCLUSION AND RECOMMENDATIONS

5.1 Conclusion

In addressing the treatment of tannery wastewater, the synthesis, characterization and fabrication of kaolin, kaolin/TiO_2, kaolin/ZnO and kaolin/TiO_2/ZnO nanocomposites filter were undertaken. The TiO_2 and ZnO nanoparticles prepared at optimum pH using the sol-gel method embedded in kaolin via wet impregnation method were used for the batch experiment. The synthesized adsorbents were characterized using XRD, FTIR, HRTEM, SAED, EDX, HRSEM, XPS and BET before they were used for adsorption of chloride, COD, BOD, sulphate, nitrate, zinc, lead, cadmium and chromium. The adsorption studies were performed to investigate the adsorption capacity of the synthesized kaolin and nanocomposites under different condition such as contact time, dosage and temperature. The kinetic and isotherm studies were used to describe the adsorption equilibria of the pollutants onto the adsorbents. The data on the influence of temperature on the adsorption system are used in the thermodynamic studies. Sequel to this information, the following conclusions are drawn:

a) The characterization result showed that anatase phase of the synthesized TiO_2 nanoparticles and zincite phase of ZnO nanoparticles were formed on the plate-like beneficiated kaolin when calcined at 450 ^oC.

b) It was established that the pH played a key role on the identification, structures and morphologies of the synthesized TiO_2 and ZnO nanoparticles. XRD, HRSEM, HRTEM, FTIR, EDX and BET confirmed the synthesis of the nanoparticles which contained functional groups, and mesopores that allowed for the maximum adsorption of pollutants studied.

c) The optimum conditions for conductivity, total hardness, total alkalinity, chloride, COD, BOD, sulphate, nitrate, zinc, lead, cadmium and chromium adsorption were established using 0.2 g of the adsorbent, pH = 5.84 with 150 rpm shaking speed. The adsorption process was greatly dependent on dosage and temperature with percentage pollutant removal increasing in dose and temperature. The increase in dosage which increased the number of available active sites for the uptake of the pollutants have suggested to be responsible for the increase in the adsorption rate. It is also suggested that the adsorption mechanism is chemisorption since it was temperature dependent.

d) The adsorption data fitted best the R-P isotherm model followed by Jovanovic model. Hence, the surface adsorption can be considered as homogeneous with monolayer coverage and high maximum adsorption energy due to some mechanical contacts between the liquid-solid interfaces. The results provided from the various kinetic models employed show a good correlation of the Avrami kinetic model, for the adsorption of the pollutants onto the adsorbents. Thus, the adsorptions were assumed to be through multiple adsorption systems. The Boyd and intra-particle diffusion model as rate-determining steps controlled the adsorption process mechanism. Their plots do not pass through the origin, indicating some degree of boundary layer diffusion attributable to chemical reactions through ion exchange, bulk, film and pore diffusion to the external surfaces of the adsorbents.

e) The thermodynamic parameters (ΔH = +ve and ΔS = +ve) indicate that the adsorption processes were spontaneous and endothermic. This result was supported by the increasing adsorption of chloride, COD, BOD, sulphate, nitrate, zinc, lead, cadmium and chromium with increase in temperature.

f) The mechanistic pathways from the preparation of the nanocomposites from kaolin, TiO_2 and ZnO were obtained from the elemental compositions and functional groups, suggesting hydrogen bonding, formation of electron donor-acceptor and dispersion interactions. The anti-bactericidal properties of the adsorbents used in this study could be attributed to the physicochemical properties of the nanoparticles as well as large surfaces.

g) The nanocomposite filters were produced for the treatment of tannery wastewater was resistant to a temperature above 900 ^oC and the loaded amount of sawdust to the filter pot formulation served as the determinant of flow rate and percentage porosity of the filter pot. The slowest flow rate was associated with high amounts of loaded kaolin, concluding that the flow rate of the wastewater through the filter pots increased with porosity. The performance of the nanocomposite pot filters used in this study was attributed to their physicochemical and antibacterial properties as well as large surfaces.

5.2 Recommendations

Based on the analysis and conclusions of the research work, the ensuing recommendations for future research are as follows:

a) Investigations in this study were promising for the development of kaolin/ZnO/TiO_2 nanocomposites at different ratios of the nanoparticles for the production of filter pots in tannery wastewater treatment. Despite the bright future of the nanocomposites, the management of the exhausted nanoadsorbents is a paramount issue and has to be taken care. The end of life (regeneration) of the nanoadsorbents should carried out.

b) The need to further investigate the use of the nanocomposites filter pots in large scale is imperative. This will serve as a low-cost filters in industries for wastewater treatment

applications. Also, it would be interesting to explore different industrial wastewater for comparison and establishment of its possible benefits for other treatment purposes.

c) The information on the mechanical properties of the nanocomposite filter pots such as strength should be provided. The leaching of ZnO and TiO_2 nanoparticles and other elements from kaolin/ZnO/TiO_2 filter pots should be examined by analyzing filtrates using Inductively Coupled Plasma (ICP) technique, in order to know the composition of the filtrates.

d) Nanocomposite filters should be affordable, eco-friendly and add environmental value in the wastewater filtration technique. Attempts should be made to module nanocomposite filter pots production locally and industrially.

e) Further study on leaching of nanocomposite filter pot should be investigated

REFERENCES

Abbas, M., Harrache, Z. & Trari, M. (2019). Removal of gentian violet in aqueous solution by activated carbon equilibrium, kinetics, and thermodynamic study. *Adsorption Science and Technology,* 37(7-8), 1-24.

Abdullah, N.S.A., So'aib, S., & Krishnan, J. (2017). Effect of calcination temperature on ZnO/TiO_2 composite in photocatalytic treatment of phenol under visible light. *Malaysian Journal of Analytical Sciences*, 21(1), 173-181.

Abukhadra, M.R. & Mohamed, A.S. (2019). Adsorption removal of safranin dye contaminants from water using various types of natural zeolite. *Silicon,* 11(3), 1635-1647.

Acosta-Humánez, M., Montes-Vides, L. & Almanza-Montero, O. (2015). Sol-gel synthesis of zinc oxide nanoparticle at three different temperatures and its characterization via XRD, IR and EPR. *DYNA,* 83(195), 224-228.

Adebayo, E.A., Elegbede, J.A. & Oke, M.A. (2021). Nanotechnology and water processing: A review. *The Future of Effluent Treatment Plants*, 2021, 683-714.

Adekeye, D.K., Popoola, O.K., Asaolu, S.S., Adebawore, A.A., Aremu, O.I. & Olabode, K.O. (2019). Adsorption and Conventional Technologies for Environmental Remediation and Decontamination of Heavy Metals: An Overview. *International Journal of Research and Review,* 6(8), 505-516.

Adeyemo, A.A., Adeoye, I.O. & Bello, O.S. (2015). Adsorption of dyes using different types of clay: a review. *Applied Water Science,* 7(2), 543-568.

Adeyi, A.A., Abayomi, T.G., Purkait, M.K. & Mondal, P. (2019). Adsorptive Removal of Phosphate from Aqueous Solution by Magnetic-Supported Kaolinite: Characteristics, Isotherm and Kinetic Studies. *Open Journal of Applied Sciences*, 9(7), 544-563.

Agartan, L., Kapusuz, D., Park, J. & Ozturk, A. (2013). Effect of H_2O/TEOT ratio on photocatalytic activity of sol-gel derived TiO_2 powder. *Nanomaterials and Energy,* 2(6), 280-287.

Aguiar, J.E., Cecilia, J.A., Tavares, P.A.S., Azevedo, D.C.S., Castellón, E.R., Lucena, S.M.P. & Silva-Junior, I.J. (2017). Adsorption study of reactive dyes onto porous clay heterostructures. *Applied Clay Science,* 135, 36-44.

Ahmed, E., Abdulla, H.M., Mohamed, A.H. & El-Bassuony, A.D. (2016). Remediation and recycling of chromium from tannery wastewater using combined chemical-biological treatment system. *Process Safety and Environmental Protection,* 104, 1-10.

Akhter, M., Habib, G. & Qama, S.U. (2018). Application of Electrodialysis in Waste Water Treatment and Impact of Fouling on Process Performance. *Journal of Membrane Science and Technology,* 8(2), 1-8.

Akkari, M., Aranda, P., Belver, C., Bedia, J., Amara, A.B.H. & Ruiz-Hitzky, E. (2018). ZnO/sepiolite heterostructured materials for solar photocatalytic degradation of pharmaceuticals in wastewater. *Applied Clay Science*, 156, 104-109.

Akkari, M., Aranda, P., Mayoral, A., García-Hernández, M., Amarab, A.B. & Ruiz-Hitzkya, E. (2017). Sepiolite nanoplatform for the simultaneous assembly of magnetite and zinc oxide nanoparticles as photocatalyst for improving removal of organic pollutants. *Journal of Hazardous Materials,* 340, 281-290.

Akkari, M., Aranda, P., Rhaiem, H.B., Amara, A.B.H. & Ruiz-Hitzky, E. (2016). ZnO/clay nanoarchitectures: Synthesis, characterization and evaluation as photocatalysts. *Applied Clay Science,* 131, 131-139.

Alemu, T., Lemma, E., Mekonnen, A. & Leta, S. (2016). Performance of pilot scale anaerobic-SBR system integrated with constructed wetlands for the treatment of tannery wastewater. *Environmental Processes*, 3(4), 815-827.

Al-Essa, K. & Khalili, F. (2018). Heavy Metals Adsorption from Aqueous Solutions onto Unmodified and Modified Jordanian Kaolinite Clay: Batch and Column Techniques. *American Journal of Applied Chemistry,* 6(1), 25-34.

Alexander, J.A., Ahmad Zaini, M.A., Surajudeen, A., Aliyu, E.N.U. & Omeiza, A.U. (2019). Surface modification of low-cost bentonite adsorbents-A review. *Particulate Science and Technology*, 37(5), 538-549.

Ali, M.M., Ali, M.L., Islam, M.S. & Rahman, M.Z. (2016). Preliminary assessment of heavy metals in water and sediment of Karnaphuli River, Bangladesh. *Environmental Nanotechnology, Monitoring and Management*, 5, 27-35.

Aljlil, S. A. & Alsewailem, F. D. (2014). Adsorption of Cu and Ni on bentonite clay from waste water. *Athens Journal of Natural & Formal Sciences*, 1(1), 21-30.

Al-Shaeri, M., Satar, R., Ahmed, S. I., Oves, M., Ansari, S.A. & Chibber, S. (2019). Utilization of Doped Nanoparticles of ZnO and TiO_2 as Antimicrobial Agent. *Oriental Journal of Chemistry*, 35(3), 1235-1243.

Alsaleh, K.A., Meuser, H., Usman, A.R., Al-Wabel, M.I. & Al-Farraj, A.S. (2018). A comparison of two digestion methods for assessing heavy metals level in urban soils influenced by mining and industrial activities. *Journal of Environmental Management*, 206, 731-739.

Alshameri, A., He, H., Zhu, J., Xic, Y., Zhu, R., Ma, L. & Tao, Q. (2017). Adsorption of ammonium by different natural clay minerals: Characterization, kinetics and adsorption isotherms. *Applied Clay Science,* 159, 83-93.

American Public Health Association (APHA), (2017). Standard Methods for the Examination of Water and Wastewater, 23rd ed., APHA American Public Health Association, Washington, D.C., 2017.

Amin, M.T., Alazb, A.A. & Shafiq, M. (2015). Adsorptive Removal of Reactive Black 5 from Wastewater Using Bentonite Clay: Isotherms, Kinetics and Thermodynamics. *Sustainability,* 7, 15302-15318.

Anirudhan, T.S. & Ramachandran, M. (2015). Adsorptive removal of basic dyes from aqueous solutions by surfactant modified bentonite clay (organoclay): Kinetic and competitive adsorption isotherm. *Process Safety and Environment Protection,* 95, 215-225

Anjum, M., Miandad, R., Waqas, M., Gehany, F. & Barakat, M.A. (2016). Remediation of wastewater using various nanomaterials. *Arabian Journal of Chemistry,* 1, 1-34.

Aroke, U.O., Abdulkarim, A. & Ogubunka, R.O. (2013). Fourier-transform infrared characterization of kaolin, granite, bentonite and barite. *ATBU Journal of Environmental Technology*, 6(1), 42-53.

Arokianathana, M. S., Muralidharana, V., Irudayarajana, L., Sundaramoorthyb, S., Baddipudia, R. & Palanivela, S. (2019). Recovery and reuse of spent chrome tanning effluent from tannery using electro-oxidation technique. *Desalination and Water Treatment*, 156, 323-330.

Aryanto, D., Jannah, W.N., Sudiro, M.T., Wismogroho, A.S., Sebayang, P., Sugianto, A. & Marwoton, P. (2017). Preparation and structural characterization of ZnO thin films by sol-gel method. *IOP Conf. Series: Journal of Physics: Conference Series*, 817, 1-8.

Asamoah, R. B., Nyankson, E., Annan, E., Agyei-Tuffour, B., Efavi, J. K., Kan-Dapaah, K., Apalangya, V.A., Damoah, L.N.W., Dodoo-Arhin, D., Tiburu, E.K., Kwofie, S.K., Onwona-Agyeman, B. & Yaya, A. (2018). Industrial Applications of Clay Materials from Ghana (A Review). *Oriental Journal of Chemistry,* 34(4), 1719-1734.

Ashraf, R., Riaz, S., Hhaleeq-ur-Rehman, M. & Naseem, S. (2013). Synthesis and Characterization of ZnO Nanoparticles. *Advances in Nano, Biomechanics, Robotics and Energy Research (ANBRE),* 13, 287-296.

Askari, M.B., Banizi, Z.T., Seifia, M., Dehaghi, S.B. & Veisi, P. (2017). Synthesis of TiO_2 nanoparticles and decorated multi-wall carbon nanotube (MWCNT) with anatase TiO_2 nanoparticles and study of optical properties and structural characterization of TiO_2/MWCNT nanocomposite. *Optik,* 149, 447-454.

Asses, N. & Ayed, L. (2021). Physicochemical and biological treatment of textile wastewater. *The Future of Effluent Treatment Plants*, 2021, 307-334.

Atuyambe, L., Neema, S. & Orisakwe, O.E. (2017). Prof Sunita Facknath, Faculty of Agriculture, University of Mauritius Prof Charles Wambebe, International Biomedical Research in Africa, Abuja/Makerere Medical School, Nigeria. International Council for Science (ICSU) Regional Office for African Science. Plan Health and Human well-being.

Avrami, M. (1940). Kinetics of phase change: transformation-time relations for random distribution of nuclei. *The Journal of Chemical Physics,* 8, 212-224.

Awaleh, M.O. & Soubaneh, Y.D. (2014). Waste Water Treatment in Chemical Industries: The Concept and Current Technologies. *Hydrology Current Research,* 5(1), 164-175.

Ayawei, N., Ebelegi, A.N., & Wankasi, D. (2017). Modelling and interpretation of adsorption isotherms. *Journal of Chemistry*, 1, 1-11.

Ayoub Khan, S., Fuzail Siddiqui, M. & Alam Khan, T. (2019). Ultrasonic-assisted synthesis of polyacrylamide/bentonite hydrogel nanocomposite for the sequestration of lead and cadmium from aqueous phase: Equilibrium, kinetics and thermodynamic studies. *Ultrasonics Sonochemistry,* 60, 1-11.

Bagheri, S., Chekin, F. & Abd-Hamid, S.B. (2014). Gel-Assisted Synthesis of Anatase TiO_2 Nanoparticles and Application for Electrochemical Determination of L-Tryptophan. *Russian Journal of Electrochemistry,* 50(10), 947-952.

Bahafid, W., Joutey, N.T., Asri, M., Sayel, H., Tirry, N., El Ghachtouli, N. & Sayel, N.T.H. (2017). Yeast biomass: an alternative for bioremediation of heavy metals. *Yeast-Industrial Applications*, 1, 269-289.

Bahar, M., Mozaffari, M. & Esmaeili, S. (2017). Effect of different alcohols, gelatinizing times, calcination and microwave on characteristics of TiO_2 nanoparticles synthesized by sol-gel method. *Journal of Theoretical and Applied Physics*, 11, 79-86.

Barman, B.C., Juel, M.A.I. & Hashem, M.A. (2017). Tannery Wastewater Treatment Using Low Cost Coagulants with Simple Coagulation-Filtration Process. *Engineering International*, 5(2), 75-82.

Basnet, P., Chanu, T.I., Samanta, D. & Chatterjee, S. (2018). A review on bio-synthesized zinc oxide nanoparticles using plant extracts as reductants and stabilizing agents. *Journal of Photochemistry and Photobiology B: Biology,* 183, 201-221.

Belver, C., Han, C., Rodriguez, J.J., & Dionysiou, D.D. (2017). Innovative W-doped titanium dioxide anchored on clay for photocatalytic removal of atrazine. *Catalysis Today*, 280, 21-28.

Bergaya, F. & Vayer, M. (1997). CEC of clays: measurement by adsorption of a copper ethylenediamine complex. *Applied Clay Science*, 12(3), 275-280.

Bergman, S.L., Sahasrabudhe, G.S., Ji, H., Cava, R.J. & Bernasek, S.L. (2017). Useful X-ray Photoelectron Spectroscopy-Based Chemical Tool: Differential Charging Studies of Complex Composite Materials. *Chemistry of Materials,* 29(10), 4162-4166.

Bezirgiannidis, A., Plesia-Efstathopoulou, A., Ntougias, S. & Melidis, P. (2019). Combined chemically enhanced primary sedimentation and biofiltration process for low cost municipal wastewater treatment. *Journal of Environmental Science and Health, Part A*, 54(12), 1227-1232.

Bhardwaj, R., Bharti, A., Singh, J.P., Chae, K.H., Goyal, N. & Gautam, S. (2018). Structural and electronic investigation of ZnO nanostructures synthesized under different environments. *Heliyon,* 4, 1-21.

Bhattachajee, C., Samanta, H.S. & Das, R. (2016). Influence of Nanoparticles for Wastewater Treatment- A Short Review. *Austin Chemical Engineering,* 3(3), 1036-1041.

Boudjemaa, A. & Gómez-Ruiz, S. (2020). Titanium Oxide-Based Nanomaterials with Photocatalytic Applications in Environmental Chemistry. In *Environmental Nanotechnology*, 4, 215-263.

Boutra, B. & Trari, M. (2017). Solar photodegradation of a textile azo dye using synthesized ZnO/Bentonite. *Water Science and Technology*, 75(5), 1211-1220.

Boyd, G.E., Adamson, A.W. & Myers, L.S. (1947). The exchange adsorption of ions from aqueous solutions by organic zeolites. II. Kinetics. *Journal of American Chemical Society*, 69, 2836-2848.

Briffa, S.M. (2017). *Synthesis and ageing transformations of manufactured metal oxide nanomaterials* (Doctoral dissertation, University of Birmingham), pp. 1-391

Bruanuer, S., Emmett, P.H. & Teller, E. (1938). Adsorption of gases in multimolecular layers. *Journal of American Chemical Society,* 60, 309-316.

Bulta, A.L. & Micheal, G.A.W. (2019). Evaluation of the efficiency of ceramic filters for water treatment in Kambata Tabaro zone, southern Ethiopia. *Environmental Systems Research,* 8(1), 1-15.

Caponi, N., Collazzo, G.C., Jahn, S.L., Dotto, G.L., Mazutti, M.A. & Foletto, E.L. (2017). Use of Brazilian Kaolin as a Potential Low-cost Adsorbent for the Removal of Malachite Green from Coloured Effluents. *Materials Research,* 1, 1-9.

Cardenas, M.A.R., Ali, I., Lai, F.Y., Dawes, L., Thier, R. & Rajapakse, J. (2016). Removal of micropollutants through a biological wastewater treatment plant in a subtropical climate, Queensland-Australia. *Journal of Environmental Health Science and Engineering,* 14(14), 1-10.

Carrier, B., Vandamme, M., Pellenq, R.J.M. & Van Damme, H. (2014). Elastic Properties of Swelling Clay Particles at Finite Temperature upon Hydration. *The Journal of Physical Science,* 118, 8933-8943.

Carrier, B., Wang, L., Vandamme, M., Pellenq, R.J.M., Bornert, M., Tanguy, A. & Van Damme, H. (2013). ESEM Study of the Humidity-Induced Swelling of Clay Films. *Langmuir,* 29, 12823-12833.

Chai, W., Huang, Y., Su, S., Han, G., Liu, J. & Cao, Y. (2017). Adsorption behavior of Zn (II) onto natural minerals in wastewater. A comparative study of bentonite and kaolinite. *Physicochemical Problems of Mineral Processing*, 53, 264-278.

Chandrasekaran, K., Selvaraj, H. & Sundaram, M. (2019). Electrochemical oxidation with the aerobic pretreatment process for sulfate-rich tannery effluent. *Environmental Science and Pollution Research,* 26(12), 12194-12204.

Chang, J.S., Strunk, J., Chong, M.N., Poh, P.E. & Ocon, J.D. (2020). Multi-dimensional zinc oxide (ZnO) nanoarchitectures as efficient photocatalysts: What is the fundamental factor that determines photoactivity in ZnO?. *Journal of Hazardous Materials,* 381, 1-16.

Chaturvedi, S. & Dave, P. N. (2019). Water Purification Using Nanotechnology an Emerging Opportunities. *Chemical Methodologies*, 3(1), 115-144.

Chaudhary, P., Chhokar, V., Kumar, A. & Beniwal, V. (2017). Bioremediation of tannery wastewater. In *Advances in Environmental Biotechnology,* Springer, Singapore, pp. 125-144.

Chen, Y., Xu, X., Fang, J., Zhou, G., Liu, Z., Wu, S., Xu, W., Chu, J. & Zhu, X. (2014). Synthesis of BiOI-TiO2 composite nanoparticles by microemulsion method and study on their photocatalytic activities. *The Scientific World Journal*, 2014, 1-8

Chinoune, K., Bentaleb, K., Bouberka, Z., Nadim, A. & Maschke, U. (2016). Adsorption of reactive dyes from aqueous solution by dirty bentonite. *Applied Clay Science,* 123, 64-75.

Chouchene, B., Chaabane, T.B., Mozet, K., Girot, E., Corbel, S., Balan, L., Medjandi, G. & Schneider, R. (2017). Porous Al-doped ZnO rods with selective adsorption properties. *Applied and Surface Sciences,* 409, 102-110.

Chowdhary, P., Bharagava, R.N., Mishra, S. & Khan, N. (2020). Role of Industries in Water Scarcity and Its Adverse Effects on Environment and Human Health. In *Environmental Concerns and Sustainable Development*, 235-256.

Chowdhury, M., Mostafa, M.G., Biswas, T.K., Mandal, A. & Saha, A.K. (2015). Characterization of the effluents from leather processing industries. *Environmental Processes*, 2(1), 173-187.

Clay Minerals Society (2018). The Clay Minerals Society Glossary of Clay Science. The Clay Minerals Society, Chantilly, VA. pp. 1-342.

Cook, S., Dylla, M.T., Rosenberg, R.A., Mansley, Z.R., Snyder, G.J., Marks, L.D. & Fong, D.D. (2019). The Vacancy-Induced Electronic Structure of the $SrTiO_{3-\delta}$ Surface. *Advanced Electronic Materials*, *5*(1), 1-9.

da Silva Lopes, J., Rodrigues, W.V., Oliveira, V.V., Braga, A.D.N.S., da Silva, R.T., França, A.A.C., da Paz, E.C., Osajima, J.A. & da Silva Filho, E.C. (2019). Modification of kaolinite from Pará/Brazil region applied in the anionic dye photocatalytic discoloration. *Applied Clay Science*, 168, 295-303.

Danks, A.E., Hall, S.R. & Schnepp, Z.J.M.H. (2016). The evolution of 'sol-gel'chemistry as a technique for materials synthesis. *Materials Horizons*, 3(2), 91-112.

Dargo, H. & Ayalew, A. (2014). Tannery waste water treatment: a review. *International Journal of Emerging Trends in Science and Technology*, 1(9), 1488-1494.

Dariani, R.S., Esmaeili, A., Mortezaali, A., & Dehghanpour, S. (2016). Photocatalytic reaction and degradation of methylene blue on TiO_2 nano-sized particles. *Optik*, 127, 714-7154.

Dazzi, A. & Prater, C. B. (2017). AFM-IR: technology and applications in nanoscale infrared spectroscopy and chemical imaging. *Chemical Reviews*, 117(7), 5146-5173.

De Boer, J.H. (1953). *The Dynamical Character of Adsorption* (Oxford University Press, Oxford, 1953). . Aufl. X V, 239 S., 45 Abb. gebd. s. 30.-. Angewandte Chemie, 65(16), 431-431.

De Gisi, S., Lofrano, G., Grassi, M. & Notarnicola, M. (2016). Characteristics and adsorption capacities of low-cost sorbents for wastewater treatment: A review. *Sustainable Materials and Technologies*, 9, 10-40.

de Oliveira da Mota, I., Adilson de Castro, J., de Góes Casqueira, R. & de Oliveira Junior, A.G. (2015). Study of electroflotation method for treatment of wastewater from washing soil contaminated by heavy metals. *Journal of Material Research and Technology*, 4(2), 109-113.

de Oliveira-Pereira, L., Sales, I.M., Zampiere, L.P., Vieira, S.S., do Rosário Guimarães, I. & Magalhães, F. (2019). Preparation of magnetic photocatalysts from TiO_2, activated carbon and iron nitrate for environmental remediation. *Journal of Photochemistry and Photobiology A: Chemistry*, 382, 1-9.

Dediu, V., Musat, V. & Cernica, I. (2019). Nb-TiO_2/ZnO nanostructures for chemoresistive alcohol sensing. *Applied Surface Science*, 488, 70-76.

Dědková, K., Janíková, B., Matějová, K., Peikertová, P., Neuwirthová, L., Holešinský, J. & Kukutschová, J. (2015). Preparation, characterization and antibacterial properties of

ZnO/kaoline nanocomposites. *Journal of Photochemistry and Photobiology B: Biology*, 148, 113-117.

de-Luna, M.D.G., Laciste, M.T., Tolosa, N.C. & Lu, M. (2018). Effect of catalyst calcination temperature in the visible light photocatalytic oxidation of gaseous formaldehyde by multi-element doped titanium dioxide. *Environmental Science and Pollution Research*, 25(15), 15216-15225.

Devi, M., Panigrahi, M.R. & Singh, U.P. (2014). Synthesis of TiO_2 nanocrystalline powder prepared by sol-gel technique using TiO_2 powder reagent. *Advances in Applied Science Research*, 5(3) 140-145.

Divya, C., Janarthanan, B., Premkumar, S. & Chandrasekaran, J. (2017). Titanium Dioxide Nanoparticles Preparation for Dye Sensitized Solar Cells Applications using Sol-Gel Method. *Journal of Advanced Physical Sciences*, 1(1), 4-6.

Dixit, S., Yadav, A., Dwivedi, P.D. & Das, M. (2015) Toxic hazards of leather industry and technologies to combat threat: a review. *Journal of Cleaner Production*, 87, 39-49.

Djellabi, R., Ghorab, M.F., Cerrato, G., Morandi, S., Gatto, S., Oldani, V., Di Michele, A. & Bianchi, C.L. (2014). Photoactive TiO_2–montmorillonite composite for degradation of organic dyes in water. *Journal of Photochemistry and Photobiology A: Chemistry*, 295, 57-63.

Dodoo-Arhin, D., Buabeng, F.P., Mwabora, J.M., Amaniampong, P.N., Agbe, H., Nyankson, E., Obada, D.O., & Asiedu, N.Y. (2018). The effect of titanium dioxide synthesis technique and its photocatalytic degradation of organic dye pollutants. *Heliyon*, 4(7), 1-23.

Donkadokula, N. Y., Kola, A. K., Naz, I. & Saroj, D. (2020). A review on advanced physico-chemical and biological textile dye wastewater treatment techniques. *Reviews in Environmental Science and Biotechnology*, 19, 543-560

Dubinin, M.M. & Radushkevich, L.V. (1947). Equation of the characteristic curve of activated charcoal. *Proceedings of the Academy of Sciences, Physical Chemistry Section*, 55, 331-333.

Ealias, A.M. & Saravanakumar, M.P. (2017). A review on the classification, characterisation, synthesis of nanoparticles and their application. In *IOP Conference Series of Material and Science Engineering*, 263, 1-16.

Ekpunobi, U.E., Agbo, S.U. & Ajiwe, V.I.E. (2018). Evaluation of the mixtures of clay, diatomite, and sawdust for production of ceramic pot filters for water treatment interventions using locally sourced materials. *Journal of Environmental Chemical Engineering*, 7(1), 1-9.

EL-Mekkawi, D.M., Labib, A.A., Mousa, H.A., Galal, H.R. & and Mohamed, W.A.A. (2017). Preparation and Characterization of Nano Titanium Dioxide Photocatalysts via Sol Gel Method over Narrow Ranges of Varying Parameters. *Oriental Journal of Chemistry*, 33(1), 41-51.

El-Naggar, I. M., Ahmed, S.A., Shehata, N., Sheneshen, E.S., Fathy, M. & Shehata, A. (2019). A novel approach for the removal of lead (II) ion from wastewater using Kaolinite/Smectite natural composite adsorbent. *Applied Water Science*, 9(1). 1-7.

Elovich, S.Y. & Larinov, O.G. (1962). Theory of adsorption from solutions of non-electrolytes on solid (I) equation adsorption from solutions and the analysis of its simplest form, (II) verification of the equation of adsorption isotherm from solutions. *Izvestiya Akademii Nauk SSSR, Otdelenie Khimicheskikh Nauk*, 2(2), 209.

Enang, R. K., Yerima, B. P. K., Kome, G. K., & Van Ranst, E. (2018). Assessing the effectiveness of the Walkley-Black method for soil organic carbon determination in tephra soils of Cameroon. *Communications in Soil Science and Plant Analysis*, 49(19), 2379-2386.

Erdem, B., Erdem, M. & Özcan, A.S. (2016). Adsorption of Reactive Black 5 onto quaternized 2-dimethylaminoethyl methacrylate based polymer/clay nanocomposites. *Adsorption*, 22(4-6), 767-776.

Fadzil, M.A., Muhd Nurhasri, M.S., Norliyati, M.A., Hamidah, M.S., Wan Ibrahim, M.H. & Assrul, R. Z. (2017). Characterization of Kaolin as Nano Material for High Quality Construction. MATEC Web of Conferences, 103, 09019.

Fatiha, M., & Belkacem, B. (2016). Adsorption of methylene blue from aqueous solutions using natural clay. *Journal of Materials and Environmental Science*, 7(1), 285-292.

Fernández-Catalá, J., Cano-Casanova, L., Lillo-Ródenas, M.A., Berenguer-Murcia, A. & Cazorla-Amorós, D. (2017). Synthesis of TiO_2 with Hierarchical Porosity for the Photooxidation of Propene. *Molecules*, 22, 2243-2259.

Fersi, C., Gamra, A.B., Bozrati, H., Gorgi, C. & Irmani, A. (2018). Characterizing the performance of coagulation-flocculation using natural coagulants as pretreatment of tannery wastewater. *Journal of Materials and Environmental Sciences*, 9(8), 2379-2386.

Flory, P.J. (1941). Thermodynamics of High Polymer Solutions. *The Journal of Chemical Physics*, 9, 660.

Freundlich, H.M.F. (1906). Over the adsorption in solution. *The Journal of Physical Chemistry*, 57, 385-470.

Fu, R., Yin, Q., Guo, X., Tong, X. & Wang, X. (2017). Evolution of mesoporous TiO_2 during fast sol-gel synthesis. *Research on Chemical Intermediates*, 43(11), 6433-6445.

Futalan, C.M., Huang, Y.S., Chen, J.H. & Wan, M.W. (2018). Arsenate removal from aqueous solution using chitosan-coated bentonite, chitosan-coated kaolinite and chitosan-coated sand: parametric, isotherm and thermodynamic studies. *Water Science and Technology*, 78(3), 676-689.

Gatta, G., Gagliardi, A., Disciglio, G., Lonigro, A., Francavilla, M., Tarantino, E. & Giuliani, M. (2018). Irrigation with Treated Municipal Wastewater on Artichoke Crop: Assessment of Soil and Yield Heavy Metal Content and Human Risk. *Water*, 10(3), 255-272.

Gehrke, I., Geiser, A. & Somborn-Schulz, A. (2015). Innovations in nanotechnology for water treatment. *Nanotechnology, Science and Applications*, 8, 1-17.

Geyikco, F. & Buyukgungor, H. (2013). Factorial Experimental Design for Adsorption Silver ions from Water onto Montmorillonite. *Acta Geodynamic Geomater*, 10(3), 363-370.

Golsheikh, A.M., Kamali, K.Z., Huang, N.M. & Zak, A.K. (2018). Effect of calcination temperature on performance of ZnO nanoparticles for dye-sensitized solar cells. *Powder Technology*, 329, 282-287.

Gong, W., Jiang, M., Han, P., Liang, G., Zhang, T. & Liu, G. (2019). Comparative analysis on the sorption kinetics and isotherms of fipronil on nondegradable and biodegradable microplastics. *Environmental Pollution*, 254, 1-9.

González, P. & Pliego-Cuervo, Y.B. (2014). "Adsorption of Cd(II), Hg(II) and Zn(II) from aqueous solution using mesoporous activated carbon produced from *Bambusa vulgaris striata*." *Chemical Engineering and Research Design*, 92(11), 2715-2724.

Guillaume, P.L.A., Chelaru, A.M., Visa, M. & Lassiné, O. (2018). "Titanium Oxide-Clay" as Adsorbent and Photocatalysts for Wastewater Treatment. *Journal of Membrane Science and Technology*, 8(1), 176-186.

Gusain, R., Gupta, K., Joshi, P. & Khatri, O.P. (2019). Adsorptive removal and photocatalytic degradation of organic pollutants using metal oxides and their composites: A comprehensive review. *Advances in Colloid and Interface Science*, 272, 1-23.

Hadjltaief, H.B., Gálvez, M.E., Zina, M.B., & Da Costa, P. (2019). TiO_2/clay as a heterogeneous catalyst in photocatalytic/photochemical oxidation of anionic reactive blue 19. *Arabian Journal of Chemistry*, 12(7), 1454-1462.

Hadjltaief, H. B., Zina, M. B., Galvez, M. E. & Da Costa, P. (2016). Photocatalytic degradation of methyl green dye in aqueous solution over natural clay-supported ZnO-TiO_2 catalysts. *Journal of Photochemistry and Photobiology A: Chemistry*, 315, 25-33.

Hadjltaief, H.B., Ameur, S.B., Da Costa, P., Zina, M.B. & Galvez, M.E. (2018). Photocatalytic decolorization of cationic and anionic dyes over ZnO nanoparticle immobilized on natural Tunisian clay. *Applied Clay Science*, 152, 148-157.

Hadjltaief, H.B., Zina, M.B., Galvez, M.E. & Costa, P.D. (2017). Photocatalytic degradation of methyl green dye in aqueous solution over natural clay-supported ZnO-TiO_2 catalysts. *Journal of Photochemistry and Photobiology A: Chemistry*, 315, 25-33.

Haider, A.J., Al-Anbari. R.H., Kadhim, G.R. & Salame, C.T. (2017). Exploring potential Environmental application TiO_2 Nanoparticles. *Energy Procedia*, 119, 332-345.

Hajjaji, W., Andrejkovičová, S., Pullar, R.C., Tobaldi, D.M., Lopez-galindo, A., Jammousi, F., Rocha, F. & Labrincha, J.A. (2016). Effective removal of anionic and cationic dyes by kaolinite and TiO_2/kaolinite composites. *Clay Minerals*, 51, 19-27.

Hall, S.K. (2020). Metal exposure and toxic responses. In *chemical exposure and toxic responses* (pp. 21-37). CRC Press.

Hamadneh, I., Alatawi, A., Zalloum, R., Albuqain, R., Alsotari, S., Khalili, F.I. & Al-Dujaili, A.H. (2019). Comparison of Jordanian and standard diatomaceous earth as an adsorbent for removal of Sm(III) and Nd(III) from aqueous solution. *Environmental Science and Pollution Research*, 26(20), 20969-20980.

Hansen, É., de Aquim, P.M. & Gutterres, M. (2021). Environmental assessment of water, chemicals and effluents in leather post-tanning process: A review. *Environmental Impact Assessment Review*, 89, 1-7.

Haq, S., Rehman, W., Waseem, M., Javed, R., Rehman, M. & Shahid, M. (2018). Effect of heating on the structural and optical properties of TiO_2 nanoparticles: antibacterial activity. *Applied Nanoscience*, 8, 11-18.

Harrache, Z., Abbas, M., Aksil, T. & Trari, M. (2019). Thermodynamic and kinetics studies on adsorption of Indigo Carmine from aqueous solution by activated carbon. *Microchemical Journal*, 144, 180-189.

Hasan, A. M., Dey, S. C., Rahman, M. M., Zakaria, A. M., Sarker, M., Ashaduzzaman, M. D. & Shamsuddin, S. M. (2020). A kaolinite/TiO_2/ZnO -based novel ternary composite for photocatalytic degradation of anionic azo dyes. *Bulletin of Materials Science*, 43(1), 1-9.

Hashem, M.A., Hasan, M., Momen, M.A., Payel, S. & Nur-A-Tomal, M.S. (2020). Water hyacinth biochar for trivalent chromium adsorption from tannery wastewater. *Environmental and Sustainability Indicators*, 5, 1-6.

Hayle, S.T. & Gonfa, G.G. (2014). Synthesis and characterization of titanium oxide nanomaterials using sol-gel method. *American Journal of Nanoscience and Nanotechnology*, 2(1), 1-7.

He, F., Ma, F., Li, J., Li, T. & Li, G. (2014). Effect of calcination temperature on the structural properties and photocatalytic activities of solvothermal synthesized TiO_2 hollow nanoparticles. *Ceramic International*, 40, 6441-6446.

Hosseini, M., Haghighatzadeh, A. & Mazinani, B. (2019). Enhanced third-order optical susceptibility in heterogeneous wurtzite ZnO/anatase TiO_2 core/shell nanostructures via controlled TiO_2 shell thickness. *Optical Materials*, 92, 1-10.

Huang, X., Qu, Y., Cid, C.A., Finke, C., Hoffmann, M.R., Lim, K. & Jiang, S.C. (2016). Electrochemical disinfection of toilet wastewater using wastewater electrolysis cell. *Water Research,* 92, 164-172.

Huang, Z., Li, Y., Chen, W., Shi, J., Zhang, N., Wang, X., Li, Z., Gao, L. & Zhang, Y. (2017). Modified bentonite adsorption of organic pollutants of dye wastewater. *Materials Chemistry and Physics,* 202, 266-276.

Iaiche, S. & Djelloul, A. (2015). $ZnO/ZnAl_2O_4$ Nanocomposite Films Studied by X-Ray Diffraction, FTIR, and X-Ray Photoelectron Spectroscopy. *Journal of Spectroscopy*, 2015, 1-9.

Ibrahim, M.M. & Asal, S. (2017). Physicochemical and photocatalytic studies of Ln^{3+}- ZnO for water disinfection and wastewater treatment applications. *Journal of Molecular Structure,* 1149, 404-413.

Inkson, B.J. (2016). Scanning electron microscopy (SEM) and transmission electron microscopy (TEM) for materials characterization. In *Materials characterization using nondestructive evaluation (NDE) methods* (pp. 17-43). Woodhead Publishing.

Islam, M. & Basu, S. (2015). Effect of morphology and pH on (photo) electrochemical degradation of methyl orange using TiO_2/Ti mesh photocathode under visible light. *Journal of Environmental Chemical Engineering*, 3, 2323-2330.

Islam, S.Z., Nagpure, S., Kim, D.Y. & Rankin, S.E. (2017). Synthesis and Catalytic Applications of Non-Metal Doped Mesoporous Titania. *Inorganics,* 5(15), 1-43.

Jahan, M.A.A., Akhtar, N., Khan, N.M.S., Roy, C.K., Islam, R. & Nurunnabi (2014). Characterization of tannery wastewater and its treatment by aquatic macrophytes and algae. *Bangladesh Journal of Scientific and Industrial Research,* 49(4), 233-242.

Jeevanandam, J., Barhoum, A., Chan, Y.S., Dufresne, A. & Danquah, M.K. (2018). Review on nanoparticles and nanostructured materials: history, sources, toxicity and regulations. *Beilstein Journal of Nanotechnology*, 9, 1050-1074.

Ji, Z. (2018). Treatment of heavy-metal wastewater by vacuum membrane distillation: effect of wastewater properties. *IOP Conf. Series: Earth and Environmental Science,* 108, 1-4.

Jossens, L., Prausnitz, J.M., Fritz, W., Schlunder, E.U. & Myers, A.L. (1978). "Thermodynamics of multi-solute adsorption from dilute aqueous solutions." *Chemical Engineering Science,* 33(8), 1097-1106.

Jovanovic, D.S. (1969). Physical adsorption of gases I: isotherms for monolayer and multilayer adsorption. *Colloid Polymer Science,* 235, 1203-1214.

Jura, G. & Harkins, W.D. (1944). Surfaces of Solids. XI. Determination of the Decrease (π) of Free Surface Energy of a Solid by an Adsorbed Film. *Journal of American Chemical Society,* 66(8), 1366-1373.

Jurablu, S., Farahmandjou, M. & Firoozabadi, T.P. (2015). Sol-Gel Synthesis of Zinc Oxide (ZnO) Nanoparticles: Study of Structural and Optical Properties. *Journal of Sciences, Islamic Republic of Iran,* 26(3), 281-285.

Kaneva, N., Bojinova, A. & Papazova, K. (2016). Photocatalytic degradation of Reactive Black 5 and Malachite Green with ZnO and lanthanum doped nanoparticles. *Journal of Physics: Conference Series,* 682, 1-7.

Kavitha, M., Gopinathan, C. & Pandi, P. (2014). Synthesis and Characterization of TiO_2 Nanopowders in Hydrothermal and Sol-Gel Method. *International Journal of Advancements in Research and Technology,* 2(4), 102-108.

Kayani, Z.N., Saleemi, F, & Batool, I. (2015). Effect of calcination temperature on the properties of ZnO nanoparticles. *Applied Physics A: Material Science and Processing,* 1, 1-8.

Khaki, M.R.D., Shafeeyan, M.S., Raman, A.A.A. & Daud, W.M.A.W. (2017). Application of doped photocatalysts for organic pollutant degradation-A review. *Journal of Environmental Management*, 198, 78-94.

Khalid, N.R., Majid, A., Tahir, M.B., Niaz, N.A. & Khalid, S. (2017). Carbonaceous-TiO_2 nanomaterials for photocatalytic degradation of pollutants: A review. *Ceramics International*, 43(17), 14552-14571.

Khalid, S., Shahid, M., Natasha, Bibi, I., Sarwar, T., Shah, A. & Niazi, N. (2018). A Review of Environmental Contamination and Health Risk Assessment of Wastewater Use for Crop Irrigation with a Focus on Low and High-Income Countries. *International Journal of Environmental Research and Public Health,* 15(5), 895-930.

Khan, H. (2017). Sol-gel synthesis of TiO_2 from $TiOSO_4$: characterization and UV photocatalytic activity for the degradation of 4-chlorophenol. *Reaction Kinetics, Mechanisms and Catalysis*, 121(2), 811-832.

Khan, I., Saeed, K. & Khan, I. (2017). Nanoparticles: Properties, Applications and Toxicities. *Arabian Journal of Chemistry,* 5, 1-23.

Khan, I., Saeed, K. & Khan, I. (2019). Nanoparticles: Properties, applications and toxicities. *Arabian Journal of Chemistry,* 12(7), 908-931.

Kiseler, A.V.C. (1958). "Vapour adsorption in the formation of adsorbate Molecule Complexes on the surface." *Kolloid Zhur,* 20, 338-348.

Kloprogge, J.T. (2019). *Spectroscopic Methods in the Study of Kaolin Minerals and Their Modifications*. Springer Mineralogy, pp. 1-434.

Koble, R.A. & Corrigan, T.E. (1952). "Adsorption isotherms for pure hydrocarbons." *Industrial and Engineering Chemistry*, 44(2), 383-387.

Konduri, M.K.R. & Fatehi, P. (2017). Influence of pH and ionic strength on flocculation of clay suspensions with cationic xylan copolymer. *Colloids and Surfaces A*, 530, 20-32.

Korpe, S., Bethi, B., Sonawane, S.H. & Jayakumar, K.V. (2019). Tannery wastewater treatment by cavitation combined with advanced oxidation process (AOP). *Ultrasonics Sonochemistry*, 59, 104723.

Koutu, V., Dhakar, R., Ojha, P., Shastri, L. & Malik, M.M. (2020). Structural and optical studies of TiO_2:Ag_2O nanocomposite by sol-gel method. *Materials Science Poland*, 38(2), 263-270.

Kumar, A., Yadav, N., Bhatt, M., Mishra, N.K., Chaudhary, P. & Singh, R. (2015). Sol-Gel Derived Nanomaterials and It's Applications: A Review. *Research Journal of Chemical Sciences*, 5(12), 98-105.

Kumar, S., Maurya, V.K. & Saxena, S.K. (2020). *Emerging and Re-emerging Water-Associated Infectious Diseases*. In Water-Associated Infectious Diseases, pp. 27-51.

Kumar, S.G. & Rao, K.K. (2014). Polymorphic phase transition among the titania crystal structures using a solution-based approach: from precursor chemistry to nucleation process. *Nanoscale*, 6(20), 11574-11632.

Ladshaw, A.P., Wiechert, A.I., Welty, A.K., Lyon, K.L., Law, J.D., Jubin, R.T., Tsouris, C. & Yiacoumi, S., (2019). Adsorbents and adsorption models for capture of Kr and Xe gas mixtures in fixed-bed columns. *Chemical Engineering Journal*, 375, 1-11.

Lagergren, S. (1898). About the theory of so-called adsorption of soluble substances. *Kungliga Svenska Vetenskapsakademiens*, 4, 1-39.

Langat, N.K. (2018). *Isolation and Molecular Characterization of Chromium Reducing Bacterial Strains from Selected Chrome Contaminated Tannery Waste Sites in Nairobi, Kenya* (Doctoral dissertation, COHES-JKUAT), pp. 1-60.

Langmuir, I. (1916). The constitutional and fundamental properties of solids and liquids. *Journal of American Chemical Society*, 38, 2221-2295.

Laysandra, L., Sari, M.W.M.K., Soetaredjo, F.E., Foe, K., Putro, J.N., Kurniawan, A., Ju, Y. & Ismadji, S. 2017. Adsorption and photocatalytic performance of bentonite-titanium dioxide composites for methylene blue and rhodamine B decoloration. *Heliyon*, 3, 1-22.

Le Luu, T., Tien, T.T., Duong, N.B. & Phuong, N.T.T. (2020). Tannery Wastewater Treatment after Biological Pretreatment by Using Electrochemical Oxidation. In *Frontiers in Water-Energy-Nexus-Nature-Based Solutions, Advanced Technologies and Best Practices for Environmental Sustainability*, 61-163.

Leila, D., Mar, L.G., Fatima, B., Abddelyamine, N., Ali, B. & Nacereddine, H. (2018). Effect of polyethylene glycol and propyltrimethoxysilane on structural and optical properties of zinc oxide nanoparticles synthesized by sol-gel process. *Journal of Theoretical and Applied Physics*, 12(3), 159-167.

León, A., Reuquen, P., Garín, C., Segura, R., Vargas, P., Zapata, P. & Orihuela, P. A. (2017). FTIR and Raman characterization of TiO_2 nanoparticles coated with polyethylene glycol as carrier for 2-methoxyestradiol. *Applied Sciences*, 7(1), 49-57.

Li, H., Wang, H., Liu, Q., Tan, Y., Jiang, N. & Lin, Y. (2016). Evaporation process for treating high-salinity industrial wastewater at low temperatures and ambient pressure. *Desalination and Water Treatment*, 1, 1-13.

Lin, D., Zhou, S., Lu, L., Shi-yang, C., Ling-fang, Y., Xiu-zhen, Y, & Li-shan, L. (2104). Adsorption of hexavalent chromium onto kaolin clay-based adsorbent. *Journal of Central South University*, 21, 3918-3926.

Lin, J.C., Sopajaree, K., Jitjanesuwan, T. & Lu, M. (2018). Application of visible light on copper-doped titanium dioxide catalyzing degradation of chlorophenols. *Separation and Purification Technology,* 191, 233-243.

Liu, L., Ou, H., Hong, K. & Wang, L. (2018). Evidence of a strong electron–hole separation effect in ZnO@TiO_2 core/shell nanowires. *Journal of Alloys and Compounds*, 749, 217-220.

Liu, R., Ji, Z., Wang, J. & Zhang, J. (2018). Mesocrystalline TiO_2/sepiolite composites for the effective degradation of methyl orange and methylene blue. *Frontiers of Materials Science*, 12(3), 292-303.

Liu, Z., Wang, R., Kan, F. & Jiang, F. (2014). Synthesis and Characterization of TiO_2 Nanoparticles. *Asian Journal of Chemistry*, 26(3), 655-659.

Lu, H., Wang, J., Wang, T., Wang, N., Bao, Y. & Hao, H. (2017). Crystallization techniques in wastewater treatment: An overview of applications. *Chemosphere,* 173, 474-484.

Lukman, S., Essa, M.H., Mu'azu, N.D., Bukhari, A. & Basheer, C. (2013). Adsorption and Desorption of Heavy Metals onto Natural Clay Materials: Influence of Initial pH. *Journal of Environmental Science and Technology*, 6(1), 1-15.

Mabrouki, H., & Akretche, D.E. (2015). Diclofenac potassium removal from water by adsorption on natural and pillared clay. *Desalination and Water Treatment,* 57(13), 6033-6043.

Magdy, A., Fouad, Y.O., Abdel-Aziz, M.H. & Konsowa, A.H. (2017). Synthesis and characterization of Fe_3O_4/kaolin magnetic nanocomposite and its application in wastewater treatment. *Journal of Industrial and Engineering Chemistry*, 56, 299-311.

Mahammedi, F. & Benguella, B. (2016). Adsorption of methylene blue from aqueous solutions using natural clay. *Journal of Materials and Environmental Sciences*, 7(1), 85-292.

Mahamudul H.M.D., Hosain, S., Asaduzzaman, A. M., Haque, M.A. & Roy, U.K. (2016). Prevalence of Health Diseases among Bangladeshi Tannery Workers and associated Risk factors with Workplace Investigation. *Journal of Pollution Effects and Control*, 4(4), 175-177.

Manikandan, B., Endo, T., Kaneko, S., Murali, K.R. & John, R. (2018). Properties of sol gel synthesized ZnO nanoparticles. *Journal of Materials Science: Materials in Electronics*, 29(11), 9474-9485.

Manikandan, B., Endo, T., Kaneko, S., Murali, K.R. & John, R. (2017). Properties of sol gel synthesized ZnO nanoparticles. *Journal of Materials Science: Materials in Electronics*, 29(11), 9474-9485.

Marco-Brown, J.L., Guz, L., Olivelli, M.S., Schampera, B., Sánchez, R.T., Curutchet, G. & Candal, R. (2018). New insights on crystal violet dye adsorption on montmorillonite: kinetics and surface complexes studies. *Chemical Engineering Journal*, 333, 495-504.

Mast, J., Verleysen, E. & De Temmerman, P.J. (2015). Physical characterization of nanomaterials in dispersion by transmission electron microscopy in a regulatory framework. In *Advanced Transmission Electron Microscopy*, 1, 249-270.

Matter, F., Luna, A.L. & Niederberger, M. (2019). From colloidal dispersions to aerogels: How to master nanoparticle gelation. *Nano Today*, 30, 1-21.

Mekatel, E., Amokrane, S., Aid, A., Nibou, D. & Trari, M. (2015). Adsorption ofmethyl orange on nanoparticles of a synthetic zeolite NaA/CuO. *ComptesRendus Chimie*, 18, 336-344.

MiarAlipour, S., Friedmann, D., Scott, J. & Amal, R. (2017). TiO_2/porous adsorbents: Recent advances and novel applications. *Journal of Hazardous Material*, 341, 404-423

MiarAlipour, S., Friedmann, D., Scott, J. & Amal, R. (2018). TiO_2/porous adsorbents: Recent advances and novel applications. *Journal of Hazardous Materials*, 341, 404-423.

Mirjalili, F., Manafi, S. & Farahbakhsh, I. (2017). Preparation and Characterization of TiO_2 Nanoparticles Prepared by Sol-Gel Method. *Advanced Ceramics Progress*, 3(3), 38-47.

Mishra, A., Mehta, A., Sharma, M. & Basu, S. (2017). Enhanced heterogeneous photodegradation of VOC and dye using microwave synthesized TiO_2/Clay nanocomposites: a comparison study of different type of clays. *Journal of Alloys and Compounds*, 694, 574-580.

Missengue, R.N.M. (2012). Silver/Zeolite Nanocomposite Based Clay Filters for Water Disinfection. A thesis submitted in fulfilment of the requirements for the degree of Magister Scientiae in the Department of Chemistry, University of the Western Cape. pp. 29-30.

Mitra, S., Sarkar, A. & Sen, S. (2017). Removal of chromium from industrial effluents using nanotechnology: a review. *Nanotechnology for Environmental Engineering*, 2(1), 1-14.

Modwi, A., Abbo, M.A., Hassan, E.A. & Houas, A. (2016). Effect of annealing on physicochemical and photocatalytic activity of Cu5% loading on ZnO synthesized by sol-gel method. *Journal of Material Science: Materials in Electron*, 27(12), 12974-12984.

Mohan, A.C. & Renjanadevi, B. (2016). Preparation of Zinc Oxide Nanoparticles and its Characterization Using Scanning Electron Microscopy (SEM) and X-Ray Diffraction (XRD). *Procedia Technology*, 24, 761-766.

Mohite, V.S., Mahadik, M.A., Kumbhar, S.S., Kothavale, V.P., Moholkar, A.V., Rajpure, K.Y. & Bhosale, C.H. (2015). Photo-electrocatalytic degradation of benzoic acid using sprayed TiO_2 thin films. *Ceramic International*, 41, 2202-2208.

Mohsenipour, M., Shahid, S., & Ebrahimi, K. (2015). Nitrate Adsorption on Clay Kaolin: Batch Tests. *Journal of Chemistry*, 1, 1-7.

Mokhena, T.C., John, M.J., Sibeko, M.A., Agbakoba, V.C., Mochane, M.J., Mtibe, A., Mokhothu, T.H., Motsoeneng, T.S., Phiri, M.M., Phiri, M.J. & Hlangothi, P.S. (2020). Nanomaterials: Types, Synthesis and Characterization. In *Nanomaterials in Biofuels Research*, 1, 115-141.

Morales, J., Maldonado, A. & Olvera, M.D.L.L. (2013, September). Synthesis and characterization of nanoestructured TiO_2 anatase-phase powders obtained by the homogeneous precipitation method. In *2013 10th International Conference on Electrical Engineering, Computing Science and Automatic Control (CCE)* (pp. 391-394). IEEE.

Motazedian, F., Wu, Z., Zhang, J., Shariat, B.S., Jiang, D., Martyniuk, M., Liu, Y. & Yang, H. (2019). Determining intrinsic stress and strain state of fibre-textured thin films by X-ray diffraction measurements using combined asymmetrical and Bragg-Brentano configurations. *Materials and Design*, 181, 1-8.

Motshekga, S.C., Ray, S.S., Onyango, M.S. & Momba, M.N.B. (2016). Development of Silver and Zinc Oxide Decorated Nanoclay Containing Polymeric Composites for Water Disinfection Applications. *AIP Conference Proceedings*, 1664, 1-5.

Mouiya, M., Abourriche, A., Bouazizi, A., Benhammou, A., El Hafiane, Y., Abouliatim, Y., Nibou, L., Oumam, M., Ouammou, M., Smith, A. & Hannache, H. (2018). Flat ceramic microfiltration membrane based on natural clay and Moroccan phosphate for desalination and industrial wastewater treatment. *Desalination*, 427, 42-50.

Mouiya, M., Bouazizi, A., Abourriche, A., Benhammou, A., El Hafiane, Y., Ouammou, M., Abouliatim, Y., Younssi, S.A., Smith, A. & Hannache, H. (2019). Fabrication and characterization of a ceramic membrane from clay and banana peel powder: Application to industrial wastewater treatment. *Materials Chemistry and Physics,* 227, 291-301.

Mourdikoudis, S., Pallares, R.M. & Thanh, N.T.K. (2018). Characterization techniques for nanoparticles: comparison and complementarity upon studying nanoparticle properties. *Nanoscale,* 10(27), 12871-12934.

Mousa, K.M. & Hadi, H.J. (2016). Coagulation/Flocculation Process for Produced Water Treatment. *International Journal of Current Engineering and Technology,* 6(2), 551-555.

Moussaoui, R., Elghniji, K., Mosbah, M.B., Elaloui, E. & Moussaoui, Y. (2017). Sol-gel synthesis of highly TiO_2 aerogel photocatalyst via high temperature supercritical drying. *Journal of Saudi Chemical Society,* 21(6), 751-760.

Mrad, M., Chouchene, B. & Chaabane, T.B. (2018). Effects of zinc precursor, basicity and temperature on the aqueous synthesis of ZnO nanocrystals. *South African Journal of Chemistry,* 71(1), 103-110.

Mu'azu, N.D. & Jarrah, N. (2017). Influence of Bentonite Proportion in Natural Clay on Pb^{2+} ions Sorption: Response Surface Methodology, Kinetics and Equilibrium Studies. *Soil and Sediment Contamination: An International Journal,* 26(78), 691-708.

Muniz-Miranda, M., Zoppi, A., Muniz-Miranda, F. & Calisi, N. (2020). Palladium Oxide Nanoparticles: Preparation, Characterization and Catalytic Activity Evaluation. *Coatings,* 10(3), 207.

Mutuma, B.K., Shao, G.N., Kim, W.D. & Kim, H.T. (2015). Sol-gel synthesis of mesoporous anatase-brookite and anatase-brookite-rutile TiO_2 nanoparticles and their photocatalytic properties. *Journal of Colloid Interface and Science,* 442, 1-7.

Naik, P.K. (2017). Water crisis in Africa: myth or reality? *International Journal of Water Resources Development*, 33(2), 326-339.

Nasirian, M. & Mehrvar, M. (2016). Modification of TiO_2 to Enhance Photocatalytic Degradation of Organics in Aqueous Solutions. *Journal of Environmental Chemical Engineering,* 4, 4072-4082.

National Environmental Standards and Regulations Enforcement Agency (Establishment) (NESREA) (2009). S.I. No. 28 of 2009.

Novikova, L. & Belchinskaya, L. (2016). Adsorption of Industrial Pollutants by Natural and Modified Aluminosilicates. Clays, Clay Minerals and Ceramic Materials Based on Clay Minerals. IntechOpen Limited, London, SE1 9SG, United Kingdom, pp. 89-128

Oladoja, N.A. (2016). A critical review of the applicability of Avrami fractional kinetic equation in adsorption-based water treatment studies. *Desalination and Water Treatment*, 57(34), 15813-15825.

Olubayode S.A., Awokola O.S., Dare E.O., & Olateju O.T. (2016). Suitability of Selected Nigeria Clay Deposit for Production of Clay Based Ceramic Water Filters. *American Chemical Science Journal,* 12(3), 1-7.

Olusegun, S.J., de Sousa Lima, L.F., & Mohallem, N.D.S. (2018). Enhancement of adsorption capacity of clay through spray drying and surface modification process for wastewater treatment. *Chemical Engineering Journal,* 334, 1719-1728.

Ong, C.B., Ng, L.Y., & Mohammad, A. (2018). A review of ZnO nanoparticles as solar photocatalysts: Synthesis, mechanisms and applications. *Renewable and Sustainable Energy Reviews,* 81, 536-551.

Pal, B., Cao, Y., Liu, X., Wen, F., Kareev, M., N'Diaye, A.T., Shafer, P., Arenholz, E. & Chakhalian, J. (2019). Anomalous orbital structure in two-dimensional titanium dichalcogenides. *Scientific Reports*, 9(1), 1-7.

Parra, M.R. & Haque, F.Z. (2014). Aqueous chemical route synthesis and the effect of calcination temperature on the structural and optical properties of ZnO nanoparticles. *Journal of Materials Research and Technology,* 3(4), 363–369.

Pavel, K. & Radovan, K. (2015). The Effect of Calcination on the Structure of Inorganic TiO_2 Nanofibers. Oct 14^{th} -16^{th} 2015, Brno, Czech Republic, EU. NanoCon. pp. 1-4.

Peeters, B. (2015). Wastewater Sludge Centrifugation before Drying. Chemical Engineering, New York-Mcgraw Hill Incorporated then Chemical Week Publishing Llc- 122(4), 56-60.

Phonkhokkong, T., Thongtem, S., Thongtem, C.S., Phuruangrat, A. & Promnopas, W. (2016). Synthesis and Characterization of TiO_2 Nanopowders for Fabrication of Dye Sensitized Solar Cells. *Digest Journal of Nanomaterials and Biostructures,* 11(1), 81-90.

Pinto, A.C.S., Grossi, L., Carvalho de Melo, R.A., Macedo de Assis, T., Ribeiro, V.M., Amaral, M.S.C. & Figueiredo, K.C. (2017). Carwash wastewater treatment by micro and ultrafiltration membranes: Effects of geometry, pore size, pressure difference and feed flow rate in transport properties. *Journal of Water Process Engineering,* 17, 143-148.

Pookmanee, P. & Phanichphant, S. (2014). Titanium dioxide powder prepared by a sol-gel method. *Journal of Ceramic Processing Research,* 10(2), 167-170.

Pourshadlou, S., Mobasherpour, I., Majidian, H., Salahi, E., Shirani Bidabadi, F., Mei, C.T. & Ebrahimi, M. (2020). Adsorption system for Mg^{2+} removal from aqueous solutions using bentonite/γ-alumina nanocomposite. *Journal of Colloid and Interface Science,* 568, 245-254.

Prabakaran, S., Nisha, K.D., Harish, S., Archana, J., Navaneethan, M., Ponnusamy, S., Muthamizhchelvan, C., Ikeda, H. & Hayakawa, Y. (2019). Synergistic effect and enhanced electrical properties of $TiO_2/SnO_2/ZnO$ nanostructures as electron extraction layer for solar cell application. *Applied Surface Science*, 498, 1-12.

Preethi, J., Farzana, M.H. & Meenakshi, S. (2017). Photo-reduction of Cr(VI) using chitosan supported zinc oxide materials. *International Journal of Biological Macromolecules*, 104, 1783-1793.

Preocanin, T., Abdelmonem, A., Montavon, G. & Luetzenkirchen, J. (2016). Charging behavior of clays and clay minerals in aqueous electrolyte solutions-experimental methods for measuring the charge and interpreting the results. *Clays, Clay Minerals and Ceramic Materials Based on Clay Minerals*, 1, 51-88.

Prusty, D., Pryamitsyn, V. & Olvera de la Cruz, M. (2018). Thermodynamics of Associative Polymer Blends. *Macromolecules*, 51(15), 5918-5932.

Puri, C. & Sumana, G. (2018). Highly effective adsorption of crystal violet dye from contaminated water using graphene oxide intercalated montmorillonite nanocomposite. *Applied Clay Science*, 166, 102-112.

Qin, R., Meng, F., Khan, M. W., Yu, B., Li, H., Fan, Z. & Gong, J. (2019). Fabrication and enhanced photocatalytic property of TiO_2-ZnO composite photocatalysts. *Materials Letters*, 240, 84-87.

Rafiq, Z., Nazir, R., Shahwar, D., Shah, M.R. & Ali, S. (2014). Utilization of magnesium and zinc oxide nano-adsorbents as potential materials for treatment of copper electroplating industry wastewater. *Journal of Environmental Chemical Engineering*, 2, 642-651.

Rahman, A., Kishimoto, N. & Urabe, T. (2015). Adsorption characteristics of clay adsorbents-sepiolite, kaolin and synthetic talc-for removal of Reactive Yellow 138:1. *Water and Environment Journal*, 29, 375-382.

Rao, B.G., Mukherjee, D. & Reddy, B.M. (2017). Novel approaches for preparation of nanoparticles. Nanostructures for Novel Therapy, Synthesis, Characterization and Applications, A volume in Micro and Nano Technologies. pp. 1-36.

Redlich, O. & Peterson, D.L. (1959). "A useful adsorption isotherm." *The Journal of Physical Chemistry*, 63(6), 1024-1024.

Rida, K., Bouraoui, S. & Hadnine, S. (2013). Adsorption of methylene blue from aqueous solution by kaolin and zeolite. *Applied Clay Science*, 83-84, 99-105.

Romeiro, A., Freitas, D., Azenha, M.E., Canle, M. & Burrows, H.D. (2017). Effect of calcination temperature on the photocatalytic efficiency of acidic sol-gel synthesized TiO_2 nanoparticles in the degradation of alprazolam. *Photochemical and Photobiological Sciences*, 1, 1-37.

Ruiz-Hitzky, E., Aranda, P., Akkari, M., Khaorapapong, N. & Ogawa, M. (2019). Photoactive nanoarchitectures based on clays incorporating TiO_2 and ZnO nanoparticles. *Beilstein Journal of Nanotechnology*, 10, 1140-1156.

Sadegh, H. & Ali, G. A. (2021). Potential applications of nanomaterials in wastewater treatment: nanoadsorbents performance. In *Research Anthology on Synthesis, Characterization, and Applications of Nanomaterials* (pp. 1230-1240). IGI Global.

Sagadevan, S., Venilla, S., Marlinda, A.R., Johan, M., Wahab, Y.A., Zakaria, R., Umar, A., Hegazy, H.H., Algarni, H. & Ahmad, N. (2020). Effect of Synthesis Temperature on the Morphologies, Optical and Electrical Properties of MgO Nanostructures. *Journal of Nanoscience and Nanotechnology*, 20(4), 2488-2494.

Sahel, K., Bouhent, M., Belkhadem, F., Ferchichi, M., Dappozze, F., Guillard, C. & Figueras, F. (2014). Photocatalytic degradation of anionic and cationic dyes over TiO_2 P25, and Ti-pillared clays and Ag-doped Ti-pillared clays. *Applied Clay Science*, 95, 205-210.

Salavati-Niasari, M., Soofivand, F., Sobhani-Nasab, A., Shakouri-Arani, M., Faal, A.Y. & Bagheri, S. (2016). Synthesis, characterization, and morphological control of $ZnTiO_3$ nanoparticles through sol-gel processes and its photocatalyst application. *Advanced Powder Technology*, 27(5), 2066-2075.

Samans, R., Blanke, J., Hanouz, M.D. & Corrigan, G. (2017). *The Inclusive Growth and Development Report*. World Economic Forum, Geneva, pp. 1-75.

Sani, H.A., Ahmad, M.B., Hussein, M.Z., Ibrahim, N.A., Musa, A. & Saleh, T.A. (2017). Nanocomposite of ZnO with montmorillonite for removal of lead and copper ions from aqueous solutions. *Process Safety and Environmental Protection*, 109, 97-105.

Saranya, D. & Shanthakumar, S. (2019a). Green microalgae for combined sewage and tannery effluent treatment: Performance and lipid accumulation potential. *Journal of Environmental Management*, 241, 167-178.

Saranya, D. & Shanthakumar, S. (2019b). Opportunities for phycoremediation approach in tannery effluent: A treatment perspective. *Environmental Progress & Sustainable Energy*, 38(3). 1-13.

Sarma, G.K., Gupta, S.S. & Bhattacharyya, K.G. (2019). Removal of hazardous basic dyes from aqueous solution by adsorption onto kaolinite and acid-treated kaolinite: kinetics, isotherm and mechanistic study. *SN Applied Sciences*, 1(3), 211-225.

Saxena, G., Chandra, R. & Bharagava, R. N. (2016). Environmental pollution, toxicity profile and treatment approaches for tannery wastewater and its chemical pollutants. In *Reviews of Environmental Contamination and Toxicology*, 240, 31-69.

Sayehi, M., Sahnoun, R.D., Fakhfakh, S. & Baklouti, S. (2018). Effect of elaboration parameters of a membrane ceramic on the filtration process efficacy. *Ceramics International*, 44(5), 5202-5208.

Sdiri, A.T., Higashi, T. & Jamoussi, F. (2014). Adsorption of copper and zinc onto natural clay in single and binary systems. *International Journal of Environment and Science Technology,* 11, 1081-1092.

Selman, A.M., Hassan, Z. & Husham, M. (2014). Structural and photoluminescence studies of rutile TiO_2 nanorods prepared by chemical bath deposition method on Si substrates at different pH values. *Measurement,* 56, 155-162.

Shaban, M., Mohamed, F. & Abdallah, S. (2018). Production and Characterization of Superhydrophobic and Antibacterial Coated Fabrics Utilizing ZnO Nanocatalyst. *Scientific Reports,* 8, 1-15.

Shaban, M., Mohamed, F. & Abdallah, S. (2018). Production and characterization of superhydrophobic and antibacterial coated fabrics utilizing ZnO nanocatalyst. *Scientific Reports,* 8(1), 1-15.

Sharma, A., Karn, R.K. & Pandiyan, S.K. (2014). Synthesis of TiO_2 Nanoparticles by Sol-gel Method and Their Characterization. *Journal of Basic and Applied Engineering Research,* 1(9), 1-5.

Shehap, A.M., & Akil, D.S. (2016). Structural and optical properties of TiO_2 nanoparticles/PVA for different composites thin films. *International Journal of Nanoelectronics and Materials,* 9, 17-36.

Shivaraju, H. P., Egumbo, H., Madhusudan, P., Anil Kumar, K.M. & Midhun, G. (2018). Preparation of affordable and multifunctional clay-based ceramic filter matrix for treatment of drinking water. *Environmental Technology,* 40(13), 1633-1643.

Singh, G. (2014). Infrared (IR) Spectroscopy Analysis Methods. *International Research Journal of Management Science and Technology,* 5(6), 98-101.

Singh, H.B., Mishra, S., Fraceto, L.F. & de Lima, R. (2018). *Emerging Trends in Agri-nanotechnology: Fundamental and Applied Aspects*: CABI, 27 Apr 2018, Technology and Engineering, pp. 1-322.

Singh, P.K., Mukherjee, S., Ghosh, C.K. & Maitra, S. (2017). Influence of precursor type on structural, morphological, dielectric and magnetic properties of TiO_2 nanoparticles. *Cerâmica,* 63, 549-556.

Sips, R. (1948). "On the structure of a catalyst surface." *The Journal of Chemical Physics,* 16(5), 490-495.

Sirelkhatim A., Mahmud S., Seeni A., Kaus N. H. M., Ann L. C., Bakhori S.K.M., Hasan, H. & Mohamad, D. (2015). Review on zinc oxide nanoparticles: antibacterial activity and toxicity mechanism. *Nano-Micro Letter,* 7, 219-242.

Sirirerkratana, K., Kemacheevakul, P. & Chuangchote, S. (2019). Color removal from wastewater by photocatalytic process using titanium dioxide-coated glass, ceramic tile, and stainless steel sheets. *Journal of Cleaner Production*, 215, 123-130.

Sivagami, K., Sakthivel, K.P. & Nambi, I.M. (2018). Advanced oxidation processes for the treatment of tannery wastewater. *Journal of Environmental Chemical Engineering*, 6(3), 3656-3663.

Sodhi, V., Bansal, A. & Jha, M.K. (2020). Minimization of excess bio-sludge and pollution load in oxic-settling-anaerobic modified activated sludge treatment for tannery wastewater. *Journal of Cleaner Production*, 243, 118492.

Soltani, R.D.C., Jorfi, S., Ramezani, H. & Purfadakari, S. (2016). Ultrasonically induced ZnO-biosilica nanocomposite for degradation of a textile dye in aqueous phase. *Ultrasonics Sonochemistry*, 28, 69-78.

Sonawane, G.H., Patil, S.P., & Shrivastava, V.S. (2017). Photocatalytic degradation of safranine by ZnO–bentonite: photodegradation versus adsorbability. *Journal of the Institution of Engineers (India): Series E*, 98(1), 55-63.

Soni, H., Kumar, J.N., Patel, K. & Kumar, R.N. (2016). Photocatalytic decoloration of three commercial dyes in aqueous phase and industrial effluents using TiO_2 nanoparticles. *Desalination and Water Treatment*, 57(14), 6355-6364.

Soyekwo, F., Zhang, Q., Qu, Y., Lin, Z., Wu, X., Zhu, A. & Liu, Q. (2019). Tetraamminezinc complex integrated interpenetrating polymer network nanocomposite membrane for phosphorous recovery. *AIChE Journal*, 65(2), 755-765.

Sponza, D.T. & Oztekin, R. (2015). Ciproxin Removal from a Raw Wastewater by Nano Bentonite-ZnO: Comparison of Adsorption and Photooxidation Processes. Recent Adv. Environ. Biological Eng., 978(1), 18-27.

Sun, C., Xu, Q., Xie, Y., Ling, Y., & Hou, Y. (2018). Designed synthesis of anatase-TiO_2 (B) biphase nanowire/ZnO nanoparticle heterojunction for enhanced photocatalysis. *Journal of Materials Chemistry A*, 6(18), 8289-8298.

Sun, W., Ma, G., Sun, Y., Liu, Y., Song, N., Xu, Y. & Zheng, H. (2017). Effective Treatment of High Phosphorus Pharmaceutical Wastewater by Chemical Precipitation. *The Canadian Journal of Chemical Engineering*, 1, 1-24.

Syngouna, V.I., Chrysikopoulos, C.V., Kokkinos, P., Tselepi, M.A. & Vantarakis, A. (2017). Cotransport of human adenoviruses with clay colloids and TiO_2 nanoparticles in saturated porous media: Effect of flow velocity. *Science of the Total Environment*, 598, 160-167.

Szczepanik, B., Rogala, P., Słomkiewicz, P. M., Banaś, D., Kubala-Kukuś, A. & Stabrawa, I. (2017). Synthesis, characterization and photocatalytic activity of TiO_2-halloysite and Fe_2O_3-halloysite nanocomposites for photodegradation of chloroanilines in water. *Applied Clay Science*, 149, 118-126.

Taghlidabad, R. H., Sepehr, E., Khodaverdiloo, H., Samadi, A. & Rasouli-Sadaghiani, M.H. (2020). Characterization of cadmium adsorption on two cost-effective biochars for water treatment. *Arabian Journal of Geosciences*, 13, 448-457.

Talaiekhozani, A., Heydari Chaleshtori, A., Banisharif, F., Eskandari, Z., Nasiri, M., Aminsharei, F., Park, J., Rezania, S. & Bazrafshan, M. (2019). Removal of Acid Orange 7 dye from wastewater using combination of ultraviolet radiation, ultrasonic method, and MgO nanoparticles. *Environmental Health Engineering and Management Journal*, 6(3), 157-170.

Tan, J., Huang, Y., Wu, Z., & Chen, X. (2017). Ion Exchange Resin on Treatment of Copper and Nickel Wastewater. *IOP Conf. Series: Earth and Environmental Science*, 94, 1-6.

Temkin, M.I. & Pyzhev, V. (1940). Kinetics of ammonia synthesis on promoted iron catalyst. *Acta Physicochimica*, 12, 327-356.

The News, (2014). Challenges Facing Nigeria's Leather Industry. August, 13, 2014.

Thirumavalavan, M., Huang, K. & Lee, J. (2013). Preparation and Morphology Studies of Nano Zinc Oxide Obtained Using Native and Modified Chitosans. *Materials*, 6, 4198-4212.

Thommes, M., Kaneko, K., Neimark, A.V., Olivier, J.P., Rodriguez-Reinoso, F., Rouquerol, J. & Sing, K.S. (2015). Physisorption of gases, with special reference to the evaluation of surface area and pore size distribution (IUPAC Technical Report). *Pure and Applied Chemistry*, 87(9-10), 1051-1069.

Tong, Y., McNamara, P.J. & Mayer, B.K. (2019). Adsorption of organic micropollutants onto biochar: A review of relevant kinetics, mechanisms and equilibrium. *Environmental Science: Water Research and Technology*, 5(5), 821-838.

Tsega, M., & Dejene, F. B. (2017). Influence of acidic pH on the formulation of TiO_2 nanocrystalline powders with enhanced photoluminescence property. *Heliyon*, 3(2), 1-16.

Turan, N.G. & Ozgonenel, O. (2013). Study of Montmorillonite Clay for the Removal of Copper (II) by Adsorption: Full Factorial Design Approach and Cascade Forward Neural Network. *The Scientific World Journal*, 2013, 1-11.

Uddin, F. (2018). *Montmorillonite: An Introduction to Properties and Utilization. Current Topics in the Utilization of Clay in Industrial and Medical Applications*. IntechOpen Limited, London, SE1 9SG, United Kingdom, pp. 3-24

Uddin, M.K. (2016). A review on the adsorption of heavy metals by clay minerals, with special focus on the past decade. *Chemical Engineering Journal*, 308, 438-462.

Ullatti, S.G. & Periyat, P. (2017). Sol-Gel Synthesis of Titanium Dioxide. Sol-Gel Materials for Energy. *Environment and Electronic Applications*, 1, 271-283.

UNDESA (United Nations Department of Economic and Social Affairs), (2013). World Population Prospects: The 2012 Revision. New York, Population Division, United Nations (UN). http://esa.un.org/wpp/

United Nation (UN), (2016). *World Water Development Report*. World Water Assessment Programme (WWAP). 22 March 2016, Geneva, Switzerland

Unuabonah, E.I., Ugwuja, C.G., Omorogie, M.O., Adewuyi, A., & Oladoja, N.A. (2017). Clays for Efficient Disinfection of Bacteria in Water. *Applied Clay Science*, 151, 211-223.

Vahidhabanu, S., Karuppasamy, D., Adeogun, A.I. & Babu, B. (2017). Impregnation of zinc oxide modified clay over alginate beads: a novel material for the effective removal of Congo red from wastewater. *RSC Advance*, 7, 5669-5678.

Vaizoğullar, A.İ. (2017). TiO_2/ZnO supported on sepiolite: preparation, structural characterization, and photocatalytic degradation of flumequine antibiotic in aqueous solution. *Chemical Engineering Communications*, 204(6), 689-697.

Valášková, M. (2015). Clays, Clay Minerals and Cordierite Ceramics - A Review. *Ceramics-Silikáty*, 59(4), 331-340.

Vardikar, H.S., Bhanvase, B.A., Rathod, A.P. & Sonawane, S.H. (2018). Sonochemical synthesis, characterization and sorption study of Kaolin-Chitosan-TiO_2 ternary nanocomposite: Advantage over conventional method. *Materials Chemistry and Physics*, 217, 457-467.

Vasistha, P. & Ganguly, R. (2020). Water quality assessment of natural lakes and its importance: An overview. *Materials Today: Proceedings*, 1, 1-9.

Venzke, C.D., Rodrigues, M.A.S., Giacobbo, A., Bacher, L.E., Lemmertz, I.S., Viegas, C., Striving, J. & Pozzebon, S. (2017). "Application of reverse osmosis to petrochemical industry wastewater treatment aimed at water reuse". *Management of Environmental Quality: An International Journal*, 28(1), 70-77.

Verma, T., Tiwari, S., Tripathi, M., & Ramteke, P.W. (2019). Treatment and Recycling of Wastewater from Tannery. *In Advances in Biological Treatment of Industrial Waste Water and their Recycling for a Sustainable Future*, Singh, R.L., Singhj, R.P., Eds.; Springer: Singapore, pp. 51-90.

Wang, C., Luo, S., Liu, C. & Chen, C. (2020). WO_3 Quantum Dots Enhanced the Photocatalytic Performances of Graphene Oxide/TiO_2 Films under Flowing Dye Solution. *Inorganic Chemistry Communications*, 115, 1-7.

Wang, C., McNew, C.P., Lyon, S.W., Walter, M.T., Volkman, T.H., Abramson, N., Sengupta, A., Wang, Y., Neto, A.A.M., Pangle, L. & Troch, P.A. (2019). Particle tracer transport in a sloping soil lysimeter under periodic, steady state conditions. *Journal of Hydrology*, 569, 61-76.

Wang, G., Xu, D., Guo, W., Wei, X., Sheng, Z. & Li, Z. (2017). Preparation of TiO_2 nanoparticle and photocatalytic properties on the degradation of phenol. 2nd International Conference on Advances in Energy Resources and Environmental Engineering. IOP Conference series: Earth and Environmental Science 59, pp. 1-6.

Wang, H., Zhou, P., Guo, R., Wang, Y., Zhan, H. & Yuan, Y. (2018). Synthesis of Rectorite/Fe_3O_4/ZnO Composites and Their Application for the Removal of Methylene Blue Dye. *Catalyst*, 8, 107-124.

Wang, H., Zhou, P., Wang, J., Wang, Y., Wei, J., Zhan, H., Guo, R. & Zhang, Y. (2018). Synthesis and Characterization of Rectorite/ZnO/TiO 2 Composites and Their Properties of Adsorption and Photocatalysis for the Removal of Methylene Blue Dye. *Journal of Wuhan University of Technology-Material Sciences and Education*, 33(3), 729-735.

Wang, L. (2019). Preparation of ZnO and TiO_2 Photocatalyst and Degradation Effect of Dyestuff. *Archivos Latinoamericanos de Nutrición*, 69(1), 99-106

Weber, W.J., & Morris, J.C. (1963). Kinetics of adsorption on carbon from solution. *Journal of the Sanitary Engineering Division,* 89, 31-60.

World Health Organization (WHO) (2002). *The World Health Report 2002. Reducing risks, promoting healthy life*. World Health Organization, Geneva.

World Health Organization (WHO), (2015). Progress on sanitation and Drinking-water: Fact sheet No. 391, 29 June 2015 <http://www.who.int/mediacentre/factsheets/fs391/en/>.

Wu, A., Wang, D., Wei, C., Zhang, X., Liu, Z., Feng, P., Ou, X., Qiang, Y., Garcia, H. & Niu, J. (2019). A comparative photocatalytic study of TiO_2 loaded on three natural clays with different morphologies. *Applied Clay Science*, 183, 1-12.

Xue, J., Shen, Q., Yang, F., Liang, W., & Liu, X. (2014). Investigation on the influence of pH on structure and photoelectrochemical properties of CdSe electrolytically deposited into TiO_2 nanotube arrays. *Journal of Alloys Compound*. 607, 163-168.

Yahaya, M.M., Azam, M.A., Teridi, M.A.M., Singh, P.K. & Mohamad, A.A. (2017). Recent Characterization of Sol-Gel Synthesized TiO_2 Nanoparticles. INTECH, pp. 109-129.

Yang, C., Zhu, Y., Wang, J., Li, Z., Su, X., & Niu, C. (2015). Hydrothermal synthesis of TiO_2-WO_3-bentonite composites: conventional versus ultrasonic pretreatments and their adsorption of methylene blue. *Applied Clay Science*, 105, 243-251.

Yin, Q., Xiang, J., Wang, X., Guo, X. & Zhang, T. (2016). Preparation of highly crystalline mesoporous TiO_2 by sol-gel method combined with two-step calcining process. *Journal of Experimental Nanoscience*, 11(14), 1127-1137.

Yu, P., Wang, Z., Lai, P., Zhang, P. & Wang, J. (2019). Evaluation of mechanic damping properties of montmorillonite/organo-modified montmorillonite-reinforced cement paste. *Construction and Building Materials*, 203, 356-365.

Yu, Z., Song, W., Li, J. & Li, Q. (2020). Improved simultaneous adsorption of Cu(II) and Cr(VI) of organic modified metakaolin-based geopolymer. *Arabian Journal of Chemistry*, 13(3), 1-15.

Yudoyono, G., Ichzan, N., Zharvan, V., Daniyati, R., Santoso, H., Indarto, B., Pramono, Y.D., Zainuri, M. & Darminto, (2016). Effect of Calcination Temperature on the Photocatalytic Activity of TiO_2 Powders Prepared by Co-Precipitation of $TiCl_3$. The 3rd International Conference on Advanced Materials Science and Technology (ICAMST 2015), AIP Conference Proceeding, 1725, pp 1-7.

Zahedi, Y., Fathi-Achachlouei, B. & Yousefi, A.R. (2017). Physical and mechanical properties of hybrid montmorillonite/zincoxide reinforced carboxymethyl cellulose nanocomposites. *International Journal of Biological Macromolecules*, 108, 863-873

Zekic, E. Vukovic, Z. & Halkijevic, I. (2018). Application of nanotechnology in wastewater treatment. *Građevinar,* 70(4), 315-323.

Zen, S. & El Berrichi, F.Z. (2014). Adsorption of tannery anionic dyes by modified kaolin from aqueous solution. *Desalination and Water Treatment*, 57(13), 6024-6032.

Zen, S., El Berrichi, F.Z., Abidi, N., Duplay, J., Jada, A. & Gasmi, B. (2018). Activated kaolin's potential adsorbents for the removal of Derma Blue R67 acid dye: kinetic and thermodynamic studies. *Desalination and Water Treatment*, 112, 196-206.

Zereffa, E.A. & Bekalo, T. B. (2017). Clay Ceramic Filter for Water Treatment. *Materials Science and Applied Chemistry*, 34(1), 69-74.

Zhang, Y., Wu, B., Xu, H., Liu, H., Wang, M., He, Y. & Pan, B. (2016). Nanomaterials-enabled water and wastewater treatment. *NanoImpact*, 3(4), 22-39.

Zhao, Q., Zhao, X. & Cao, J. (2020). Advanced Nanomaterials for Degrading Persistent Organic Pollutants. In *Advanced Nanomaterials for Pollutant Sensing and Environmental Catalysis*, 1, 249-305.

Zinatloo-Ajabshir, S. & Salavati-Niasari, M. (2016). Facile route to synthesize zirconium dioxide (ZrO_2) nanostructures: structural, optical and photocatalytic studies. *Journal of Molecular Liquids*, 216, 545-551.

Zou, C., Jiang, W., Liang, J., Guan, Y. & Sun, X. (2019). Desorption Regeneration Performance of Magnetic Bentonite after Pb(II) Adsorbed. *ChemistrySelect*, 4(4), 1306-1315.

Zyoud, A.H., Zorba, T., Helal, M., Zyoud, S., Qamhiya, N., Hajamohideen, A.R., Zyoud, S. & Hilal, H.S. (2019). Direct sunlight-driven degradation of 2-chlorophenol catalyzed by kaolinite-supported ZnO. *International Journal of Environmental Science and Technology*, 16(10), 6267-6276.

APPENDICES

Appendix A

Effect of contact time

Table 1: Effect of Contact Time on the Removal of COD from Tannery Wastewater

Sample	Mass (g)	pH	Temp.	Optimum time (min)	Maximum removal (%)
Kaolin	0.20	5.84	29	15	72.81
KT	0.20	5.84	29	10	81.95
KZ	0.20	5.84	29	15	84.72
KTZ11	0.20	5.84	29	10	86.44
KTZ21	0.20	5.84	29	15	87.51
KTZ12	0.20	5.84	29	20	93.91

Table 2: Effect of Contact Time on the Removal of BOD from Tannery Wastewater

Sample	Mass (g)	pH	Temp.	Optimum time (min)	Maximum removal (%)
Kaolin	0.20	5.84	29	25	80.73
KT	0.20	5.84	29	15	89.75
KZ	0.20	5.84	29	15	92.59
KTZ11	0.20	5.84	29	10	93.41
KTZ21	0.20	5.84	29	10	93.58
KTZ12	0.20	5.84	29	10	93.67

Table 3: Effect of Contact Time on the Removal of Chloride from Tannery Wastewater

Sample	Mass (g)	pH	Temp.	Optimum time (min)	Maximum removal (%)
Kaolin	0.20	5.84	29	15	66.75
KT	0.20	5.84	29	15	75.81
KZ	0.20	5.84	29	10	82.81
KTZ11	0.20	5.84	29	10	85.81
KTZ21	0.20	5.84	29	10	88.18
KTZ12	0.20	5.84	29	15	89.42

Table 4: Effect of Contact Time on the Removal of Sulphate from Tannery Wastewater

Sample	Mass (g)	pH	Temp.	Optimum time (min)	Maximum removal (%)
Kaolin	0.20	5.84	29	10	71.11
KT	0.20	5.84	29	15	86.61
KZ	0.20	5.84	29	15	86.75
KTZ11	0.20	5.84	29	20	87.09
KTZ21	0.20	5.84	29	15	87.62
KTZ12	0.20	5.84	29	10	87.46

Table 5: Effect of Contact Time on the Removal of Nitrate from Tannery Wastewater

Sample	Mass (g)	pH	Temp.	Optimum time (min)	Maximum removal (%)
Kaolin	0.20	5.84	29	10	61.45
KT	0.20	5.84	29	15	91.19
KZ	0.20	5.84	29	15	92.31
KTZ11	0.20	5.84	29	15	92.98
KTZ21	0.20	5.84	29	15	93.09
KTZ12	0.20	5.84	29	20	95.60

Table 6: Effect of Contact Time on the Removal of Zinc from Tannery Wastewater

Sample	Mass (g)	pH	Temp.	Optimum time (min)	Maximum removal (%)
Kaolin	0.20	5.84	29	10	66.32
KT	0.20	5.84	29	15	72.08
KZ	0.20	5.84	29	15	75.98
KTZ11	0.20	5.84	29	15	76.33
KTZ21	0.20	5.84	29	15	84.60
KTZ12	0.20	5.84	29	20	89.33

Table 7: Effect of Contact Time on the Removal of Lead from Tannery Wastewater

Sample	Mass (g)	pH	Temp.	Optimum time (min)	Maximum removal (%)
Kaolin	0.20	5.84	29	10	64.94
KT	0.20	5.84	29	20	74.71
KZ	0.20	5.84	29	15	74.77
KTZ11	0.20	5.84	29	20	78.41
KTZ21	0.20	5.84	29	20	80.71
KTZ12	0.20	5.84	29	25	83.53

Table 8: Effect of Contact Time on the Removal of Cadmium from Tannery Wastewater

Sample	Mass (g)	pH	Temp.	Optimum time (min)	Maximum removal (%)
Kaolin	0.20	5.84	29	20	66.91
KT	0.20	5.84	29	20	70.16
KZ	0.20	5.84	29	20	71.72
KTZ11	0.20	5.84	29	25	73.61
KTZ21	0.20	5.84	29	15	76.16
KTZ12	0.20	5.84	29	15	86.74

Table 9: Effect of Contact Time on the Removal of Chromium from Tannery Wastewater

Sample	Mass (g)	pH	Temp.	Optimum time (min)	Maximum removal (%)
Kaolin	0.20	5.84	29	15	53.01
KT	0.20	5.84	29	20	70.63
KZ	0.20	5.84	29	20	71.01
KTZ11	0.20	5.84	29	25	82.27
KTZ21	0.20	5.84	29	20	84.68
KTZ12	0.20	5.84	29	25	87.23

Effect of dosage

Table 10: Effect of Adsorbent Dosage on the Removal of Chloride from Tannery Wastewater

Sample	pH	Temp.	Optimum time (min)	Maximum removal (%)
Kaolin	5.84	29	15	74.86
KT	5.84	29	15	76.17
KZ	5.84	29	10	76.36
KTZ11	5.84	29	10	76.73
KTZ21	5.84	29	10	77.78
KTZ12	5.84	29	15	77.92

Table 11: Effect of Adsorbent Dosage on the Removal of COD from Tannery Wastewater

Sample	pH	Temp.	Optimum time (min)	Maximum removal (%)
Kaolin	5.84	29	15	90.04
KT	5.84	29	10	92.96
KZ	5.84	29	15	93.49
KTZ11	5.84	29	10	94.96
KTZ21	5.84	29	15	95.16
KTZ12	5.84	29	20	95.25

Table 12: Effect of Adsorbent Dosage on the Removal of BOD from Tannery Wastewater

Sample	pH	Temp.	Optimum time (min)	Maximum removal (%)
Kaolin	5.84	29	25	89.73
KT	5.84	29	15	94.24
KZ	5.84	29	15	94.98
KTZ11	5.84	29	10	95.49
KTZ21	5.84	29	10	96.23
KTZ12	5.84	29	10	96.89

Table 13: Effect of Adsorbent Dosage on the Removal of Sulphate from Tannery Wastewater

Sample	pH	Temp.	Optimum time (min)	Maximum removal (%)
Kaolin	5.84	29	10	80.30
KT	5.84	29	15	89.17
KZ	5.84	29	15	89.81
KTZ11	5.84	29	20	90.44
KTZ21	5.84	29	15	91.10
KTZ12	5.84	29	10	91.78

Table 14: Effect of Adsorbent Dosage on the Removal of Nitrate from Tannery Wastewater

Sample	pH	Temp.	Optimum time (min)	Maximum removal (%)
Kaolin	5.84	29	10	92.39
KT	5.84	29	15	96.53
KZ	5.84	29	15	96.77
KTZ11	5.84	29	15	96.86
KTZ21	5.84	29	15	96.87
KTZ12	5.84	29	20	96.96

Table 15: Effect of Adsorbent Dosage on the Removal of Cadmium from Tannery Wastewater

Sample	pH	Temp.	Optimum time (min)	Maximum removal (%)
Kaolin	5.84	29	10	70.79
KT	5.84	29	15	92.70
KZ	5.84	29	15	98.10
KTZ11	5.84	29	15	99.05
KTZ21	5.84	29	15	100
KTZ12	5.84	29	20	100

Table 16: Effect of Adsorbent Dosage on the Removal of Lead from Tannery Wastewater

Sample	pH	Temp.	Optimum time (min)	Maximum removal (%)
Kaolin	5.84	29	10	75.29
KT	5.84	29	20	87.06
KZ	5.84	29	15	95.29
KTZ11	5.84	29	20	98.24
KTZ21	5.84	29	20	99.41
KTZ12	5.84	29	25	100

Table 17: Effect of Adsorbent Dosage on the Removal of Chromium from Tannery Wastewater

Sample	pH	Temp.	Optimum time (min)	Maximum removal (%)
Kaolin	5.84	29	20	87.81
KT	5.84	29	20	88.62
KZ	5.84	29	20	99.19
KTZ11	5.84	29	25	100
KTZ21	5.84	29	15	100
KTZ12	5.84	29	15	100

Table 18: Effect of Adsorbent Dosage on the Removal of Zinc from Tannery Wastewater

Sample	pH	Temp.	Optimum time (min)	Maximum removal (%)
Kaolin	5.84	29	15	72.29
KT	5.84	29	20	75.90
KZ	5.84	29	20	80.36
KTZ11	5.84	29	25	83.13
KTZ21	5.84	29	20	84.34
KTZ12	5.84	29	25	88.19

Effect of Temperature

Table 19: Effect of Temperature on the Removal of Chloride from Tannery Wastewater

Sample	Mass (g)	pH	Optimum time (min)	Maximum removal (%)
Kaolin	0.20	5.84	15	55.15
KT	0.20	5.84	15	67.01
KZ	0.20	5.84	10	65.69
KTZ11	0.20	5.84	10	66.36
KTZ21	0.20	5.84	10	67.13
KTZ12	0.20	5.84	15	68.38

Table 20: Effect of Temperature on the Removal of COD from Tannery Wastewater

Sample	Mass (g)	pH	Optimum time (min)	Maximum removal (%)
Kaolin	0.20	5.84	15	85.38
KT	0.20	5.84	10	90.29
KZ	0.20	5.84	15	90.37
KTZ11	0.20	5.84	10	90.69
KTZ21	0.20	5.84	15	91.70
KTZ12	0.20	5.84	20	92.82

Table 20: Effect of Temperature on the Removal of BOD from Tannery Wastewater

Sample	Mass (g)	pH	Optimum time (min)	Maximum removal (%)
Kaolin	0.20	5.84	25	86.31
KT	0.20	5.84	15	89.56
KZ	0.20	5.84	15	90.37
KTZ11	0.20	5.84	10	91.67
KTZ21	0.20	5.84	10	91.99
KTZ12	0.20	5.84	10	92.13

Table 21: Effect of Temperature on the Removal of Sulphate from Tannery Wastewater

Sample	Mass (g)	pH	Optimum time (min)	Maximum removal (%)
Kaolin	0.20	5.84	10	81.55
KT	0.20	5.84	15	85.36
KZ	0.20	5.84	15	85.73
KTZ11	0.20	5.84	20	86.39
KTZ21	0.20	5.84	15	86.48
KTZ12	0.20	5.84	10	87.09

Table 22: Effect of Temperature on the Removal of Nitrate from Tannery Wastewater

Sample	Mass (g)	pH	Optimum time (min)	Maximum removal (%)
Kaolin	0.20	5.84	10	70.58
KT	0.20	5.84	15	76.29
KZ	0.20	5.84	15	82.66
KTZ11	0.20	5.84	15	83.09
KTZ21	0.20	5.84	15	86.31
KTZ12	0.20	5.84	20	85.46

Table 23: Effect of Temperature on the Removal of Zinc from Tannery Wastewater

Sample	Mass (g)	pH	Optimum time (min)	Maximum removal (%)
Kaolin	0.20	5.84	10	71.43
KT	0.20	5.84	15	77.14
KZ	0.20	5.84	15	78.10
KTZ11	0.20	5.84	15	83.18
KTZ21	0.20	5.84	15	84.44
KTZ12	0.20	5.84	20	96.83

Table 24: Effect of Temperature on the Removal of Lead from Tannery Wastewater

Sample	Mass (g)	pH	Optimum time (min)	Maximum removal (%)
Kaolin	0.20	5.84	10	54.12
KT	0.20	5.84	20	92.35
KZ	0.20	5.84	15	95.06
KTZ11	0.20	5.84	20	97.82
KTZ21	0.20	5.84	20	98.41
KTZ12	0.20	5.84	25	99.12

Table 25: Effect of Temperature on the Removal of Cadmium from Tannery Wastewater

Sample	Mass (g)	pH	Optimum time (min)	Maximum removal (%)
Kaolin	0.20	5.84	20	89.43
KT	0.20	5.84	20	91.87
KZ	0.20	5.84	20	95.94
KTZ11	0.20	5.84	25	91.87
KTZ21	0.20	5.84	15	97.81
KTZ12	0.20	5.84	15	92.68

Table 26: Effect of Temperature on the Removal of Chromium from Tannery Wastewater

Sample	Mass (g)	pH	Optimum time (min)	Maximum removal (%)
Kaolin	0.20	5.84	15	76.87
KT	0.20	5.84	20	78.92
KZ	0.20	5.84	20	81.93
KTZ11	0.20	5.84	25	81.33
KTZ21	0.20	5.84	20	83.02
KTZ12	0.20	5.84	25	87.59

Appendix B

Isotherm Models

Redlich-Peterson Model

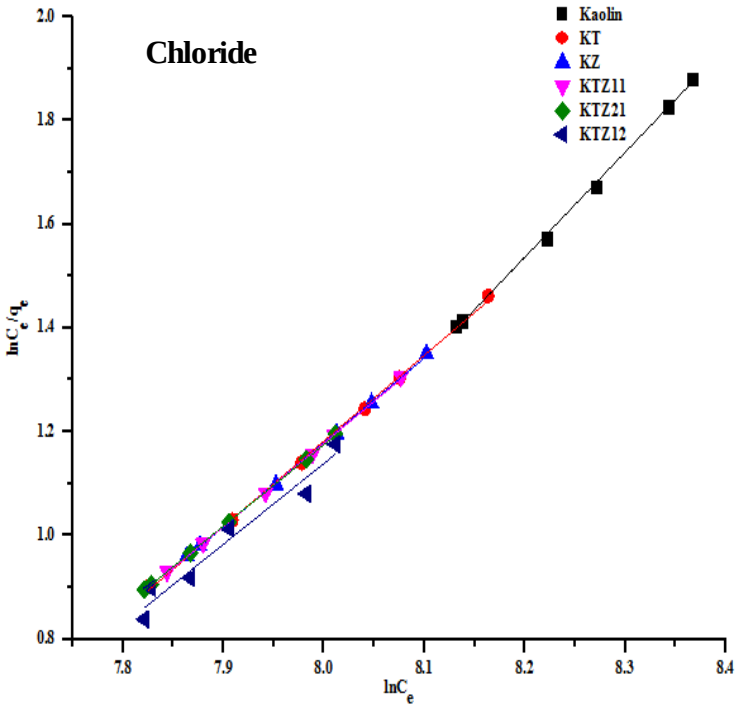

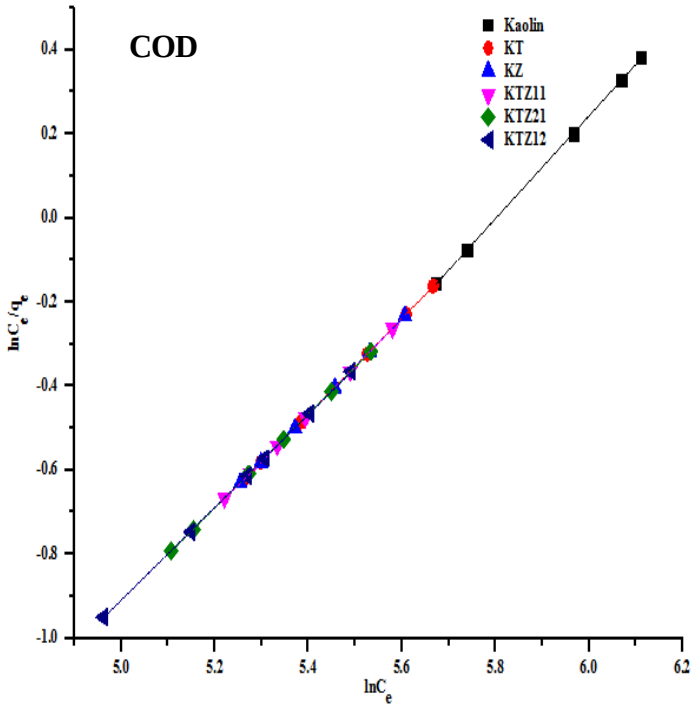

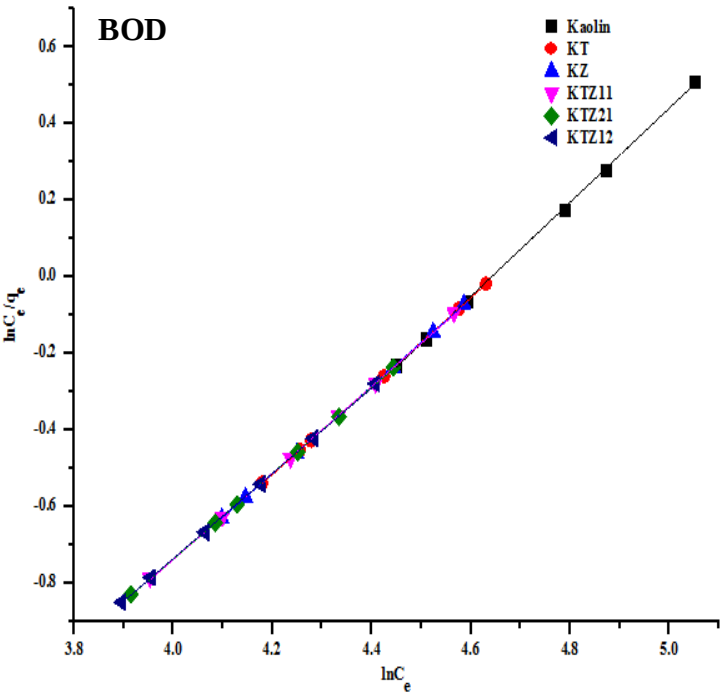

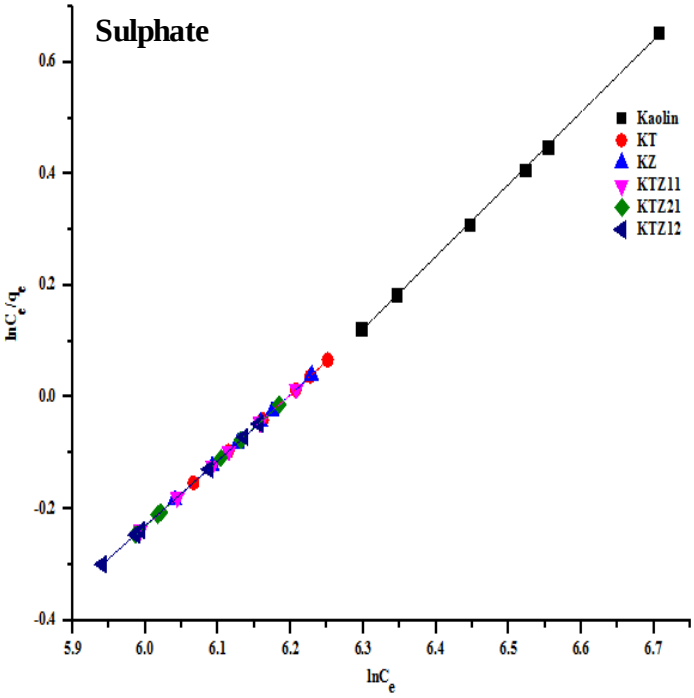

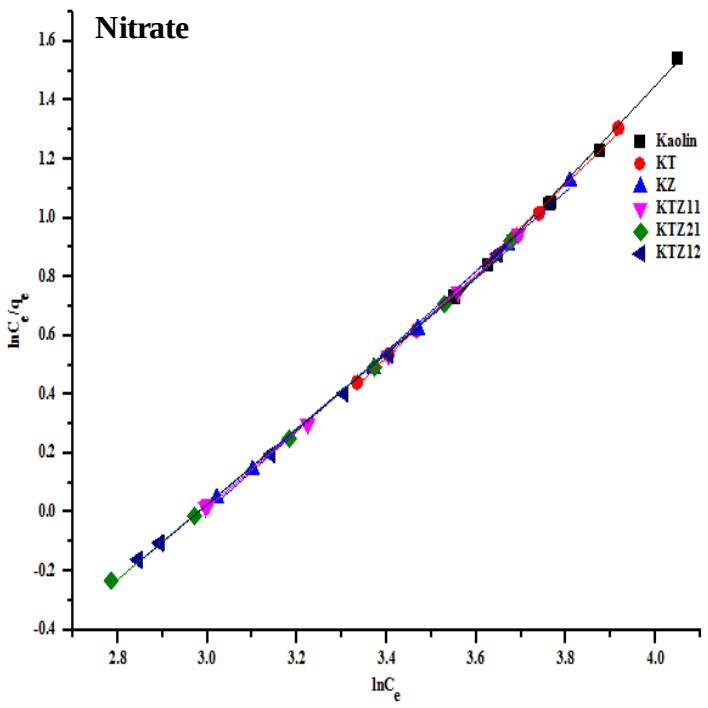
Nitrate
Kaolin
KT
KZ
KTZ11
KTZ21
KTZ12
lnC_e/q_e
lnC_e

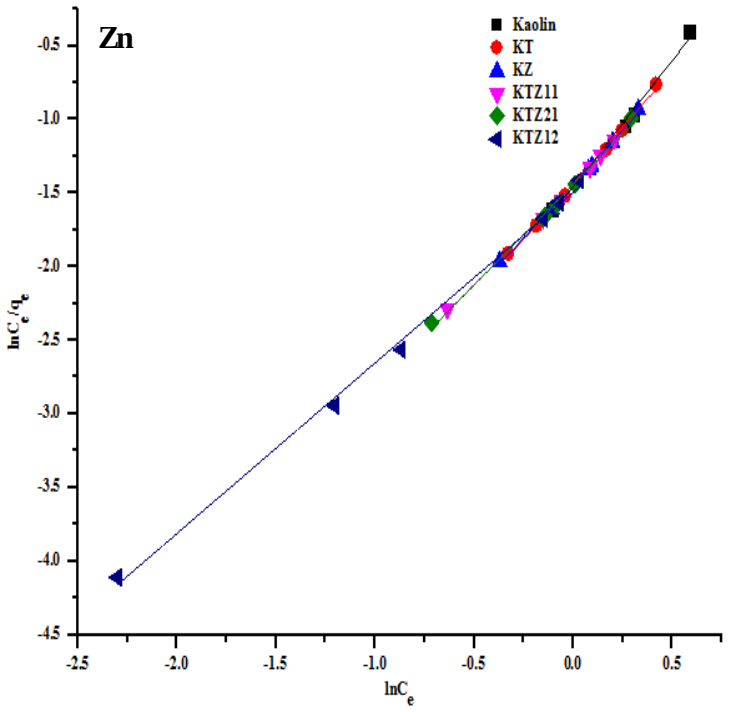
Zn
Kaolin
KT
KZ
KTZ11
KTZ21
KTZ12
lnC_e/q_e
lnC_e

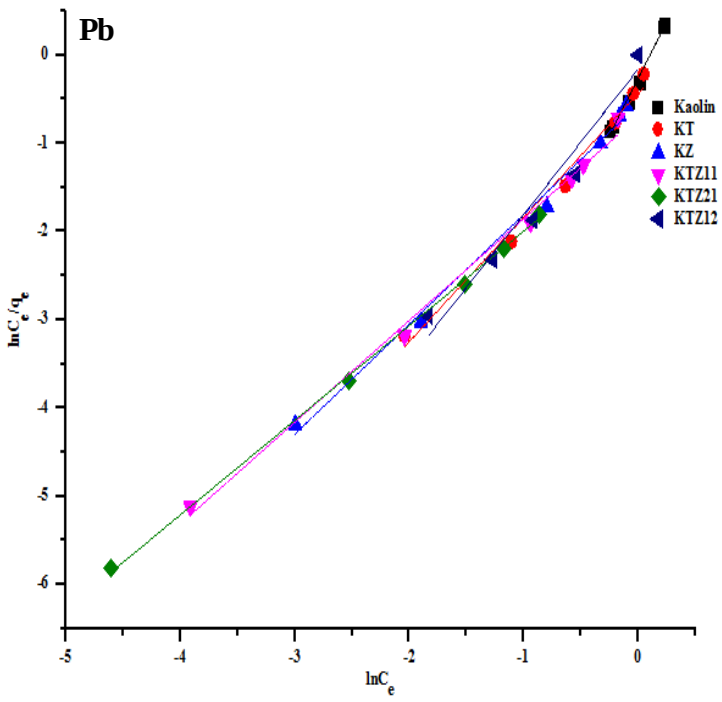
Pb
Kaolin
KT
KZ
KTZ11
KTZ21
KTZ12
lnC_e/q_e
lnC_e

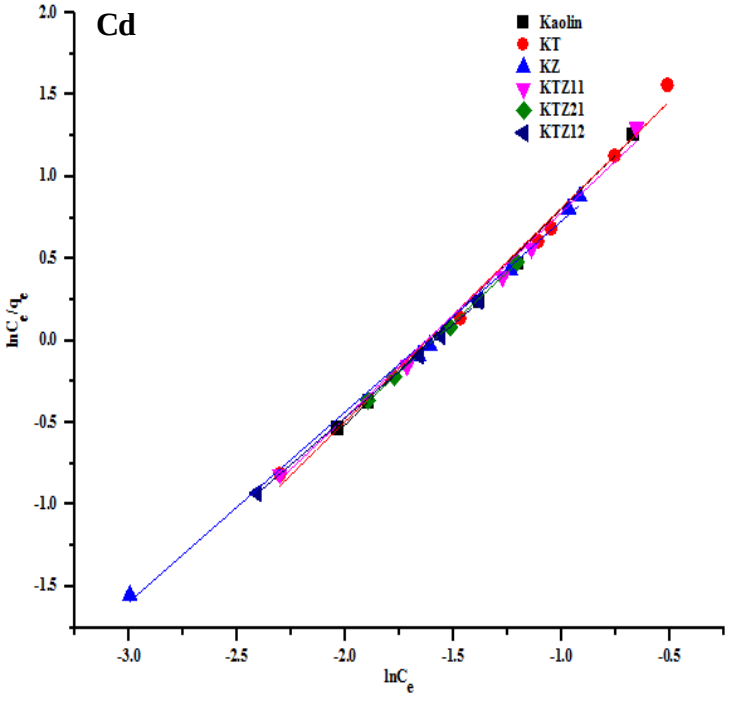
Cd
Kaolin
KT
KZ
KTZ11
KTZ21
KTZ12
lnC_e/q_e
lnC_e

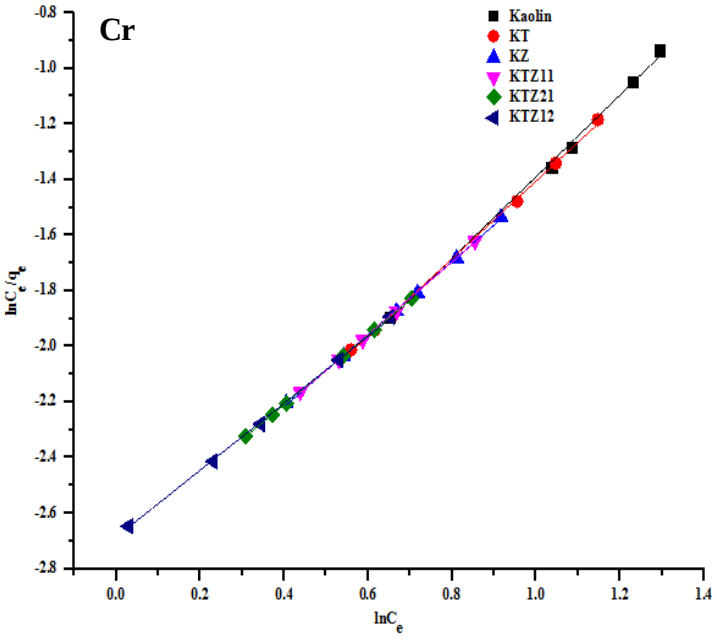
Cr
Kaolin
KT
KZ
KTZ11
KTZ21
KTZ12
-0.8
-1.0
-1.2
-1.4
-1.6
-1.8
-2.0
-2.2
-2.4
-2.6
-2.8
0.0
0.2
0.4
0.6
0.8
1.0
1.2
1.4
lnC_e/q_e
lnC_e

Appendix C

Halsey Model

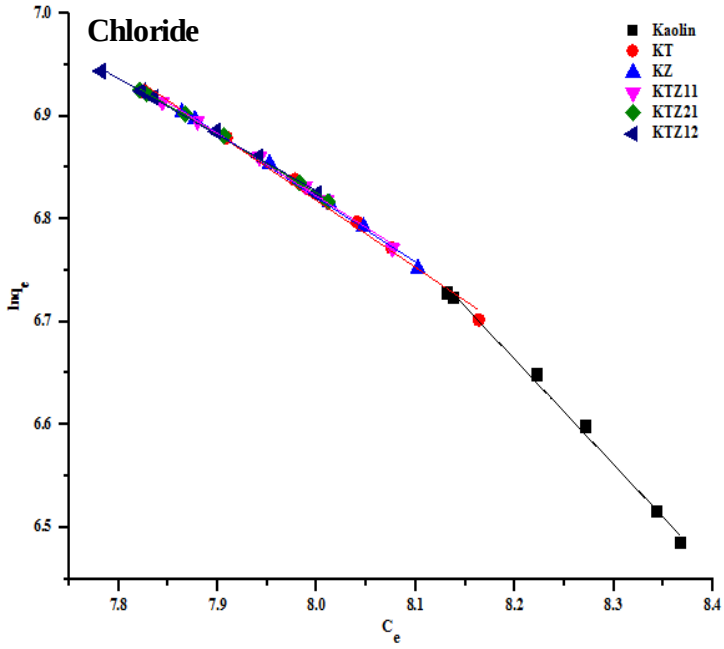

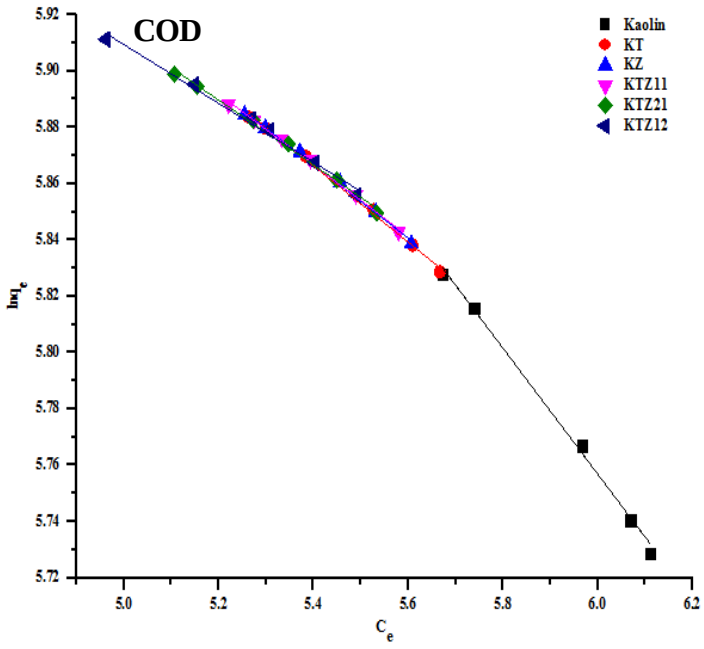

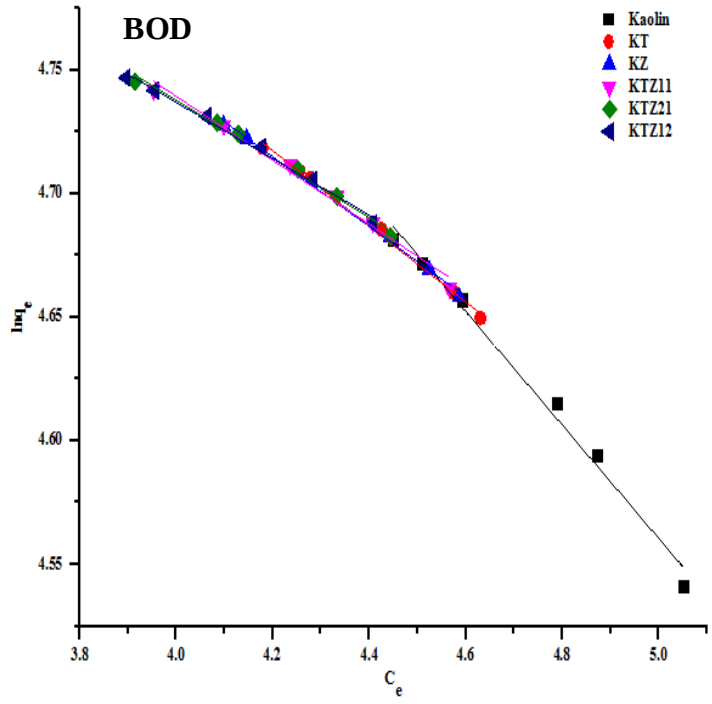

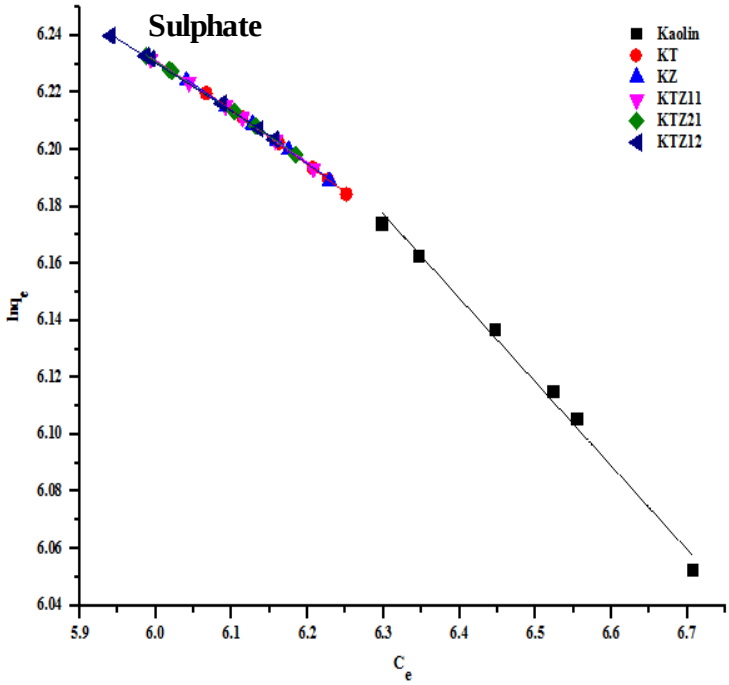

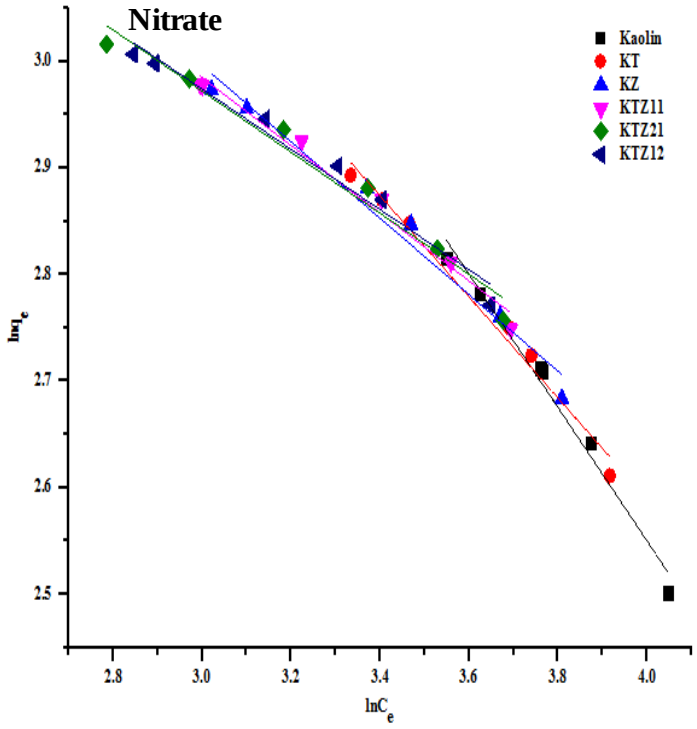
Nitrate
Kaolin
KT
KZ
KTZ11
KTZ21
KTZ12
lnq_e
lnC_e

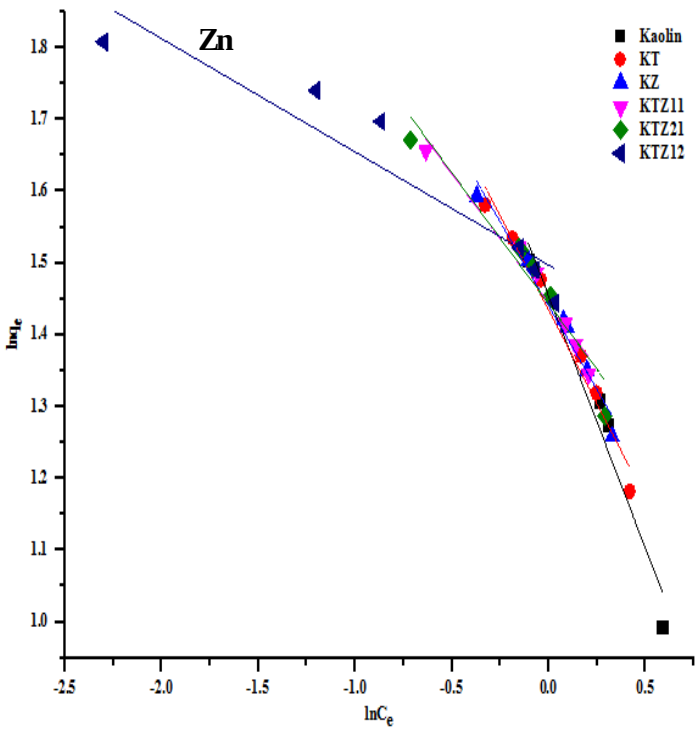
Zn
Kaolin
KT
KZ
KTZ11
KTZ21
KTZ12
lnq_e
lnC_e

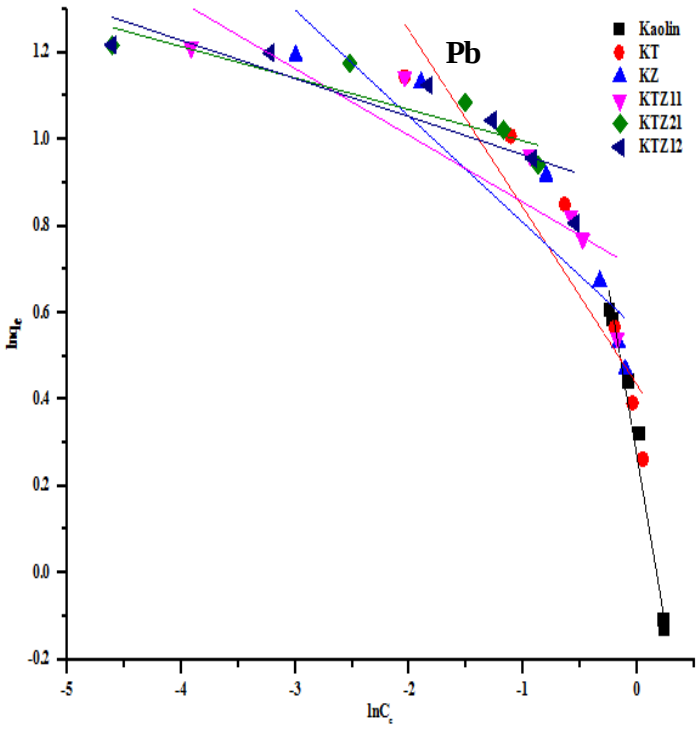
Pb
Kaolin
KT
KZ
KTZ11
KTZ21
KTZ12
lnq_e
lnC_e

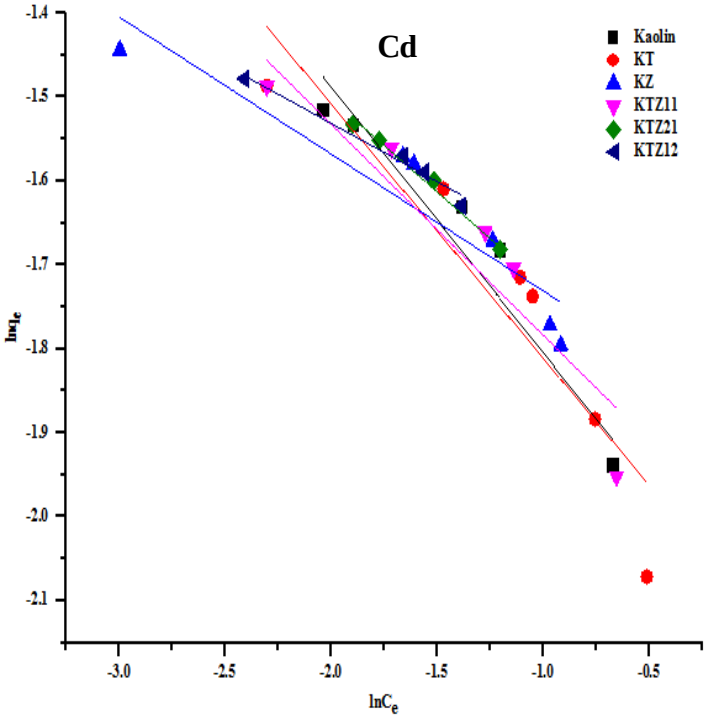
Cd
Kaolin
KT
KZ
KTZ11
KTZ21
KTZ12
lnq_e
lnC_e

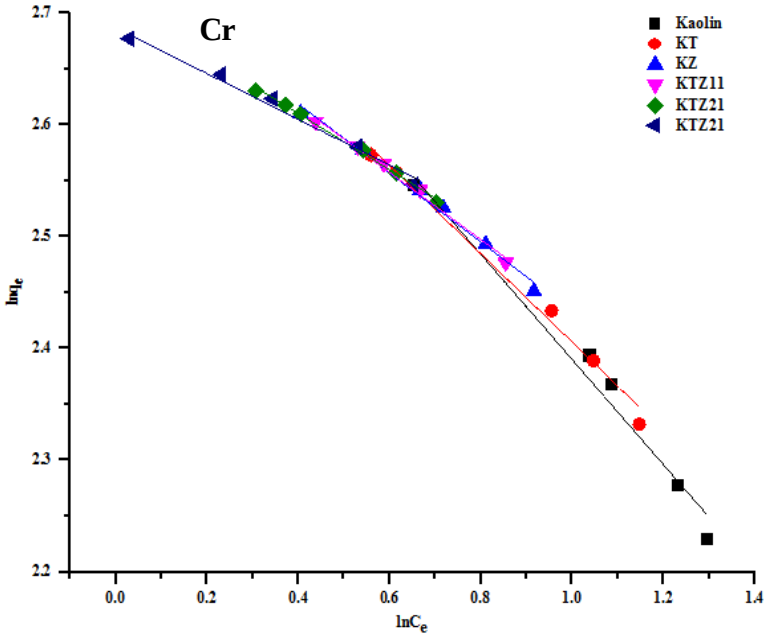
Cr
Kaolin
KT
KZ
KTZ11
KTZ21
KTZ21
lnqe
lnCe
2.7
2.6
2.5
2.4
2.3
2.2
0.0
0.2
0.4
0.6
0.8
1.0
1.2
1.4

Appendix D

Jovanovic Model

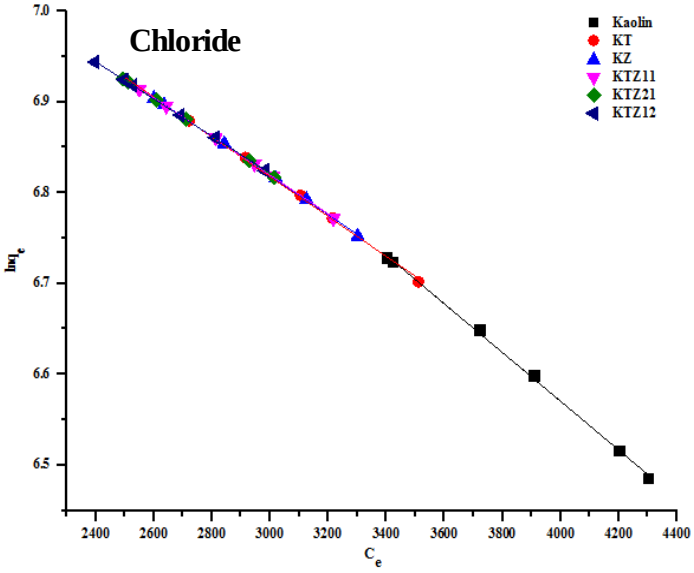

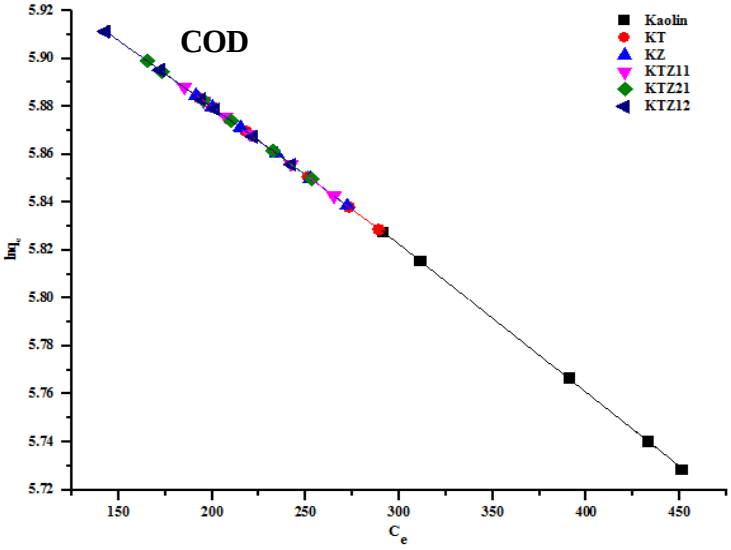

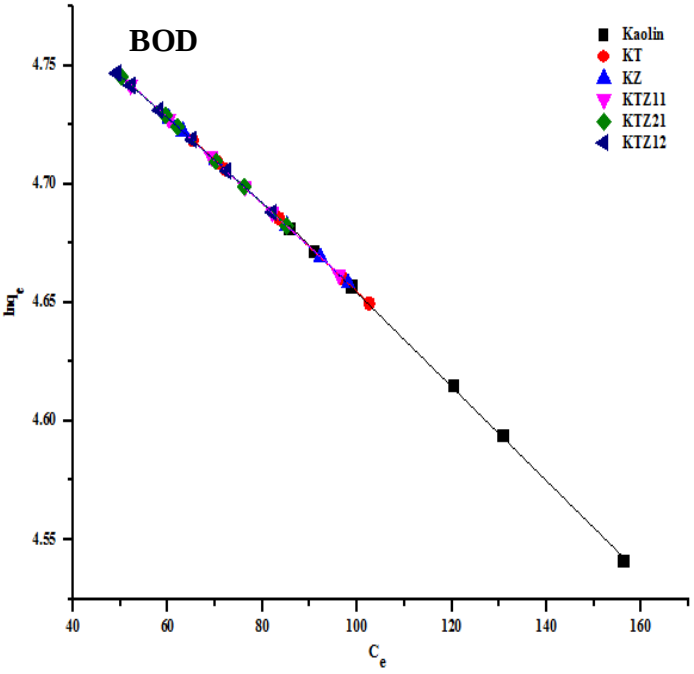

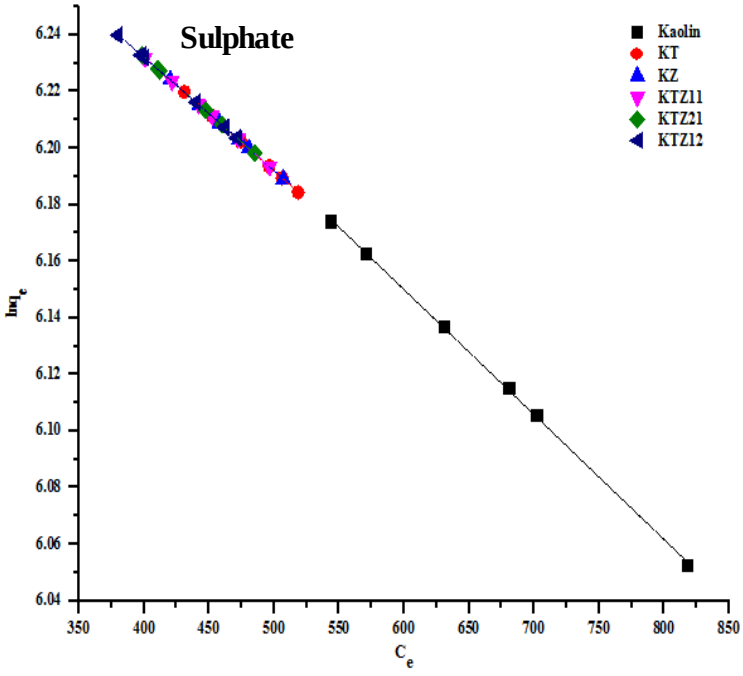

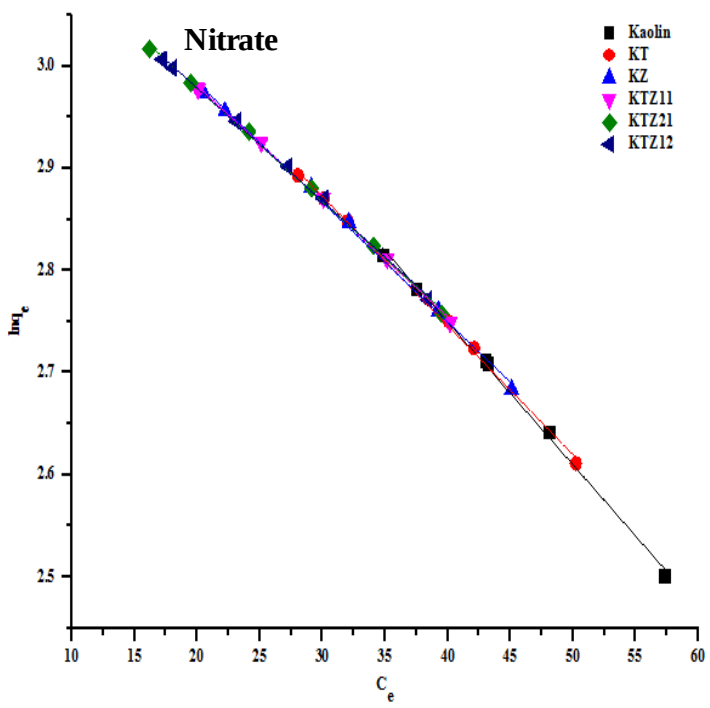
Nitrate
Kaolin
KT
KZ
KTZ11
KTZ21
KTZ12
lnq_e
C_e

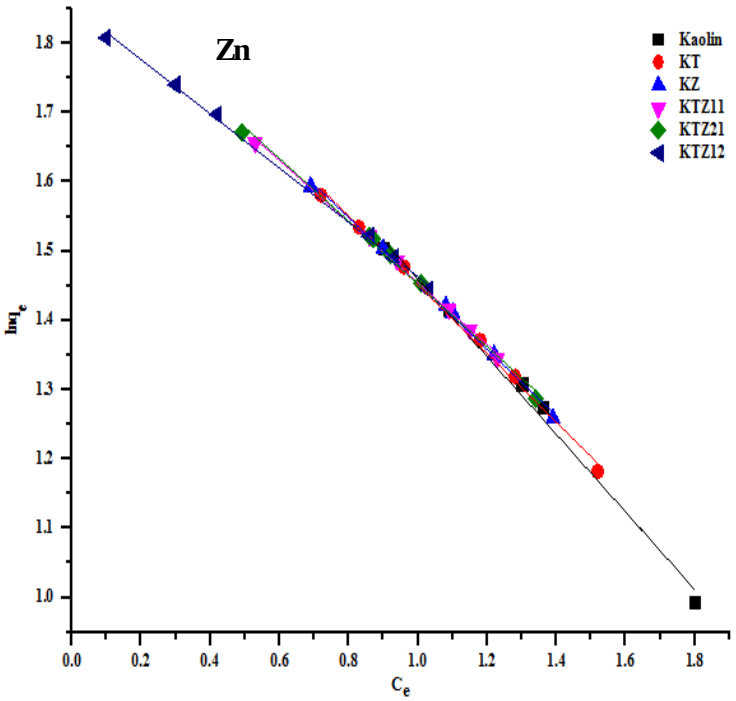
Zn
Kaolin
KT
KZ
KTZ11
KTZ21
KTZ12
lnq_e
C_e

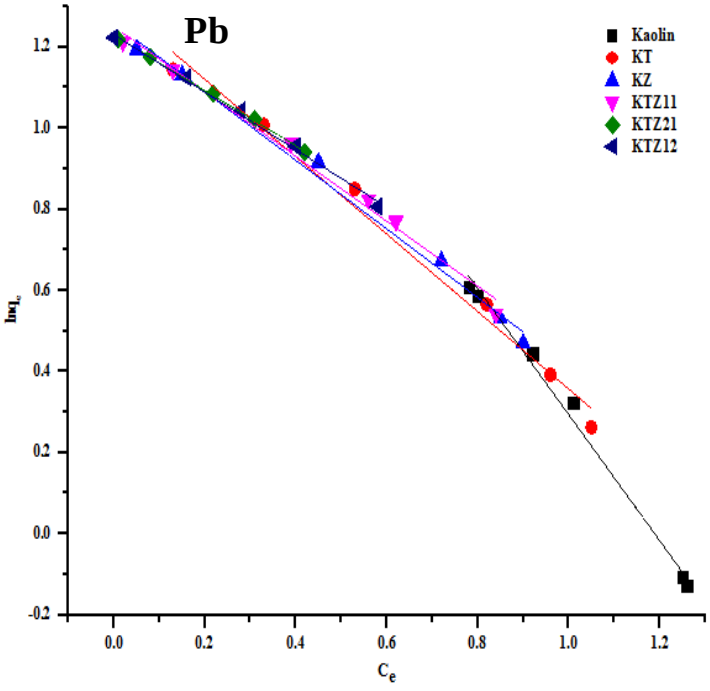
Pb
Kaolin
KT
KZ
KTZ11
KTZ21
KTZ12
lnq_e
C_e

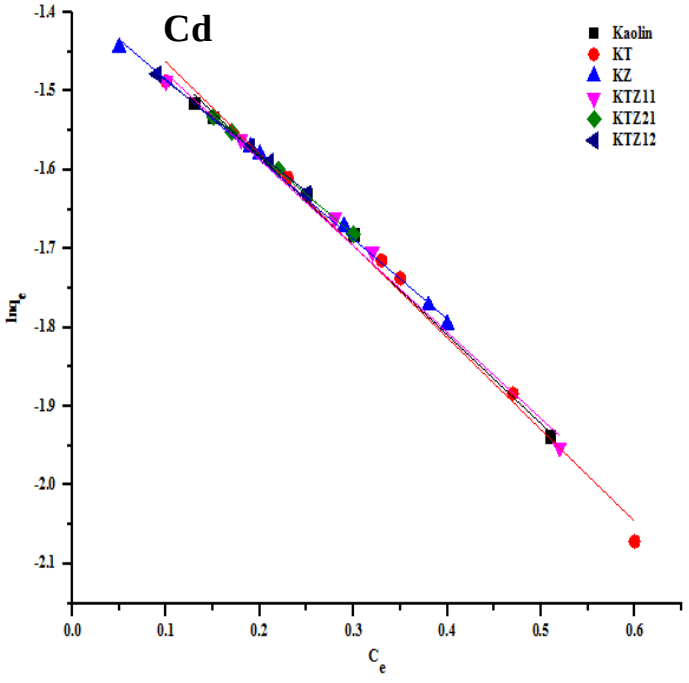
Cd
Kaolin
KT
KZ
KTZ11
KTZ21
KTZ12
lnq_e
C_e

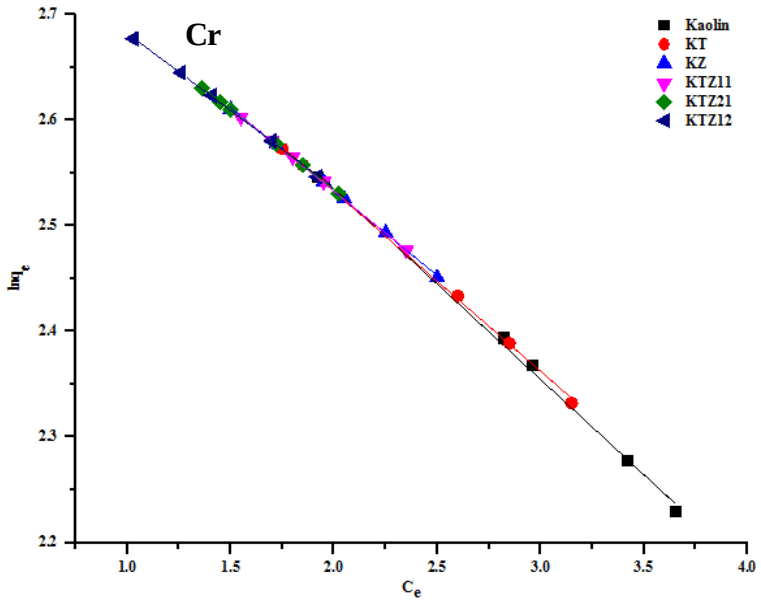
Cr
Kaolin
KT
KZ
KTZ11
KTZ21
KTZ12
lnq_e
C_e
2.7
2.6
2.5
2.4
2.3
2.2
1.0
1.5
2.0
2.5
3.0
3.5
4.0

Appendix E

Flory-Huggins Model

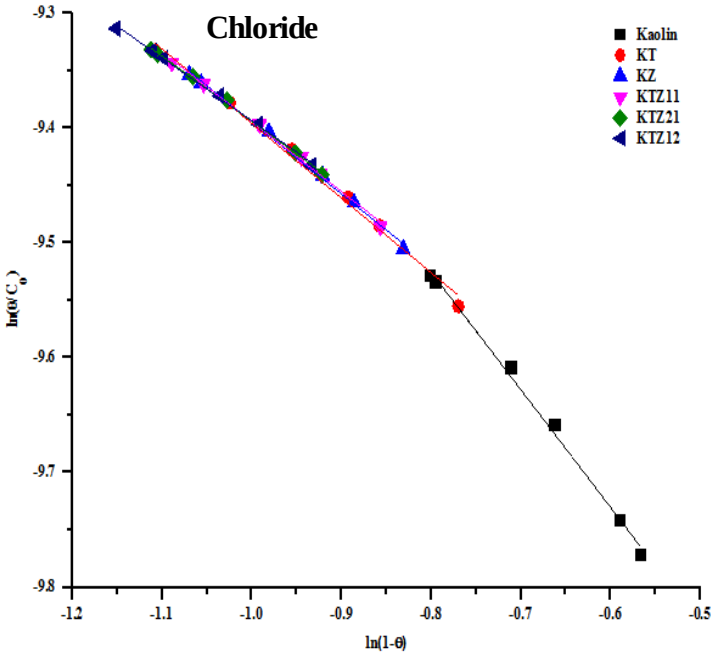

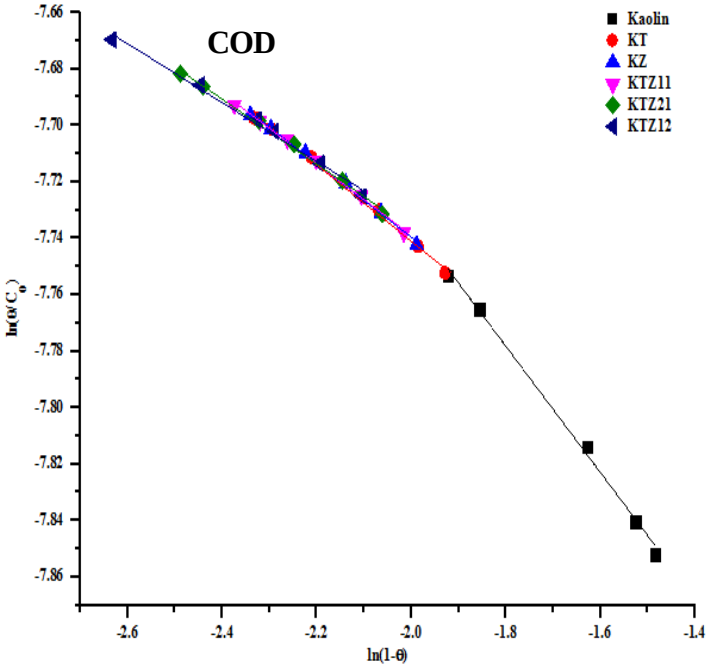

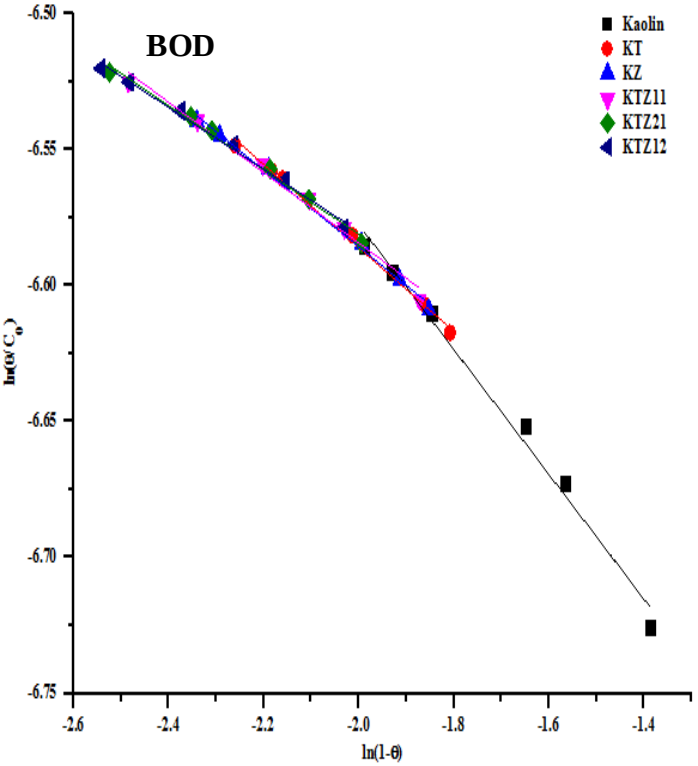

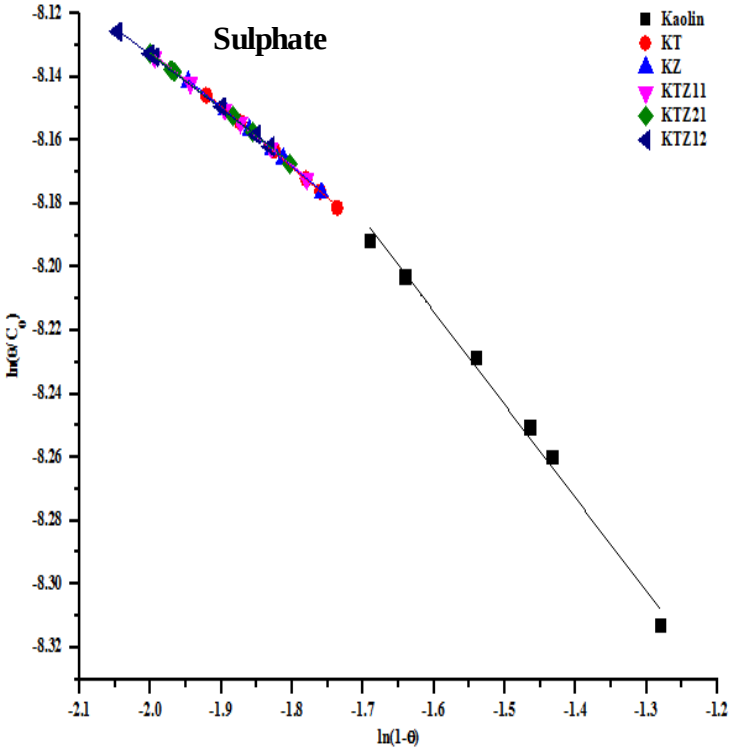

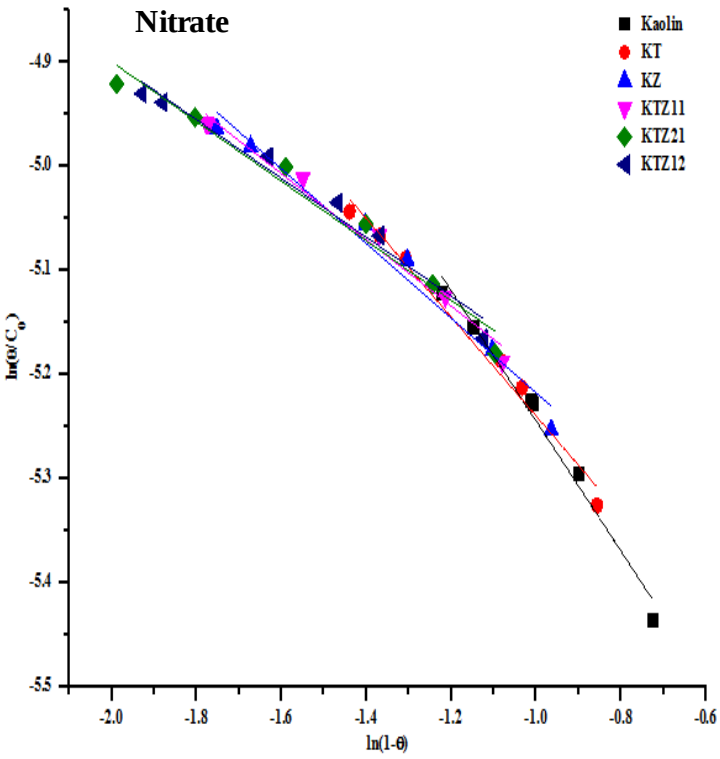
Nitrate
Kaolin
KT
KZ
KTZ11
KTZ21
KTZ12
ln(Θ/C0)
ln(1-Θ)

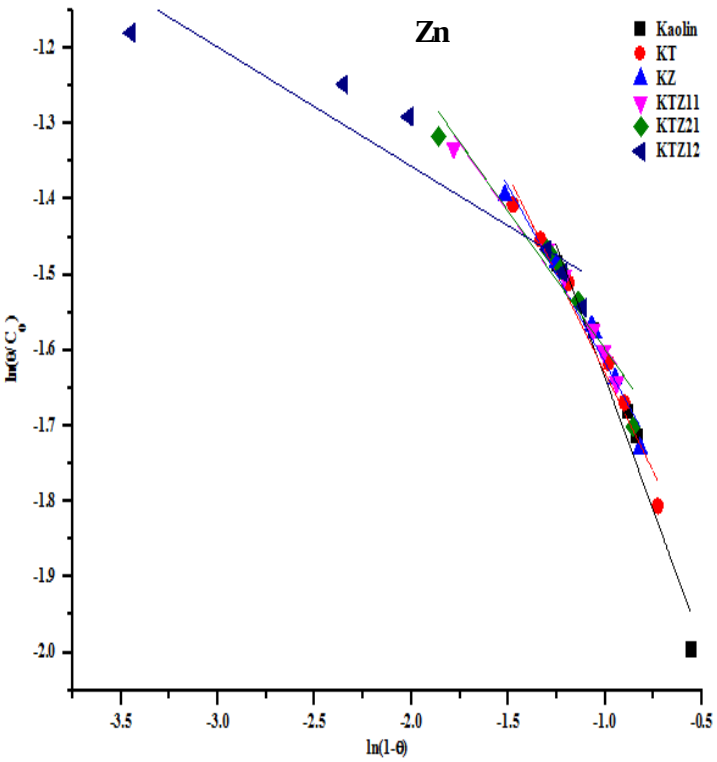
Zn
Kaolin
KT
KZ
KTZ11
KTZ21
KTZ12
ln(Θ/C0)
ln(1-Θ)

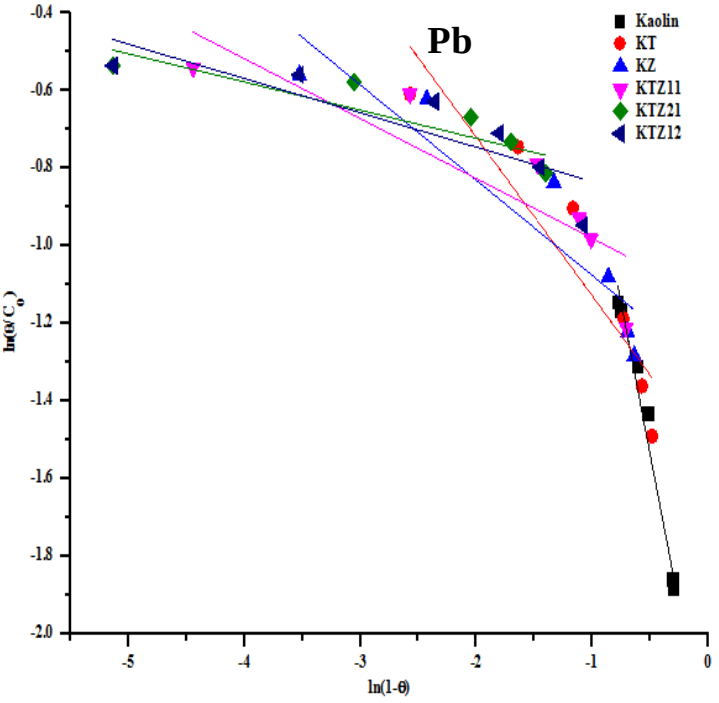
Pb
Kaolin
KT
KZ
KTZ11
KTZ21
KTZ12
ln(Θ/C0)
ln(1-Θ)

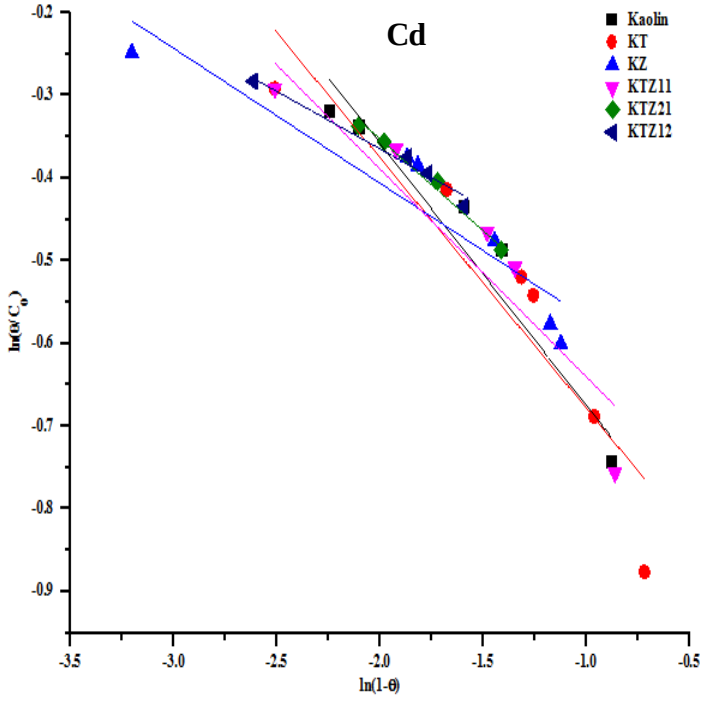
Cd
Kaolin
KT
KZ
KTZ11
KTZ21
KTZ12
ln(Θ/C0)
ln(1-Θ)

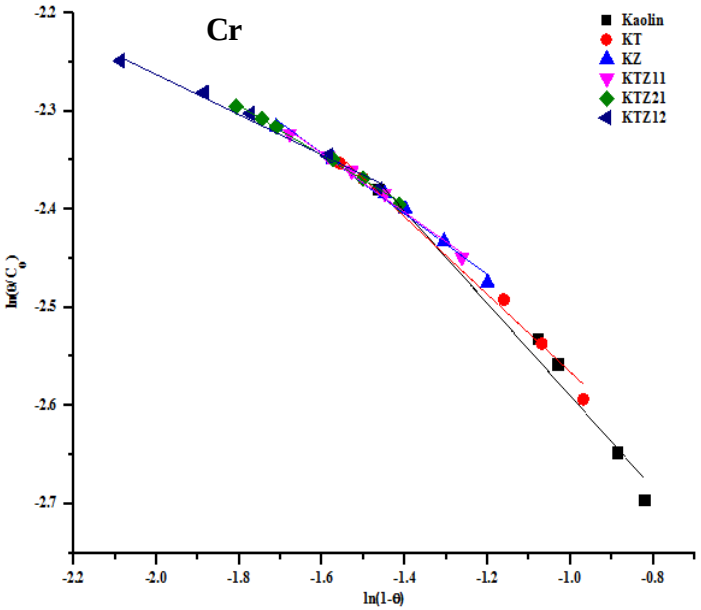
Cr
Kaolin
KT
KZ
KTZ11
KTZ21
KTZ12
ln(θ/C_o)
ln(1-θ)
-2.2
-2.3
-2.4
-2.5
-2.6
-2.7
-2.2
-2.0
-1.8
-1.6
-1.4
-1.2
-1.0
-0.8

Appendix F

Kinetic Models

Fractional Power

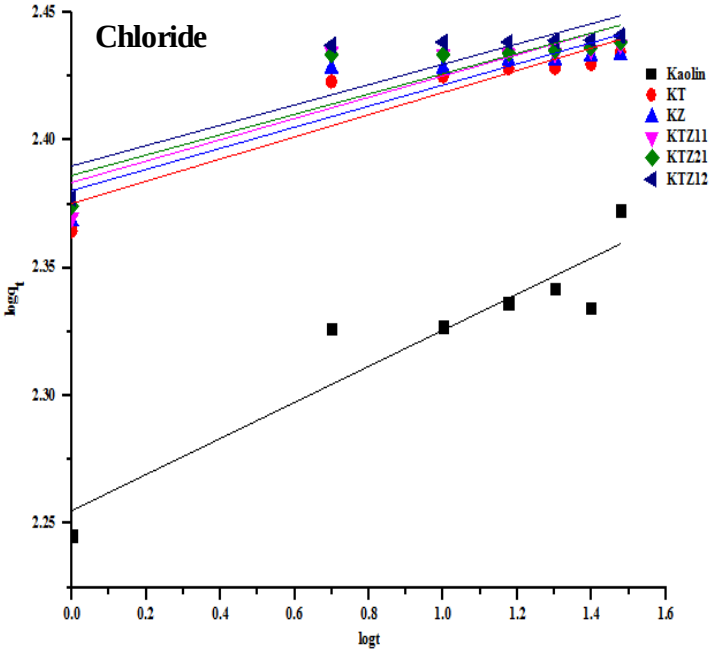

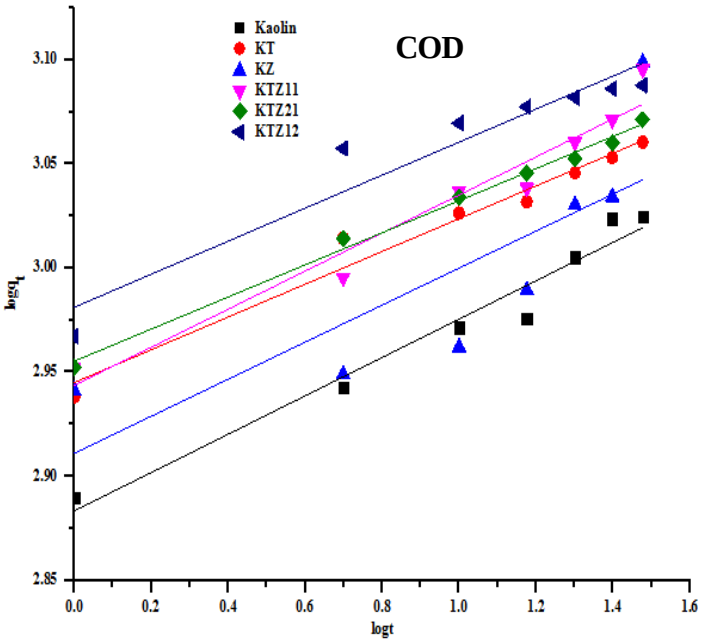

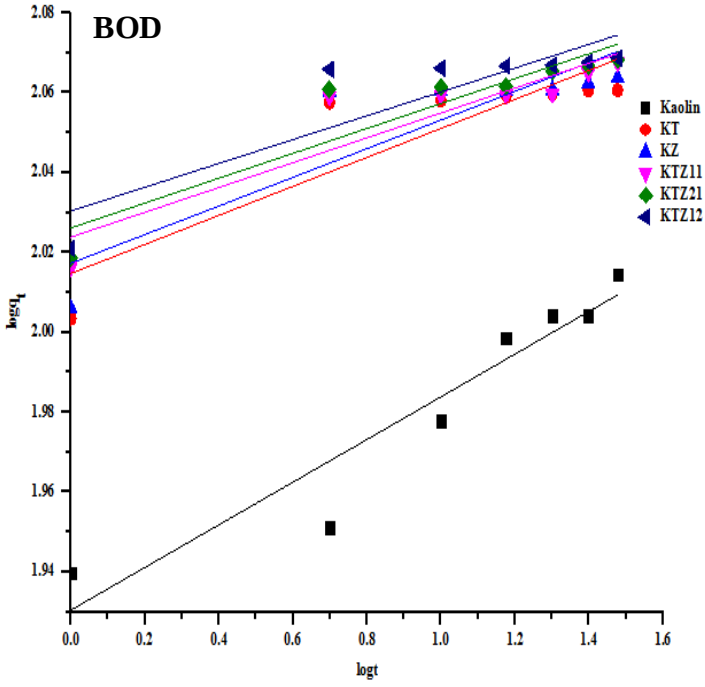

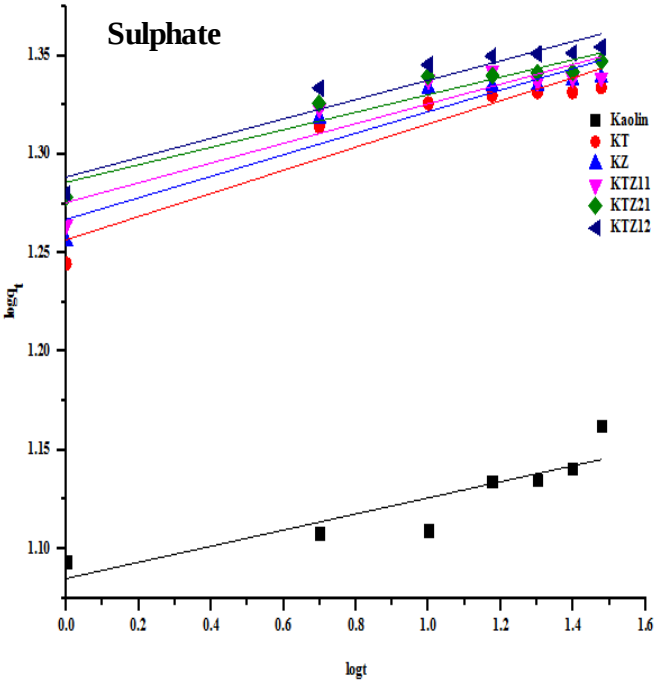

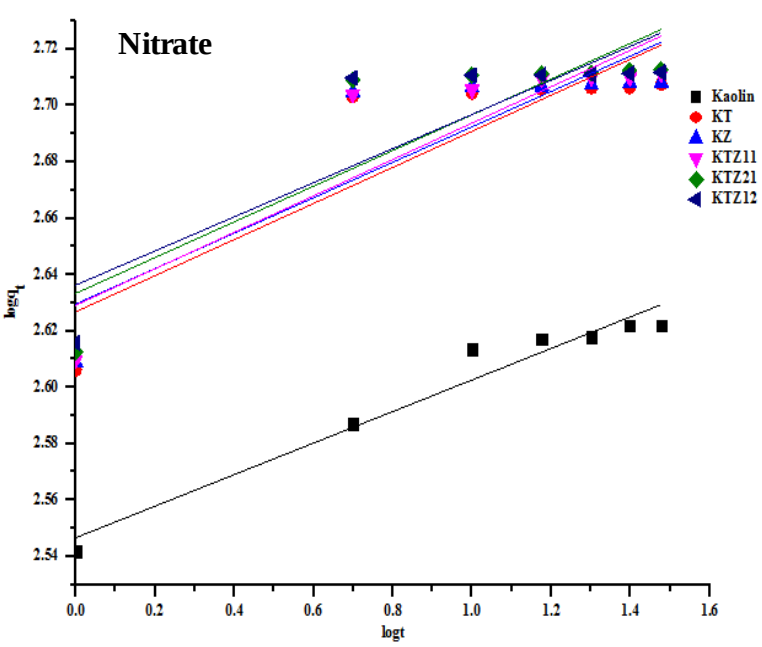
Nitrate
Kaolin
KT
KZ
KTZ11
KTZ21
KTZ12
logqt
logt

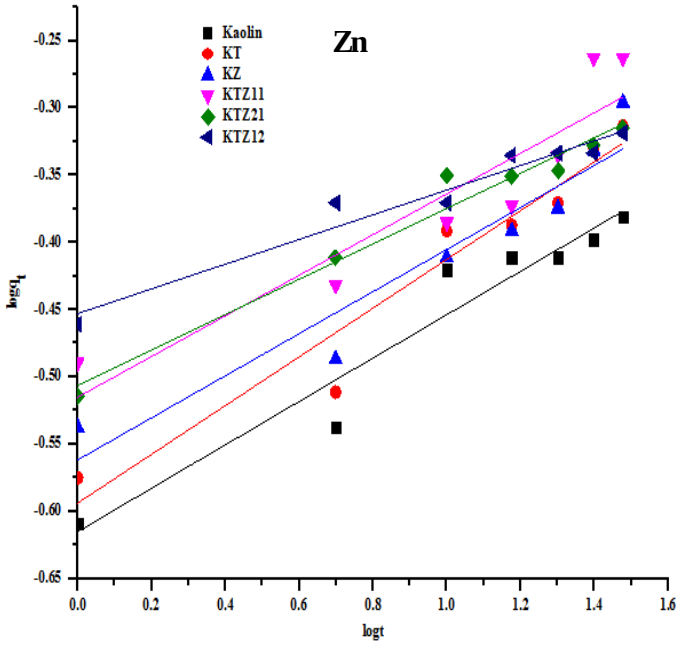
Zn
Kaolin
KT
KZ
KTZ11
KTZ21
KTZ12
logqt
logt

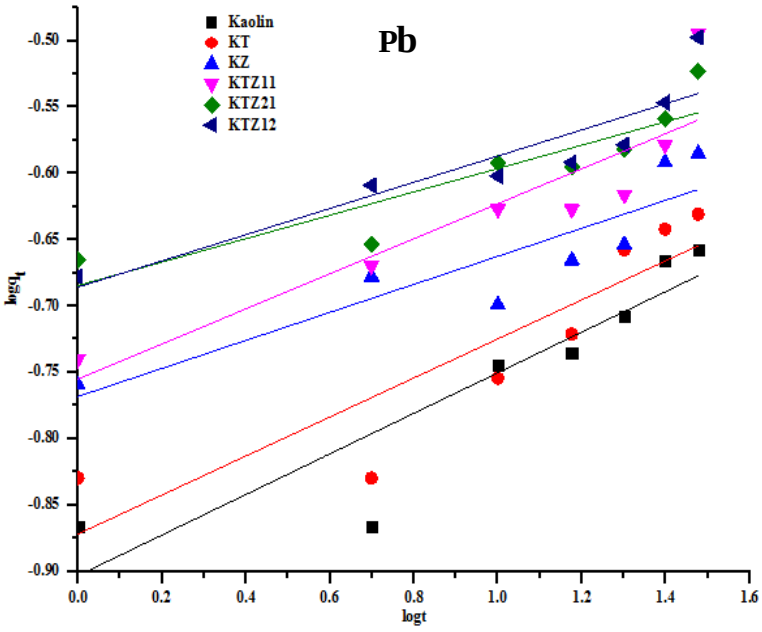
Pb
Kaolin
KT
KZ
KTZ11
KTZ21
KTZ12
logqt
logt

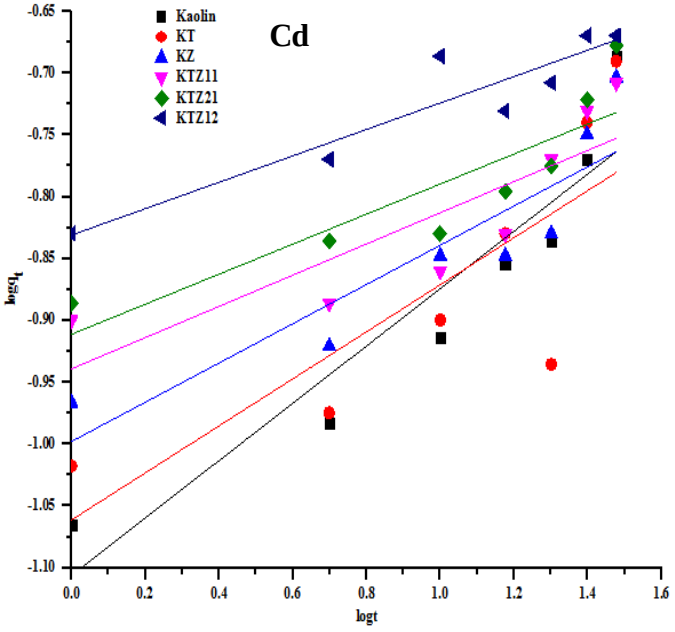
Cd
Kaolin
KT
KZ
KTZ11
KTZ21
KTZ12
logqt
logt

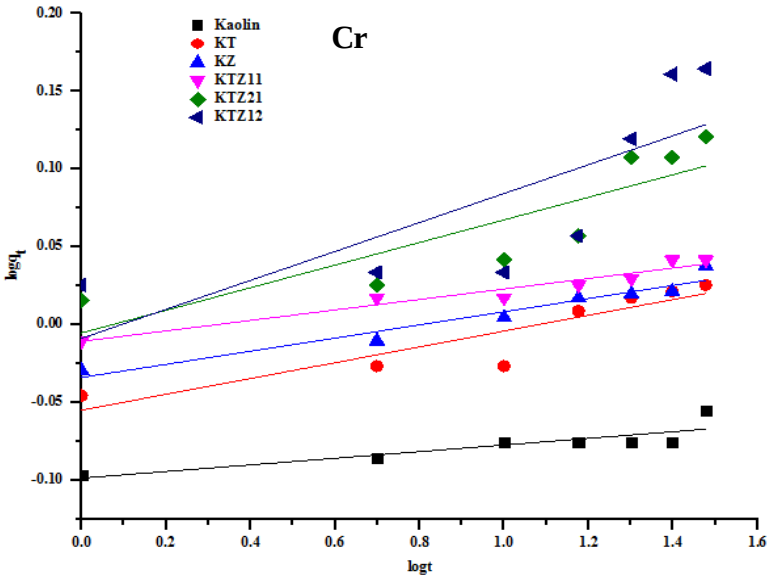
Cr
Kaolin
KT
KZ
KTZ11
KTZ21
KTZ12
0.20
0.15
0.10
0.05
0.00
-0.05
-0.10
logq
0.0
0.2
0.4
0.6
0.8
1.0
1.2
1.4
1.6
logt

Appendix G

Bangham Model

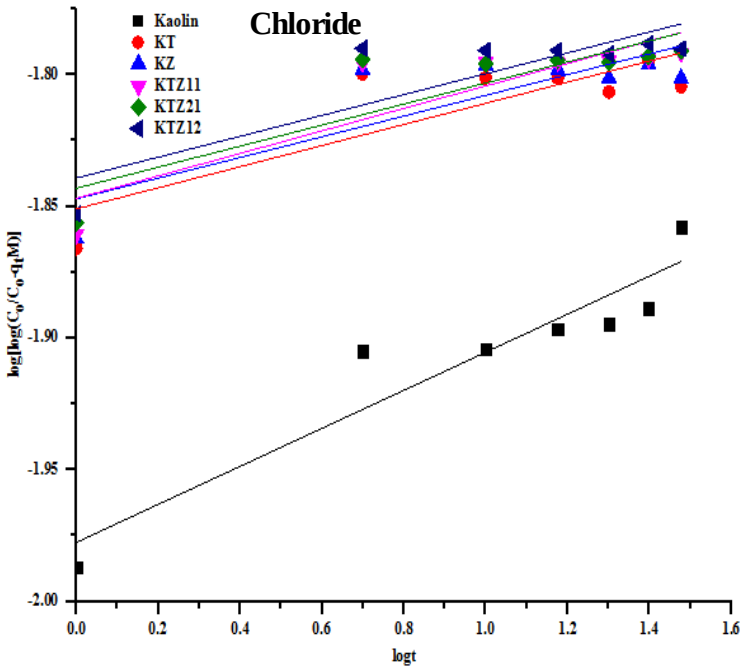

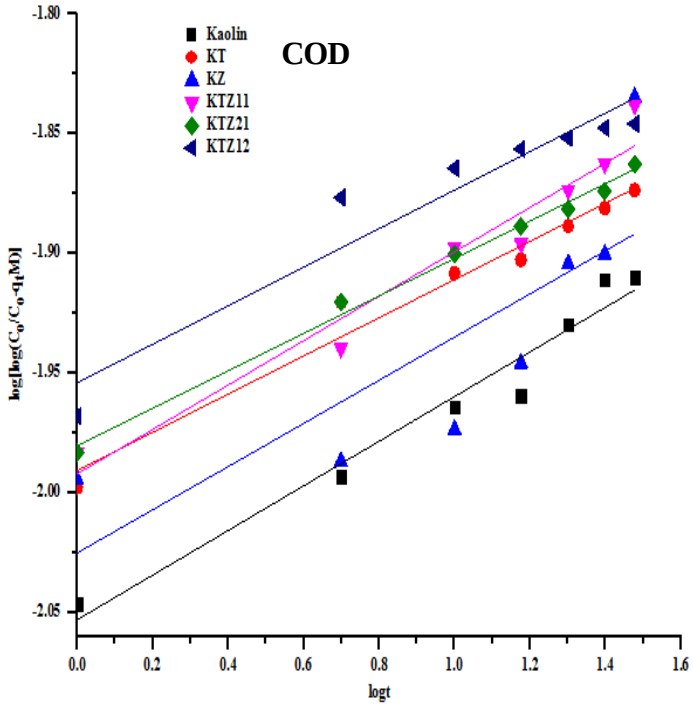

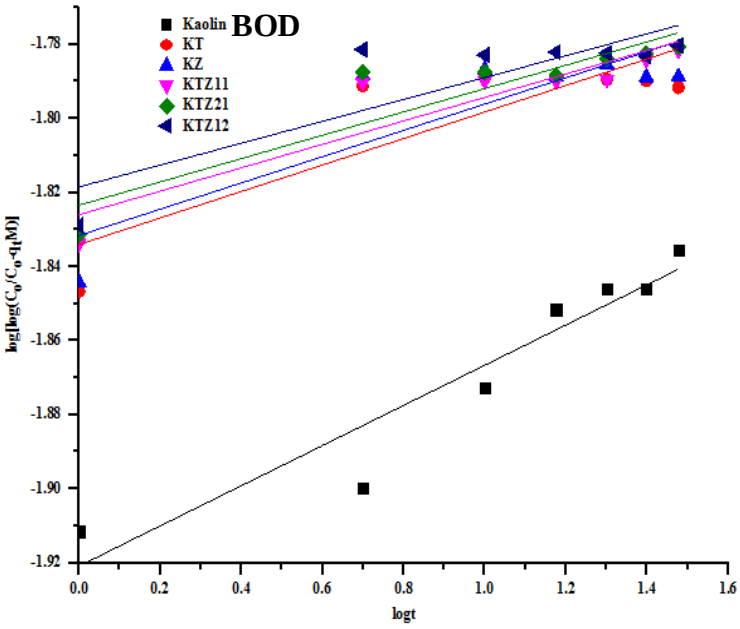

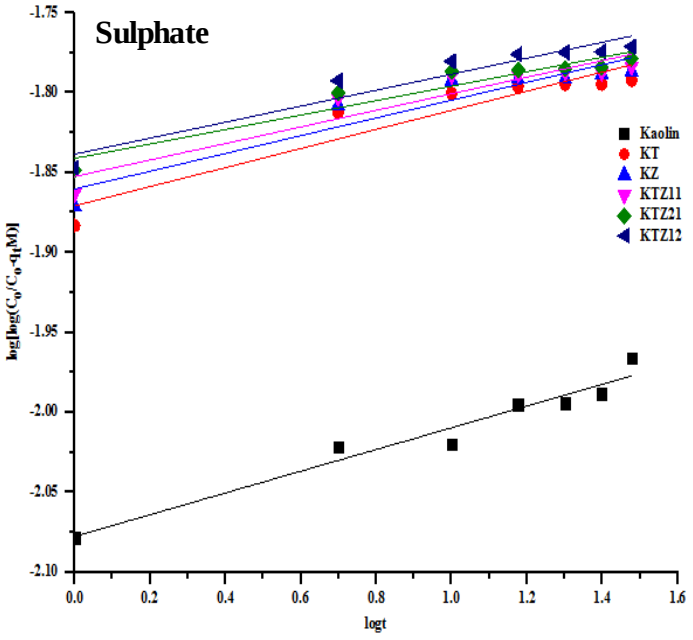

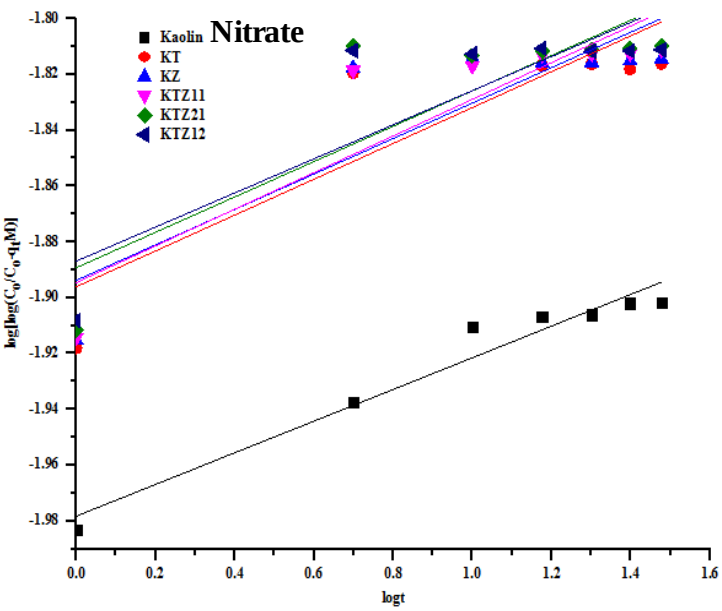
Nitrate
Kaolin
KT
KZ
KTZ11
KTZ21
KTZ12
log[log(C0/C0-qt[M])]
logt

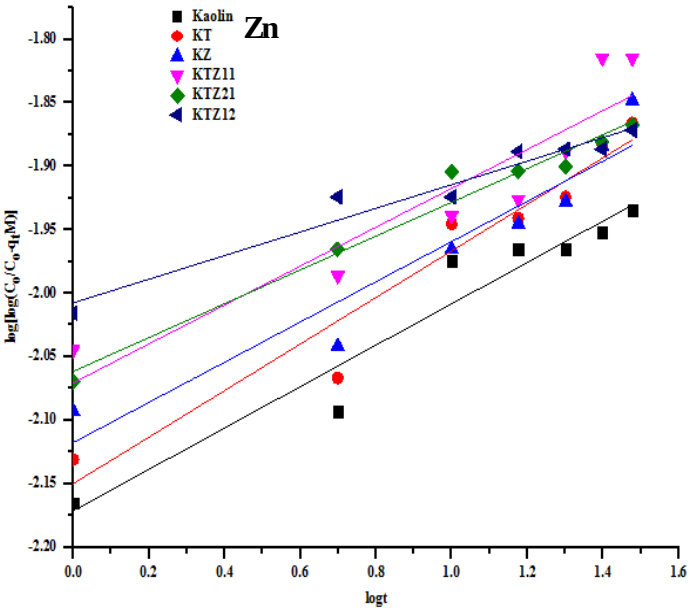
Zn
Kaolin
KT
KZ
KTZ11
KTZ21
KTZ12
log[log(C0/C0-qt[M])]
logt

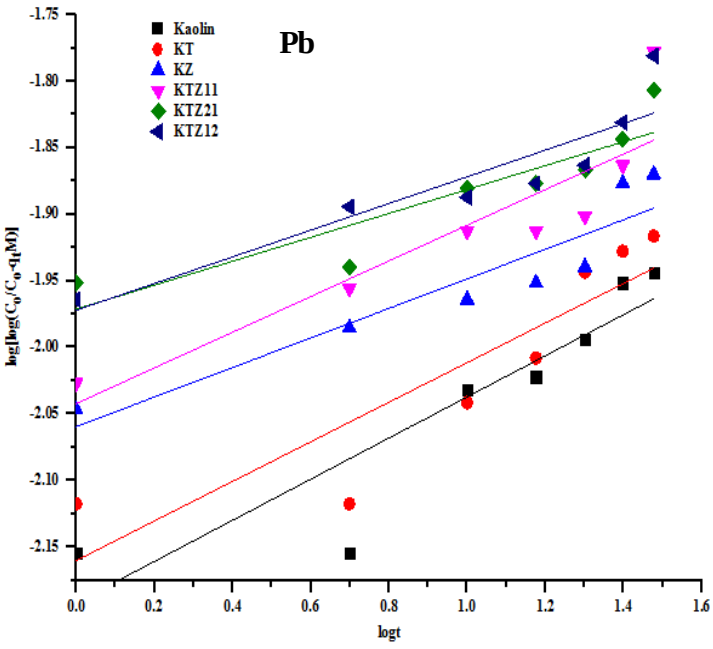
Pb
Kaolin
KT
KZ
KTZ11
KTZ21
KTZ12
log[log(C0/C0-qt[M])]
logt

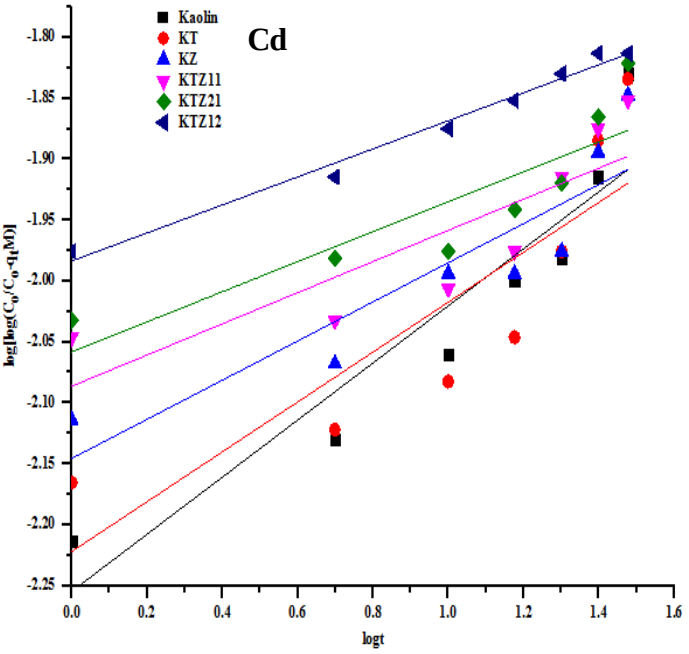
Cd
Kaolin
KT
KZ
KTZ11
KTZ21
KTZ12
log[log(C0/C0-qt[M])]
logt

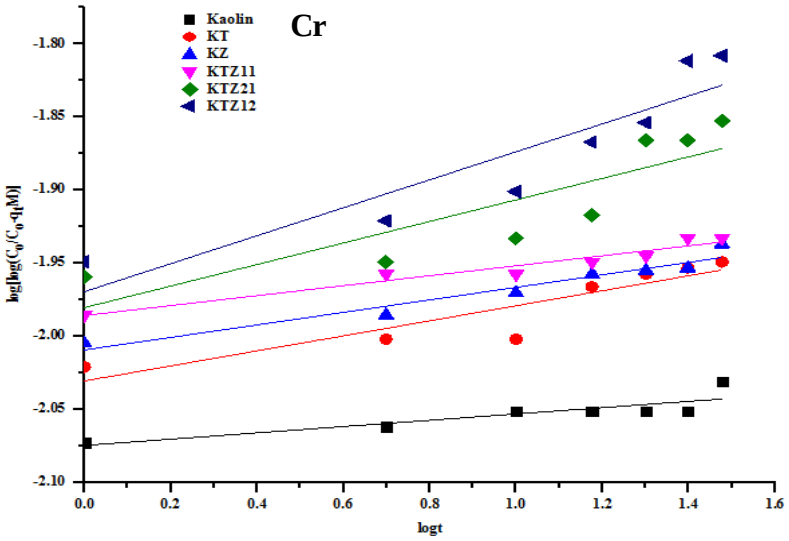
Cr
Kaolin
KT
KZ
KTZ11
KTZ21
KTZ12
-1.80
-1.85
-1.90
-1.95
-2.00
-2.05
-2.10
0.0
0.2
0.4
0.6
0.8
1.0
1.2
1.4
1.6
logt

Appendix H

Avrami Model

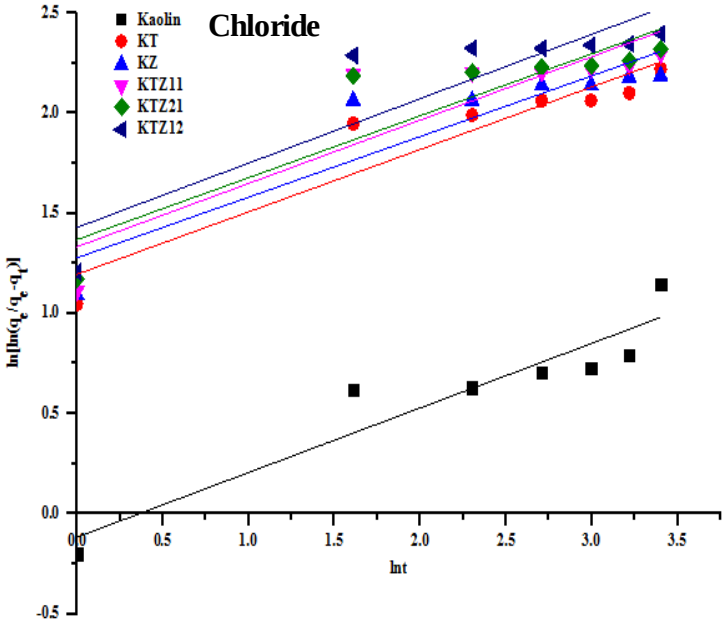

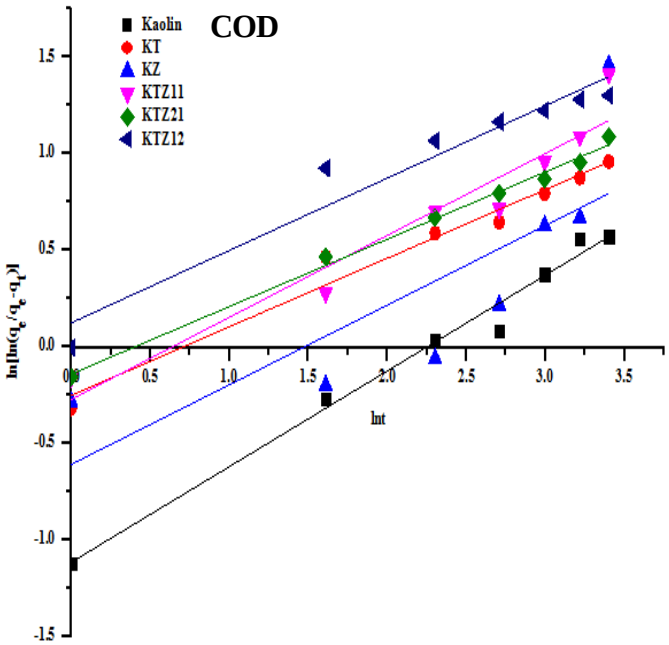

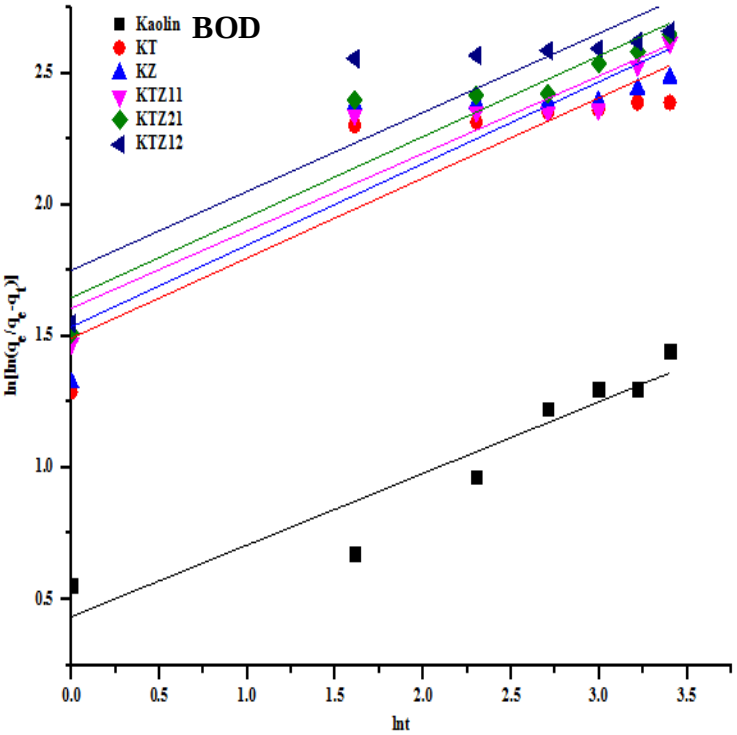

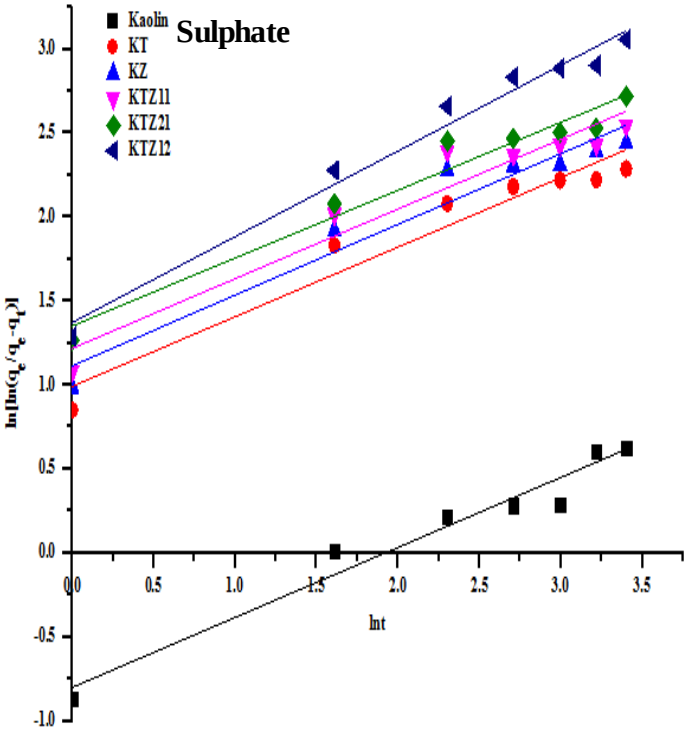

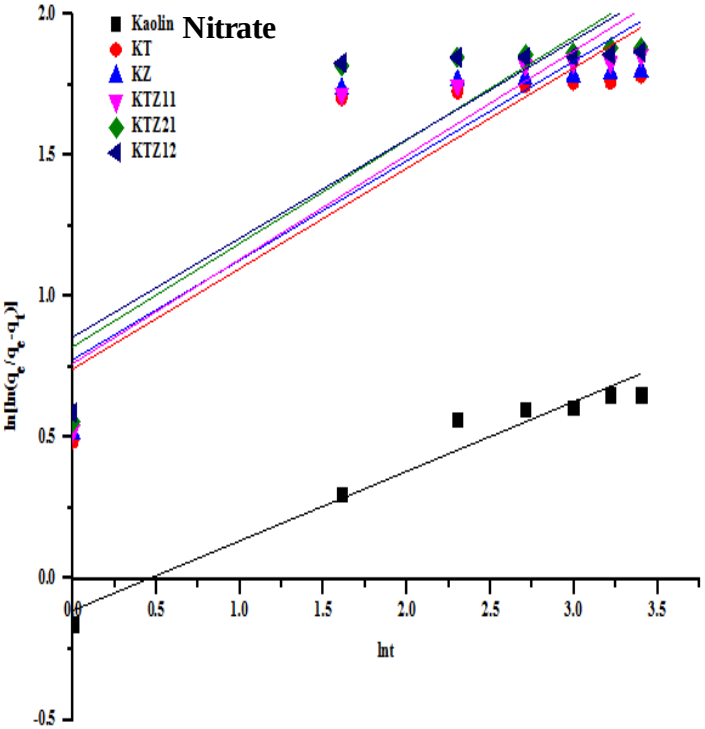
Nitrate
Kaolin
KT
KZ
KTZ11
KTZ21
KTZ12
ln[ln(qe/qe-qt)]
lnt

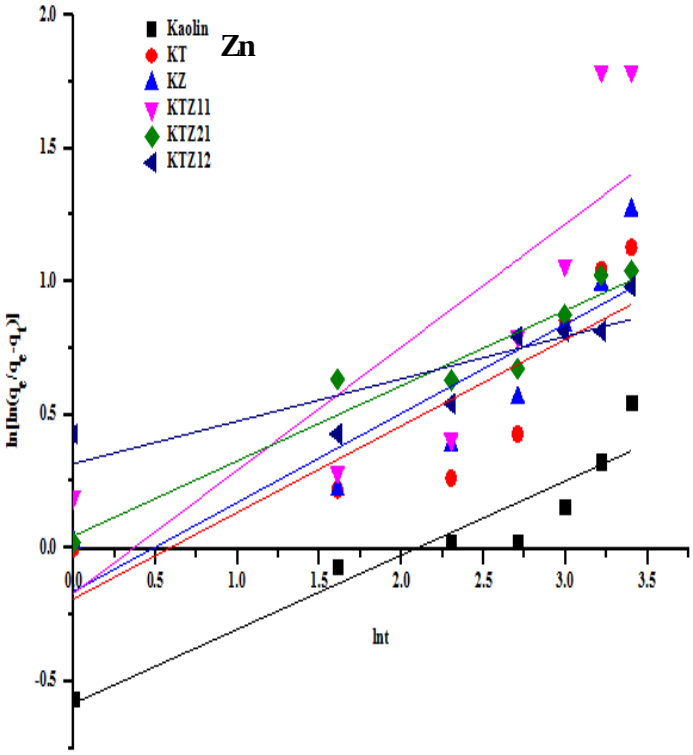
Zn
Kaolin
KT
KZ
KTZ11
KTZ21
KTZ12
ln[ln(qe/qe-qt)]
lnt

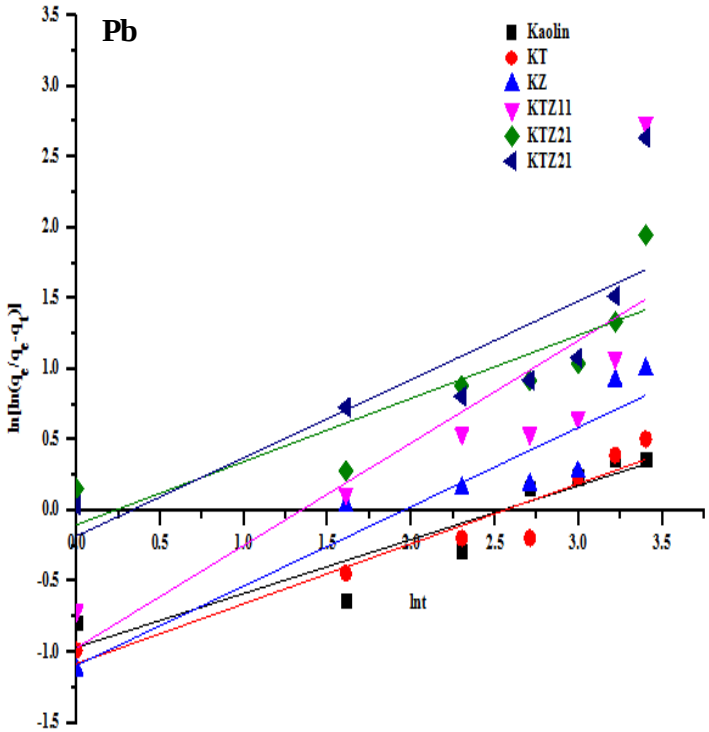
Pb
Kaolin
KT
KZ
KTZ11
KTZ21
KTZ21
ln[ln(qe/qe-qt)]
lnt

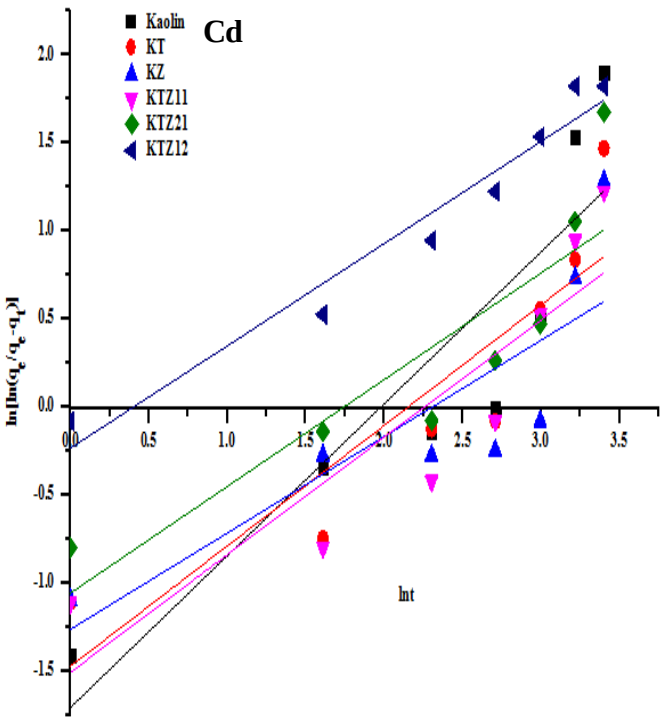
Cd
Kaolin
KT
KZ
KTZ11
KTZ21
KTZ12
ln[ln(qe/qe-qt)]
lnt

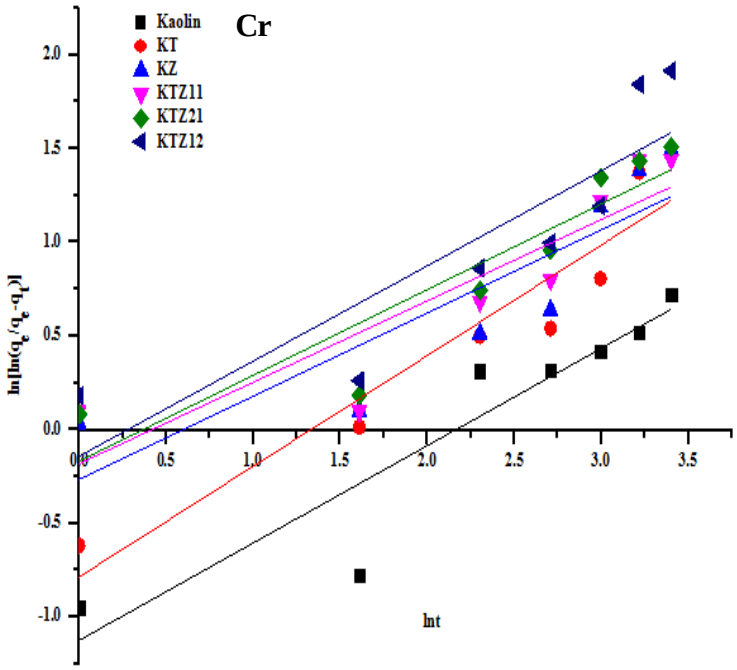
Cr
Kaolin
KT
KZ
KTZ11
KTZ21
KTZ12
ln[ln(q_e/q_e-q_t)]
lnt
2.0
1.5
1.0
0.5
0.0
-0.5
-1.0
0.0
0.5
1.0
1.5
2.0
2.5
3.0
3.5

Appendix I

Thermodynamic Studies

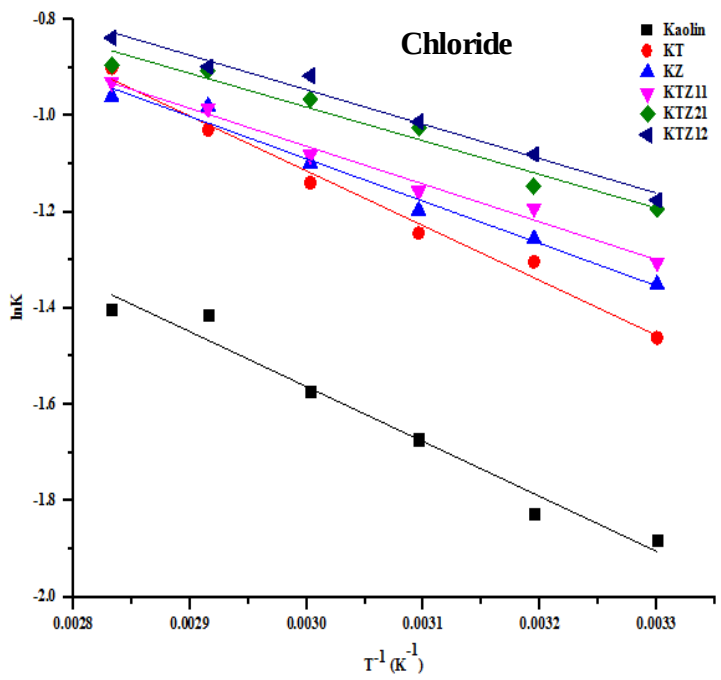

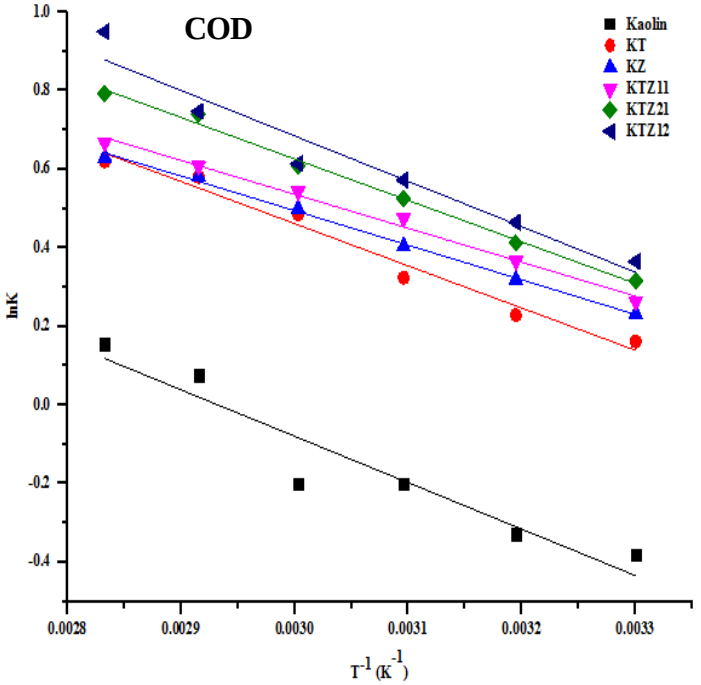

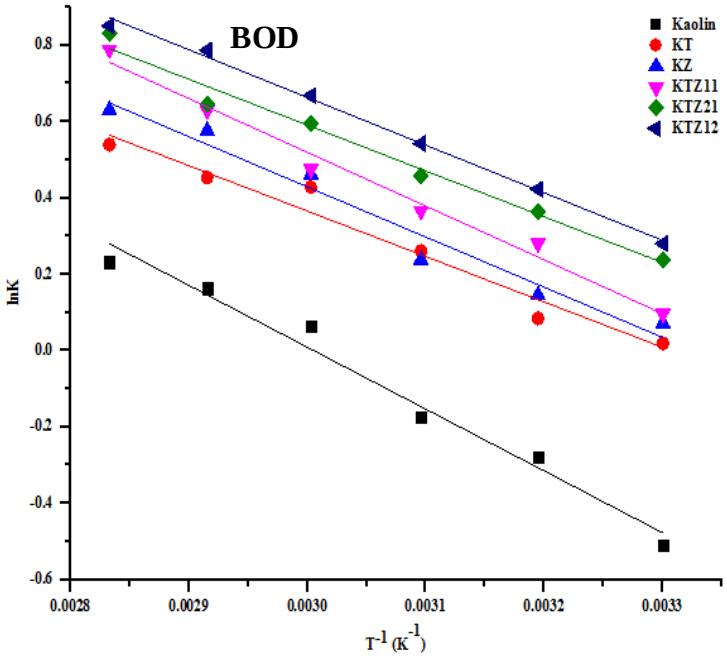

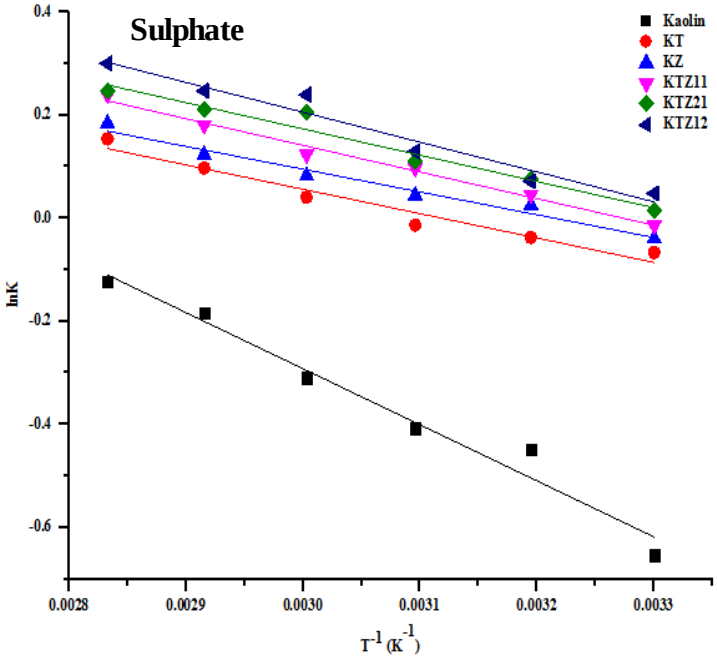

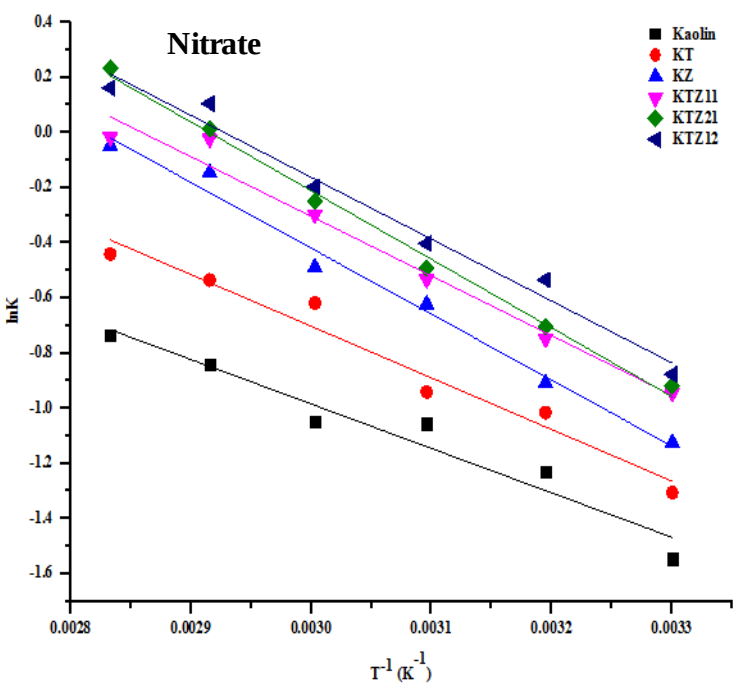
Nitrate
Kaolin
KT
KZ
KTZ11
KTZ21
KTZ12
lnK
T-1 (K-1)

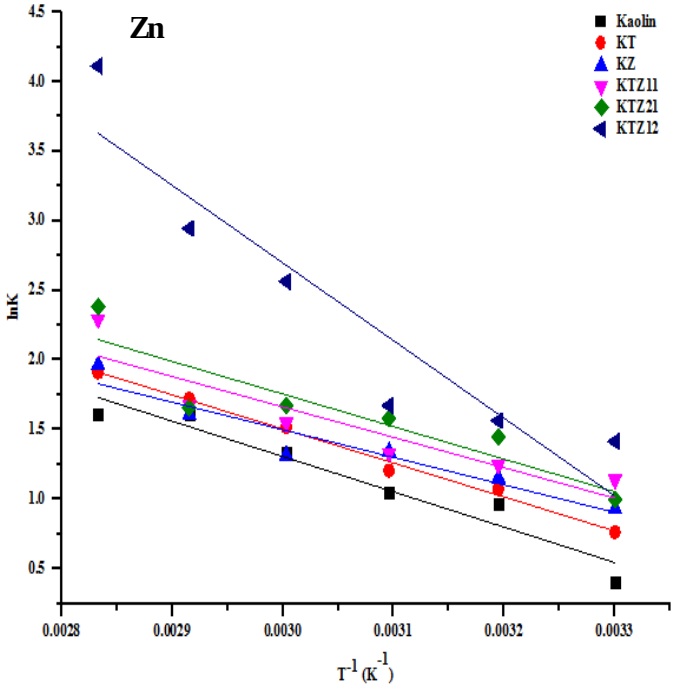
Zn
Kaolin
KT
KZ
KTZ11
KTZ21
KTZ12
lnK
T-1 (K-1)

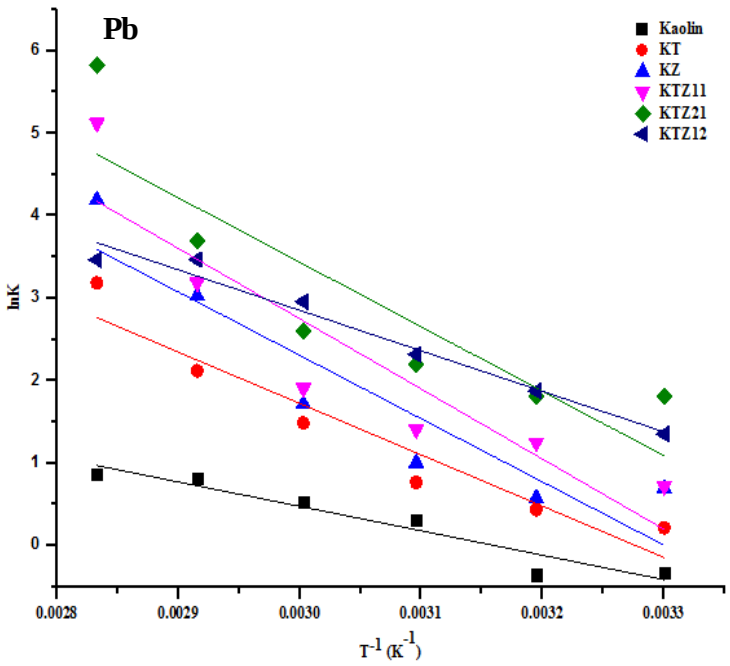
Pb
Kaolin
KT
KZ
KTZ11
KTZ21
KTZ12
lnK
T-1 (K-1)

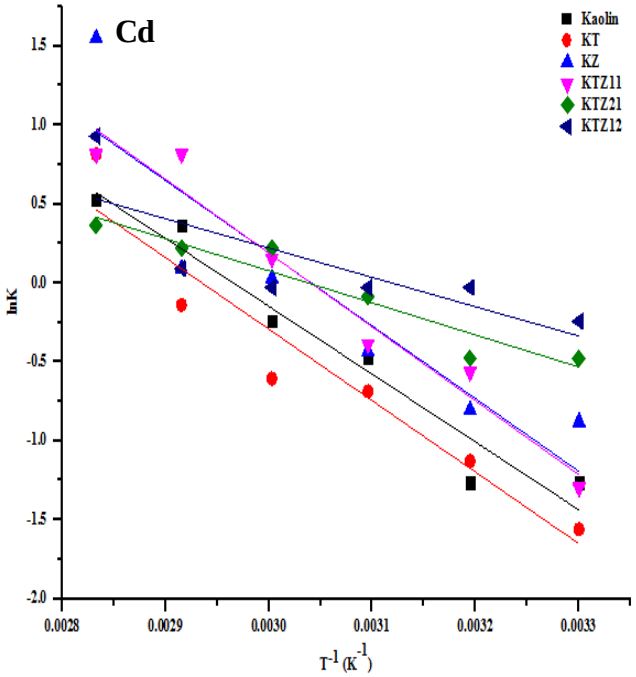
Cd
Kaolin
KT
KZ
KTZ11
KTZ21
KTZ12
lnK
T-1 (K-1)

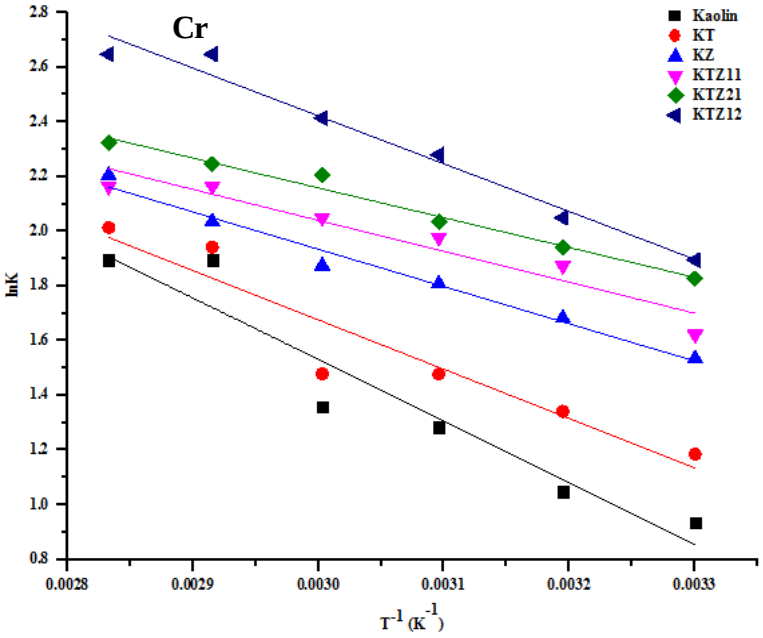
Cr
Kaolin
KT
KZ
KTZ11
KTZ21
KTZ12
lnK
T-1 (K-1)
2.8
2.6
2.4
2.2
2.0
1.8
1.6
1.4
1.2
1.0
0.8
0.0028
0.0029
0.0030
0.0031
0.0032
0.0033

Appendix J

Preparation of reagents

All reagents used for this analysis were of Analytical grade and were used without further purification. Deionized water was used for the preparation of all reagents. All apparatus utilized in this study were washed with detergent and rinsed thoroughly with deionized water and then dried in an oven. The calculation of mole for the preparation of the concentrations of liquid reagents was achieved as follows:

$$\text{Mole} = \frac{\text{S.G} \times \%\text{Purity} \times 10}{\text{M.W}} \qquad (3.1)$$

where S.G = Specific gravity and M.W = Molecular weight

Preparation of 0.05 M of $[Cu(EDA)_2]^{2+}$ Solution

About 50.0 cm^3 of 1.0 M $CuCl_2$ and 102.0 cm^3 of 1.0 M ethylenediamine $[Cu(EDA)_2]^{2+}$ solutions were thoroughly mixed in a conical flask. The slight excess of the amine ensured a complete formation of the complex reaction. The solution was diluted to 1000 cm^3 de-ionized water and 0.05 M $[Cu(en)_2]^{2+}$ solution was obtained.